
Multi-Photon Entanglement

Experimental Observation, Characterization, and
Application of up to Six-Photon Entangled States

Witłef Wieczorek



München 2009

Multi-Photon Entanglement

**Experimental Observation, Characterization, and
Application of up to Six-Photon Entangled States**

Witlef Wieczorek

Dissertation
an der Fakultät für Physik
der Ludwig-Maximilians-Universität
München

vorgelegt von
Witlef Wieczorek
aus Berlin

München, den 03.11.2009

Erstgutachter: Prof. Dr. Harald Weinfurter

Zweitgutachter: Prof. Dr. Steffen Glaser

Tag der mündlichen Prüfung: 17.12.2009

Nicht die Notwendigkeit,
sondern der Zufall ist voller Zauber.

Milan Kundera, *Die unerträgliche
Leichtigkeit des Seins*

Contents

Abstract	xv
Zusammenfassung	xvi
1 Introduction	1
2 Multi-partite entanglement	5
2.1 Classifications of quantum states	6
2.1.1 Qubit notation and entanglement	6
2.1.2 Classifications	9
2.2 Entanglement detection and measures of entanglement	13
2.2.1 Entanglement detection	13
2.2.2 Entanglement measures	18
2.3 Experimental observation using photons	22
2.3.1 Photon sources	23
2.3.2 Photon processing	28
3 Observation of a family of four-photon entangled states	33
3.1 Multi-photon interference	34
3.2 Entanglement detection	40
3.3 Entanglement properties	46
3.4 Publications	48
P3.1 Experimental Observation of an Entire Family of Four-Photon En- tangled States	49
P3.2 Multi-Photon Interference as a Tool to Observe Families of Multi- Photon Entangled States	53
4 Four-qubit entanglement for revealing anyonic features	63
4.1 Anyons, the quantum Hall effect, topological quantum computation	64
4.2 Toric code	67
4.3 Minimal implementation	70
4.4 Publication	74
P4.1 Revealing anyonic features in a toric code quantum simulation	75

5	Symmetric entangled Dicke states of up to six photons	85
5.1	High power SPDC photon source based on a femtosecond UV cavity	86
5.2	Entanglement detection, properties, and applications	91
5.3	Phase estimation	96
5.4	Publications	101
P5.1	Experimental Entanglement of a Six-Photon Symmetric Dicke State	102
P5.2	Multiqubit entanglement engineering via projective measurements .	106
P5.3	Practical methods for witnessing genuine multi-qubit entanglement in the vicinity of symmetric states	114
P5.4	Ultraviolet enhancement cavity for ultrafast nonlinear optics	132
6	Conclusions and outlook	139
	Appendix	142
A	SPDC photon state	143
A.1	Non-collinear type II SPDC	143
A.2	Collinear type II SPDC	146
B	Measurement settings and counting statistics	149
B.1	Measurement settings	149
B.2	Counting statistics	155
C	SPDC higher order noise	157
C.1	Model	158
C.2	Higher order noise in the four-photon family experiment	160
C.3	Higher order noise in the six-photon Dicke experiment	162
D	FPGA controlled coincidence logic	167
	Publication list	171
	Bibliography	173
	Acknowledgements	198
	Curriculum vitae	201

List of Figures

2.1	Bloch sphere	7
2.2	Separability and classification of two- and three-qubit states	10
2.3	Graph states and Dicke states	12
2.4	Entanglement witness	15
2.5	Type II SPDC sources	25
2.6	Beam splitter and polarization analysis	29
3.1	Schematic layouts for SPDC experiments	36
3.2	Setup for the observation of the family of four-photon entangled states	37
3.3	Two- and four-photon HOM-type interference	40
3.4	Detection of entanglement for the states $ \Psi_4(\alpha)\rangle$	43
3.5	3-tangle and concurrence for states obtained of $ \Psi_4(\alpha)\rangle$	47
4.1	Braiding of particles in three and two dimensions	65
4.2	Quantum Hall effect	66
4.3	Toric code	69
4.4	Correlation function for demonstrating anyonic features and statistics	73
5.1	Time and frequency domain picture of ultrashort pulses	88
5.2	Experimental setup of femtosecond UV cavity and $ D_6^{(3)}\rangle$ state	89
5.3	Calculated power enhancement for the implemented UV cavity	90
5.4	Telecloning with $ D_6^{(3)}\rangle$	96
5.5	Correlation function of the states $ D_6^{(3)}\rangle$ and $ \text{GHZ}_6\rangle^+$	98
5.6	Measured correlation functions for $ D_6^{(3)}\rangle$	99
5.7	Improved phase sensitivity using the state $ D_6^{(3)}\rangle$	100
C.1	Model of the setup for the family $ \Psi_4(\alpha)\rangle$ experiment	159
C.2	Modeled fidelity and count rate for the family $ \Psi_4(\alpha)\rangle$ experiment	161
C.3	Modeled two-, four- and six-photon counts for the state $ D_6^{(3)}\rangle$	163
C.4	Fitted τ and η_{det} for different pump powers	165
D.1	Diagram for the FPGA realizing a coincidence unit	169

List of Tables

5.1	Fidelity of the state $ D_6^{(3)}\rangle$ and states derived thereof	92
5.2	Experimental witness values for the state $ D_6^{(3)}\rangle$ and states derived thereof	93
B.1	Measurement settings and polarization analysis	150
B.2	Measurement settings for the four-photon family experiment	151
B.3	Measurement settings for the six-photon Dicke experiment 1	152
B.4	Measurement settings for the six-photon Dicke experiment 2	153
B.5	Measurement settings for the six-photon Dicke experiment 3	154
B.6	Counting statistics for the four-photon family experiment	155
B.7	Counting statistics for the six-photon Dicke experiment	156
C.1	Model parameters for the four-photon family experiment	161
C.2	Model parameters for the $ D_6^{(3)}\rangle$ experiment	163
C.3	Modeled expectation values for the $ D_6^{(3)}\rangle$ experiment	163

List of Abbreviations

AMO	atomic, molecular and optical
APD	avalanche photo diode
BBO	β -barium-borate
BS	beam splitter
FPGA	field programmable gate array
FWHM	full width at half maximum
GDD	group delay dispersion
GHZ	Greenberger Horne Zeilinger
HOM	Hong-Ou-Mandel
HWP	half-wave plate
IR	infrared
LBO	lithium-triborate
LHV	local hidden variable
LOCC	local operations and classical communication
LU	local unitary
PBS	polarizing beam splitter
PPT	positive partial transposition
QHE	quantum Hall effect
QWP	quarter-wave plate
SFWM	spontaneous four-wave mixing

SLOCC stochastic local operations and classical communication

SNL shot noise limit

SPDC spontaneous parametric down conversion

Ti:Sa titanium:sapphire

USB universal serial bus

UV ultraviolet

YVO yttrium-vanadate

Abstract

Major efforts in quantum information science are devoted to the development of methods that are superior to the one of classical information processing, for example the quantum computer or quantum simulations. For these purposes, superposition and entangled states are considered a decisive resource. Furthermore, since the early days of quantum mechanics, entanglement has revealed the discrepancy between the quantum mechanical and the everyday life perception of the physical world. This combination of fundamental science and application-oriented research makes the realization, characterization, and application of entanglement a challenge pursued by many researchers.

In this work, the observation of entangled states of polarization encoded photonic qubits is pushed forward in two directions: flexibility in state observation and increase in photon rate. To achieve flexibility two different schemes are developed: setup-based and entanglement-based observation of inequivalent multi-photon states. The setup-based scheme relies on multi-photon interference at a polarizing beam splitter with prior polarization manipulations. It allows the observation of a family of important four-photon entangled states. The entanglement-based scheme exploits the rich properties of Dicke states under particle projections or loss in order to obtain inequivalent multi-photon entangled states. The observed states are characterized using the fidelity and entanglement witnesses.

An increase in photon rate is crucial to achieve entanglement of higher photon numbers. This holds especially, when photon sources are utilized that emit photons spontaneously. To this end, a new photon source is presented based on a femtosecond ultraviolet enhancement cavity and applied to the observation of the six-photon Dicke state with three excitations.

The implemented schemes not only allow the observation of inequivalent types of entanglement, but also the realization of various quantum information tasks. In this work, the four-photon GHZ state has been used in a quantum simulation of a minimal instance of the toric code. This code enables the demonstration of basic properties of anyons, which are quasiparticles distinct from bosons and fermions. Further, the six-photon Dicke state has been applied for quantum metrology: It allows one to estimate a phase shift with a higher precision than by using only classical resources.

Altogether, a whole series of experiments for observing inequivalent multi-photon entangled states can now be substituted by a single experimental setup based on the designs developed in this work. In addition to this new approach of photon processing, a novel photon source has been implemented, paving the way to realizations of applications requiring higher photon numbers.

Zusammenfassung

Ein Schwerpunkt der Quanteninformation liegt bei der Entwicklung von Methoden, die klassischer Informationsverarbeitung überlegen sind, zum Beispiel der Quantencomputer oder Quantensimulationen. Dafür werden Überlagerungszustände und verschränkte Zustände als entscheidende Ressource betrachtet. Des Weiteren hat Verschränkung seit den Anfängen der Quantenmechanik Widersprüche zwischen der quantenmechanischen und der alltäglichen Wahrnehmung der physikalischen Welt aufgezeigt. Die Verbindung von angewandter und grundlagenorientierter Forschung macht die Realisierung, Charakterisierung und Anwendung der Verschränkung zu einer Herausforderung, die viele Forscher verfolgen.

In dieser Arbeit wird die Realisierung verschränkter Zustände von polarisationskodierten photonischen Qubits hinsichtlich zweier Aspekte weiterentwickelt: Flexibilität bei der Zustandsherstellung und Erhöhung der Photonenzählrate. Um Flexibilität zu erreichen, werden zwei Schemen vorgestellt: aufbaubasierte und verschränkungs-basierte Herstellung verschiedener Zustände. Dem aufbaubasierten Schema liegt Mehrphotoneninterferenz an einem Strahlteiler mit vorheriger Polarisationsmanipulation zugrunde. Dadurch wird die Beobachtung einer Familie von Vierphotonen-Zuständen ermöglicht. Das verschränkungs-basierte Schema hingegen nutzt die Eigenschaften von Dickezuständen bei Projektion oder Verlust von Teilchen aus, um verschiedene Zustände zu erhalten. Die beobachteten Zustände werden durch ihre Güte und Verschränkungszeugen charakterisiert.

Eine Steigerung der Photonenzählrate ist für Mehrphotonenexperimente notwendig, insbesondere wenn Lichtquellen eingesetzt werden, die spontan Photonen emittieren. Zu diesem Zweck wird eine neue Photonenquelle präsentiert, die auf einem Femtosekundenresonator im ultravioletten Spektralbereich basiert und für die Beobachtung eines Sechspotonen-Dickezustands verwendet wird.

Die implementierten Schemen erlauben neben der Beobachtung unterschiedlicher Verschränkungsarten auch die Realisierung verschiedener Quanteninformationsaufgaben. In dieser Arbeit wird der Vierphotonen-GHZ-Zustand für eine Quantensimulation eines minimalen Toriccode angewandt. Dieser Code ermöglicht die Demonstration grundlegender Eigenschaften von Anyonen, die Quasiteilchen darstellen, die sich von Bosonen und Fermionen unterscheiden. Der Sechspotonen-Dickezustand wird für die Quantenmetrologie verwendet: Er erlaubt eine Phasenänderung mit größerer Genauigkeit zu messen als mit klassischen Mitteln allein möglich ist.

Alles in allem können verschiedene Experimente zur Beobachtung verschränkter Photonen-zustände basierend auf den in dieser Arbeit entwickelten Schemen durch einen einzigen Aufbau ersetzt werden. Zusätzlich wurde eine neuartige Photonenquelle implementiert, die die Realisierung von Anwendungen ermöglicht, die höhere Photonenzahlen benötigen.

Chapter 1

Introduction

The development of quantum mechanics in the early 20th century led to a paradigm shift in the field of physics. Quantum mechanics introduced, amongst others, quantization of energy as well as complementarity. The latter occurs for example in the duality of the wave and particle behavior of both, light and matter. The great success of quantum mechanics is evidenced by an accurate description of natural phenomena and led for example to the invention of the semiconductor transistor and the laser. These two inventions, besides others, enable nowadays the rapid processing of information. However, information, which has a huge impact on human society, is still encoded using classical means. Only towards the end of the 20th century it has been discovered that by exploiting particular features of quantum mechanical systems like superposition states a more powerful information processing is possible. This has initiated a new research field, called quantum information science [1].

Quantum mechanical states can be on one hand applied for information tasks, while on the other hand they have initiated fundamental questions about the relationship of quantum mechanics to our everyday life. Already in 1935 Erwin Schrödinger illustrated in his famous cat paradox a quantum mechanical superposition state with the unimaginable example of a cat being dead *and* alive at the same time [2]. Such a state of a macroscopic object has never been observed. In contrast, in the microscopic world superposition states of photons or atoms indeed occur and have been prepared and observed. For which object size the transition from the microscopic to the macroscopic world occurs is still under intense research [3].

Superposition states between many particles can be even more “non-classical” as evidenced by entangled states. Essentially, for an entangled state only the state of the entire system is well defined, whereas each separate particle is in a completely unknown state. Albert Einstein, Boris Podolsky, and Nathan Rosen were puzzled by these states and identified in 1935 that the assumption of quantum mechanics as a complete theory leads to a contradiction with a predetermination of physical reality or, in other words, with a local and realistic description of nature [4]. Locality imposes space-like separation of measurement events or, more specifically, that the result of a measurement on one system is independent of operations performed on another system with which it has interacted in the past.

“Reality” is understood in the sense that measurement results can be described by predetermined, hidden variables. Only 30 years later in 1964 John Bell [5] could formulate an experimentally testable condition of this question based on a local *and* realistic description of measurement results. Based on these assumptions John Bell derived an inequality that is violated by some quantum mechanical entangled states. Indeed, subsequent experiments give strong evidence of this violation [6–9] and, therefore, imply that the quantum mechanical description of the world excludes locality and realism to hold at the same time. For particular entangled states this violation becomes even more conclusive for an increasing number of particles [10].

Nowadays, superposition and entangled states of many particles are studied in quantum information with respect to their fundamental implications and possible applications. This has led to different research areas of quantum information [1, 11, 12], amongst these are quantum simulation [13], quantum computation [14, 15], quantum communication [16–18], and quantum metrology [19]. These research fields exploit superposition or entangled states of many particles in order to improve classical information processing. Different physical systems are employed for their implementation and can be roughly distinguished into atomic, molecular and optical (AMO) and solid state-based systems, see the recent *Nature Insight* [20] and *Science Feature* [21] articles. AMO systems include for example photons [22–24], trapped ions [25], atoms in optical lattices [26] or in optical cavities [27], or nuclear spins of molecules [28, 29]. Solid state systems can be based on quantum dots [30], superconducting elements [31], or color centers in diamond [32]. The necessary encoding of information can be achieved in two different ways depending on the available degrees of freedom of the system: in discrete degrees of freedom like polarization of photons or internal atomic states, or alternatively, by using continuous variables like the electric field quadrature components or the collective atomic spin. The variety of experimental implementations has rapidly increased, as each and every system exhibits its advantages and drawbacks. Current benchmarks that characterize the usefulness of a system for quantum information processing are for example its susceptibility to decoherence or its scalability [33]. Hybrid approaches promise to combine advantages of several systems, for example the storage of information by using trapped ions and the transmission of information by using photons. Currently, the highest number of individually addressable entangled particles is around ten: two entangled superconducting qubits [34, 35], three entangled carbon nuclear and electronic spins in diamond [32], six entangled photons [36–40], eight entangled ions [41], twelve nuclear spins of a molecule [29]. This experimental status reflects the difficulty in creating and controlling superposition states of many particles with unprecedented accuracy and shows that it is still a long way towards entanglement of hundreds of particles. This poses the question if the latter can ever be achieved, as it is still an open issue at which system size coherence disappears and induces the transition from a quantum to the classical world.

In this work photons are the chosen physical system for the experimental implementation of particular quantum information tasks. Information is encoded in the polarization degree of freedom yielding a two-level system, called qubit. Photons are the most successful physical system for the observation of multi-partite entanglement and proof-of-principle

demonstrations of a diversity of quantum information applications so far [23]. This is due to the fact that for photons virtually no decoherence takes place and single qubit operations are easy to implement with high accuracy. However, the major drawback of photons, their practically non-existent interaction with each other due to the smallness of the non-linear coupling, prevents a simple implementation of two-qubit gates. However, in 2001 Emanuel Knill, Raymond Laflamme, and Gerard Milburn have shown that despite this drawback linear optical quantum computation based on photons can be implemented efficiently by using single photon sources, linear optical elements and photon number resolving detectors [42]. The necessary non-linearity is shifted into the detection process [43]. An improved scheme requiring less physical resources [44] has been discovered based on a combination of the latter scheme and the measurement-based quantum computation model [45]. The latter model reduces quantum computation to the creation of a suitable multi-partite entangled state and subsequent single qubit measurements [46].

To date, true single photon sources for the realization of scalable implementations of linear optical quantum computation schemes or for multi-partite entanglement creation are still under development [47–49]. Instead, the probabilistic process of spontaneous parametric down conversion (SPDC) is widely applied to create the necessary photons [50]. In addition, one can directly exploit the photonic quantum correlations created by the SPDC source itself [51, 52]. Subsequent processing with linear optical elements and conditional detection allows one to observe the desired quantum states or to implement proof-of-principle demonstrations of quantum information applications.

In this work, the observation of entangled photonic states is pushed forward in two directions: flexibility [38, 53–55] (the corresponding publications are displayed in this work as publ. P3.1, P3.2, P5.1, and P5.2), and an increased rate in the available photons [56] (see publ. P5.4). Furthermore, multi-photon entangled states are applied for a quantum simulation of anyonic features [57] (see publ. P4.1) and also for precision measurements.

The current approach to multi-photon state observation requires for each and every state a specific SPDC source and tailored linear optical setup [58–61]. It is demonstrated in this work that this is not necessary. Rather, by using the same experimental setup the observation of an entire family of four-photon, highly entangled states is achieved by changing a single, easily accessible parameter [53] (see publ. P3.1). The scheme is based on multi-photon interference of an entangled state at a beam splitter with prior polarization manipulations [54] (see publ. P3.2). The family of four-photon entangled states consists of inequivalent types of entangled states, amongst these are the four-photon Greenberger Horne Zeilinger (GHZ) state [62–64], the four-photon symmetric Dicke state with two excitations [65] and a rotationally invariant state [59]. Though these states have been realized before [59, 64, 65], they can now be observed in a single experimental setup. Additionally, new states are identified that might find potential applications in the future. In the context of measurement-based quantum computation the universality of particular entangled states has been studied [66]. It was found that two-dimensional cluster states are a universal resource, whereas one-dimensional cluster states, GHZ states, and Dicke states are not. However, these states can outperform classical states for particular quantum information tasks, which is made use of in this work.

One of these tasks is the application of the GHZ state for a quantum simulation of anyons [57] (see publ. P4.1). Anyons are particles in the two-dimensional space, whose statistics range continuously from bosonic to fermionic [67, 68] and are expected to be detected in the fractional quantum Hall effect [69]. However, due to the continuous presence of interactions in these systems this is rather difficult and has not been clearly demonstrated so far [70, 71]. Alternatively, abstract spin lattice systems like the toric code allow the realization of anyons as quasiparticle excitations [72, 73]. It turns out that the GHZ state is the ground state of a minimal instance of the toric code. In a quantum simulation thereof, particular anyonic features and their statistical property are demonstrated by performing local operations on the GHZ state.

To entangle even more photons, a common approach is to use higher order SPDC emissions or multiple SPDC sources [36, 52]. However, higher photon numbers are emitted with exponentially decreasing rate resulting in an increase in measurement time for acquiring sufficient statistical data. Therefore, in this work it is demonstrated that the pump power for the SPDC process can be raised by using an ultraviolet (UV) enhancement cavity around the non-linear crystal [56, 74, 75] (see publ. P5.4).

This photon source is applied to the observation of the six-photon entangled symmetric Dicke state with three excitations [38, 39] (see publ. P5.1). Dicke states are an important group of states in quantum information, studied theoretically [76–81] and experimentally [38, 39, 41, 65, 82]. Initially they have been analyzed in the context of enhanced light emission from a cloud of atoms [83]. The implemented six-photon Dicke state possesses remarkable properties, for example a high entanglement persistency against qubit loss [77]. Most importantly, it can be used to obtain inequivalent classes of entanglement of a lower qubit number by means of projective measurements [55] (see publ. P5.2), which has already been identified for its four-qubit pendant [65]. Thus, these states constitute a rich resource of other highly entangled states allowing, in a different way than realized with the four-photon family experiment, a flexible generation of states. For example, observations of five-photon states and the four-photon W state that have not been observed in a linear optical system so far become possible. Tailored entanglement witnesses are used to prove entanglement for any of these states [81] (see publ. P5.3). Further, the six-photon Dicke state can be applied for certain quantum communication protocols and also for quantum metrology [19]. For the latter application it can be shown that the Dicke state outperforms classical schemes of phase estimation, for the same amount of available resources [84, 85].

The thesis is structured as follows. In chapter 2 an overview of the necessary theoretical and experimental tools to describe, characterize and experimentally observe entangled photonic quantum states is given. In chapter 3 the flexible observation of four-photon entangled states is presented. The application of the GHZ state for the simulation of a minimal instance of the toric code is explained in chapter 4. Finally, in chapter 5 the high power SPDC photon source and its application to the observation of the six-photon Dicke state is described, along with the utilization of the Dicke state for phase estimation. Chapters 3, 4 and 5 also include the relevant publications as reprints.

Chapter 2

Multi-partite entanglement

The following chapter describes the theoretical and experimental foundations for characterizing, analyzing, and realizing multi-photon entanglement. In section 2.1, the basic notation for the description of multiple qubits is introduced [1]. A formal definition of entanglement is given along with its interpretation as a non-classical property of quantum mechanical states. The experimental characterization of quantum states relies on measurement outcomes yielding information about the observed states. The measurements can be performed with the aim of determining the state's correlations. The latter can be used to distinguish between different entangled states, as it has been discovered that for more than two qubits different types of entanglement exist. Some possibilities to classify entanglement will be presented.

In an experiment the entanglement of an observed state has to be proven [86–88]. In section 2.2 criteria will be described for detecting a state as entangled. These criteria should be robust against noise, as experimental imperfections result in the observation of mixed states. As a next step one would like to quantify the amount of entanglement. For that purpose only a few entanglement measures exist, which will also be discussed.

Finally, the standard tools for an experimental implementation of entangled states using photonic qubits [23] are discussed in section 2.3. To this end, a photon source and linear optical elements for photon manipulation are commonly employed. The most suitable source for multi-photon entanglement is based on a spontaneous process in a $\chi^{(2)}$ -nonlinear crystal, namely spontaneous parametric down conversion (SPDC). This source delivers $2n$ photons in its n th order emission. The photons are fed into a linear optical network consisting of beam splitters (BSs) and phase shifters. The desired multi-photon entangled states are observed under the condition of detecting a well-defined number of photons in particular spatial modes, thus, selecting a particular spontaneous parametric down conversion (SPDC) emission order. Polarization analysis is performed in each mode to reconstruct the observed state completely or to give partial information, for example, whether the state has been entangled or how well it has been prepared.

This chapter can be used as a reference in order to acquire the basic information for chapters 3, 4 and 5, which describe experimental implementations of particular entangled quantum states and their applications.

2.1 Classifications of quantum states

The basic notation for a qubit and its measurement will be introduced, followed by the extension to multiple qubits and their characterization by means of correlations. The experimental determination of correlations constitutes a suitable means to characterize states. A state of multiple qubits can be entangled, meaning that it is impossible to write it as a product state between states of the individual subsystems. This property of quantum states leads to non-classical features like a violation of Bell inequalities.

Subsequently, different classifications of quantum states are presented. A first approach is to distinguish states according to their level of separability. This turns out to be insufficient, as already in the three-qubit case different types of genuine tri-partite entanglement exist. In particular, the criterion of equivalence under stochastic local operations and classical communication (SLOCC) identifies different entanglement classes for three-qubit states and already infinitely many classes of four-qubit states. Thus, other distinguishing criteria have to be considered as well. For example, classifying the set of symmetric states or grouping states according to their phenomenology are such criteria. The latter yields, among others, two important groups of states, the graph states and Dicke states, which are relevant for this work.

In the following, two-dimensional systems between N parties in the Hilbert space $\mathcal{H} = \mathcal{H}_1 \otimes \mathcal{H}_2 \otimes \dots \mathcal{H}_N$ of dimension 2^N are considered, whereby each $\mathcal{H}_i = \mathbb{C}^2$.

2.1.1 Qubit notation and entanglement

In this work, the notation of polarization-encoded qubits is used. A pure state of a photonic qubit, which constitutes a two level system, is described up to a global phase as [1]

$$|\psi(\theta, \phi)\rangle = \cos \frac{\theta}{2} |H\rangle + e^{i\phi} \sin \frac{\theta}{2} |V\rangle, \quad (2.1)$$

where H (V) denotes the horizontal (vertical) polarization of a photon, $\theta \in [0, \pi]$ and $\phi \in [0, 2\pi)$. The state $|\psi(\theta, \phi)\rangle$ can be represented by a vector on the Bloch sphere (fig. 2.1). A mixed state, that means a state with classical statistical distribution over pure states, is described by its density matrix

$$\rho = \sum_i p_i |\psi(\theta_i, \phi_i)\rangle \langle \psi(\theta_i, \phi_i)|, \quad (2.2)$$

which is the mixture of pure states $|\psi(\theta_i, \phi_i)\rangle$ with probabilities $p_i \geq 0$ and $\sum_i p_i = 1$.

A pure state can also be regarded as an eigenvector of an observable $\hat{\sigma}(\theta, \phi)$ along a particular basis direction, which is given as

$$\hat{\sigma}(\theta, \phi) = \sin \theta \cos \phi \hat{\sigma}_x + \sin \theta \sin \phi \hat{\sigma}_y + \cos \theta \hat{\sigma}_z, \quad (2.3)$$

where $\hat{\sigma}_x = \begin{pmatrix} 0 & 1 \\ 1 & 0 \end{pmatrix}$, $\hat{\sigma}_y = \begin{pmatrix} 0 & -i \\ i & 0 \end{pmatrix}$ and $\hat{\sigma}_z = \begin{pmatrix} 1 & 0 \\ 0 & -1 \end{pmatrix}$ are the Pauli spin matrices. Their eigenvectors define the x -, y - and z -axes of the Bloch sphere and are labeled as

$$\hat{\sigma}_x |\pm\rangle = \pm |\pm\rangle,$$

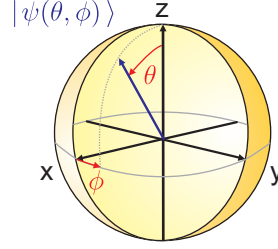


Figure 2.1: A pure state $|\psi(\theta, \phi)\rangle$ can be represented as a point (θ, ϕ) on the surface of the three-dimensional Bloch sphere. This point is given by the vector $(x, y, z) = (\cos \phi \sin \theta, \sin \phi \sin \theta, \cos \theta)$. The following points correspond to the eigenvectors of the Pauli spin matrices: $(\frac{\pi}{2}, 0), (\frac{\pi}{2}, \pi)$ for $\hat{\sigma}_x$, $(\frac{\pi}{2}, \frac{\pi}{2}), (\frac{\pi}{2}, \frac{3\pi}{2})$ for $\hat{\sigma}_y$ and $(0, 0), (\pi, 0)$ for $\hat{\sigma}_z$.

$$\begin{aligned}\hat{\sigma}_y |R\rangle &= +|R\rangle \text{ and } \hat{\sigma}_y |L\rangle = -|L\rangle, \\ \hat{\sigma}_z |H\rangle &= +|H\rangle \text{ and } \hat{\sigma}_z |V\rangle = -|V\rangle.\end{aligned}\quad (2.4)$$

The eigenvectors $|\pm\rangle = 1/\sqrt{2}(|H\rangle \pm |V\rangle)$ describe the diagonal $\pm 45^\circ$ polarization state of photons and $|R\rangle = 1/\sqrt{2}(|H\rangle + |V\rangle)$ ($|L\rangle = 1/\sqrt{2}(|H\rangle - |V\rangle)$) the right (left) circular polarization state (fig. 2.1).

The result of a measurement of the observable $\hat{\sigma}(\theta, \phi)$ for a particular state ρ is denoted as $p^\pm(\theta, \phi)$. It is calculated using the projector

$$\hat{P}^+(\theta, \phi) = (\mathbb{1} + \hat{\sigma}(\theta, \phi))/2 = |\psi(\theta, \phi)\rangle\langle\psi(\theta, \phi)| \text{ and} \quad (2.5)$$

$$\hat{P}^-(\theta, \phi) = (\mathbb{1} - \hat{\sigma}(\theta, \phi))/2 = |\bar{\psi}(\theta, \phi)\rangle\langle\bar{\psi}(\theta, \phi)| \quad (2.6)$$

onto that observable with $\bar{\psi}(\theta, \phi)$ orthogonal to $\psi(\theta, \phi)$, i.e., $\langle\bar{\psi}(\theta, \phi) | \psi(\theta, \phi)\rangle = 0$. For the state ρ one obtains $p^\pm(\theta, \phi) = \text{Tr}[\hat{P}^\pm(\theta, \phi)\rho]$ [1], which simplifies to $p^\pm(\theta, \phi) = \langle\psi | \hat{P}^\pm(\theta, \phi) | \psi\rangle$ for a pure state $\rho = |\psi\rangle\langle\psi|$.

A state describing multiple qubits is given by the sum of tensor products between basis vectors of the individual subsystems, e.g., for a two-qubit pure state between system 1 and 2 one obtains

$$|\psi(c_{HH}, c_{HV}, c_{VH}, c_{VV})\rangle_{12} = c_{HH} |HH\rangle + c_{HV} |HV\rangle + c_{VH} |VH\rangle + c_{VV} |VV\rangle, \quad (2.7)$$

with complex coefficients c_{ij} , the normalization condition $|c_{HH}|^2 + |c_{HV}|^2 + |c_{VH}|^2 + |c_{VV}|^2 = 1$ and the shorthand notation $|HH\rangle = |H\rangle_1 \otimes |H\rangle_2$ (the abbreviation $|H\rangle^{\otimes N} = |H\rangle_1 \otimes |H\rangle_2 \otimes \dots \otimes |H\rangle_N$ is also used later on). States can occur that are impossible to write as a simple tensor product of individual subsystems [89]

$$|\psi\rangle_{12} \neq |\phi\rangle_1 \otimes |\xi\rangle_2 \quad (2.8)$$

or for mixed states

$$\rho_{12} \neq \sum_i p_i(\rho_1)_i \otimes (\rho_2)_i. \quad (2.9)$$

Such states are called entangled. An example are the four Bell states

$$|\psi^\pm\rangle = (|HV\rangle \pm |VH\rangle)/\sqrt{2} \quad \text{and} \quad |\phi^\pm\rangle = (|HH\rangle \pm |VV\rangle)/\sqrt{2}. \quad (2.10)$$

In contrast, states that can be written as $|\psi\rangle_{12} = |\phi\rangle_1 \otimes |\xi\rangle_2$ or $\rho_{12} = \sum_i p_i (\rho_1)_i \otimes (\rho_2)_i$ are product states and called separable.

This rather simple mathematical definition of entanglement has deep consequences in the context of quantum mechanics and its interpretation as well as for using entanglement as a resource for quantum information applications. The term entanglement (“*Verschränkung*”) was coined by Erwin Schrödinger [2] in 1935 shortly after the work of Albert Einstein, Boris Podolsky and Nathan Rosen [4] questioning the completeness of quantum mechanics based on peculiar features of entangled states. That work was taken on by John Bell about 30 years later, who succeeded in formulating a criterion to test that question [5]. Assuming a local and realistic description of measurement results just as required by Einstein-Podolsky-Rosen, bounds on these results can be formulated. Nowadays these bounds are called Bell inequalities. The requirement of locality imposes space-like separation (in the sense of special relativity) of measurement events. More specifically, the result of a measurement on one system should be independent of operations performed on another system with which it has interacted in the past. “Reality” is understood in the sense that measurement results can be described by predetermined, hidden variables. According to the quantum mechanical description, however, Bell inequalities can be violated by entangled states. Thus, a discrepancy exists between a local-realistic and the quantum mechanical description of the physical world. However, to date no definitive answer to the question, whether the view onto the physical world is non-local and/or non-realistic has been found. Experimental and theoretical research to answer that question is still ongoing [90–95]. For philosophical implications and ongoing debates the interested reader is referred to refs. [96–102]. In this work, the focus is put on the experimental realization of entanglement, its characterization and application in quantum information. A Bell inequality is also applied in an experiment (see section 2.2 for theoretical background and section 5.2 for a particular implementation).

The complete characterization of a quantum state is given by its density matrix ρ . Amongst others, it can be written as a function of the correlations $T_{\mu_1, \dots, \mu_N}(\rho)$ of the correlation tensor $\hat{T}(\rho)$ that are defined as

$$T_{\mu_1, \dots, \mu_N}(\rho) = \text{Tr}[\rho(\hat{\sigma}_{\mu_1} \otimes \hat{\sigma}_{\mu_2} \otimes \dots \otimes \hat{\sigma}_{\mu_N})], \quad (2.11)$$

with $\hat{\sigma}_{\mu_n} \in \{\hat{\sigma}_0, \hat{\sigma}_x, \hat{\sigma}_y, \hat{\sigma}_z\}$ and $\hat{\sigma}_0 = \mathbb{1}$. In other words, correlations are the expectation values of all possible combinations of Pauli spin matrices and the identity with the state ρ . A single tensor product of Pauli spin matrices $\hat{\sigma}_{\mu_1} \otimes \hat{\sigma}_{\mu_2} \otimes \dots \otimes \hat{\sigma}_{\mu_N}$ is called measurement setting.

In an experiment one determines T_{μ_1, \dots, μ_N} from the counting statistics of N combined detector clicks, whereby the detectors are set to detect a specific photonic polarization corresponding to a specific Pauli basis setting, see section 2.3.2. The full derivation of how to calculate the correlations from the detector clicks can be found in refs. [103, 104].

Having determined the experimental $T_{\mu_1, \dots, \mu_N}(\rho_{\text{expt}})$ one can reconstruct the experimental density matrix ρ_{expt} by

$$\rho_{\text{expt}} = \frac{1}{2^N} \sum_{\mu_1, \dots, \mu_N} T_{\mu_1, \dots, \mu_N}(\rho_{\text{expt}}) \cdot (\hat{\sigma}_{\mu_1} \otimes \hat{\sigma}_{\mu_2} \otimes \dots \otimes \hat{\sigma}_{\mu_N}). \quad (2.12)$$

However, due to the limited counting statistics the reconstructed density matrix could be non-physical, i.e., exhibit negative eigenvalues. This can be accounted for by determining a physical density matrix, which resembles the experimental data most, by using for example a maximum likelihood fit, see refs. [65, 103]. Due to the exponential growth of the number of correlations with N (for photonic experiments all combinations of $\hat{\sigma}_x, \hat{\sigma}_y, \hat{\sigma}_z$ have to be measured in order to reconstruct ρ_{expt} , hence the increase grows as 3^N), it is desirable to avoid the necessity of gathering the complete information of a state. Powerful methods have been developed to give partial information, e.g., if a state was entangled or how well it was prepared. This is outlined in section 2.2.

2.1.2 Classifications

Levels of separability For an N -qubit system different levels of separability can be distinguished by partitioning the state into k disjoint subsets [fig. 2.2(a)]. A state ρ is called k -separable if there exists a convex decomposition of ρ according to [87, 105]

$$\rho = \sum_i p_i \otimes_{n=1}^k (\rho_{S_n})_i, \quad (2.13)$$

where each state $\otimes_{n=1}^k (\rho_{S_n})_i$ is a tensor product of k density matrices for some partition $(\alpha_k)_i$ using the notation $\alpha_k = \{S_1, \dots, S_k\}$, which denotes a partition of the qubits numbered by $\{1, \dots, N\}$ into k disjoint non-empty subsets with $k \leq N$. The most important levels of separability are the following: The highest hierarchy level consists of genuinely N -qubit entangled states, i.e., states that do not factorize at all ($k = 1$), which corresponds to $\rho \neq \sum_i p_i \otimes_{n=1}^k (\rho_{S_n})_i$ for $k \geq 2$. The next level are two-separable states (which are called bi-separable states in the following) $\rho = \sum_i p_i \otimes_{n=1}^2 (\rho_{S_n})_i$, i.e., states that can be factorized once. Finally, the N -separable states (also called fully-separable states) complete the hierarchy. It is useful to introduce finer classifications than only the distinction of different levels of separability as different types of genuine N -qubit entanglement exist.

SLOCC A finer classification of pure states is achieved by the stochastic local operations and classical communication (SLOCC) criterion, which groups states according to SLOCC equivalence classes. SLOCC allows a wider class of operations than local unitary (LU)¹ and local operations and classical communication (LOCC) alone. LOCC includes any possible local operation acting on each qubit with additional classical communication between

¹A unitary operator \hat{U} satisfies $\hat{U}^\dagger \hat{U} = \mathbb{1}$ and, thus, preserves the scalar product. A local unitary operation for N qubits is given as a single tensor product of unitaries acting on each subsystem as $\hat{U} = \hat{U}_1 \otimes \hat{U}_2 \otimes \dots \otimes \hat{U}_N$.

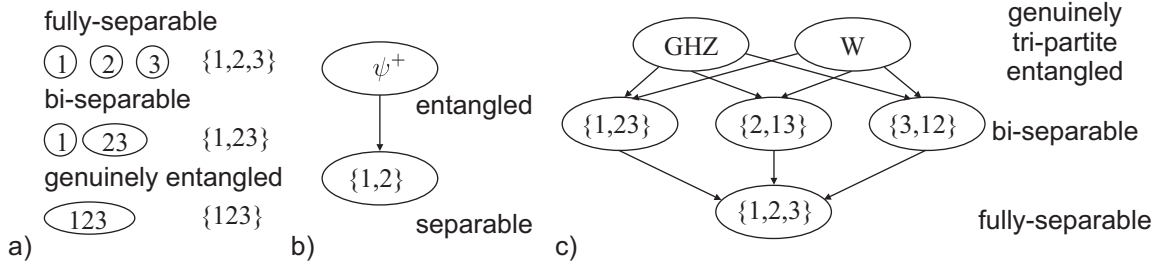


Figure 2.2: (a) Pictorial representation of the relevant types of separability for this work: fully- and bi-separable states and genuinely entangled states. SLOCC classifications: (b) For two qubits only two SLOCC classes exist, the entangled and the separable states. (c) The classification of three qubits is much richer. Two inequivalent classes of genuine tri-partite entangled states exist, followed by the bi-separable and fully-separable classes.

parties holding the qubit [106–108]. For the equivalence of states under SLOCC the task is to transform a certain state into another one with non-zero probability. If this is achieved, then two states are called SLOCC equivalent [107, 109, 110]. The criterion of SLOCC is appealing as, by definition, each SLOCC equivalent state can be used for similar quantum information applications.

Applying that criterion to a system of two qubits yields two different SLOCC classes [106–108], the class of entangled states represented by one of the Bell states and the class of separable states, e.g., $|\psi\rangle_{\text{sep}} = |\phi\rangle_1 |\xi\rangle_2$ (the split is written in shorthand notation in the following as $\{1, 2\}$) [fig. 2.2(b)]. For three qubits in a pure state six inequivalent classes can be distinguished [107] [fig. 2.2(c)]. Two classes of genuinely tripartite entangled states exist, the Greenberger Horne Zeilinger (GHZ) class and the W class, of which

$$\begin{aligned} |\text{GHZ}_3\rangle &= (|HHH\rangle + |VVV\rangle)/\sqrt{2} \text{ and} \\ |W_3\rangle &= (|HHV\rangle + |HVV\rangle + |VHH\rangle)/\sqrt{3} \end{aligned} \quad (2.14)$$

are representative states. These states can be distinguished by the 3-tangle τ_3 [111], which is a measure of three-qubit correlations and described in section 2.2. For GHZ-type states $0 < \tau_3 \leq 1$, whereas for W-type states $\tau_3 = 0$. The next hierarchy level are bi-separable states, whereby the three different partitions $\{1, 23\}$, $\{2, 13\}$ and $\{3, 12\}$ exist. Finally, the fully-separable states $\{1, 2, 3\}$ complete the three-qubit SLOCC classification. Essentially, the three-qubit classification for mixed states identifies the same classes [112].

Extending the SLOCC classification to four qubits results in infinitely many SLOCC classes [109, 113, 114]. The reason is that the number of real parameters for the SLOCC criterion grows like $6N$, whereas a generic N -qubit pure state is described by $2(2^N - 1)$ real parameters [107], i.e., for $N = 4$ SLOCC provides 24 parameters, whereas 30 would be necessary. Nevertheless, four-qubit states can be grouped into different families of entangled states containing each infinitely many SLOCC inequivalent states. Where ref. [109] discovered nine families of four-qubit states, ref. [114] found eight families based on an inductive classification scheme. Hence, alternative or additional classification criteria are necessary and are discussed in the following.

Phenomenological classification Another means to structure entangled states is to group them according to characteristic properties. For example these might consist of operational criteria such as the generation of entanglement, or the definition of the states as eigenstates of certain operators. In the following, the graph states [115, 116] and the Dicke states [77, 83] will be discussed as both groups of states are not only relevant for this work but also find wide application in the context of quantum information. Many other groups of states exist (for example the maximally mixed states [117]), which will not be discussed here.

A graph state $|g\rangle$ is characterized by a mathematical graph $g(E, V)$, whereby an edge E signifies an Ising-type next neighbor interaction, and a vertex V is a qubit [fig. 2.3(a)]. This definition directly implies a recipe to create these states experimentally. Each graph state $|g\rangle$ can be defined by its stabilizing operators \mathcal{S}_i , i.e., the state is a common eigenvector to all stabilizing operators with eigenvalue +1,

$$\mathcal{S}_i |g\rangle = + |g\rangle \forall i. \quad (2.15)$$

The set of all \mathcal{S}_i defining $|g\rangle$ is called stabilizer [116]. Graph states can be equivalent under LU operations and graph transformation rules. Applying these rules yields for two and three qubits in each case a single graph state, namely the state $|\phi^+\rangle$ and $|\text{GHZ}_3\rangle$, respectively. Generally, the states

$$|\text{GHZ}_N\rangle = (|H\rangle^{\otimes N} + |V\rangle^{\otimes N})/\sqrt{2} \quad (2.16)$$

are graph states that are defined by star-shaped graphs [fig. 2.3(a)]. The GHZ states are known as maximally entangled states and useful for a multitude of applications, such as secret-sharing [118], dense-coding [119], as a minimal toric code state [57], and for an all versus nothing violation of local realism [10, 62, 63]. For four qubits two different graph states are found, the $|\text{GHZ}_4\rangle$ state and the four-qubit cluster state $|\mathcal{C}_4\rangle = (|HHHH\rangle + |HHVV\rangle + |VVHH\rangle - |VVVV\rangle)/2$ [fig. 2.3(a)]. The latter state belongs to a subgroup of graph states called cluster states [45, 46]. It was found that cluster states are the resource for performing one-way quantum computation [45, 46, 60], an alternative computation model to the well known circuit model [1]. Particular graph states can be used for quantum error correction, which exploits their description via stabilizing operators [120]. For graph states of more qubits the reader is referred to ref.[116]. For this work only graph states up to four qubits are relevant and appear in chapters 3, 4 and 5.

Another group of states are the Dicke states [77, 83]. They are common eigenstates of the total spin operator squared, \hat{J}_N^2 , and the spin operator component in the z -direction, $\hat{J}_{N,z}$. Thereby,

$$\hat{J}_N^2 = \hat{J}_{N,x}^2 + \hat{J}_{N,y}^2 + \hat{J}_{N,z}^2 \quad \text{and} \quad \hat{J}_{N,i} = 1/2 \sum_k \hat{\sigma}_i^k, \quad (2.17)$$

with, e.g., $\hat{\sigma}_i^3 = \mathbb{1} \otimes \mathbb{1} \otimes \hat{\sigma}_i \otimes \mathbb{1} \otimes \mathbb{1} \otimes \mathbb{1}$ for $N = 6$ qubits and $i \in \{x, y, z\}$ (\hbar is set to unity). Dicke states have first been investigated with respect to light emission from a cloud of atoms [83]. In this context it has been found that atoms in a highly correlated state,

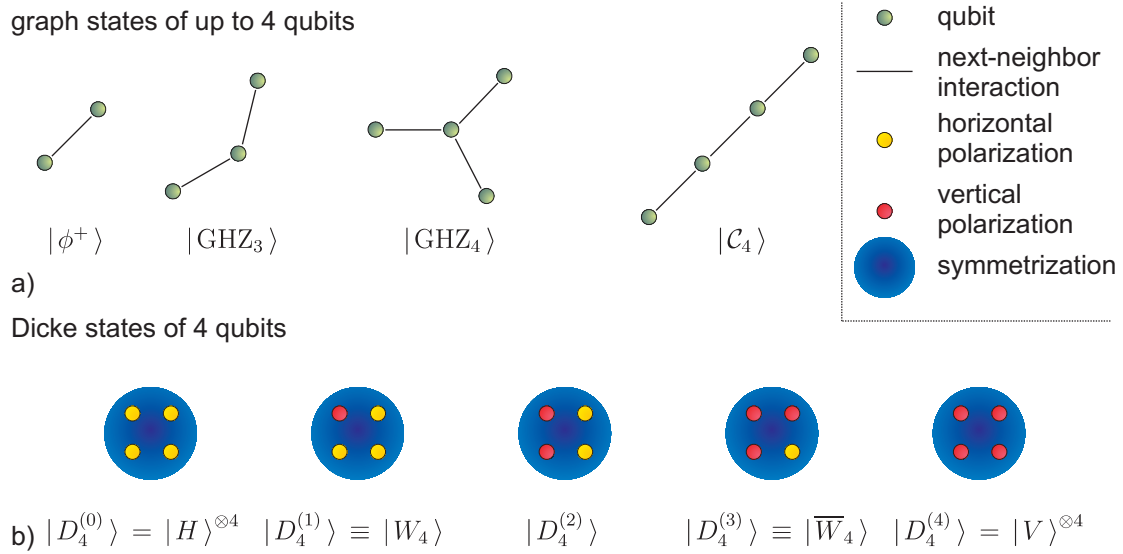


Figure 2.3: (a) All inequivalent graph states up to four qubits are shown, whereby a vertex is a qubit and an edge represents a two-qubit interaction. The states $|\text{GHZ}_N\rangle$ can always be represented by star-shaped graphs. (b) All symmetric Dicke states with maximal total spin for four qubits are schematically displayed, whereby red circles correspond to the number of excitations. The states $|W_N\rangle \equiv |D_N^{(1)}\rangle$ are the N -qubit versions of the three-qubit $|W_3\rangle \equiv |D_3^{(1)}\rangle$ state. The state $|\overline{W}_4\rangle$ is the spin flipped counterpart to $|W_4\rangle$.

a so-called Dicke state, emit radiation more strongly than when they are independent. Recently, Dicke states have found attention in the context of quantum information, both theoretically [55, 77, 78, 80, 121, 122] as well as experimentally [41, 65, 82, 123]. In this work the subgroup of Dicke states with maximal \hat{J}_N^2 is relevant. These states are symmetric under permutation of particles and can be written as

$$|D_N^{(l)}\rangle = \binom{N}{l}^{-1/2} \sum_i \mathcal{P}_i(|H^{\otimes(N-l)}V^{\otimes l}\rangle), \quad (2.18)$$

where $\sum_i \mathcal{P}_i(\dots)$ means the sum over all distinct symmetric permutations \mathcal{P}_i and l is the number of excitations, i.e., vertically polarized photons [fig. 2.3(b)]. More details are found in chapter 5, whereby the experimental implementation of some symmetric Dicke states of up to six qubits is discussed.

Classification of symmetric N -qubit states Recently, a classification of symmetric N -qubit pure states² has been carried out [125]. Many of the states for which applications have been found are symmetric, and thus play an important role in quantum information.

²Another study of symmetric states with the goal to determine maximally entangled symmetric states can be found in ref. [124].

Symmetric states can be grouped according to their degeneracy configuration and their diversity degree d_g [125], see below. Any symmetric state can be written as

$$|\psi_S\rangle = \sum_{k=0}^N c_k |D_N^{(k)}\rangle = \mathcal{N}_S \sum_{1 \leq i_1 \neq \dots \neq i_N \leq N} |\epsilon_{i_1}, \dots, \epsilon_{i_N}\rangle \quad (2.19)$$

with c_k complex coefficients³, the normalization factor \mathcal{N}_S , $|\epsilon_i\rangle = \alpha_i|+\rangle + \beta_i|-\rangle$ and $|\alpha_i|^2 + |\beta_i|^2 = 1$. The degeneracy configuration is the list of numbers of identical⁴ $|\epsilon_i\rangle$. The diversity degree is the dimension of that list. For $d_g \leq 3$ states belong to a single SLOCC class [125]. Using that classification and considering the three-qubit case, three different families can be identified, the fully-separable class ($d_g = 1$), the W class ($d_g = 2$) and the GHZ class ($d_g = 3$), which recovers the result from the SLOCC analysis apart from the classes of bi-separable states. For the four-qubit case five families of symmetric states are identified, of which four belong each to a single SLOCC class and one to a continuous set of SLOCC inequivalent states. Canonical states are $|D_4^{(0)}\rangle$ ($d_g = 1$), $|D_4^{(1)}\rangle \equiv |W_4\rangle$ ($d_g = 2$), $|D_4^{(2)}\rangle$ ($d_g = 2$), $(|D_4^{(0)}\rangle + |D_4^{(2)}\rangle)/\sqrt{2}$ ($d_g = 3$) and $(|\text{GHZ}_4\rangle + \mu|D_4^{(2)}\rangle)/\sqrt{1 + |\mu|^2}$ ($d_g = 4$) with complex $\mu \neq \pm 1/\sqrt{3}$. As this classification restricts to symmetric states it yields a reduction in the number of different families for N qubits compared to the SLOCC criterion.

Other classification schemes For a detailed description of other classification schemes (for example the local entanglability of multi-partite entangled states [126] or multidimensional determinants [127]) the reader is referred to the special literature.

2.2 Entanglement detection and measures of entanglement

In this section basic methods with the aim of detecting entanglement are described. Criteria to rule out full-separability are presented as well as criteria to prove genuine N -qubit entanglement. It is also important to give a quantitative estimate of the entanglement contained in a state. To this end entanglement measures have been developed, of which some are presented. While many measures exist for the bi-partite case, only a few are known for multi-partite states. This can partly be attributed to the appearance of different types of genuine N -qubit entanglement for $N > 2$. Excellent review articles concerning the detection and quantification of entanglement can be found in refs. [86–88, 128].

2.2.1 Entanglement detection

The following criteria can be used to detect entanglement or even genuine N -qubit entanglement.

³Only here the k excitations are represented by $|-\rangle$ and not by $|1\rangle$.

⁴ $|\epsilon_i\rangle$ and $|\epsilon_j\rangle$ are identical, if and only if $\alpha_i\beta_j - \alpha_j\beta_i = 0$.

Positive partial transposition A well known criterion to decide whether a given state is entangled is to consider the partial transposition of that state [129]. A density matrix of two qubits labeled 1 and 2 can be written as

$$\rho = \sum_{i,j \in \{H,V\}} \sum_{k,l \in \{H,V\}} \rho_{ij,kl} |i\rangle\langle j|_1 \otimes |k\rangle\langle l|_2. \quad (2.20)$$

The partial transpose with respect to one qubit, e.g., qubit 1, is defined as

$$\rho^{T_1} = \sum_{i,j \in \{H,V\}} \sum_{k,l \in \{H,V\}} \rho_{ji,kl} |i\rangle\langle j|_1 \otimes |k\rangle\langle l|_2 \quad (2.21)$$

and accordingly for qubit 2. A state is said to have a positive partial transposition (PPT) if its partial transposition has only non-negative eigenvalues, i.e., if $\rho^{T_1} \geq 0$ and $\rho^{T_2} \geq 0$, and thus describes a physical state. This holds for all separable states. If the partially transposed state exhibits at least one negative eigenvalue, the state is entangled. The opposite is only valid for 2×2 and 2×3 dimensional systems, whereby a PPT implies that ρ is separable. In higher dimensions so-called bound entangled states exist [130, 131], which have a PPT, but are entangled. The partial transposition can be interpreted as local time reversal on one subsystem [132], and thus separable states lead to physical states upon this operation in contrast to entangled states. Furthermore, the partial transposition is a positive but not completely positive map⁵. It was shown that any such map can be used for entanglement detection [133]. Most importantly entanglement witnesses (see below) are also connected with positive maps. Evaluating the PPT criterion requires the determination of the complete density matrix, and thus its derivation from experimental data scales exponentially with N . Hence, other criteria are necessary that significantly reduce the number of measurement settings.

Entanglement witness The method of entanglement witnesses [133, 134] is now routinely used in entanglement detection [41, 65, 135] for excluding full-separability or proving genuine N -qubit entanglement. It can best be envisaged when considering that (bi-)separable states form a convex set (fig. 2.4). Hence, operators $\hat{\mathcal{W}}$ exist for which $\text{Tr}[\hat{\mathcal{W}}\rho_{(\text{bi-})\text{sep}}] \geq 0 \forall \hat{\mathcal{W}}$ that fulfill $\langle \psi |_{(\text{bi-})\text{sep}} \hat{\mathcal{W}} | \psi \rangle_{(\text{bi-})\text{sep}} \geq 0$ for all (bi-)separable states $|\psi\rangle_{(\text{bi-})\text{sep}}$ [133]. In other words, the set of (bi-)separable states can be bounded by hyperplanes described by the set of operators $\hat{\mathcal{W}}$. Exactly these hyperplanes correspond to entanglement witnesses, which yield a positive expectation value for all (bi-)separable states. Hence, as soon as for a particular $\hat{\mathcal{W}}$ one finds $\text{Tr}[\hat{\mathcal{W}}\rho] < 0$, the state ρ is entangled. A commonly used witness operator is the projector-based witness of the form

$$\hat{\mathcal{W}} = \alpha \mathbb{1}^{\otimes N} - |\chi\rangle\langle\chi| \quad \text{with} \quad \alpha = \max_{|\psi\rangle_{(\text{bi-})\text{sep}}} |\langle \psi_{(\text{bi-})\text{sep}} | \chi \rangle|^2, \quad (2.22)$$

⁵An operator is called positive if and only if it is Hermitian and has non-negative eigenvalues. A map $\hat{\Theta}$ is called completely positive if and only if $\mathbb{1} \otimes \hat{\Theta}$ is positive on any finite-dimensional system.

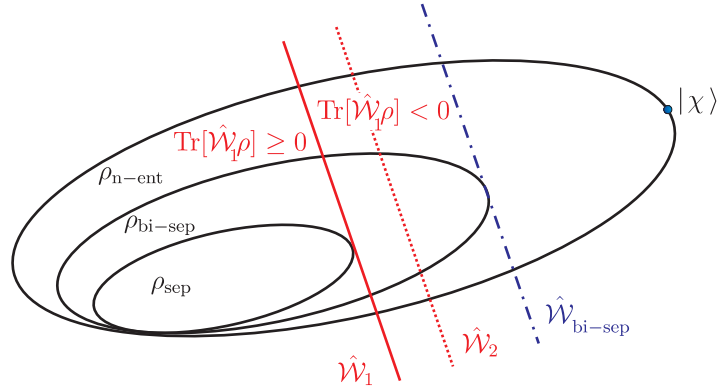


Figure 2.4: The convex sets of separable (sep), bi-separable (bi-sep) and genuinely N -qubit entangled states (n-ent) are shown. An optimal ($\hat{\mathcal{W}}_1$) and a non-optimal witness ($\hat{\mathcal{W}}_2$) detect a state as entangled for $\text{Tr}[\hat{\mathcal{W}}_i \rho] < 0$, for example for the target state $|\chi\rangle$. Its genuinely N -qubit entanglement can only be proven by $\hat{\mathcal{W}}_{\text{bi-sep}}$.

which is constructed with respect to an entangled target state $|\chi\rangle$. Thus, $\text{Tr}[\hat{\mathcal{W}}\rho'] \geq 0$ does not imply that ρ' is separable, rather, another witness $\hat{\mathcal{W}}'$ might exist for which $\text{Tr}[\hat{\mathcal{W}}'\rho'] < 0$. The optimality of a witness can be defined in the following way. The witness $\hat{\mathcal{W}}_1$ is finer than $\hat{\mathcal{W}}_2$, if the entanglement of ρ detected by $\hat{\mathcal{W}}_2$ is also detected by $\hat{\mathcal{W}}_1$, but not necessarily vice versa [136]. Hence, a witness is optimal if no finer witness exists (fig. 2.4). While witnesses are linear operators, improved witnesses for the bi-partite case can be formulated by considering non-linear extensions [137]. These non-linear witnesses detect more entangled states, and thus can be finer than any linear witness. However, the generalization of non-linear witnesses to multi-partite systems still remains an open problem.

In general, the determination of witness operators needs fewer measurement settings than the determination of the density matrix. It was even shown that for certain graph [138] or Dicke states [121] entanglement witnesses exist that require only two measurement settings independent of the number of particles. Such particular witnesses exploit symmetries in these states. However, in general the decomposition of witness operators into locally measurable observables is a nontrivial task [139, 140]. Particular examples of witness operators are given in chapters 3, 4 and 5.

Bell inequality Bell inequalities are derived assuming a local-realistic description of measurement results. Thus, they give bounds on measurement outcomes for certain measurement settings assuming that the outcomes can be described by a local hidden variable (LHV) model, and thus are predetermined and independent of the measurement itself. Entangled states exist that violate such a Bell inequality. This was first realized by John Bell [5] giving an experimentally testable formulation of the long posted Einstein-Podolsky-Rosen paradox [4]. Though Bell inequalities are constructed in the LHV space, from a quantum mechanical point of view they can be considered as non-optimal entan-

glements witnesses [141]. If a Bell inequality is violated, it reveals that the measurement results cannot be described by a LHV model and at the same time detects entanglement as, by definition, separable states can be described by a LHV model. Bell inequalities can be footed on probabilities [142] and also on correlations [143]. The latter will be used in this work in section 5.2, whereby a Bell inequality is applied. While not being essential for entanglement detection one has to keep in mind that certain requirements have to be fulfilled in order to prove a rejection of a LHV model by an experimental violation of a Bell inequality, e.g., the measurements have to be space-like separated and the ratio of detected to non-detected events has to exceed a critical value. Loopholes exist for experiments that do not fulfill such criteria (in the above examples the locality and detection loophole). Then, a description of the measurement results with LHV models exploiting these loopholes [144, 145] is possible and would explain the violation of the Bell inequality. A completely loophole-free experiment [8, 9] has not been performed to date, and thus still remains an experimental challenge, see refs. [100, 146].

Spin squeezing inequalities Entanglement detection can also be based on spin squeezing inequalities by considering the collective angular momentum components [121, 147, 148]. Generally, a state is called spin squeezed [149] if for the uncertainty relation

$$(\Delta J_z)^2 \cdot (\Delta J_y)^2 \leq \frac{1}{4} |\langle \hat{J}_x \rangle|^2, \quad (2.23)$$

with the variance $(\Delta J_i)^2 = \langle \hat{J}_i^2 \rangle - \langle \hat{J}_i \rangle^2$ one observes $(\Delta J_z)^2 < \frac{1}{2} |\langle \hat{J}_x \rangle|$. Hence, a smaller variance (spin-squeezed) in one direction implies a larger one in an orthogonal direction (anti-squeezed). Spin squeezing was observed for example in systems of atomic clouds [150, 151] or trapped atoms in optical lattices [152, 153]. In these systems in order to detect entanglement it is favorable to read-out collective observables (e.g. $\langle \hat{J}_i \rangle$, $\langle \hat{J}_i^2 \rangle$), since addressing the system as a whole is much simpler than individually addressing single particles. In addition to this continuous variable application, spin squeezing inequalities are also useful to detect entanglement in qubit systems [65, 81, 121]. This will be applied in this work, see chapters 3 and 5. To this end, the collective observables are decomposed into local measurements. Recently, the generalization of different spin squeezing inequalities, which had been constructed for different physical implementations and applications, has been carried out [147, 148]. This full set of spin squeezing inequalities for N qubits reads [147, 148]

$$\langle \hat{J}_x^2 \rangle + \langle \hat{J}_y^2 \rangle + \langle \hat{J}_z^2 \rangle \leq N(N+2)/4, \quad (2.24)$$

$$(\Delta J_x)^2 + (\Delta J_y)^2 + (\Delta J_z)^2 \geq N/2, \quad (2.25)$$

$$\langle \hat{J}_i^2 \rangle + \langle \hat{J}_j^2 \rangle - N/2 \leq (N-1) \langle \hat{J}_k^2 \rangle, \quad (2.26)$$

$$(N-1)[(\Delta J_i)^2 + (\Delta J_j)^2] \geq \langle \hat{J}_k^2 \rangle + N(N-2)/4, \quad (2.27)$$

with i, j, k all permutations of x, y, z . These eight inequalities define a polytope in the three dimensional $(\langle \hat{J}_x^2 \rangle, \langle \hat{J}_y^2 \rangle, \langle \hat{J}_z^2 \rangle)$ space, whereby states outside the polytope are entangled, see fig. 3.4 in chapter 3 for the polytope of $N = 4$.

Correlation criterion A simple geometrical criterion to exclude full-separability based on correlations was introduced in ref. [154]. If for a scalar product $\vec{s} \cdot \vec{e} < \vec{e} \cdot \vec{e}$ holds, then $\vec{s} \neq \vec{e}$. In principle, one can identify \vec{s} with the set of separable states and \vec{e} with an entangled state and the scalar product is defined in the correlation space. More specifically, the latter is given by a special scalar product only running over $j_i \in \{1, 2, 3\}$ corresponding to $\hat{\sigma}_x, \hat{\sigma}_y, \hat{\sigma}_z$ and defined as

$$(\hat{X}_N(\rho), \hat{Y}_N(\rho)) = \sum_{j_1, \dots, j_N=1}^3 X_{j_1, \dots, j_N}(\rho) Y_{j_1, \dots, j_N}(\rho). \quad (2.28)$$

The $\hat{X}_N(\rho)$ and $\hat{Y}_N(\rho)$ are identified with the correlation tensor $\hat{T}(\rho)$ of an N -qubit state ρ with components $T_{\mu_1, \dots, \mu_N}(\rho)$. Then, the aforementioned inequality can be formulated as

$$T_n^{\max} := \max_{\hat{T}_N^{\text{prod}}} (\hat{T}_N^{\text{prod}}(\rho_{\text{sep}}), \hat{T}_N(\rho)) < (\hat{T}_N(\rho), \hat{T}_N(\rho)) =: \|\hat{T}_N(\rho)\|^2 \quad (2.29)$$

with $\hat{T}_N^{\text{prod}}(\rho_{\text{sep}})$ the correlation tensor of all fully-separable states ρ_{sep} . This inequality only holds if ρ is entangled. It was shown that $T_n^{\max} \leq 1$ [154]. Hence, as soon as the sum of squared correlations $\sum_{j_1, \dots, j_N} (T_{j_1, \dots, j_N}(\rho))^2$ exceeds unity, the state is entangled. This criterion is very appealing because successive correlation measurements can be used to detect entanglement, starting with a minimum of two (see chapter 3). In terms of the number of measurement settings and their flexibility this criterion is favorable compared to most other entanglement detection criteria described so far. However, a generalization of this criterion for proving genuine N -partite entanglement has still to be carried out.

Density matrix element criterion Recently, new entanglement criteria to detect genuine N -qubit entanglement have been developed in terms on bounds on the diagonal elements $\rho_{i,i}$ and off-diagonal elements⁶ $\rho_{i,j}$ with $i \neq j$ of the density matrix ρ [155]. These criteria apply to any state and can be optimized for particular states. For example, in the case of three qubits the off-diagonal element $\rho_{1,8}$ is bounded as a function of diagonal elements like $|\rho_{1,8}| \leq \sqrt{\rho_{2,2}\rho_{7,7}} + \sqrt{\rho_{3,3}\rho_{6,6}} + \sqrt{\rho_{4,4}\rho_{5,5}}$. Violation of that bound, which is maximal for the state $|\text{GHZ}_3\rangle$, implies genuine three-qubit entanglement. For other states a local change of the basis might be necessary. Further, any bi-separable three-qubit state fulfills

$$|\rho_{2,3}| + |\rho_{2,5}| + |\rho_{3,5}| \leq \sqrt{\rho_{1,1}\rho_{4,4}} + \sqrt{\rho_{1,1}\rho_{6,6}} + \sqrt{\rho_{1,1}\rho_{7,7}} + (\rho_{2,2} + \rho_{3,3} + \rho_{5,5})/2. \quad (2.30)$$

Bounds have been explicitly given for the four-qubit states $|\text{GHZ}_4\rangle$, $|D_4^{(1)}\rangle$ and $|D_4^{(2)}\rangle$ [155]. To evaluate the inequalities from experimental data, in general, the complete density matrix has to be known. However, diagonal elements of a density matrix can be measured with a single measurement setting. For particular cases, off-diagonal elements can be measured with only a few settings reducing the experimental effort considerably, for example for the states $|\text{GHZ}_N\rangle$ [156], or estimated for the states $|D_N^{(1)}\rangle$.

⁶Here, the elements $\rho_{i,j}$ of the density matrix are written in shorthand notation using $i \in \{1, 2, \dots, 2^N\}$ corresponding to $HH \dots H, HH \dots V, \dots, VV \dots V$ and similarly for j . For example for two qubits one has $i \in \{1, 2, 3, 4\}$ corresponding to HH, HV, VH, VV .

Other criteria Further criteria to detect entanglement include, amongst others, the reduction criterion, the range criterion, the matrix realignment criterion, the majorization criterion and the usage of covariance matrices. As these criteria are not applied in this work the interested reader is referred to review articles [87, 88].

2.2.2 Entanglement measures

An entanglement measure $E(\rho)$ quantifies the amount of entanglement of a state ρ . This basic idea was introduced first in the context of quantum communication protocols. Consider for example the teleportation protocol [157, 158]. The Bell state $|\psi^-\rangle$ is the resource to teleport an unknown state from one location to another one using two additional bits of classical communication. The usefulness of any state for that protocol can be quantified by asking how many copies of that state are necessary in order to retrieve n Bell states. This defines an entanglement measure, called the distillable entanglement [87, 128]. Another question could be, how many Bell states does one need in order to synthesize n copies of an arbitrary state. This is quantified by the entanglement cost [87, 128].

While these two measures are operational and difficult to compute in the general case (i.e. for mixed states), another approach is to demand that an entanglement measure conforms with certain requirements. Two basic requirements should be fulfilled [87], namely

- (i) $E(\rho_{\text{sep}}) = 0$ for separable states ρ_{sep} and
- (ii) monotonicity, which means $E(\Lambda^{\text{LOCC}}\rho) \leq E(\rho)$, i.e., $E(\rho)$ can only decrease under LOCC (Λ^{LOCC}).

While the first requirement appears naturally, the second one goes along with the observation that entanglement cannot be created by LOCC. Further requirements can be useful, but are not necessary [87];

- (iii) $E(\rho)$ is invariant under LU operations,
- (iv) convexity: $E(\sum_k p_k \rho_k) \leq \sum_k p_k E(\rho_k)$, and
- (v) additivity: $E(\rho^{\otimes n}) = nE(\rho)$, where $\rho^{\otimes n}$ means n copies of the state ρ .

In general, a specific entanglement measure fulfills not all of these requirements.

In the following, the most important entanglement measures are summarized. Some of these can be used to quantify the amount of entanglement created in an experiment. Note, here the difficulty lies with mixed states. A measure $E(|\phi\rangle)$ for pure states $|\phi\rangle$ can be extended to mixed states via the convex-roof extension [159]:

$$E(\rho) = \inf_{p_k, |\phi_k\rangle} \sum_k p_k E(|\phi_k\rangle), \quad (2.31)$$

where $\rho = \sum_k p_k |\phi_k\rangle\langle\phi_k|$ and the optimization is done over all possible decompositions. For only a few measures the optimization can be done analytically.

Maximal singlet fraction and fidelity The maximal singlet fraction is not a measure in the aforementioned sense, but it quantifies the usefulness of a state for teleportation [160]. It denotes the maximal fidelity with a singlet (or Bell state) under any trace preserving LOCC:

$$\text{MSF}(\rho) = \max_{\text{LOCC}} \langle \psi^- | \Lambda^{\text{LOCC}} \rho \Lambda^{\text{LOCC}\dagger} | \psi^- \rangle. \quad (2.32)$$

The maximal singlet fraction can be used to calculate the maximal achievable teleportation fidelity f_{tele} using the state ρ as

$$f_{\text{tele}} = (d \cdot \text{MSF}(\rho) + 1)/(d + 1) \quad (2.33)$$

with $d = 2$ for qubits.

In general, the fidelity $F_\sigma(\rho)$ quantifies the overlap of a state ρ with another state σ and is defined as [1, 161]

$$F_\sigma(\rho) = \text{Tr}[\sqrt{\sqrt{\sigma}\rho\sqrt{\sigma}}]^2. \quad (2.34)$$

For pure states $\sigma = |\psi\rangle\langle\psi|$ this equation reduces to $F_\psi(\rho) = \langle\psi|\rho|\psi\rangle$. In this work, the state $|\psi\rangle$ resembles the target state and ρ the observed state of the experiment. The fidelity can be applied for a comparison between different physical systems realizing multipartite entangled states.

Entanglement of formation The entanglement of a pure state can be measured by the reduced von Neumann entropy

$$S(\rho_1) = -\text{Tr}[\rho_1 \log_2 \rho_1], \quad (2.35)$$

where

$$\rho_1 = \text{Tr}_2[\rho_{12}] = \sum_{m \in \{H,V\}} \sum_{i,j \in \{H,V\}} \sum_{k,l \in \{H,V\}} |i\rangle\langle j|_1 \otimes \langle m|k\rangle\langle l|m\rangle_2 \quad (2.36)$$

denotes the partial trace over subsystem 2 and $\rho_{12} = |\psi\rangle\langle\psi|$ is a pure state. This measures the local mixedness⁷, because maximally entangled states (Bell states) are maximally mixed when only one subsystem is considered, whereas a subsystem of a separable pure state is pure. The entanglement of formation $E_F(\rho)$ [162] is defined via the convex-roof extension of $S(\rho_1)$ as

$$E_F(\rho) = \inf_{p_k, |\phi_k\rangle} \sum_k p_k S((\rho_1)_k), \quad (2.37)$$

i.e., the least probable reduced von Neumann entropy of any ensemble of pure states realizing ρ . $E_F(\rho)$ can be interpreted in terms of the minimal number of Bell states necessary to build a copy of the state ρ [162]. It has been found that $E_F(\rho)$ can be computed analytically for bi-partite mixed states via the concurrence.

⁷The linear entropy $4/3(1 - \text{Tr}[\rho^2])$ is another entropic measure for the local mixedness, with $\text{Tr}[\rho^2]$ the purity of ρ .

Concurrence The concurrence is defined as

$$C(|\psi\rangle) = \sqrt{2(1 - \text{Tr}[\rho_1^2])} = \langle \psi | \hat{\Theta} | \psi \rangle, \quad (2.38)$$

where $\hat{\Theta}\psi = (\hat{\sigma}_y \otimes \hat{\sigma}_y)\psi^*$ is an anti-unitary transformation and $*$ denotes the complex conjugation [163]. The expression $\langle \psi | \hat{\Theta} | \psi \rangle$ finds an interpretation as the fidelity of a state $|\psi\rangle$ to its universal⁸ spin flipped counterpart. For the Bell states a universal spin flip on both qubits always yields the same Bell state, whereas for separable states an orthogonal state is obtained. Thus, the concurrence can quantify the amount of entanglement. An analytical expression for the concurrence for mixed states has been found [164]:

$$C(\rho) = \max(0, \lambda_1 - \lambda_2 - \lambda_3 - \lambda_4), \quad (2.39)$$

where the λ_i are the eigenvalues in decreasing order of the matrix $\sqrt{\rho}\sqrt{\hat{\Theta}\rho\hat{\Theta}}$. It has been shown that $C(\rho)$ can be used to calculate the entanglement of formation for two qubits as

$$E_F(\rho) = h((1 + \sqrt{1 - C(\rho)^2})/2), \quad (2.40)$$

where $h(x) = -x \log x - (1 - x) \log(1 - x)$ is the binary entropy function. Note, $C(\rho)^2$ is sometimes denoted as tangle $\tau(\rho)$. The concurrence can also be measured directly for two qubits, without determining the density matrix, by a measurement on two copies of a pure state [165–168]. If these two copies are not ideal, i.e., in a mixed state, then a lower bound on the concurrence can be estimated [169, 170]. Recently, the latter idea has been implemented and discussed in refs. [171, 172].

Negativity The violation of the PPT criterion can be quantified via the negativity [173, 174]

$$\mathcal{N}(\rho) = (\|\rho^{T_1}\|_1 - 1)/2 = \sum_{\lambda_i < 0} \lambda_i \quad (2.41)$$

with the trace norm of an operator \hat{A} defined as $\|\hat{A}\|_1 = \text{Tr}[\sqrt{\hat{A}^\dagger \hat{A}}]$ and where the λ_j are the eigenvalues of ρ^{T_1} (see eq. 2.21). While the negativity is convex, it is not additive. However the logarithmic negativity [174]

$$E_{\mathcal{N}}(\rho) = \log_2 \|\rho^{T_1}\|_1 = \log_2 (2\mathcal{N}(\rho) + 1) \quad (2.42)$$

is additive, but not convex. Note, negativity and concurrence can be used in experiments to quantify the amount of entanglement as they are easily computable for mixed states. To this end, however, the determination of the density matrix is required.

The tripartite negativity [175, 176] is an extension of negativity to the three-qubit case and is defined as the geometric mean of the negativities for all bi-partitions [175],

$$\mathcal{N}_3(\rho) = (\mathcal{N}_{\{1,23\}}(\rho)\mathcal{N}_{\{2,13\}}(\rho)\mathcal{N}_{\{3,12\}}(\rho))^{1/3}. \quad (2.43)$$

⁸The operations $\hat{\sigma}_x$ or $\hat{\sigma}_y$ do not flip $|+\rangle \leftrightarrow |-\rangle$ or $|R\rangle \leftrightarrow |L\rangle$, respectively, but $\hat{\sigma}_y\psi^*$ does.

This can be used to quantify the amount of W type entanglement in a three-qubit state as it is a measure of the residual bi-partite entanglement. Below, the 3-tangle is considered, which, in contrast, quantifies the amount of GHZ type entanglement in a three-qubit pure state.

3-tangle For pure three-qubit states the 3-tangle, $\tau_3(|\psi\rangle)$, is a measure of entanglement [111]. It is defined as [111, 177]

$$\begin{aligned}\tau_3(|\psi\rangle) &= 4|d_1 - 2d_2 + 4d_3| \text{ with} & (2.44) \\ d_1 &= c_{HHH}^2 c_{VVV}^2 + c_{HHV}^2 c_{VVH}^2 + c_{HVV}^2 c_{VHV}^2 + c_{VHH}^2 c_{HVV}^2, \\ d_2 &= c_{HHH} c_{VVV} c_{HVV} c_{VHH} + c_{HHH} c_{VVV} c_{VHV} c_{HVV} + c_{HHH} c_{VVV} c_{VHV} c_{HVV} \\ &\quad + c_{HVV} c_{VHH} c_{VHV} c_{HVV} + c_{HVV} c_{VHH} c_{VHV} c_{HVV} + c_{VHV} c_{HVV} c_{VHV} c_{HVV}, \\ d_3 &= c_{HHH} c_{VVV} c_{VHV} c_{HVV} + c_{VVV} c_{HHH} c_{HVV} c_{VHH},\end{aligned}$$

where the c_{ijk} with $i, j, k \in \{H, V\}$ denote the coefficients of a state $|\psi\rangle$ in the computational basis. For pure states the monogamy relation

$$(C_{1|23}(|\psi\rangle))^2 = (C_{12}(\rho_{12}))^2 + (C_{13}(\rho_{13}))^2 + \tau_3(|\psi\rangle) \quad (2.45)$$

holds. It states that the entanglement between subsystem 1 and subsystems $\{2, 3\}$ is distributed in three forms, namely as entanglement between subsystem 1 and 2, between subsystem 1 and 3 and tri-partite entanglement between all 3 subsystems. The 3-tangle can be used to distinguish between the W and GHZ classes of pure states, as $0 < \tau_3(|\text{GHZ}_{\text{class}}\rangle) \leq 1$ and $\tau_3(|W_{\text{class}}\rangle) = 0$. To further rule out bi-separability ($\tau_3(|\phi_{\text{bi-sep}}\rangle) = 0$), one has also to calculate the local entropy of each pair in order to demonstrate W type entanglement [107]. Recently, in the work of refs. [177–179] an extension of τ_3 to a family of mixed three-qubit states was achieved. This family is composed of rank two mixed states of the form $\rho(p) = p|\text{GHZ}_3\rangle\langle\text{GHZ}_3| + (1-p)|W_3\rangle\langle W_3|$. Further, one can decide on analytical grounds for *any* rank two three-qubit mixed state $\rho = p|\psi\rangle\langle\psi| + (1-p)|\chi\rangle\langle\chi|$ if it has vanishing τ_3 or not.

Geometric measure of entanglement The geometric measure of entanglement [180, 181], $E_G(|\psi\rangle)$, quantifies the minimal distance of $|\psi\rangle$ to the set of fully-separable states $|\phi\rangle_{\text{sep}}$. It is defined for pure states as

$$E_G(|\psi\rangle) = 1 - \sup_{|\phi\rangle_{\text{sep}}} |\langle\phi_{\text{sep}}|\psi\rangle|^2, \quad (2.46)$$

as one minus the maximal overlap with pure fully-separable states. Most importantly, the geometric measure can be estimated from experimental data [182–184] yielding a lower bound on $E_G(\rho)$ for the mixed state ρ . To this end, consider for example the special case of an entanglement witness of the form $\hat{W} = \alpha\mathbb{1} - |\psi\rangle\langle\psi|$ to detect entanglement in the vicinity of $|\psi\rangle$, where $\alpha = |\langle\phi_{\text{sep}}|\psi\rangle|^2$ denotes the maximal overlap with fully-separable

states and $E_G(|\psi\rangle)$ for the pure state $|\psi\rangle$ is known. The Legendre transform $\hat{E}_G(r\hat{\mathcal{W}})$ [182] is used to estimate $E_G(\rho)$:

$$\hat{E}_G(r\hat{\mathcal{W}}) = \begin{cases} r\alpha & \text{for } r \geq 0 \\ \left[\sqrt{(1-r)^2 + 4rE_G(|\psi\rangle)} + 2\alpha r - r - 1 \right] / 2 & \text{for } r < 0, \end{cases}$$

Then, an optimization is performed over all r such that

$$E_G(\rho) \geq \sup_r \{r \cdot \text{Tr}[\rho\hat{\mathcal{W}}] - \hat{E}_G(r\hat{\mathcal{W}})\}, \quad (2.47)$$

where $\text{Tr}[\rho\hat{\mathcal{W}}]$ is the experimentally determined expectation value of $\hat{\mathcal{W}}$.

Robustness The robustness [185] of an entangled state ρ quantifies by how much it can be mixed with a separable state σ_{sep} such that the overall state is still entangled, i.e., the maximal p in $\rho_{\text{mix}} = (1-p)\rho + p\sigma_{\text{sep}}$. In this work, robustness will be used in order to evaluate the noise tolerance for various entanglement detection criteria, where, for simplicity σ_{sep} is assumed to be white noise $\mathbb{1}^{\otimes N}/2^N$. Alternatively, the critical visibility $\nu_{\text{crit}} = (1-p)$ is considered.

This completes the methods for detecting and quantifying entanglement.

2.3 Experimental observation using photons

The necessary experimental methods to observe entanglement using polarization-encoded photonic qubits are discussed in the following. To this end, a photon source delivering a certain number of photons is required. A source that is widely used in photonic quantum information experiments is based on the non-linear process of spontaneous parametric down conversion (SPDC). In this process, basically $2n$ low energy photons (mostly in the infrared (IR)-wavelength region) are created by probabilistic down conversion of n higher energy photons (mostly in the UV-wavelength region). In particular cases one can directly make use of the quantum correlations between the photons created by the source [51, 186]. However, the probabilistic production of photons demands high pump powers to achieve sensible count rates for acquiring sufficient statistical data. Therefore, the pump power is concentrated in ultrashort pulses. Another photon source applied in multi-photon entanglement experiments is a strongly attenuated weak coherent beam, i.e., faint laser pulses, used for example in combination with SPDC sources.

Subsequently, the photons are manipulated by linear optical elements. This includes for example interference of photons or polarization manipulations and finally, a distribution into a well defined number of spatial modes. Polarization analysis in each mode is performed in order to acquire information about the multi-photon states. The desired multi-photon states are observed under the condition of detecting a single photon in each of the spatial modes [42, 43], see for example fig. 3.1. This condition selects a subspace of the complete space of all possible photon distributions in the linear optical setup. In general, this method of state observation works only probabilistically.

2.3.1 Photon sources

Two distinct approaches to realizing photon sources for quantum information processing exist, namely sources based on spontaneous, non-linear processes and deterministic sources. Both approaches should ideally fulfill the following requirements: the creation of a particular number of photons in well defined spatial, spectral, temporal and polarization modes at sufficient production rates. These requirements are demanding and, so far, no photon source exists fulfilling all these requirements at the same time in a satisfactory way [47–49]. However, this would be necessary to implement scalable linear optical quantum computing based on single photon sources, linear optical elements and photon number resolving detectors, as has been described in ref. [42]. Hence, current photon sources allow for the demonstration of proof-of-principle implementations without claiming scalability. To date, entanglement between at most six photons has been observed [36–39], which is basically limited by low production rates and low detection efficiency in current linear optical experiments.

Probabilistic sources are based on spontaneous processes like SPDC or spontaneous four-wave mixing (SFWM). SPDC photon sources are the workhorse for most experiments in optical quantum information processing. To name just a few, SPDC sources are used as heralded single photon sources for quantum cryptographic applications [16], for demonstrating the violation of Bell inequalities [8, 51, 187], for multi-photon entanglement experiments [36, 53, 58, 65, 188, 189], and proof-of-principle demonstrations of applications [60, 158, 190, 191]. For the observation of $2N$ -partite entangled photonic states, one uses the simultaneous but probabilistic photon pair emission from N SPDC sources or the N th higher order emission from a single SPDC source, which is described in the following, see also fig. 3.1.

Ideally, one would like to use deterministic sources delivering single photons on demand. These can be realized in various physical systems [47–49], for example, nitrogen vacancy centers in diamond [192], quantum dots [193], single atoms in a cavity [194] and molecules [195]. However, so far, the production rates are too low and often the experimental effort is too high, for example a cryogenic environment or intricate laser systems are necessary. Hence, these sources are not yet suitable for multi-photon entanglement experiments.

Spontaneous parametric down conversion The SPDC is a non-linear $\chi^{(2)}$ process of non-inversion symmetric crystals, whereupon to first order two photons, called signal and idler, are created by probabilistic down conversion of a pump photon. It can be described by considering that the presence of an electric field \mathbf{E} inside a crystal induces a polarization \mathbf{P} . In an anisotropic medium the polarization P_i along a particular direction depends on the three components $i, j, k, l \in \{x, y, z\}$ of the electric field expressed in a power series [196]

$$P_i(\mathbf{E}) = \epsilon_0 \left(\sum_j \chi_i^{(1)j} E_j + \sum_{j,k} \chi_i^{(2)j,k} E_j E_k + \sum_{j,k,l} \chi_i^{(3)j,k,l} E_j E_k E_l + \dots \right), \quad (2.48)$$

with ϵ_0 the dielectric constant. The electric susceptibilities $\chi^{(m)}$ of order m are, in the general case, tensors. They are of strength $\chi^{(1)} \approx 1$, $\chi^{(2)} \approx 10^{-10}$ cm/V and $\chi^{(3)} \approx 10^{-17}$ cm²/V², i.e., the coupling of the electric field with the crystal decreases rapidly with (m). The term proportional to $\chi^{(2)}$ is responsible for three-wave mixing (three photon interaction) used for sum- and difference-frequency conversion, second harmonic generation, and SPDC, whereupon the latter can only be understood when quantizing the relevant fields as it represents a spontaneous process. The term proportional to $\chi^{(3)}$ describes four-wave mixing responsible for the non-linear refractive index and SFWM. The following description is restricted to the process of SPDC.

Energy and momentum conservation must be fulfilled between the three interacting waves, hence,

$$\hbar\omega_p = \hbar\omega_s + \hbar\omega_i + \Delta E \quad \text{and} \quad \hbar\mathbf{k}_p = \hbar\mathbf{k}_s + \hbar\mathbf{k}_i + \hbar\Delta\mathbf{k} \quad (2.49)$$

with $\Delta E = 0$ and $\Delta\mathbf{k} = 0$. Thereby, ω_m with $m \in \{p, s, i\}$ denotes the frequency of pump, signal and idler waves and the absolute value of the wave vector is given as $|\mathbf{k}_m| = \omega_m n(\omega_m)/c$, where $n(\omega_m)$ is the refractive index and c the speed of light. The condition $\Delta\mathbf{k} = 0$ is called phase-matching (only in that case the SPDC process yields a considerable emission) and can be reached in naturally occurring crystals by using the effect of birefringence, for example, in negative ($n_e < n_o$), uniaxial crystals, whereby a special direction called the optical axis exists. The plane containing the optical axis and the incident wave vector is called the principal plane. Light polarized perpendicular (parallel) to that plane is called ordinary, o (extraordinary, e). To achieve $\Delta\mathbf{k} = 0$ one exploits that the refractive index for ordinarily polarized light does not depend on the propagation direction, whereas for extraordinarily polarized light it does. Then, two types of phase-matching can be distinguished: type I and type II. For type I (type II) phase-matching the pump is an e -wave and the signal and idler are o -(e - and o -) waves. Furthermore, depending on the relative orientation of the momentum vectors, collinear ($\mathbf{k}_p \parallel \mathbf{k}_s \parallel \mathbf{k}_i$) and non-collinear ($\mathbf{k}_p, \mathbf{k}_s, \mathbf{k}_i$ arbitrary directions fulfilling momentum conservation) phase-matching might occur. This is achieved, for example, by tuning of the crystal tilt, which changes the angle θ between the incident wave and the optical axis and as a result $n_e(\theta)$. In this work collinear [fig. 2.5(a)] and non-collinear type II [fig. 2.5(b)] phase-matching in β -barium-borate (BBO) crystals (β -BaB₂O₄, negative uniaxial) is used with a pump wave length at 390 nm. The degenerate case is considered, i.e., whereby the wavelength of the down converted signal and idler fields are equal and twice that of the pump field.

In the following the appearance of higher order terms in the SPDC process is discussed, which can directly be used for multi-photon entanglement experiments [52, 197]. SPDC is a non-classical process induced by fluctuations of the vacuum field. To this end, the interaction Hamiltonian [50]

$$\hat{\mathcal{H}}_I = \int_V dV \hat{\mathbf{E}}_p^{(+)} \hat{\mathbf{E}}_s^{(-)} \hat{\mathbf{E}}_i^{(-)} + h.c. \quad (2.50)$$

is considered, where $h.c.$ denotes the Hermitian conjugate. A single mode description of each electric field operator $\hat{\mathbf{E}}^{(\pm)}$ is sufficient to illustrate the appearance of higher order

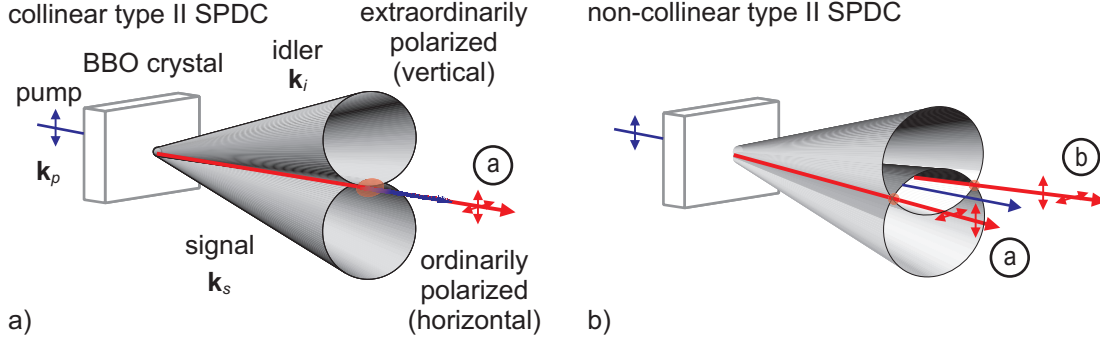


Figure 2.5: (a) The degenerate signal and idler photons in type II collinear SPDC are emitted in two cones that intersect along one line. Coupling into a single mode fiber defines the spatial mode a . (b) For type II non-collinear SPDC the cones intersect along two lines, defining modes a and b .

SPDC emissions. However, a multimode treatment, which considers a superposition of modes represented by monochromatic plane waves, is necessary for a proper calculation of the spatial, spectral and intensity distribution of the SPDC field. This is not the aim here and the interested reader is referred to the special literature on SPDC in general [198–201] and pulsed pump SPDC in particular [202–204]. Another assumption is the utilization of the proper polarizations, thus, the vector notation is dropped. The pump can be treated classically as a plane wave with a complex field amplitude

$$\hat{E}_p^{(+)} = E_{0;p} e^{i(k_p x - \omega_p t)} \quad (2.51)$$

with $E_{0;p}$ denotes the amplitude of the pump field. This simplification is possible because the interaction $\chi^{(2)}$ is very weak such that few pump photons are down converted (on the order of 10^{-10}). In contrast, the signal and idler fields have to be quantized by using the electric field operators,

$$\hat{E}_{s,i}^{(-)} = E_{0;s,i} \hat{a}^\dagger e^{-i(k_{s,i} x - \omega_{s,i} t)} \quad (2.52)$$

with the $E_{0;s,i}$ incorporate the parameters from field quantization, and $\hat{E}_{s,i}^{(+)} = (\hat{E}_{s,i}^{(-)})^\dagger$, where $\hat{E}_{s,i}^{(-)}$ corresponds to photon emission described by the creation operator \hat{a}^\dagger and $\hat{E}_{s,i}^{(+)}$ to photon annihilation described by the annihilation operator \hat{a} . The label a denotes the spatial mode of the photons. With the integration in eq. 2.50 taken over $\int_V dV$ one essentially obtains the phase-matching condition, see for example refs. [50, 205] (for a very long crystal with a large surface and a plane wave pump with a coherence time longer than the crystal length and infinite transversal extent, the phase-matching condition is essentially given by a δ -function yielding eq. 2.49). Assuming that the result is known and given as κ with $\kappa \propto |E_{0;p}| \chi^{(2)}$, then, for collinear (cl) and non-collinear (ncl) type II phase-matching one obtains the Hamiltonians [50, 206]

$$\hat{\mathcal{H}}_{1,\text{cl}} = i\hbar\kappa_{\text{cl}} \hat{a}_H^\dagger \hat{a}_V^\dagger + h.c., \quad (2.53)$$

$$\hat{\mathcal{H}}_{1,\text{ncl}} = i\hbar\kappa_{\text{ncl}} (\hat{a}_H^\dagger \hat{b}_V^\dagger - \hat{a}_V^\dagger \hat{b}_H^\dagger) + h.c. \quad (2.54)$$

For type II collinear SPDC photons of orthogonal polarization are created in a single spatial mode a [fig. 2.5(a)]. In contrast, for type II non-collinear SPDC the photons are created in two spatial modes a and b [fig. 2.5(b)], with a superposition of having a horizontally polarized photon in mode a and a vertically polarized photon in mode b or vice versa⁹.

To derive the state vector of the down converted fields one usually applies first order perturbation theory, approximating

$$|\psi\rangle_{\text{cl}} = e^{-\frac{i}{\hbar} \int dt \hat{\mathcal{H}}_{\text{I,cl}} t} |\text{vac}\rangle \quad (2.55)$$

as $|\psi\rangle_{\text{cl}} \approx (1 - \frac{i}{\hbar} \int dt \hat{\mathcal{H}}_{\text{I,cl}} t) |\text{vac}\rangle$ and accordingly for $|\psi\rangle_{\text{ncl}}$ with $|\text{vac}\rangle$ the vacuum state. However, continuing the expansion of the exponential to higher orders is necessary as these are used in the following experiments. A detailed derivation can be found in appendix A according to refs. [52, 206]. The result is

$$\begin{aligned} |\psi\rangle_{\text{cl}} &= \frac{1}{\cosh \tau_{\text{cl}}} \sum_{n=0}^{\infty} \frac{\tanh^n \tau_{\text{cl}}}{n!} (\hat{a}_H^\dagger \hat{a}_V^\dagger)^n |\text{vac}\rangle \\ &= \frac{1}{\cosh \tau_{\text{cl}}} \sum_{n=0}^{\infty} \tanh^n \tau_{\text{cl}} |n_H, n_V\rangle_a \end{aligned} \quad (2.56)$$

$$\begin{aligned} |\psi\rangle_{\text{ncl}} &= \frac{1}{\cosh^2 \tau_{\text{ncl}}} \sum_{n=0}^{\infty} \frac{\tanh^n \tau_{\text{ncl}}}{n!} (\hat{a}_H^\dagger \hat{b}_V^\dagger - \hat{a}_V^\dagger \hat{b}_H^\dagger)^n |\text{vac}\rangle \\ &= \frac{1}{\cosh^2 \tau_{\text{ncl}}} \sum_{n=0}^{\infty} \tanh^n \tau_{\text{ncl}} \\ &\quad \cdot \sum_{m=0}^n (-1)^m |m_H, (n-m)_V\rangle_a |(n-m)_H, m_V\rangle_b, \end{aligned} \quad (2.57)$$

with $\tau_{\text{cl}} \propto \kappa_{\text{cl}} t \propto |E_{0;p}| \chi^{(2)} t$ and $|n_H, n_V\rangle_a$ denotes n horizontally and n vertically polarized photons in mode a and accordingly for the non-collinear case.

These states illustrate that an SPDC source emits in its n th order emission $2n$ photons generated from the conversion of n pump photons. By selecting the first order emission of a type II non-collinear SPDC, one obtains the Bell state $|\psi^-\rangle$ directly from the SPDC source [51]. Higher order emission in combination with BSs can also be used for a simple observation of entangled, rotationally symmetric states [40, 59], see section 3.1.

Approximating $\tanh \tau \approx \tau$ for $\tau \ll 1$ yields a count rate $\propto \tau^{2n} \propto (|E_{0;p}| \chi^{(2)})^{2n}$ for the n th order emission (see appendix A). Hence, the count rate depends on the pump power $P_{0;p}$ according to

$$\tau^{2n} \propto |E_{0;p}|^{2n} \propto (P_{0;p})^n. \quad (2.58)$$

For conventional non-linearities and pump powers the probability to simultaneously generate n photon pairs is rather low. Therefore, the common approach is to concentrate the pump energy in short pulses to increase this probability per pulse.

⁹The phase between the two possibilities can easily be changed by a phase shifter in one of the spatial modes.

The experiments discussed in chapters 3 and 4 use the second order emission ($n = 2$) of a type II non-collinear SPDC source, i.e., the state

$$\begin{aligned} |\psi\rangle_{\text{ncl},2} &\propto \frac{\tanh^2 \tau_{\text{ncl}}}{2 \cosh^2 \tau_{\text{ncl}}} (\hat{a}_H^\dagger \hat{b}_V^\dagger - \hat{a}_V^\dagger \hat{b}_H^\dagger)^2 |\text{vac}\rangle \\ &= \frac{\tanh^2 \tau_{\text{ncl}}}{\cosh^2 \tau_{\text{ncl}}} (|0_H, 2_V\rangle_a |2_H, 0_V\rangle_b - |1_H, 1_V\rangle_a |1_H, 1_V\rangle_b + |2_H, 0_V\rangle_a |0_H, 2_V\rangle_b). \end{aligned} \quad (2.59)$$

The selection of the second order emission, i.e., four photons of the state of eq. 2.57, is performed by detecting exactly four photons in the linear optical setup. Further, for the experiment described in chapter 5 the third order emission of a type II collinear SPDC source is used,

$$|\psi\rangle_{\text{cl},3} \propto \frac{\tanh^3 \tau_{\text{cl}}}{6 \cosh \tau_{\text{cl}}} (\hat{a}_H^\dagger \hat{a}_V^\dagger)^3 |\text{vac}\rangle = \frac{\tanh^3 \tau_{\text{cl}}}{\cosh \tau_{\text{cl}}} |3_H, 3_V\rangle_a. \quad (2.60)$$

To select this state exactly six photons have to be detected.

The aforementioned description was based on a single mode treatment of SPDC. In order to use the SPDC photons for quantum information purposes it is sufficient that they are spatially, spectrally and temporally indistinguishable [207]. Spatial indistinguishability is achieved by coupling the SPDC emission into single mode fibers [208] that inherently only allow the propagation of the TEM₀₀ mode. Due to the different propagation directions for extraordinary and ordinary light in a birefringent crystal, transversal walk-off between the signal and idler photons occurs. This is partly compensated by using a half-wave plate (HWP) switching horizontal and vertical polarization followed by a half as thick, non-pumped BBO crystal [51, 205]. It is known that the spectra of idler and signal photons are different in a pulsed pumped type II process, originating essentially from the difference in their group velocities and the broadband pump [209–211]. Therefore the photons are spectrally filtered by using an interference filter of a certain bandwidth or a thin optical crystal could be used, both reducing the photon count rate. Different group velocities also imply temporal distinguishability. This is compensated by the HWP and the additional BBO crystal mentioned previously [51, 205]. Finally, observing higher order emissions requires that the photons are not emitted as multiples of distinguishable pairs. This requires that the information about their creation time (within the coherence or pulse length of the pump) has to be washed out [212, 213]. This is also facilitated by the interference filter, which broadens the coherence length of the SPDC photons such that it is impossible to acquire information about their exact creation time. Note, in principle a strong cw-pump can also be used to observe higher order emissions. However, the condition of temporal indistinguishability then demands strong filtering of the SPDC emission [214], and thus a drastic reduction in count rate. A systematic study of the most appropriate parameter set (pump pulse duration, pump wavelength, filter bandwidth) for an ideal multi-photon SPDC source is still missing.

Weak coherent beam Many applications in quantum information require single photons. A source delivering single photons and matching in all degrees of freedom already

generated SPDC photons can be realized by another SPDC process and very weak pumping. The detection of one photon, e.g., the signal, heralds the presence of the other photon, e.g., the idler [207].

An attenuated coherent beam can be employed to approximate a single photon source, which can also match SPDC photons [215]. This has the advantage of a tunable production rate of photons. The state of a coherent beam is given as [50]

$$|\psi\rangle_w = e^{-|\tau_w|^2/2} \cdot \sum_{n=0}^{\infty} \frac{(\tau_w)^n}{n!} (\hat{w}_j^\dagger)^n |\text{vac}\rangle, \quad (2.61)$$

where \hat{w}_j^\dagger is the creation operator of a photon with polarization j in spatial mode w , $\tau_w = |\tau_w|e^{i\phi_w}$, $|\tau_w|^2$ is the mean photon number, and $|\tau_w|^2 e^{-|\tau_w|^2}$ is the probability for the photon state $|1\rangle$. Hence, for sufficiently low pump powers the probability $|\tau_w|^4 e^{-|\tau_w|^2}/2$ of the undesired state $|2\rangle$ is very low. Thus, a weak coherent beam can approximate a single photon source. However, the Poissonian counting distribution of $|\psi\rangle_w$ will always introduce two-photon terms acting as noise [55, 216].

Experimental implementation In order to pump the SPDC process ultrashort pulses are required. Pump pulses with a central wavelength of 390 nm are used resulting for the degenerate case in down converted photons at 780 nm. The wavelength has been chosen such that high efficiency detectors can be employed in the experiments. To create the UV pump pulses, first a titanium:sapphire (Ti:Sa) oscillator is pumped by a 10 W cw-diode pumped solid state laser at 532 nm. The oscillator delivers 130 fs pulses centered at 780 nm with an average power of 2 W and a repetition rate of 80.8 MHz. Subsequently, these IR photons are up converted in a 3 mm thick lithium-triborate (LBO) crystal via second harmonic generation to ultraviolet (UV) pulses with a central wavelength of 390 nm and an average power between 560-800 mW. The UV pulses are focused into a BBO crystal. For the experiments described in chapters 3 and 4 a 2 mm thick, uncoated BBO crystal in type II non-collinear configuration is pumped with the UV pump beam having a waist of 200 μm . For the experiment described in chapter 5 a femtosecond UV enhancement cavity around a 1 mm thick, anti-reflection coated BBO crystal has been implemented in order to enhance the UV pump power to up to 7 W. The details of that setup are described in chapter 5.¹⁰

2.3.2 Photon processing

For multi-photon entanglement experiments the desired photonic quantum states are usually not directly observed in the emission of the SPDC source itself. The photons are further processed by linear optical elements like BSs and phase shifters. Linear refers to passive

¹⁰The cw-diode pumped solid state laser is a 10 W Millennia[®] XS by Spectra Physics[®], the Ti:Sa oscillator is a Tsunami[®] by Spectra Physics[®]. The uncoated BBO crystals are bought at Foctek[®], whereas the coated BBO crystals at Newlight Photonics[®].

optical elements that conserve the photon number, i.e., no non-linear photon conversion takes places. This allows interference of photons, but no direct photon-photon interaction. However, two-qubit interactions are required to, e.g., create graph states. This problem is circumvented by implementing the non-linearity in the detection process [42, 43]. The photons are distributed in a well-defined number of spatial modes, which corresponds to the particle number of the entangled state. Only under the condition of observing a single photon in each of these modes, the desired multi-photon states are observed. However, due to the usage of BSs, the distribution of the photons into spatial modes works only probabilistically, and thus results in a non-unit probability to observe the desired states.

At the same time a state is observed it is also destroyed. This drawback could be circumvented by a non-destructive photonic filter [217–219], which lets pass a certain number of photons, or by measuring the photon number non-destructively (for example through a quantum non-demolition measurement [220–222]) in each spatial mode. These schemes would preserve the polarization properties of photons and yield information about the photon number in each mode. However, to date, such measurements are in practice infeasible to perform for multi-photon experiments.

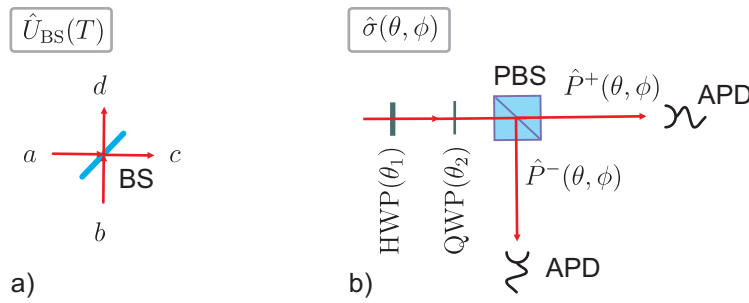


Figure 2.6: (a) Pictorial representation of a beam splitter (BS) with input modes a and b and output modes c and d . (b) A polarization analysis projects onto the eigenstates of $\hat{\sigma}(\theta, \phi)$ by using a half-wave plate (HWP), a quarter-wave plate (QWP), and a polarizing beam splitter (PBS) with photon detection using avalanche photo diodes (APDs).

Beam splitters BSs distribute or mix photons in spatial modes and can be polarization dependent or independent. A BS is a four port device with two input modes denoted as a and b and two output modes denoted as c and d [fig. 2.6(a)]. A lossless BS is assumed with real transmittance $T \in \mathbb{R}$ and real reflectance $R \in \mathbb{R}$ such that $T + R = 1$. The transformation for a BS for the annihilation operators can be written as [223]

$$\hat{a} \rightarrow \sqrt{T}\hat{c} + i\sqrt{R}\hat{d} \quad \text{and} \quad \hat{b} \rightarrow \sqrt{T}\hat{d} + i\sqrt{R}\hat{c}, \quad (2.62)$$

or equivalently it can be formulated in matrix form as

$$\begin{pmatrix} \hat{c} \\ \hat{d} \end{pmatrix} = \hat{U}_{\text{BS}}(T) \begin{pmatrix} \hat{a} \\ \hat{b} \end{pmatrix} = \begin{pmatrix} \sqrt{T} & i\sqrt{R} \\ i\sqrt{R} & \sqrt{T} \end{pmatrix} \begin{pmatrix} \hat{a} \\ \hat{b} \end{pmatrix}. \quad (2.63)$$

The BS introduces a phase shift of $e^{i\pi/2}$ upon reflection, which ensures its unitarity [224]. A commonly used BS is $\hat{U}_{\text{BS}}(\frac{1}{2}) = (\mathbb{1} + i\hat{\sigma}_x)/\sqrt{2}$ (50:50 BS). Further, the annihilation operators and transmittances can depend on the polarization, which can be incorporated by considering an additional subscript. For example, a PBS transmits only horizontal polarization and reflects only vertical polarization. This can be described by $\hat{U}_{\text{BS},H}(1)$ acting on horizontally polarized photons and $\hat{U}_{\text{BS},V}(0)$ acting on vertically polarized photons. Mathematically, this corresponds to the tensor product between the spatial and polarization modes.

Phase shifters Further elements include phase shifters, which can rotate polarization states or simply change the phase between two polarization states. Here, horizontal and vertical polarization is used as polarization basis. The most commonly used phase shifts are $\lambda/2$ (HWP) and $\lambda/4$ (QWP) implemented by zero-order, uniaxial birefringent crystals, whose optical axis and the horizontal polarization enclose the angle θ . Their transformations are given by [225]

$$\text{HWP}(\theta) = \begin{pmatrix} \cos 2\theta & \sin 2\theta \\ \sin 2\theta & -\cos 2\theta \end{pmatrix} = \sin 2\theta \hat{\sigma}_x + \cos 2\theta \hat{\sigma}_z, \quad (2.64)$$

$$\begin{aligned} \text{QWP}(\theta) &= \begin{pmatrix} \cos^2 \theta - i \sin^2 \theta & (1+i) \cos \theta \sin \theta \\ (1+i) \cos \theta \sin \theta & -i \cos^2 \theta + \sin^2 \theta \end{pmatrix} \\ &= \frac{1}{2} ((1-i)\mathbb{1} + 2(1+i) \cos \theta \sin \theta \hat{\sigma}_x + (1+i) \cos 2\theta \hat{\sigma}_z). \end{aligned} \quad (2.65)$$

In particular, $\text{HWP}(0) = \hat{\sigma}_z$, $\text{HWP}(22.5^\circ) = (\hat{\sigma}_x + \hat{\sigma}_z)/\sqrt{2}$ (so-called Hadamard transformation) and $\text{HWP}(45^\circ) = \hat{\sigma}_x$. An arbitrary unitary transformation acting on the polarization states of photons can be implemented by two QWPs and a HWP in the order $\text{QWP}(\theta_1)$, $\text{HWP}(\theta_2)$, and $\text{QWP}(\theta_3)$ with appropriate chosen angles θ_1, θ_2 and θ_3 . In some cases only a phase shift between horizontal and vertical polarization is necessary. This can simply be implemented by varying the thickness of a birefringent crystal via rotating it around its optical axis, which is perpendicular to the horizontal polarization. This can be represented by

$$\begin{aligned} \text{PS}(\phi) &= \begin{pmatrix} i \cos(\phi/2) + \sin(\phi/2) & 0 \\ 0 & i \cos(\phi/2) - \sin(\phi/2) \end{pmatrix} \\ &= i \cos(\phi/2) \mathbb{1} + \sin(\phi/2) \hat{\sigma}_z. \end{aligned} \quad (2.66)$$

Experimentally, a pair of birefringent yttrium-vanadate (YVO) crystals is used. Their optical axes are oriented perpendicular to each other to compensate dispersion effects [104]. Then, only the difference in crystal thickness causes the phase shift. In the experiment the $\text{PS}(\phi)$ is used to compensate undesired phase shifts introduced by BSs.

Polarization analysis and data acquisition Finally, in order to analyze the polarization state of the photons a HWP, QWP and PBS are used [fig. 2.6(b)]. While the

PBS projects the photons onto horizontal and vertical polarization, i.e., the eigenvectors of $\hat{\sigma}_z$, the combination of HWP and QWP rotates any incoming polarization onto the latter two polarizations up to a global phase. The overall transformation projects onto the eigenvectors of $\hat{\sigma}(\theta, \phi)$. In particular, to measure the projector onto the most commonly used bases $\hat{\sigma}_x$, $\hat{\sigma}_y$ and $\hat{\sigma}_z$, the following angles have to be set QWP(0°)HWP(22.5°), QWP(45°)HWP(0°) and QWP(0°)HWP(0°). This can be easily verified by calculating

$$\hat{\sigma}_z = (\text{QWP}(\theta_2)\text{HWP}(\theta_1)) \hat{\sigma}(\theta, \phi) (\text{QWP}(\theta_2)\text{HWP}(\theta_1))^\dagger \quad (2.67)$$

with $\hat{\sigma}(\pi/2, 0) = \hat{\sigma}_x$, $\hat{\sigma}(\pi/2, \pi/2) = \hat{\sigma}_y$, and $\hat{\sigma}(0, 0) = \hat{\sigma}_z$, respectively. For an arbitrary polarization setting θ_1 and θ_2 have to be calculated.

The probabilities $p^\pm(\theta, \phi)$ of a particular polarization basis setting correspond to a local measurement setting of $\hat{\sigma}(\theta, \phi)$ and are used to calculate the single qubit correlation $T_{\hat{\sigma}(\theta, \phi)}(\rho) = \text{Tr}[\rho \hat{\sigma}(\theta, \phi)] = p^+(\theta, \phi) - p^-(\theta, \phi)$. The probabilities $p^\pm(\theta, \phi)$ can be determined by the relative frequencies of the measured counts at the output ports of the PBS. To analyze multi-photon states, each spatial mode is equipped with a polarization analysis. Combined data yield the correlations $T_{\mu_1, \dots, \mu_N}(\rho)$, for details see refs. [103, 104].

For photon counting silicon APDs are used, which have a detection efficiency of about 55% at a wavelength of 780 nm. To take the difference in detector efficiency of the detectors at each PBS output port into account, the measured counts in each PBS output are corrected by the relative detector efficiency. Errors on the data are deduced by Gaussian error propagation from Poissonian counting statistics and errors on the independently determined relative detector efficiencies [104]. The detection signals are fed into a coincidence unit capable of registering all possible coincidences between all detectors. For the experiments described in chapters 3 and 4 (chapter 5) 8 (12) detectors have been used in order to detect the polarization states of four (six) photons. Two different types of coincidence units have been used, an asynchronous and a synchronous version. The asynchronous coincidence unit [226] opens a coincidence window of about 8 ns, which is smaller than the pulse separation of 12 ns, upon registering a click from any channel and registers all possible additional detector clicks. However, it is capable of registering a maximal rate of 1 MHz only, which was not sufficient for the six photon experiment. To this end a new coincidence unit has been developed based on a field programmable gate array (FPGA) controlled logic, which is described in appendix D. This unit samples detector clicks with the repetition rate of the laser, and thus has a maximal detection rate of 80.8 MHz.¹¹

In this chapter the necessary theoretical and experimental tools to describe, characterize, and observe photonic entangled states have been presented. Now, particular experimental implementations are discussed.

¹¹The manufacturers for the optical components used in the experiments are: 50:50 BS (Newport[®]), PBS (Linos[®]), HWP and QWP (Foctek[®], CeNing[®]), YVO crystals (Foctek[®], CeNing[®]). The detectors are SPCM-AQ4C modules from Perkin Elmer[®]. Both coincidence logic units are home-made [226] (see appendix D).

Chapter 3

Observation of a family of four-photon entangled states

The combination of SPDC photon sources with linear optical elements is the most successful method to date for the observation of multi-partite entanglement. This is evidenced by the fact that the diversity of observed entangled states is largest for that physical implementation, see for example refs. [36–39, 53, 58–60, 64, 65, 82, 189]. However, so far for each and every state a new experimental setup had to be designed. In this chapter a scheme for observing a multitude of different four-photon entangled states in a single setup and its experimental implementation is presented [53] (see publ. P3.1). This is achieved by varying a single, easily accessible experimental parameter. In principle, the scheme is extendable to arbitrary photon numbers, yet due to current technological limits is only in immediate reach for six photons [54] (see publ. P3.2).

In section 3.1 the flexible state observation is described. Essentially, this scheme is based on the combination of multi-photon interference of an entangled input state at a beam splitter and prior polarization manipulations. A detailed description of the experimental implementation is outlined in publ. P3.1 and P3.2. Here, an overview of multi-photon interference and its application for multi-photon entanglement observation, a short summary of the implementation of the four- and six-photon family and the experimental verification of four-photon interference is given. In section 3.2 important states of the family of four-photon entangled states along with the detection of their entanglement are presented. To this end different criteria are applied to exclude full-separability and to prove genuine four-photon entanglement based on the methods described in section 2.2. These methods can be compared with respect to the necessary number of measurement settings and the robustness against white noise. Finally, in section 3.3 the properties of the states contained in the family are examined in order to stimulate new applications. The analysis of the properties and the comparison of various tools to detect entanglement (apart from proving genuine four-photon entanglement) go beyond publ. P3.1 and P3.2.

3.1 Multi-photon interference

Multi-photon interference for SPDC experiments In a quantum mechanical description of the phenomenon of interference it is known that, if different possibilities lead to exactly the same physical situation, then the corresponding amplitudes add up coherently and not the probabilities of each possibility. This potentially leads to an enhancement or suppression of the total probability of the corresponding measurement outcome.

Generally, interference phenomena connected with a single detection event such as Young's double slit experiment¹ are called one-photon interference or second-order interference. The intensity depends on the product of two electric field operators,

$$\propto \langle \hat{E}^{(-)}(x)\hat{E}^{(+)}(x) \rangle. \quad (3.1)$$

In contrast, two-photon interference or fourth-order interference occurs, whenever a simultaneous double detection event leads to interference. This is proportional to

$$\langle \hat{E}^{(-)}(x_1)\hat{E}^{(-)}(x_2)\hat{E}^{(+)}(x_2)\hat{E}^{(+)}(x_1) \rangle. \quad (3.2)$$

The generalization to N -photon interference is straightforward [227]. A coincident measurement scheme exploiting two-photon interference was first suggested by Hanbury Brown and Twiss to determine the apparent angular size of distant stars [228]. Another striking example for two-photon interference occurs at a 50:50 BS, where a single photon enters each input port. The two incident photons leave the BS only bunched, either both at the one or the other output port, but never at different output ports due to destructive interference. This experiment was first performed by C. Hong, Z. Ou and L. Mandel [229]. Generally, one-photon interference shows oscillations on the order of the wavelength. In contrast, two-photon interference exhibits a dependence on the order of the coherence length of the interfering photons and is usually measured as a dip in the two-photon count rate.

Since the observation of the Hong-Ou-Mandel (HOM) dip many experiments were performed to show the different nature of one- and two-photon interference, see for example ref. [230]. Two-photon interference is now widely applied in quantum information processing, for example for the creation of entanglement between two distant atoms through interference of emitted photons at a BS [79, 231–236], for the observation of multi-photon entangled states through interference of photons at BSs [36, 64, 158, 188, 189] or for the enhancement of phase sensitivity beyond the classical limit [237, 238].

In the following multi-photon interference between $2N$ photons is referred to in an even stricter sense, namely it is required that all $2N$ photons interfere at a single BS [223]. For example, N photons impinge on the BS from each input mode [85]. Then, interference occurs if the photons are indistinguishable [212, 213]. Such experiments have

¹Thomas Young performed at the beginning of the 19th century the well known double slit experiment, whereby coherent light originating from two close positions interferes, resulting in a modulation of the light intensity in the transversal plane behind the slit. At that time the experimental result was interpreted as light behaving like a wave. Nowadays one knows through quantum mechanics of the duality between the wave and particle description of light.

been performed with four [197, 238, 239] and six photons [240, 241], whereby the input state to the BS was a product state. In this work it is demonstrated that the usage of multi-photon interference is of additional benefit for multi-photon state observation by exploiting *entangled* multi-photon states as input for the BS and prior polarization manipulations. At first, the progress in multi-photon entanglement observation is recapitulated. Note, as has been described in section 2.3, all these experiments rely on the conditional detection of $2N$ photons in $2N$ spatial modes.

Historically, it was first demonstrated that two-photon entangled states can be created directly from the source without the need for interference [51]. The first order type II non-collinear SPDC emission was used that directly emits a Bell state (see eq. 2.57). The next experimental step was the realization of various four-photon experiments, among these were the demonstration of the teleportation² [158] and entanglement swapping [242] protocols. Following these experiments, the observation of the three photon GHZ state [58, 187] has been performed motivated by its all versus nothing violation of LHV models [62, 63]. For that state, the second order emission of a type II source was exploited².

Generally, photon processing in SPDC-based experiments can be divided into three major experimental schemes:

- (i) interferometric overlap of single photons or of single photons from entangled Bell states at BSs (relying on two-photon interference) [fig. 3.1(a)],
- (ii) symmetric distribution of photons via BSs (without utilizing any interferometric overlap) [fig. 3.1(b), (c)],
- (iii) interferometric overlap of multiple photons at BSs (multi-photon interference) (fig. 3.2).

The observation of N -partite GHZ states relies on scheme (i). Fusing single photons from entangled Bell pairs at PBSs allows the synthesis of arbitrarily large GHZ states [215, 243, 244] [fig. 3.1(a)]. This method was used to observe four- [64], five- [188] and six-photon GHZ states [36] and can also be applied for synthesizing one- and two-dimensional cluster states by inserting HWPs in front or after the PBSs [244], for example for a six-photon cluster state [36]. Instead of a PBS, a partially polarizing BS enabled one to observe a four-photon cluster state [189]. All these experiments required multiple interferometrically stable (on the order of the coherence length of the photons), mode matched overlaps of photons, which for large photon numbers complicates the optical alignment and stability.

Scheme (ii) is performed without the need for interference and exploits higher order SPDC emissions in combination with subsequent symmetric distribution of photons using polarization independent BSs. Along that line, higher order SPDC emissions of a non-collinear type II source can be used (eq. 2.57). The photons of the N th order emission created in modes a and b are distributed by polarization independent BSs into $2N$ spatial modes [fig. 3.1(b)], yielding the $2N$ qubit, rotationally symmetric state [245]. This

²In principle, only three photons are necessary for the teleportation protocol or the observation of the GHZ state. The fourth photon merely serves as a trigger photon.

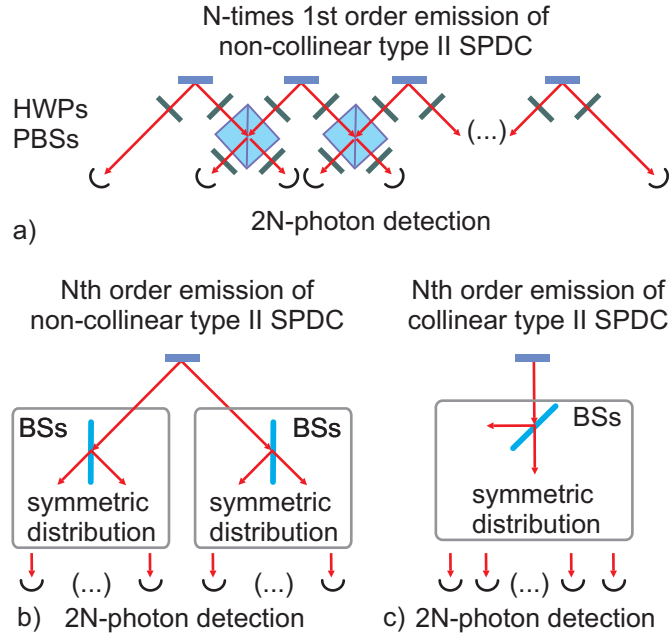


Figure 3.1: (a) Fusion of single photons from N Bell pairs at PBSs allows the observation of $2N$ -partite $|\text{GHZ}_{2N}\rangle$ states, and with additional HWPs, also cluster states. (b) The symmetric distribution of the N th order non-collinear type II SPDC emission leads to the observation of $2N$ -partite entangled, rotationally symmetric states. (c) In contrast, the symmetric distribution of the N th order collinear type II SPDC emission leads to the observation of $2N$ -partite entangled symmetric Dicke states with N excitations, $|D_{2N}^{(N)}\rangle$.

scheme was used to observe the four-photon [59] and recently also the six-photon rotationally symmetric states [40]. By using a collinear type II source and subsequent photon distribution, symmetric Dicke states can be observed [fig. 3.1(c)], which has been realized for two [123], four [65] and recently six photons [38, 39]. The latter experiment is described in chapter 5. These experiments are based on conditional detection of $2N$ photons in $2N$ separate spatial modes and have the advantage of inherent stability and simplicity as no interferometric overlaps are necessary. However, the probability to observe the desired state is lower compared to scheme (i) due to the utilization of BSs (see also footnote 11 of appendix C.3).

Finally, in scheme (iii) higher order SPDC emissions in combination with interferometric overlaps are utilized. For example, the observation of the four-photon cluster state can also be realized by using the indistinguishability of second order and two first order SPDC emissions through overlap at PBSs [60].

However, the aforementioned experiments are not flexible, as for each quantum state a new linear optical setup had to be built. In refs. [53, 54] (publ. P3.1 and P3.2) a method has been presented to design a linear optical network, where, by changing an easily adjustable experimental parameter, an entire family of four-photon entangled states can be observed. This scheme is in principle extendable to arbitrary photon numbers. In the following, a

short summary of the required experimental steps to observe the family of entangled states is given, details are outlined in publ. P3.1 and P3.2.

At the heart of the experiment is the interference of the N th order type II non-collinear SPDC emission (eq. 2.57) on a BS with prior polarization manipulations at the BS input modes. The BS output modes are divided into $2N$ spatial modes by polarization-independent BSs in order to observe the desired $2N$ -partite entangled states. The experimental implementation of the scheme for $N = 2$ can be found in ref. [53] (publ. P3.1) and its extension to $N = 3$ in ref. [54] (publ. P3.2). The limit for higher N is set by the low count rate of current SPDC sources and noise originating from undesired higher order emissions (see appendix C). This scheme can be attributed to the last type of SPDC experiments.

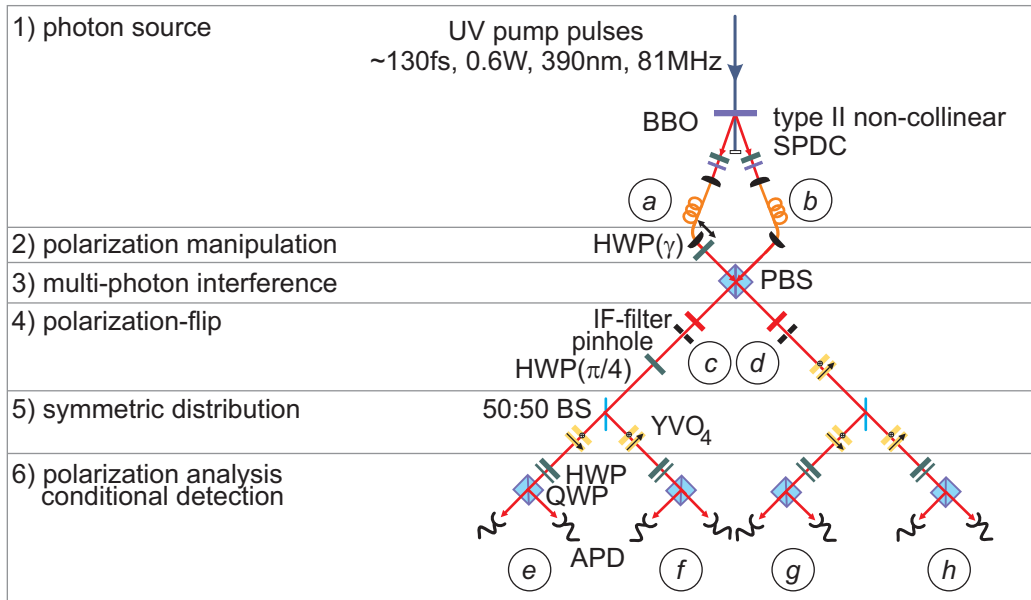


Figure 3.2: Schematic experimental setup for the observation of the family of states $|\Psi_4(\alpha)\rangle = \alpha(\gamma)|\psi^+\rangle \otimes |\psi^+\rangle + \sqrt{1 - \alpha(\gamma)^2}|\text{GHZ}'_4\rangle$.

In ref. [54] (publ. P3.2) the interference at various types of BSs is considered. It turns out, that the simplest and most powerful one is the interference at a PBS. The four-photon experiment can be divided into the following stages (fig. 3.2):

- (1) Photons from the 2nd order SPDC emission³ $[\propto (\hat{a}_H^\dagger \hat{b}_V^\dagger + \hat{a}_V^\dagger \hat{b}_H^\dagger)^2 |\text{vac}\rangle]$ are emitted into spatial modes a and b ,
- (2) subsequent polarization rotation in mode a with a HWP(γ),
- (3) interference of photons in mode a and b on a PBS,

³Here, a phase of $e^{i\cdot 0} = 1$ between the two terms is considered, see also footnote 9 of section 2.3.

- (4) polarization-flip in its output mode c using a HWP($\pi/4$),
- (5) symmetric distribution into four spatial modes labeled with e, f, g and h and
- (6) conditional detection.

Following the formalism described in section 2.3.2 one can easily calculate that the following family of states is observed [53, 172] (publ. P3.1),

$$\begin{aligned} |\Psi_4(\alpha)\rangle &= \alpha(\gamma) |\psi^+\rangle \otimes |\psi^+\rangle + \sqrt{1 - \alpha(\gamma)^2} |\text{GHZ}'_4\rangle, \\ \text{with } |\psi^+\rangle &= 1/\sqrt{2}(|HV\rangle + |VH\rangle), \\ |\text{GHZ}'_4\rangle &= 1/\sqrt{2}(|HHVV\rangle + |VVHH\rangle), \end{aligned} \quad (3.3)$$

the amplitude

$$\alpha(\gamma) = (2 \cos 4\gamma) / \sqrt{48p_4(\gamma)}, \quad (3.4)$$

and the observation probability

$$p_4(\gamma) = (5 - 4 \cos 4\gamma + 3 \cos 8\gamma) / 48, \quad (3.5)$$

and $\gamma \in [0, \frac{\pi}{4}]$. Hence, states with $\alpha \in [-1/\sqrt{3}, 1]$ can be observed. The observation of the six-photon family is carried out along similar steps [54] (publ. P3.2): third order SPDC emission, HWP(γ) in mode a , interference at a PBS and subsequent distribution into six spatial modes⁴. One obtains the states

$$\begin{aligned} |\Psi_6(\gamma)\rangle &= \beta(\gamma) |\text{GHZ}_6^-\rangle + \delta(\gamma) (|\overline{W}_3\rangle \otimes |\overline{W}_3\rangle - |W_3\rangle \otimes |W_3\rangle), \\ \text{with } |\text{GHZ}_6^-\rangle &= 1/\sqrt{2}(|H\rangle^{\otimes 6} - |V\rangle^{\otimes 6}), \end{aligned} \quad (3.6)$$

and

$$\begin{aligned} \beta(\gamma) &= 2(\sin 2\gamma)^2 / \sqrt{7 + 4 \cos 4\gamma + 5 \cos 8\gamma}, \\ \delta(\gamma) &= -(1 + 3 \cos 4\gamma) / (\sqrt{2} \sqrt{7 + 4 \cos 4\gamma + 5 \cos 8\gamma}), \\ \beta(\gamma)^2 + 2\delta(\gamma)^2 &= 1. \end{aligned} \quad (3.7)$$

The state observation probability is given as

$$p_6(\gamma) = \frac{2}{81} (\cos \gamma \sin \gamma)^2 (7 + 4 \cos 4\gamma + 5 \cos 8\gamma). \quad (3.8)$$

The experimental implementation of the four-photon family of states (eq. 3.3) will be discussed in the following. The six-photon family (eq. 3.6) is in experimental reach by using the SPDC source described in chapter 5 in a non-collinear arrangement.

⁴Here, a polarization-flip in one of the PBS output modes is not considered.

Experimental four-photon interference Before characterizing the states $|\Psi_4(\alpha)\rangle$, the observation of four-photon interference is demonstrated. For that purpose the state obtained for $\alpha = -\sqrt{1/3}$ ($\gamma = \pi/4$) is considered

$$|\Psi_4(\pi/4)\rangle = \sqrt{1/3}|\psi^+\rangle \otimes |\psi^+\rangle - \sqrt{2/3}|\text{GHZ}'_4\rangle \equiv |\Psi_4^-\rangle, \quad (3.9)$$

i.e., the four-photon, rotationally symmetric state. Due to the state's symmetry, the same structure is obtained when transformed to the \pm -basis, $\sqrt{1/3}|\psi^+\rangle \otimes |\psi^+\rangle - \sqrt{2/3}|\text{GHZ}'_4\rangle$. In general, it remains invariant under any local unitary transformation acting identically on each qubit.

To observe the state $|\Psi_4^-\rangle$ four photons have to add coherently. To this end, the temporal overlap between modes a and b is varied by changing the distance between the output coupler in mode a and the PBS. If the temporal modes of a and b are distinguishable, the state of the four photons behind the PBS is essentially an incoherent mixture of the polarization states $|H\rangle$ and $|V\rangle$ [246]. Thus, a measurement in the \pm -basis results in equal probabilities for each possible four-photon event. For example, the event $\{+ - - -\}$ is observed with the probability $1/(2^4)$. In contrast, for a coherent overlap the state $|\Psi_4^-\rangle$ is observed, whose amplitude for the term $|+ - - -\rangle$ is zero. This is shown in fig. 3.3(a), where the temporal overlap between modes a and b is changed. The expected decrease in count rate for $\{+ - - -\}$ is observed and a visibility of $\mathcal{V}_4 = 0.794 \pm 0.038$ is determined from a Gaussian fit [229]. Its full width at half maximum (FWHM) is $B_4 = (93 \pm 8) \mu\text{m}$.

To distinguish four- from two-photon interference the four-photon dip is compared to a two-photon dip. The latter can be observed by detecting two photons originating from the first order SPDC emission. Again, the case $\gamma = \pi/4$ is considered with an ideal state $|\psi^-\rangle$ observed for example in modes e and h . In this case, a transformation to the \pm -basis yields no contribution for the event $\{- -\}$. In contrast, an incoherent overlap results in a probability of $1/2^2$ for that event. This can be interpreted as HOM-type interference and is shown in fig. 3.3(b). The visibility of $\mathcal{V}_2 = 0.885 \pm 0.003$ is higher than \mathcal{V}_4 . The simple assumption that the four-photon visibility can be estimated from the two-photon visibility squared $(\mathcal{V}_2)^2 = 0.783 \pm 0.004$ corresponds closely to the observed \mathcal{V}_4 . The non-ideal visibility is attributed to higher order SPDC emissions (see appendix C) and a remaining degree of distinguishability by spatial and spectral mode mismatch at the PBS. The FWHM of the two-photon dip is $B_2 = (135 \pm 1) \mu\text{m}$. The coherence length⁵ of the photons is given as $l_c = \sqrt{2}B_2 = (191 \pm 2) \mu\text{m}$ [229], which corresponds closely to the interference filter bandwidth⁶ of $l_{c,\text{IF}} = 200 \mu\text{m}$. For the four-photon case the coherence

⁵Here, the definition of the coherence length follows [229]: the measured FWHM of the two-photon dip is identical to the coherence length divided by $\sqrt{2}$. In [229] it is derived that the two-photon count rate is proportional to $e^{-(\Delta\omega\delta\tau)^2}$ if the spectral function of a single photon is proportional to $e^{-(\Delta\omega\tau)^2/2}$, where $\Delta\omega$ is a frequency bandwidth (for example a filter bandwidth) and $\delta\tau$ is the two-photon arrival time difference at the BS. The FWHM of these two functions differs by a factor of $\sqrt{2}$.

⁶The interference filters have approximately a FWHM of $\Delta\lambda_{\text{IF}} = 3 \text{ nm}$ centered at $\lambda_{\text{IF}} = 780 \text{ nm}$ corresponding to a coherence length of $l_{c,\text{IF}} = \lambda_{\text{IF}}^2/\Delta\lambda_{\text{IF}} = 200 \mu\text{m}$. The old interference filter exhibits a Gaussian spectral shape (L.O.T. Andover ANDV7351, $\Delta\lambda_{\text{IF}} = 3.1 \text{ nm}$ yielding $l_{c,\text{IF}} = 195 \mu\text{m}$), the new one a rectangular spectral shape (Semrock[®] Maxline[®] 780-3, $\Delta\lambda_{\text{IF}} = 2.8 \text{ nm}$ yielding $l_{c,\text{IF}} = 220 \mu\text{m}$).

length is calculated as $l_c = (\sqrt{2})^2 B_4 = (186 \pm 16) \mu\text{m}$ yielding a similar result. Hence, the difference in the FWHM can be used to distinguish four- from two-photon interference.

At a later stage the two-photon visibility has been improved to $\mathcal{V}_2 = 0.959 \pm 0.004$ with $l_c = 234 \pm 3 \mu\text{m}$ [fig. 3.3(c)] by using pinholes behind the PBS to improve the spatial mode overlap and an interference filter with higher transmission and rectangular spectral shape. The higher transmission increases the overall detection efficiency and at the same time reduces noise (see appendix C for details). All further data presented in this chapter are measured with that configuration. The data used for chapter 4 have been measured with the Gaussian shaped interference filter. In the following, prominent states of $|\Psi_4(\alpha)\rangle$ and the detection of their entanglement is discussed.

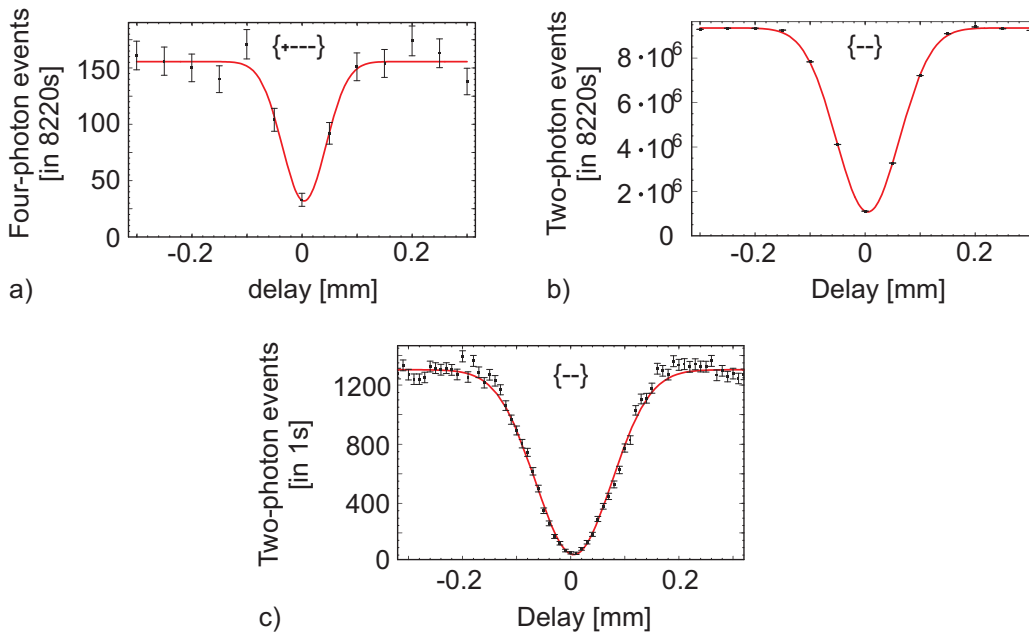


Figure 3.3: (a) Four-photon interference observed for the event $\{+---\}$ compared to (b) two-photon interference observed for $\{--\}$. The higher visibility and FWHM for the latter case can be clearly observed. (c) Using pinholes and an interference filter with rectangular spectral shape improves the visibility compared to (b).

3.2 Entanglement detection

Important states of the family $|\Psi_4(\alpha)\rangle$ Now, it is demonstrated that the family $|\Psi_4(\alpha)\rangle$ contains important and well known states that are useful for different quantum information applications [see refs. [53, 172] (publ. P3.1)] :

- $\alpha = 0$ ($\gamma = \pi/8$): The four-photon GHZ state is obtained. This state is widely applied in quantum information. GHZ states are well known for their all versus

nothing violation of LHV models, which can be demonstrated by so-called Mermin inequalities for arbitrarily large GHZ states [10]. Further, GHZ states find many more applications, for example for secret-sharing [118]. Recently, it has been shown that the four-qubit GHZ state is the ground state of a minimal instance of the toric code model [57], which is discussed in chapter 4.

- $\alpha = \pm\sqrt{1/3}$ ($\gamma = 0.098\pi$ and $\gamma = \pi/4$): For $\alpha = \pm\sqrt{1/3}$ the four-photon states $|\Psi_4^\pm\rangle$ are observed. These states can be transformed into each other by a LU transformation. The state $|\Psi_4^-\rangle$ has the remarkable property that it is invariant under any LU transformation acting identically on each qubit. It can form one of the two basis states for decoherence-free communication [247]. Further, the state itself and the state obtained after projection of one qubit find an application for telecloning [248, 249].
- $\alpha = \sqrt{2/3}$ ($\gamma = \pi/12$): The four-photon symmetric Dicke state with two excitations $|D_4^{(2)}\rangle$ is observed for this value. It is useful for telecloning [249] and open destination teleportation [188]. Further, it can be used to obtain via a single projective measurement states of the two inequivalent classes of tri-partite entanglement [107], which has been discovered in ref. [65]. These properties will be elaborated on in more detail in chapter 5, where the observation of the six-photon Dicke state $|D_6^{(3)}\rangle$ is discussed, which exhibits similar properties.
- $\alpha = 1$ ($\gamma = 0$): The state $|\psi^+\rangle \otimes |\psi^+\rangle$ is the only bi-separable state of the family. It can be transformed into the singlet state $|\psi^-\rangle \otimes |\psi^-\rangle$ via LU transformations. Together with the state $|\Psi_4^-\rangle$ it forms a basis for decoherence-free communication. Furthermore, $|\psi^+\rangle \otimes |\psi^+\rangle$ can also be used to obtain the states $|\text{GHZ}_3\rangle$ or $|W_3\rangle$ via gate operations acting on two of its qubits [250, 251].

These states are well known in quantum information and have already been independently implemented experimentally [59, 64, 65, 252]. However, the states $|\Psi_4(\alpha)\rangle$ contain for all other values of α states that have not been observed so far. Additionally, each state belongs to a different SLOCC class [53, 172], because $|\Psi_4(\alpha)\rangle$ can be attributed to the class G_{abcd} of SLOCC inequivalent states of the four-qubit classification of ref. [109]. The states in the G_{abcd} class are given by

$$G_{abcd} = \frac{a+d}{2}(|0000\rangle + |1111\rangle) + \frac{a-d}{2}(|0011\rangle + |1100\rangle) + \frac{b+c}{2}(|0101\rangle + |1010\rangle) + \frac{b-c}{2}(|0110\rangle + |1001\rangle), \quad (3.10)$$

with $\{a, b, c, d\} \in \mathbb{C}$ and a non-negative real part. A parameter comparison with eq. 3.3 yields

$$\begin{aligned} a = -d &= \sqrt{(1-\alpha^2)/2} \\ b &= \alpha \\ c &= 0. \end{aligned}$$

Surprisingly, when considering the correlations $T_{i,j,k,l}(\Psi_4(\alpha))$ with $i, j, k, l \in \{0, x, y, z\}$ the aforementioned states occur at crossing points of different correlations [53, 172] (see fig. 2 of publ. P3.1). Three more crossing points can be identified for:

- $\alpha = \pm\sqrt{\frac{1}{6}(3 - \sqrt{3})}$ ($\gamma = 0.1034\pi$ and $\gamma = 0.174\pi$): These two states can be transformed into each other via a LU transformation and therefore can be considered as a single new state.
- $\alpha = \sqrt{1/2}$ ($\gamma = 0.091\pi$): This state is an equal superposition of the $|\text{GHZ}'_4\rangle$ and the $|\psi^+\rangle \otimes |\psi^+\rangle$ part.
- $\alpha = \sqrt{\frac{1}{6}(3 + \sqrt{3})}$ ($\gamma = 0.076\pi$): Though this state looks similar to the one observed for $\alpha = \sqrt{\frac{1}{6}(3 - \sqrt{3})}$, both are SLOCC inequivalent.

So far, applications or special properties for the latter states are still missing. In the following the verification of entanglement for $|\Psi_4(\alpha)\rangle$ is described. The aforementioned nine states are selected for an experimental analysis, which can be regarded as a representative choice for the family $|\Psi_4(\alpha)\rangle$.

Excluding full-separability To rule out full-separability, criteria are applied that have been presented in section 2.2. Further, they are analyzed with respect to their robustness against white noise. The correlation criterion, the method of entanglement witnesses and the spin squeezing inequalities are applied to exclude full-separability. All criteria have the major advantage of requiring dramatically fewer measurement settings compared to a full state tomography [for the implemented measurement settings and achieved counting statistics see appendix B, for a tomography of the states observed for $\alpha = 0$ ($|\text{GHZ}'_4\rangle$), $\alpha = -\sqrt{\frac{1}{6}(3 - \sqrt{3})}$, $\alpha = -\sqrt{1/3}$ ($|\Psi_4^-\rangle$), and $\alpha = 1$ ($|\psi^+\rangle \otimes |\psi^+\rangle$) see fig. 3 in publ. P3.1].

Correlation criterion For $|\Psi_4(\alpha)\rangle$ one obtains independent of α

$$T_{x^{\otimes 4}}(\Psi_4(\alpha)) = T_{y^{\otimes 4}}(\Psi_4(\alpha)) = T_{z^{\otimes 4}}(\Psi_4(\alpha)) = 1. \quad (3.11)$$

Hence, already two correlations are sufficient in order to prove entanglement as $[T_{x^{\otimes 4}}(\Psi_4(\alpha))]^2 + [T_{y^{\otimes 4}}(\Psi_4(\alpha))]^2 = 2 > T_n^{\max}$ with $T_n^{\max} \leq 1$ the maximal value for fully-separable states. Experimentally, the values depicted in fig. 3.4(a) have been determined, thereby proving entanglement. Evaluating the robustness to white noise⁷ yields a critical visibility of $\nu_{\text{crit}} = 1/2$ independent of α [fig. 3.4(e)]. The criterion requires minimally only two measurement settings, yet, compared to the following criteria it does not give always the best noise robustness.

⁷Here, the critical visibility is defined as the maximal ν_{crit} for which $\max_{\hat{T}_N^{\text{prod}}}(\hat{T}_N^{\text{prod}}(\rho_{\text{sep}}), \nu_{\text{crit}}\hat{T}_N(\rho)) < (\nu_{\text{crit}}\hat{T}_N(\rho), \nu_{\text{crit}}\hat{T}_N(\rho))$ holds. The robustness to white noise would increase if all three perfect four-qubit correlations are used. A critical visibility of 1/3 would be achieved. Further, an even lower critical visibility can be reached. For example, for $\alpha = 0$ ($|\text{GHZ}'_4\rangle$) the visibility reduces to 1/9 when all nine perfect GHZ four-qubit correlations are used.

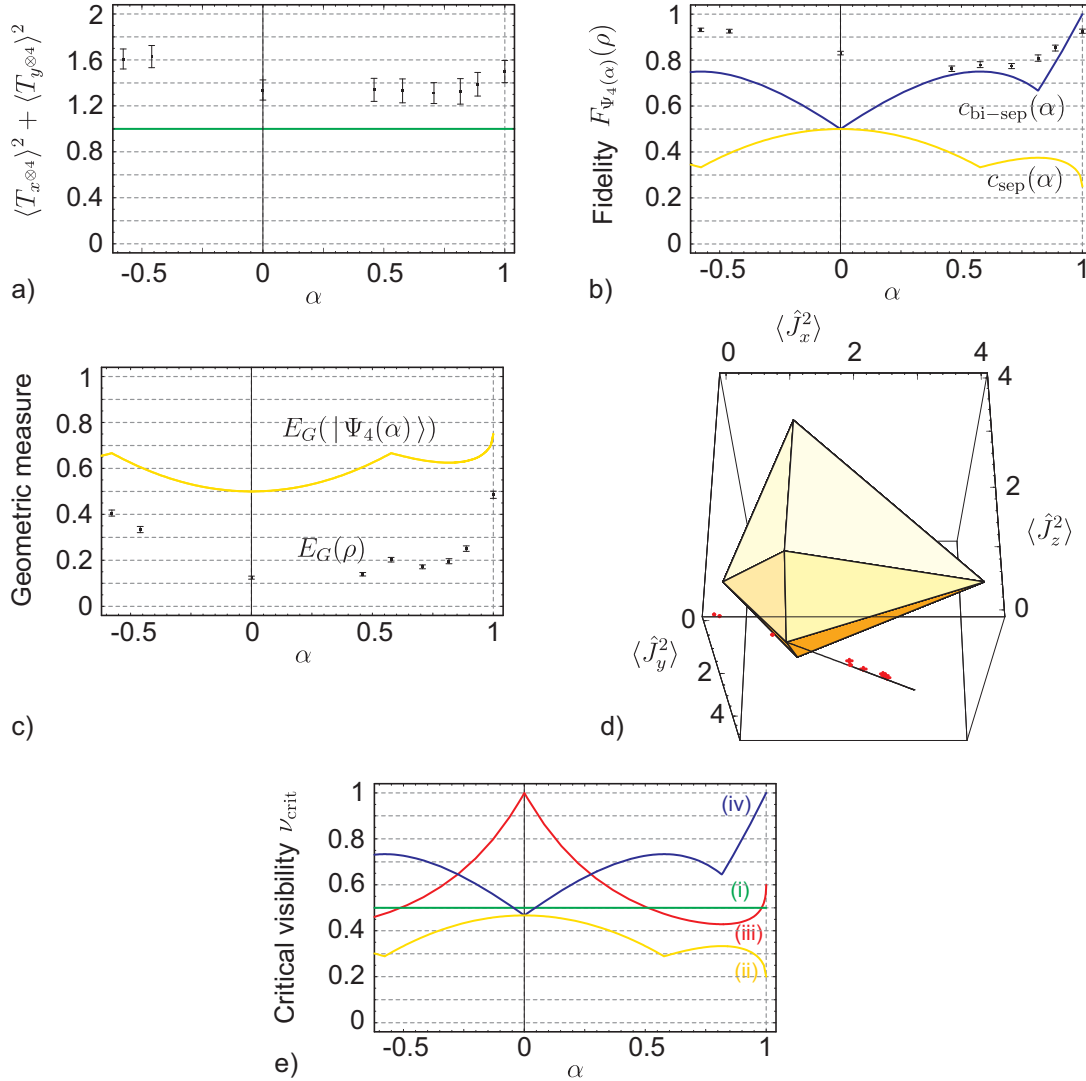


Figure 3.4: Detection of entanglement for the states $|\Psi_4(\alpha)\rangle$: (a) The correlation criterion excludes full-separability for values larger than 1. (b) The fidelity has to be larger than $c_{\text{sep}}(\alpha)$ to exclude full-separability or larger than $c_{\text{bi-sep}}(\alpha)$ to detect genuine four-photon entanglement using projector-based witnesses (eq. 3.12). (c) The expected $[E_G(|\Psi_4(\alpha)\rangle)]$ and experimentally estimated $[E_G(\rho)]$ geometric measure of entanglement. (d) Spin-squeezing polytope for four qubits in the $(\langle \hat{J}_x^2 \rangle, \langle \hat{J}_y^2 \rangle, \langle \hat{J}_z^2 \rangle)$ space. The straight line is the expected result for the states $|\Psi_4(\alpha)\rangle$, the red points the experimentally determined values. (e) Critical visibilities ν_{crit} for the states $\rho_{\text{mix}} = \nu_{\text{crit}} |\Psi_4(\alpha)\rangle\langle \Psi_4(\alpha)| + (1 - \nu_{\text{crit}}) \mathbb{1}^{\otimes 4}/2^4$ such that the corresponding criterion detects ρ_{mix} still as entangled. The curves are shown for the (i) correlation criterion, (ii) witness excluding full-separability, (iii) spin-squeezing inequalities and (iv) witness to detect genuine four-photon entanglement.

Entanglement witness An entanglement witness excluding full separability for the family $|\Psi_4(\alpha)\rangle$ is

$$\hat{\mathcal{W}}_{\text{sep}} = c_{\text{sep}}(\alpha)\mathbb{1}^{\otimes 4} - |\Psi_4(\alpha)\rangle\langle\Psi_4(\alpha)|. \quad (3.12)$$

Its expectation value is given by $\text{Tr}[\hat{\mathcal{W}}_{\text{sep}}\rho] = c_{\text{sep}}(\alpha) - F_{\Psi_4(\alpha)}(\rho)$. Hence, as soon as the fidelity $F_{\Psi_4(\alpha)}(\rho) > c_{\text{sep}}(\alpha)$ [253], the experimental states are proven to be entangled. The values depicted in fig. 3.4(b) have been determined from the measurements. All states fulfill $F_{\Psi_4(\alpha)}(\rho) > c_{\text{sep}}(\alpha)$ and therefore are entangled. The robustness against white noise is shown in fig. 3.4(e). For all states this criterion tolerates more noise than the correlation criterion. However, the determination of the fidelity requires, depending on the particular value of α , at most 21 measurement settings, compared to only two for the correlation criterion.

Geometric measure of entanglement The witness's measurement data allow the estimation of a lower bound on the geometric measure of entanglement by using the optimization method described in section 2.2. The result $E_G(\rho)$ is shown in fig. 3.4(c) and compared with the geometric measure $E_G(|\Psi_4(\alpha)\rangle)$ for the pure states. While the estimated values are lower than the theoretically expected ones, qualitatively, their dependence on α is reproduced. Furthermore, the highest value is found for the state $|\psi^+\rangle \otimes |\psi^+\rangle$, which is a bi-separable state. One has to keep in mind that this measure quantifies the distance to fully-separable states. Obviously the state $|\psi^+\rangle \otimes |\psi^+\rangle$ is further apart than any four-photon entangled state of the family. This shows that genuine four-qubit entanglement compared to another type of entanglement of a four-qubit state does not necessarily imply the largest value for the geometric measure of entanglement.

Spin squeezing inequalities The spin-squeezing inequalities can also be used to detect entanglement. All fully-separable states lie within a polytope in the $(\langle\hat{J}_x^2\rangle, \langle\hat{J}_y^2\rangle, \langle\hat{J}_z^2\rangle)$ space [fig. 3.4(d)] given by the corner points [147, 148]

$$\begin{aligned} A_x &= \{(4, 1, 1), (1, 4, 1), (1, 1, 4)\}, \\ B_x &= \{(0, 1, 1), (1, 0, 1), (1, 1, 0)\} \end{aligned} \quad (3.13)$$

for $\langle\hat{J}_x\rangle = \langle\hat{J}_y\rangle = \langle\hat{J}_z\rangle = 0$, which holds for $|\Psi_4(\alpha)\rangle$. The observed expectation values $\langle\hat{J}_i^2\rangle$ for $|\Psi_4(\alpha)\rangle$ are shown as a straight line. Clearly, all states lie outside the polytope except for $\alpha = 0$ ($|\text{GHZ}'_4\rangle$), which touches the polytope at the point $(0, 1, 1)$. The values determined for the experimentally observed states lie outside the region of full-separability. For some states that criterion is more robust against white noise than the correlation criterion [fig. 3.4(e)] and requires only three measurement settings.

The particular criterion one chooses for data evaluation depends on the actual experiment. One has to decide if the number of measurement settings or the robustness against white noise is more important. The described experiment profited from stability and high count

rates. Therefore, a comparison of the criteria in an experimental setting has been possible. That might not always be the case.

Another important aspect is the available measurement time and the related question of how to use this time efficiently: are few or many measurement settings in a given amount of time more suitable to yield a small error on the expectation value of a certain operator. This has been considered in ref. [172] for a selection of four-qubit operators. Generally, the error scales as A/\sqrt{N} , where N is the number of counts collected per measurement setting and is expected to be the same for all required measurement settings. The factor A depends on the actual operator and its decomposition in measurement settings, but is independent of N . The factor A has been found to differ about 25% between the considered operators in ref.[172]. Hence, for experiments reaching a low count rate operators are preferable, which have a small value of A .

Proving genuine four-photon entanglement Genuine four-photon entanglement can be proven based on, among others, the method of entanglement witnesses, Bell inequalities and the newly developed density matrix element criterion. In this work, the former criterion is applied as the latter one will still be optimized for the states $|\Psi_4(\alpha)\rangle$, details will be found in ref. [254].

Entanglement witness An entanglement witness proving genuine four-photon entanglement is analogous to the aforementioned witness, but the bound on the fidelity becomes stricter: $F_{\Psi_4(\alpha)}(\rho) > c_{\text{bi-sep}}(\alpha)$ [53] (publ. P3.1), which is depicted in fig. 3.4(b). All experimentally observed states are genuine four-photon entangled, except for the bi-separable state $|\psi^+\rangle \otimes |\psi^+\rangle$. Their robustness against white noise is worse than for the witness $\hat{\mathcal{W}}_{\text{sep}}$ [fig. 3.4(e)]. This is due to the fact that the space of bi-separable states is larger than the one of the fully-separable states. The evaluation of both witnesses requires the same number of measurement settings.

Bell inequalities For the states $|\text{GHZ}'_4\rangle$, $|D_4^{(2)}\rangle$ and $|\Psi_4^-\rangle$ characteristic Bell inequalities based on four-qubit correlations are known [10, 255]. Thereby, a characteristic Bell inequality for a state $|\psi\rangle$ yields the highest violation of a LHV model only for the state $|\psi\rangle$. At the same time it can be used to prove genuine four-qubit entanglement. Similar to witness operators the maximal value achieved for any bi-separable state can be calculated in order to obtain a bound for the characteristic Bell inequality. Surpassing this bound proves genuine N -qubit entanglement. This is explained in detail in refs. [172, 255] and therefore will not be repeated here (for the state $|D_4^{(2)}\rangle$ see also section 5.2).

To summarize, full-separability has been excluded and genuine four-photon entanglement has been proven for a variety of different entangled states by applying various entanglement detection methods. This can be regarded as a comparison of different entanglement criteria in the experimental setting, which might be useful to decide on the applicability of a criterion for a particular physical implementation.

3.3 Entanglement properties

In the following, a short overview of some entanglement properties worth studying is presented. These properties include the achievable entanglement after projection of photons and the remaining entanglement after loss of photons. The former is called entanglement connectedness and the latter entanglement persistency [46, 76, 256]. The family of states $|\Psi_4(\alpha)\rangle$ with $\alpha \in [0, 1]$ is considered (the states obtained for $\alpha \in [-1/\sqrt{3}, 0]$ are LU equivalent to the states with $\alpha \in [0, 1/\sqrt{3}]$).

Projective measurements An arbitrary projective measurement (section 2.1) can be described by the application of the projector $\hat{P}^+(2\theta, \phi) = |\psi(2\theta, \phi)\rangle\langle\psi(2\theta, \phi)| = (\mathbb{1} + \hat{\sigma}(2\theta, \phi))/2$. Applying a projection on photons 1 or 2 (3 or 4) of the state $|\Psi_4(\alpha)\rangle$ yields the same state due to the particular permutational symmetry of $|\Psi_4(\alpha)\rangle$. The obtained state is denoted as $|\psi_{234}\rangle(|\psi_{123}\rangle)$:

$$\begin{aligned} |\psi_{234}\rangle &= \cos\theta |\overline{W}_t\rangle + e^{-i\phi} \sin\theta |W_t\rangle, \\ |\psi_{123}\rangle &= \hat{S}_{24} |\psi_{234}\rangle, \\ \text{with } |W_t\rangle &= \sqrt{1-\alpha^2} |VHH\rangle + \alpha/\sqrt{2} (|HHV\rangle + |HVV\rangle), \\ |\overline{W}_t\rangle &= \sqrt{1-\alpha^2} |HVV\rangle + \alpha/\sqrt{2} (|VHV\rangle + |VVH\rangle). \end{aligned} \quad (3.14)$$

Thereby, \hat{S}_{24} is the swap operator⁸ exchanging photons 2 and 4, and thus $|\psi_{234}\rangle$ and $|\psi_{123}\rangle$ are LU equivalent.

To analyze these states the 3-tangle is chosen (see section 2.2, for GHZ-class states: $0 < \tau_3(|\text{GHZ}_{\text{class}}\rangle) \leq 1$). Fig. 3.5(a) shows the 3-tangle for the states $|\psi_{234}\rangle$ and $\alpha \in [0, 1]$, $\theta \in [0, \pi/2]$ and $\phi = 0$ [$\tau_3(|\psi_{234}\rangle)$ is independent of ϕ]. The maximal value $\tau_3(|\psi_{234}\rangle) = 1$ is obtained for $\alpha = 0$ and $\theta = \pi/4$. This corresponds to a projective measurement on the state $|\text{GHZ}'_4\rangle$ in the + basis and yields the three-photon GHZ state, $|\text{GHZ}'_3\rangle = 1/\sqrt{2}(|HVV\rangle + |VHH\rangle)$, which has maximal 3-tangle. A local maximum $\tau_3(|\psi_{234}\rangle) = 1/3$ is obtained for $\alpha = \sqrt{2/3}$ and $\theta = \pi/4$ corresponding to a measurement on the state $|D_4^{(2)}\rangle$ in the + basis and yields a so-called G -state $|G\rangle = (|W_3\rangle + |\overline{W}_3\rangle)/\sqrt{2}$ [257], a superposition of two three-photon W states. In ref. [55, 104] (publ. P5.2) an explicit probabilistic transformation is given that increases the 3-tangle to unity for this state.

Remarkably, for $\alpha = \sqrt{2/3}$ and $\theta = \pi/2$, which corresponds again to a measurement on the state $|D_4^{(2)}\rangle$, yet, in the V -basis, the three-photon W state is obtained ($\tau_3(|W_{\text{class}}\rangle) = 0$). Hence, both inequivalent classes of tri-partite entanglement can be accessed via projective measurements on $|D_4^{(2)}\rangle$. This has been highlighted and experimentally demonstrated in ref. [65]. Note, a further projective measurement can lead to two-photon entangled states, for example $|\psi^+\rangle$.

⁸The swap operator \hat{S}_{ij} exchanges qubits i and j and is given by $\hat{S}_{ij} = 1/2(\mathbb{1}_i \otimes \mathbb{1}_j + \hat{\sigma}_{x;i} \otimes \hat{\sigma}_{x;j} + \hat{\sigma}_{y;i} \otimes \hat{\sigma}_{y;j} + \hat{\sigma}_{z;i} \otimes \hat{\sigma}_{z;j})$.

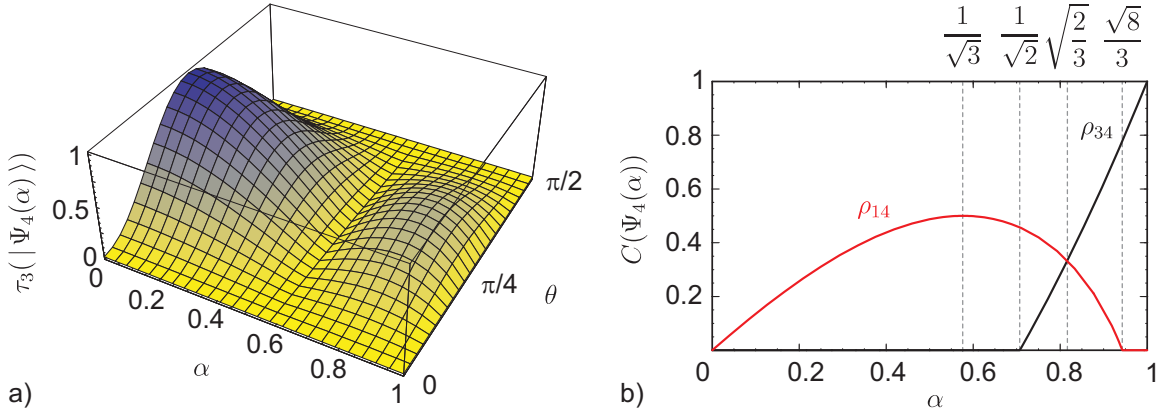


Figure 3.5: (a) 3-tangle for states obtained of $|\Psi_4(\alpha)\rangle$ after a single projective measurement $\hat{P}^+(2\theta, \phi) = |\psi(2\theta, \phi)\rangle\langle\psi(2\theta, \phi)|$ with $\phi = 0$. (b) Concurrence for two-photon mixed states ρ_{34} (black) and ρ_{14} (red) obtained after loss of two photons of $|\Psi_4(\alpha)\rangle$.

Photon loss Loss of photons 1 or 2 (3 or 4) of the states $|\Psi_4(\alpha)\rangle$ results formally in the same state, denoted as ρ_{234} (ρ_{123}):

$$\begin{aligned}\rho_{234} &= 1/2(|W_t\rangle\langle W_t| + |\bar{W}_t\rangle\langle\bar{W}_t|), \\ \rho_{123} &= \hat{S}_{24}\rho_{234}\hat{S}_{24}^\dagger.\end{aligned}\quad (3.15)$$

The mixed states ρ_{234} and ρ_{123} are LU equivalent and of rank two with purity $\text{Tr}[(\rho_{234})^2] = 1/2$ independent of α . It has been shown that, though the 3-tangle is defined for pure states, for any rank two mixed state it can be decided on analytical grounds if it has vanishing 3-tangle or not [177–179]. For the states of eq. 3.15, the 3-tangle is zero as it is zero for the pure states in the decomposition of the mixed states ρ_{234} . The pure states of the decomposition can each be transformed into W states with $\tau_3 = 0$ via local filtering on a single photon (formally equivalent to SLOCC).

A loss of a further photon results in two-photon mixed states. Due to the permutational symmetry of the states $|\Psi_4(\alpha)\rangle$ two different scenarios can be identified, (i) loss of photons $\{1, 2\}$ or (ii) $\{2, 3\}$. The remaining cases are equivalent to these two, namely (i) $\{3, 4\}$ or (ii) $\{1, 3\}$, $\{1, 4\}$, $\{2, 4\}$. The state after loss of photons $\{1, 2\}$ is given as

$$\rho_{34} = \alpha^2 |\psi^+\rangle\langle\psi^+| + (1 - \alpha^2)/2(|HH\rangle\langle HH| + |VV\rangle\langle VV|). \quad (3.16)$$

Hence, one obtains a mixture between an entangled state and correlated noise. This type of state has been shown to exhibit so-called “hidden” non-locality, see ref. [258]. The state obtained after loss of photons $\{2, 3\}$ is

$$\begin{aligned}\rho_{14} &= (2 - \alpha^2 - 2\sqrt{2\alpha^2 - 2\alpha^4})/4 |\psi^-\rangle\langle\psi^-| + (2 - \alpha^2 + 2\sqrt{2\alpha^2 - 2\alpha^4})/4 |\psi^+\rangle\langle\psi^+| \\ &\quad + \alpha^2/4(|HH\rangle\langle HH| + |VV\rangle\langle VV|).\end{aligned}\quad (3.17)$$

To analyze these states the concurrence is chosen, whose result is shown in fig. 3.5(b). For the states ρ_{34} the concurrence increases monotonically from 0 to 1 for $\alpha > 1/\sqrt{2}$, which

corresponds to one of the new states of the family. For $\alpha < 1/\sqrt{2}$ the concurrence is zero. The highest value is obtained for $\alpha = 1$, i.e., a loss of photons $\{1, 2\}$ of $|\psi^+\rangle \otimes |\psi^+\rangle$ results in the maximally entangled state $|\psi^+\rangle$. For the states ρ_{14} the behavior is different. Between $0 < \alpha < \sqrt{8}/3$ a non-zero concurrence is obtained with the highest value at $\alpha = \sqrt{1/3}$ (loss of two photons from $|\Psi_4^+\rangle$). For all other values of α the concurrence is zero. An equal value for the concurrence of ρ_{34} and ρ_{14} is found for $\alpha = \sqrt{2/3}$, which corresponds to a loss of two photons of the symmetric Dicke state $|D_4^{(2)}\rangle$.

When three photons are lost from the states $|\Psi_4(\alpha)\rangle$, the remaining photon is maximally mixed for all α , i.e., its von Neumann entropy is equal to one. This property is characteristic for the class G_{abcd} of four-qubit entangled states of the classification in ref. [109].

The observation of an entire family of four-photon entangled states in a single setup allows, on one hand, a study of different methods of entanglement detection and entanglement properties as a function of a single experimental parameter. This has not been possible before. On the other hand, the flexible observation of different entangled states allows one to perform different applications. One of the resulting states, namely the GHZ state, can be used for a simulation of anyonic features, which is discussed in the following chapter. The four-photon family of states has also been applied for evaluating the usefulness of different states for the quantum minority game, see refs. [172, 259].

3.4 Publications

P3.1

PRL 101, 010503 (2008)

PHYSICAL REVIEW LETTERS

week ending
4 JULY 2008

Experimental Observation of an Entire Family of Four-Photon Entangled States

Witold Wieczorek,^{1,2,*} Christian Schmid,^{1,2} Nikolai Kiesel,^{1,2} Reinhold Pohlner,^{1,2}
Otfried Gühne,^{3,4} and Harald Weinfurter^{1,2}¹Max-Planck-Institut für Quantenoptik, Hans-Kopfermann-Straße 1, D-85748 Garching, Germany²Department für Physik, Ludwig-Maximilians-Universität, D-80797 München, Germany³Institut für Quantenoptik und Quanteninformation, Österreichische Akademie der Wissenschaften, A-6020 Innsbruck, Austria⁴Institut für Theoretische Physik, Universität Innsbruck, Technikerstraße 25, A-6020 Innsbruck, Austria

(Received 16 April 2008; published 3 July 2008)

A single linear-optical setup is used to observe an entire family of four-photon entangled states. This approach breaks with the inflexibility of present linear-optical setups usually designed for the observation of a particular multipartite entangled state only. The family includes several prominent entangled states that are known to be highly relevant for quantum information applications.

DOI: 10.1103/PhysRevLett.101.010503

PACS numbers: 03.67.Bg, 03.67.Mn, 42.50.Ex, 42.65.Lm

Multipartite entanglement is a vital resource for numerous quantum information applications such as quantum computation, quantum communication, and quantum metrology. So far, the biggest variety of multipartite entangled states was studied using photonic qubits (e.g., [1–6]). As there is no efficient way of creating entanglement between photons by direct interaction, entangled photonic states are generally observed by a combination of a source of entangled photons and their further processing via linear-optical elements and conditional detection. Based on this approach, experiments were designed for the observation of a single, e.g., [1–5], or two [6] multipartite entangled state(s).

Here we break with this inflexibility by designing a single linear optics setup for the observation of an entire family of four-photon entangled states. The states of the family are conveniently chosen by one experimental parameter. Thereby, states that differ strongly in their entanglement properties are accessible in the same experiment [7]. We demonstrate the functionality of the scheme by the observation and analysis of a selection of distinguished entangled states.

The family that can be observed experimentally is given by the superposition of the tensor product of two Bell states and a four-qubit *GHZ* state:

$$|\Psi(\gamma)\rangle = \alpha(\gamma)|\psi^+\rangle \otimes |\psi^+\rangle + \sqrt{1 - \alpha(\gamma)^2}|GHZ\rangle, \quad (1)$$

where $|\psi^+\rangle = 1/\sqrt{2}(|HV\rangle + |VH\rangle)$ and $|GHZ\rangle = 1/\sqrt{2}(|HHVV\rangle + |VVHH\rangle)$ [8,9]. We use the notation for polarization encoded qubits, where, e.g., $|HHVV\rangle = |H\rangle_e \otimes |H\rangle_f \otimes |V\rangle_g \otimes |V\rangle_h$, $|H\rangle$ and $|V\rangle$ denote linear horizontal and vertical polarization, respectively, and the subscript denotes the spatial mode of each photon. Here the real amplitude $\alpha(\gamma)$, with $|\alpha(\gamma)| \leq 1$, is determined by a single, experimentally tunable parameter γ , which is set by the orientation of a half-wave plate (HWP). Thus, we are able to change continuously from the product of two Bell states over a number of interesting genuinely four-partite

entangled states to the four-qubit *GHZ* state. According to the four-qubit SLOCC (stochastic local operations and classical communication) classification in Ref. [10], the family $|\Psi(\gamma)\rangle$ is a subset of the generic family G_{abcd} of four-qubit entangled states. Note that $|\Psi(\gamma)\rangle$ represents a different class of SLOCC equivalent states for each value of $|\alpha(\gamma)|$.

The experimental setup that allows a flexible observation of the family $|\Psi(\gamma)\rangle$ is depicted in Fig. 1. Four photons originate from the second-order emission of a spontaneous parametric down-conversion (SPDC) process [11] in a 2-mm-thick β -barium borate (BBO) crystal arranged in a noncollinear type II configuration. The crystal is pumped by UV pulses with a central wavelength of 390 nm and an average power of 600 mW obtained from a frequency-doubled Ti:sapphire oscillator (pulse length 130 fs). The four photons are emitted into two spatial modes *a* and *b* [12]:

$$1/(2\sqrt{3})[(a_H^\dagger b_V^\dagger)^2 + (a_V^\dagger b_H^\dagger)^2 + 2a_H^\dagger a_V^\dagger b_H^\dagger b_V^\dagger]|\text{vac}\rangle, \quad (2)$$

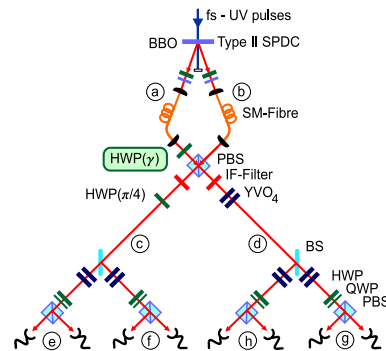


FIG. 1 (color online). Schematic experimental setup for the observation of the family $|\Psi(\gamma)\rangle$. For details, see the text.

where m_j^\dagger is the creation operator of a photon having polarization j in mode m and $|\text{vac}\rangle$ is the vacuum state. A HWP and a 1-mm-thick BBO crystal compensate walk-off effects. The spatial modes a and b are defined by coupling the photons into single mode (SM) fibers. Spectral selection is achieved by 3 nm FWHM interference filters (IF) centered around 780 nm. A HWP in mode a transforms the polarization of the photons. The orientation of the optical axis γ of this HWP is the tuning parameter of the family. Subsequently, the modes a and b are overlapped at a polarizing beam splitter (PBS) with its output modes denoted by c and d . A HWP oriented at $\pi/4$ behind the PBS transforms the polarization of the photons in mode c from $H(V)$ into $V(H)$. Subsequently, the modes c and d are split into the output modes e, f and g, h , respectively, via polarization-independent beam splitters (BS). Birefringence of the beam splitters is compensated by a pair of perpendicularly oriented birefringent yttrium-vanadate (YVO_4) crystals. Finally, the polarization state of each photon is analyzed with a HWP, a quarter-wave plate (QWP), and a PBS. The photons are detected by fiber-coupled single photon detectors and registered by a multi-channel coincidence unit.

Under the condition of detecting one photon of the second-order SPDC emission in each spatial output mode, the family of states $|\Psi(\gamma)\rangle$ is observed, where the amplitude $\alpha(\gamma)$ depends on the HWP angle γ via $\alpha(\gamma) = (2 \cos 4\gamma)/\sqrt{48p(\gamma)}$, with $\gamma \in [0, \pi/4]$. This occurs with a probability $p(\gamma) = (5 - 4 \cos 4\gamma + 3 \cos 8\gamma)/48$ (Fig. 2). Only for a few states of the family is a dedicated setup known [2–5]. For these particular cases, the respective state is observed with equal or higher probability. Here, however, we profit from the flexibility to choose various entangled states using the same setup.

Let us illustrate the described state observation scheme by examining the action of the HWP together with the PBS. We note that only the case where two photons are found in each spatial mode c and d behind the PBS, respectively, can lead to a detection event in each of the four output modes e, f, g, h . First, we consider a HWP oriented at $\gamma = 0$. This setting leaves the polarization of each photon unchanged. Each of the first two terms of Eq. (2) results in four photons in the same spatial mode behind the PBS and, thus, does not contribute to a fourfold coincidence in the output modes. However, the last term of Eq. (2) yields two photons in each mode behind the PBS, whose state is $\propto c_H^\dagger c_V^\dagger d_H^\dagger d_V^\dagger |\text{vac}\rangle$. A symmetric distribution of these photons leads to the observation of a Bell state in modes e, f and in modes g, h , respectively: $|\Psi(0)\rangle = |\psi^+\rangle \otimes |\psi^+\rangle$. Conversely, the last term of Eq. (2) can be suppressed by interference when the HWP is oriented at $\gamma = \pi/8$ transforming H/V into \pm polarization [$|\pm\rangle = 1/\sqrt{2}(|H\rangle \pm |V\rangle)$]. Then two photons in each mode c and d can originate only from the first two terms of Eq. (2) and result in the state $\propto [(c_H^\dagger d_H^\dagger)^2 + (c_V^\dagger d_V^\dagger)^2] |\text{vac}\rangle$ directly

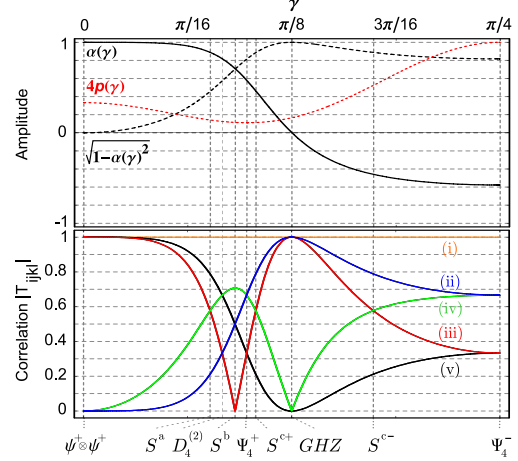


FIG. 2 (color online). The upper panel shows the dependence of the amplitudes $\alpha(\gamma)$ (solid curve) and $\sqrt{1 - \alpha(\gamma)^2}$ (dashed curve) on the tunable parameter γ for the family $|\Psi(\gamma)\rangle$. Also the probability $p(\gamma)$ (dotted curve) to observe the states $|\Psi(\gamma)\rangle$ is shown. The lower panel shows the modulus of the correlations $|T_{ijkl}|$ for the family $|\Psi(\gamma)\rangle$: (i) T_{iiii} , with $i \in \{0, x, y, z\}$; (ii) T_{00zz}, T_{xyxy} ; (iii) T_{00zz}, T_{xyxy} ; (iv) T_{ijij} ; and (v) T_{ijij} , with $i \in \{0, z\}$, $j \in \{x, y\}$. In order to obtain all 40 correlations, the following permutations starting from a normal ordering (1,2,3,4) are necessary: (1, 2) \leftrightarrow (3, 4), (1) \leftrightarrow (2), and (3) \leftrightarrow (4).

behind the PBS. This yields the GHZ state in the output modes. Continuous tuning of the HWP in the range $\gamma \in (0, \pi/8)$ and $\gamma \in (\pi/8, \pi/4)$ leads to any superposition of the states $|\psi^+\rangle \otimes |\psi^+\rangle$ and $|GHZ\rangle$ and, thus, to the observation of the entire family of states.

This family contains useful states, which, moreover, differ strongly in their entanglement properties. For example, the well-known GHZ state $[|GHZ\rangle = |\Psi(\pi/8)\rangle]$, i.e., $\alpha = 0$ [2] belongs to the graph states [13] and finds numerous applications in quantum information, e.g., [14]. The entanglement of the symmetric Dicke states [15] is known to be very robust against photon loss. Out of these states we observe with $\alpha = \sqrt{2/3}$ the state $|D_4^{(2)}\rangle = |\Psi(\pi/12)\rangle$ [3]. Remarkably, this state allows one to obtain, via a single projective measurement, states out of each of the two inequivalent classes of genuine tripartite entanglement [3,16]. The states $|\Psi_4^-\rangle = |\Psi(\pi/4)\rangle$ ($\alpha = -\sqrt{1/3}$) [4] and $|\psi^-\rangle \otimes |\psi^-\rangle$ [17] [that are equivalent under local unitary (LU) operations to $|\Psi_4^+\rangle = |\Psi(\approx 0.098\pi)\rangle$ ($\alpha = \sqrt{1/3}$) [5] and $|\psi^+\rangle \otimes |\psi^+\rangle = |\Psi(0)\rangle$ ($\alpha = 1$), respectively] are invariant under any action of the same LU transformation on each qubit, and, therefore, they form a basis for decoherence-free communication [18].

To characterize the family of states, we consider the correlations of $|\Psi(\gamma)\rangle$. Out of all 256 correlations T_{ijkl}

[19] in the standard basis, the family $|\Psi(\gamma)\rangle$ exhibits at most 40 that are nonzero. The modulus of these correlations $|T_{ijkl}|$ shows five distinct dependencies on γ , which are shown in Fig. 2. Interestingly, one finds the aforementioned states at the crossing points of some correlations. Consequently, we can identify other distinguished states at the remaining four crossing points. These are found at $\gamma \approx 0.076\pi$ ($\alpha = [1/6(3 + \sqrt{3})]^{1/2}$), $\gamma \approx 0.091\pi$ ($\alpha = \sqrt{1/2}$), $\gamma \approx 0.1034\pi$ ($\alpha = [1/6(3 - \sqrt{3})]^{1/2}$), and $\gamma \approx 0.174\pi$ ($\alpha = -[1/6(3 - \sqrt{3})]^{1/2}$). We label them for brevity by $|S^a\rangle$, $|S^b\rangle$, $|S^{c+}\rangle$, and $|S^{c-}\rangle$, respectively.

We select these nine states for an experimental characterization. As the setup is stable and delivers the states with a reasonable count rate, we are able to perform state tomography on $|GHZ\rangle$, $|S^{c-}\rangle$, $|\Psi_4^-\rangle$, and $|\psi^+\rangle \otimes |\psi^+\rangle$ of the selected set. The full tomographic data set was obtained from 81 different analysis settings for each state [3]. Because of the different probabilities to observe these states, we varied the total measurement time between 54 hours for $|\Psi_4^-\rangle$ and 202.5 hours for $|GHZ\rangle$ with count rates of 23.2 and 4.9 min^{-1} , respectively, without any realignment during each measurement run. The resulting density matrices are displayed in Fig. 3. The population and coherence terms for a GHZ state are clearly visible in Fig. 3(a). In Fig. 3(b), in addition to the GHZ part, the population and coherence terms of the $|\psi^+\rangle \otimes |\psi^+\rangle$ component appear. The (negative) coherence terms show that indeed a coherent superposition of both parts is achieved. The same structure is visible in Fig. 3(c) with an increased $|\psi^+\rangle \otimes |\psi^+\rangle$ part. Finally, in Fig. 3(d), the GHZ part has disappeared completely. This clearly illustrates that we are able to tune the relative weight between the states $|\psi^+\rangle \otimes |\psi^+\rangle$ and $|GHZ\rangle$ coherently, instead of only mixing them.

Next we focus on the quality of the states and on proving their entanglement. As a measure of the former, we evaluate the fidelity $F_{\Psi(\gamma)} = \langle \Psi(\gamma) | \rho_{\text{exp}} | \Psi(\gamma) \rangle$ for the observed states ρ_{exp} , where at most 21 measurement settings are required for the determination of $F_{\Psi(\gamma)}$ [20]. To perform these measurements for the remaining five states, the total measurement time ranged from 45.5 hours for $|S^a\rangle$ up to 112 hours for $|\Psi_4^+\rangle$, with count rates of 4.1 and 1.6 min^{-1} , respectively. The fidelities for all states are depicted in Fig. 4. We find high fidelities ranging from 0.75 up to 0.93. Obviously, the fidelity shows a dependence on γ . We emphasize that this behavior is not caused by a different optical alignment for each state; rather, it can be qualitatively attributed to different effects. Higher-order emissions of the SPDC, which can lead to additional four-fold coincidences, reduce the fidelity. For the actual experimental parameters (pair generation probability and coupling and detection efficiencies), we calculated that the fidelity for $\gamma = 0, \pi/4$ would be reduced by about 1%, while a reduction of up to 8% would be found for states around $|\Psi_4^+\rangle$. Furthermore, the fidelity of the observed states relies on the indistinguishability of the SPDC

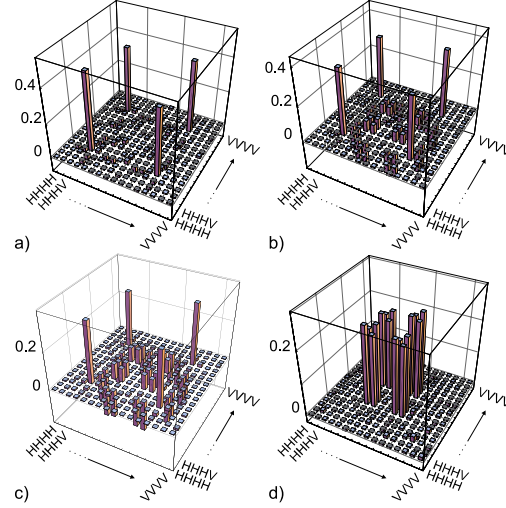


FIG. 3 (color online). The real part of experimental density matrices for the states (a) $|GHZ\rangle$, (b) $|S^{c-}\rangle$, (c) $|\Psi_4^-\rangle$, and (d) $|\psi^+\rangle \otimes |\psi^+\rangle$. For the states $|\Psi_4^-\rangle$ and $|GHZ\rangle$, the imaginary part has a peak at the off-diagonal element $|HHHH\rangle\langle VVVV|$ of 0.06 and 0.08, respectively, representing a slight imaginary phase between the terms $|HHHH\rangle$ and $|VVVV\rangle$. Otherwise, noise on the real and imaginary parts is comparable.

photons [21] and on the quality of interference. While for $\gamma = 0, \pi/4$ the PBS acts in the computational basis as a polarization filter only, for all other γ imperfect interference is relevant [22] and, thus, leads to an additional reduction of the fidelity. Considering these effects, the question arises whether the fidelity of particular states is higher when these states were observed with dedicated linear optics setups. For example, the states $|D_4^{(2)}\rangle$ and $|\Psi_4^-\rangle$ were recently observed with fidelities of $F_{D_4^{(2)}} = 0.844 \pm 0.008$ [3] and $F_{\Psi_4^-} = 0.901 \pm 0.01$ [4], respec-

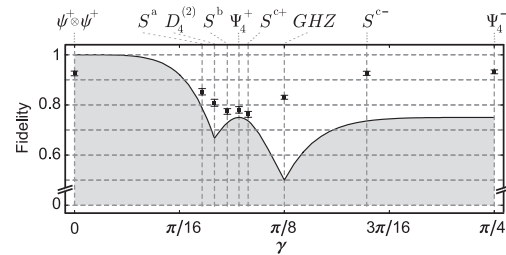


FIG. 4. Experimentally determined fidelities of nine distinguished states from the family $|\Psi(\gamma)\rangle = \alpha(\gamma)|\psi^+\rangle \otimes |\psi^+\rangle + \sqrt{1 - \alpha(\gamma)^2}|GHZ\rangle$. The minimal fidelity for proving genuine four-qubit entanglement is depicted as a solid curve.

tively. Here we achieved 0.809 ± 0.014 and 0.932 ± 0.008 , respectively, comparable with the dedicated implementations.

Finally, for proving genuine four-partite entanglement of the observed states, we apply generic entanglement witnesses $\mathcal{W}_{\Psi(\gamma)}$ [4,23]. Their expectation value depends directly on the fidelity: $\text{Tr}(\mathcal{W}_{\Psi(\gamma)}\rho_{\text{exp}}) = c(\gamma) - F_{\Psi(\gamma)}$, where $c(\gamma)$ is the maximal overlap of $|\Psi(\gamma)\rangle$ with all biseparable states. A fidelity larger than $c(\gamma)$ (solid curve in Fig. 4) detects genuine four-qubit entanglement of ρ_{exp} . We find that all experimental fidelities, except $F_{\Psi(0)}$, of course, are larger than $c(\gamma)$, thus proving four-qubit entanglement. For the biseparable entangled state $|\Psi(0)\rangle$, we apply the witness given in Ref. [24] on each pair and find -0.466 ± 0.006 and -0.461 ± 0.006 , respectively, detecting the entanglement of each pair.

In summary, we are able to observe an entire family of highly entangled four-photon states with high fidelity by using the same linear optics setup. For this purpose, a single SPDC source and one overlap on a PBS were sufficient. This is a clear improvement compared to previous dedicated linear optics realizations, where basically only one state could be observed. The general principle of commonly manipulating multiphoton states followed by interferometric overlaps at linear-optical components, of course, can be easily extended: For example, one can use the six-photon emission from the SPDC source and the presented setup or replace the PBS with a BS. Both enable the observation of different families of states [25]. Even if the weak photon-photon coupling does not allow the design of simple quantum logic gates, the utilization of higher-order emissions from an SPDC source together with multiphoton interference will enable further flexible experiments, each with numerous different and highly relevant multipartite entangled states.

We thank W. Laskowski and M. Bourennane for stimulating discussions. We acknowledge the support of this work by the DFG Cluster of Excellence MAP, the FWF, and the EU Projects QAP, SCALA, QICS, and OLAQUI. W. W. acknowledges support by QCCC of the ENB and the Studienstiftung des dt. Volkes.

*witlef.wieczorek@mpq.mpg.de

- [1] D. Bouwmeester *et al.*, Phys. Rev. Lett. **82**, 1345 (1999); M. Eibl *et al.*, Phys. Rev. Lett. **90**, 200403 (2003); P. Walther *et al.*, Nature (London) **434**, 169 (2005); B. P. Lanyon *et al.*, Phys. Rev. Lett. **100**, 060504 (2008).
- [2] J.-W. Pan *et al.*, Phys. Rev. Lett. **86**, 4435 (2001).
- [3] N. Kiesel *et al.*, Phys. Rev. Lett. **98**, 063604 (2007).
- [4] M. Bourennane *et al.*, Phys. Rev. Lett. **92**, 087902 (2004).
- [5] J.-S. Xu *et al.*, Phys. Rev. A **74**, 052311 (2006).
- [6] C.-Y. Lu *et al.*, Nature Phys. **3**, 91 (2007).
- [7] Recently, an experiment that allows one to continuously vary three photon states out of the same entanglement class was reported by B. P. Lanyon and N. K. Langford, arXiv:0802.3161.
- [8] For each $|\Psi(\gamma)\rangle$, a variety of other states can be obtained by local operations, which are easily implementable by linear-optical elements. While we focus on polarization encoding, the principle of state manipulations described here can be applied for other qubit encodings, too.
- [9] The family $|\Psi(\gamma)\rangle$ was studied theoretically with respect to the geometric measure of entanglement in the work of J. Eisert *et al.*, Phys. Rev. A **70**, 062317 (2004).
- [10] F. Verstraete *et al.*, Phys. Rev. A **65**, 052112 (2002).
- [11] P. G. Kwiat *et al.*, Phys. Rev. Lett. **75**, 4337 (1995).
- [12] H. Weinfurter and M. Żukowski, Phys. Rev. A **64**, 010102(R) (2001).
- [13] M. Hein *et al.*, Phys. Rev. A **69**, 062311 (2004).
- [14] M. Hillery *et al.*, Phys. Rev. A **59**, 1829 (1999); J.-C. Hao *et al.*, Phys. Rev. A **63**, 054301 (2001); J. K. Pachos *et al.*, arXiv:0710.0895.
- [15] R. H. Dicke, Phys. Rev. **93**, 99 (1954).
- [16] W. Dür *et al.*, Phys. Rev. A **62**, 062314 (2000).
- [17] M. Bourennane *et al.*, Phys. Rev. Lett. **92**, 107901 (2004).
- [18] J. Kempe *et al.*, Phys. Rev. A **63**, 042307 (2001).
- [19] The correlations T_{ijkl} of a four-qubit pure state $|\psi\rangle$ are given by $T_{ijkl} = \langle \psi | (\sigma^i \otimes \sigma^j \otimes \sigma^k \otimes \sigma^l) | \psi \rangle$, where $i, j, k, l \in \{0, x, y, z\}$, $\sigma^0 = \mathbb{1}$, and $\sigma^{x,y,z}$ are the usual Pauli operators.
- [20] When writing ρ_{exp} in the basis of the Pauli operators $\rho_{\text{exp}} = \sum_{ijkl} S_{ijkl} (\sigma^i \otimes \sigma^j \otimes \sigma^k \otimes \sigma^l) / 16$, where S_{ijkl} are the correlations of the experimentally observed state, we find $F_{\Psi(\gamma)} = \sum_{ijkl} S_{ijkl} T_{ijkl} / 16$. Only terms with nonzero T_{ijkl} contribute to $F_{\Psi(\gamma)}$.
- [21] W. P. Grice and I. A. Walmsley, Phys. Rev. A **56**, 1627 (1997); T. E. Keller and M. H. Rubin, *ibid.* **56**, 1534 (1997).
- [22] We find a minimal two-photon visibility at the PBS for $\gamma \approx 1.2\pi/16$ of $(94.6 \pm 1.5)\%$.
- [23] M. Horodecki *et al.*, Phys. Lett. A **223**, 1 (1996); B. M. Terhal, *ibid.* **271**, 319 (2000); M. Lewenstein *et al.*, Phys. Rev. A **62**, 052310 (2000); D. Bruß *et al.*, J. Mod. Opt. **49**, 1399 (2002).
- [24] O. Gühne *et al.*, Phys. Rev. A **66**, 062305 (2002); M. Barbieri *et al.*, Phys. Rev. Lett. **91**, 227901 (2003); C. Schuck, Diploma thesis, LMU München, 2003.
- [25] For example, the third-order emission of the SPDC is overlapped on the PBS. Subsequently, the photons are distributed onto six spatial modes. Then the HWP(γ) in front of the PBS tunes the observable six photon states: $\beta(\gamma)|GHZ_6\rangle + \sqrt{1 - \beta(\gamma)^2}/\sqrt{2}(|\bar{W}_3\rangle \otimes |W_3\rangle - |W_3\rangle \otimes |\bar{W}_3\rangle)$, where $|GHZ_6\rangle = 1/\sqrt{2}(|HHHVVVV\rangle - |VVVHHH\rangle)$, $|W_3\rangle = 1/\sqrt{3}(|HHV\rangle + |HVH\rangle + |VHH\rangle)$, and $|\bar{W}_3\rangle = 1/\sqrt{3}(|VVH\rangle + |VHV\rangle + |HVV\rangle)$.

P3.2

1704

IEEE JOURNAL OF SELECTED TOPICS IN QUANTUM ELECTRONICS, VOL. 15, NO. 6, NOVEMBER/DECEMBER 2009

Multiphoton Interference as a Tool to Observe Families of Multiphoton Entangled States

Witłef Wieczorek, Nikolai Kiesel, Christian Schmid, Wiesław Laskowski, Marek Żukowski, and Harald Weinfurter

(Invited Paper)

Abstract—Spontaneous parametric downconversion in combination with linear optics was successfully used to observe a variety of multiphoton entangled states. Yet, experiments performed so far lacked flexibility, as each of the various setups was useful for only a particular multiphoton entangled state. In this paper, we describe how, by using multiphoton interference, one can observe entire families of multiphoton entangled states in the very same linear optical setup. Our method thus goes beyond the commonly used two-photon interference and turns out to be a very useful tool for state observation. We will discuss the interference of four and six photons at different types of beam splitters and show which families of entangled states are observable. The benefits of this approach are demonstrated in a four-photon interference experiment by observing a variety of highly entangled multiphoton states.

Index Terms—Frequency conversion, interference, nonlinear optics, parametric devices, ultrafast optics.

I. INTRODUCTION

MULTIPARTITE entanglement is an important nonclassical resource for applications of quantum information. In principle, many physical systems are well suited for experimental realizations of multipartite entangled quantum states. So far, photonic qubits allowed observations of the biggest

variety of multipartite entangled states. In order to describe and categorize all these quantum states, among others, the criterion of equivalence under stochastic local operations and classical communication (SLOCC) was introduced [1]–[4]. It has already been shown [2] that for four qubits infinitely many SLOCC-inequivalent four-qubit entangled pure states exist. This classification is quite useful for multiparty quantum communication applications, where each SLOCC-inequivalent state has the potential to lead to a particular nonclassical application. Hence, a flexible method to observe—and finally to apply—many SLOCC-inequivalent states is surely desirable.

To observe multiphoton entangled states, usually, a combination of spontaneous parametric downconversion (SPDC) with linear optical elements is used. To this end, indistinguishability of photons originating from different SPDC sources or emissions is required in order to achieve multiphoton interference [5], [6] enabling the observation of entangled states. However, most earlier experiments relied on enforced indistinguishability of just two photons [7]–[9]. In this paper, we will demonstrate how four- and six-photon interference is of additional benefit as it allows one to observe whole families of entangled quantum states in a single setup. This breaks with the common approach to design a particular linear optical experiment for each quantum state. Besides possible applications in quantum communication, multiphoton interference was also proposed to be a useful tool to entangle distant atoms [10]–[16], or to improve precision measurements [17]–[21]. Previously, it was studied with respect to photon bunching and multipath interference at a beam splitter (BS) [22]–[25] as a generalization of the Hong–Ou–Mandel effect [26].

We will discuss, in Section II, the interference of four and six photons on different types of BSs and analyze the potential of these cases with respect to the observation of SLOCC-inequivalent entangled states. In Section III, we describe a particular experimental implementation using four-photon interference at a polarizing BS, which was recently performed by us [27], with special emphasis placed on the analysis of the entanglement of the various states. Finally, in Section IV, we summarize our main findings.

II. MULTIPHOTON ENTANGLEMENT VIA MULTIPHOTON INTERFERENCE

In the following, we will discuss how multiphoton interference can be used to observe various multipartite entangled states. We will study four- and six-photon interference at different kinds

Manuscript received February 8, 2009; revised May 29, 2009. First published September 29, 2009; current version published December 3, 2009. This work was supported in part by the DFG–Cluster of Excellence Munich Centre for Advanced Photonics (www.munich-photonics.de), in part by the European Union (EU) Project Qubit Applications (QAP), and in part by DAAD/MNiSW exchange program. The work of W. Wieczorek was supported by the Ph.D. programme Quantum Computing, Control and Communication (QCCC) of the Elite Network of Bavaria (ENB).

W. Wieczorek and H. Weinfurter are with the Max-Planck-Institute of Quantum Optics (MPQ), D-85748 Garching, Germany, and also with the Department for Physics, Ludwig-Maximilians-Universität (LMU) München, D-80799 Munich, Germany (e-mail: witlef.wieczorek@mpq.mpg.de; harald.weinfurter@physik.uni-muenchen.de).

N. Kiesel was with the Max-Planck-Institute of Quantum Optics (MPQ), D-85748 Garching, Germany, and also with Ludwig-Maximilians-Universität (LMU) München, D-80799 Munich, Germany. He is now with the Institute for Quantum Optics and Quantum Information (IQOQI), Austrian Academy of Sciences, A-1090 Vienna, Austria (e-mail: nikolai.kiesel@univie.ac.at).

C. Schmid was with the Max-Planck-Institute of Quantum Optics (MPQ), D-85748 Garching, Germany, and also with Ludwig-Maximilians-Universität (LMU) München, D-80799 Munich, Germany. He is now with the European Organisation for Astronomical Research in the Southern Hemisphere (ESO), D-85748 Garching, Germany (e-mail: cschmid@eso.org).

W. Laskowski and M. Żukowski are with the Institute of Theoretical Physics and Astrophysics, University of Gdańsk, PL-80-952 Gdańsk, Poland (e-mail: wieslaw.laskowski@univ.gda.pl; marek.zukowski@univie.ac.at).

Color versions of one or more of the figures in this paper are available online at <http://ieeexplore.ieee.org>.

Digital Object Identifier 10.1109/JSTQE.2009.2025697

1077-260X/\$26.00 © 2009 IEEE

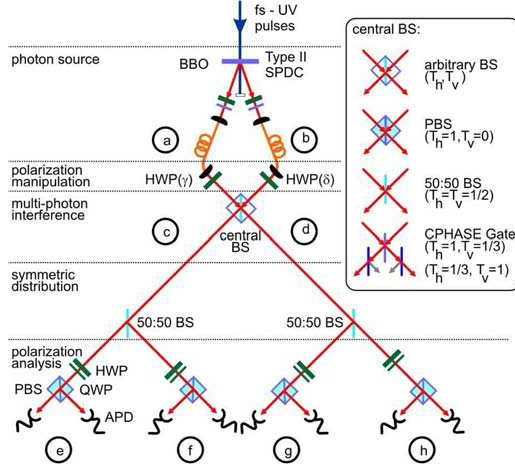


Fig. 1. Schematic experimental setup for using four-photon interference at a central BS to observe families of entangled four-photon states. BSs having different transmittances for horizontal (T_h) and vertical (T_v) polarization are used as the central BS (shown on the right). The polarization analysis of the photon states in modes e, f, g, h is performed with an HWP and a QWP in front of a PBS.

of BSs. This approach will be shown to be superior to conventional state observation schemes relying also on linear optics, most of which served to observe a single state only. With our method, it is possible to observe a multitude of different and relevant multipartite entangled states in a single linear optical setup.

The general experimental scheme to achieve this is as follows (Fig. 1). We start with a photon source that delivers $2n$ photons to two spatially distinct modes (labeled a and b), such that n photons occupy each spatial mode. Such a source is given by a type-II noncollinear SPDC that generates in its n th order emission $2n$ photons. Next, we will change the polarization state of the photons via a half-wave plate (HWP) in mode a (we will, additionally, also consider an HWP in mode b). A similar approach was pursued in a recent experiment, where an HWP at the beginning of the optical setup was used to continuously vary between three photon states out of the same entanglement class [28]. Subsequently, the photons interfere at a BS with a certain transmittance T_h (T_v) for horizontally (vertically) polarized photons. Its output modes (labeled c and d) are split by polarization independent BSs into $2n$ modes that have an equal output probability. Under the condition of having a single photon in each of the $2n$ modes, we observe the desired states. In the following, we will discuss the cases $n = 2$ and $n = 3$, and thus, the interference of four and six photons, respectively.

A. Four-Photon Interference

Let us start with the interference of four photons at a BS. To this end, we consider four photons of the second-order SPDC emission, which are in the state [29] (to assure indistinguishability

of photons coming from different SPDC pairs, one must use filters of spectral width narrower than that of the pulsed pump [5], [6])

$$\begin{aligned} & \propto (a_h^\dagger b_v^\dagger + a_v^\dagger b_h^\dagger)^2 |\text{vac}\rangle \\ & = [(a_h^\dagger b_v^\dagger)^2 + (a_v^\dagger b_h^\dagger)^2 + 2a_h^\dagger a_v^\dagger b_h^\dagger b_v^\dagger] |\text{vac}\rangle \quad (1) \end{aligned}$$

where m_i^\dagger denotes the creation operator of a photon in mode m having polarization i and $|\text{vac}\rangle$ is the vacuum state. Here and in the following, we neglect all higher order emissions, and thus, implicitly assume low conversion efficiency, e.g., due to a weak pump beam. The influence of high conversion efficiency on the state quality, in particular, for low detection efficiency, is known [30], [31] and strongly depends on the particular parameters, which will be subjected to further investigation. The HWP in mode a transforms the polarization state of the photons according to $a_h^\dagger \rightarrow \cos(2\gamma)a_h^\dagger + \sin(2\gamma)a_v^\dagger$ and $a_v^\dagger \rightarrow \sin(2\gamma)a_h^\dagger - \cos(2\gamma)a_v^\dagger$, where γ is the orientation of the optical axis with respect to the polarization of the impinging photons. Subsequently, the photons interfere on a BS with the transmittances T_h and T_v , where we assume a lossless BS, i.e., $T_h + R_h = 1$ and $T_v + R_v = 1$ hold, with R_i being reflectance of the BS. The BS transforms the photon state from input mode a to the superposition $a_i^\dagger \rightarrow \sqrt{T_i}c_i^\dagger + i\sqrt{1-T_i}d_i^\dagger$ and from input mode b to $b_i^\dagger \rightarrow \sqrt{T_i}d_i^\dagger + i\sqrt{1-T_i}c_i^\dagger$, where c and d are the output modes of the BS and $i = \sqrt{-1}$.

1) *Arbitrary BS*: We first use a central BS with T_h and T_v arbitrary, before we focus on three particular parameter sets. Splitting its two output modes into four final modes by two polarization independent BSs ($T_h = T_v = 1/2$) yields the states in modes e, f, g, h (up to normalization, for the notation of states, see Table I)

$$\begin{aligned} & a_{bs} |GHZ_4\rangle + b_{bs} |\psi^+\rangle \otimes |\psi^+\rangle \\ & + c_{bs} |HHHH\rangle + d_{bs} |VVVV\rangle \\ & - e_{bs} (|VHHH\rangle + |HVHH\rangle) \\ & - |HHVH\rangle - |HHHV\rangle \\ & - f_{bs} (|VVVH\rangle + |VVHV\rangle) \\ & - |VHVV\rangle - |HVVV\rangle \quad (2) \end{aligned}$$

where each amplitude depends on the three parameters γ , T_h , and T_v in the following way:

$$\begin{aligned} a_{bs} &= \frac{1}{\sqrt{2}}(T_v - R_h - 2T_h T_v \\ & + (T_v - R_h - 2T_h T_v - 4\sqrt{R_h T_h R_v T_v}) \cos 4\gamma) \\ b_{bs} &= 2 \left(\sqrt{R_h T_h R_v T_v} + \left(\frac{1}{2} - T_v + \sqrt{R_h T_h R_v T_v} \right. \right. \\ & \left. \left. + T_h(-1 + 2T_v) \right) \cos 4\gamma \right) \\ c_{bs} &= (6R_h T_h - 1)(\sin 2\gamma)^2 \\ d_{bs} &= (6R_v T_v - 1)(\sin 2\gamma)^2 \end{aligned}$$

TABLE I
VARIOUS MULTIPARTITE ENTANGLED STATES THAT ARE CONTAINED IN DIFFERENT FAMILIES OF STATES, WHERE EACH FAMILY CAN BE OBSERVED WITH A SINGLE SETUP

$ W_3\rangle$	$= \frac{1}{\sqrt{3}}(HHV\rangle + HVH\rangle + VHH\rangle)$
$ \bar{W}_3\rangle$	$= \frac{1}{\sqrt{3}}(VVH\rangle + VHV\rangle + HVV\rangle)$
$ GHZ_4\rangle$	$= \frac{1}{\sqrt{2}}(HHHH\rangle + VVVV\rangle)$
$ GHZ'_4\rangle$	$= \frac{1}{\sqrt{2}}(HHVV\rangle + VVHH\rangle)$
$ W_4\rangle$	$= \frac{1}{2}(HHHV\rangle + HHVH\rangle + HVHH\rangle + VHHH\rangle)$
$ \bar{W}_4\rangle$	$= \frac{1}{2}(VVVH\rangle + VVHV\rangle + VHVV\rangle + HVVV\rangle)$
$ D_4^{(2)}\rangle$	$= \frac{1}{\sqrt{6}}(HHVV\rangle + HVHV\rangle + VHHV\rangle + HVVH\rangle + VHVH\rangle + VHHH\rangle)$
$ D_4^{(2)'}\rangle$	$= \frac{1}{\sqrt{6}}(HHHH\rangle + HVHV\rangle + VHHV\rangle + HVVH\rangle + VHVH\rangle + VVVV\rangle)$
$ \psi^+\rangle \otimes \psi^+\rangle$	$= \frac{1}{2}(HVHV\rangle + VHVH\rangle + HVVH\rangle + VHHV\rangle)$
$ \psi^-\rangle \otimes \psi^-\rangle$	$= \frac{1}{2}(HVHV\rangle + VHVH\rangle - HVVH\rangle - VHHV\rangle)$
$ \phi^+\rangle \otimes \phi^+\rangle$	$= \frac{1}{2}(HHHH\rangle + HHVV\rangle + VVHH\rangle + VVVV\rangle)$
$ \phi^-\rangle \otimes \phi^-\rangle$	$= \frac{1}{2}(HHHH\rangle - HHVV\rangle - VVHH\rangle + VVVV\rangle)$
$ \Psi_4^-\rangle$	$= \sqrt{2/3} GHZ'_4\rangle - \sqrt{1/3} \psi^+\rangle \otimes \psi^+\rangle$
$ \Psi_4^-\rangle$	$= \sqrt{2/3} GHZ_4\rangle - \sqrt{1/3} \psi^+\rangle \otimes \psi^+\rangle$
$ \Psi_4^+\rangle$	$= \sqrt{2/3} GHZ_4\rangle + \sqrt{1/3} \psi^+\rangle \otimes \psi^+\rangle$
$ GHZ_6\rangle$	$= \frac{1}{\sqrt{2}}(HHHHHH\rangle + VVVVVV\rangle)$
$ GHZ_6^-\rangle$	$= \frac{1}{\sqrt{2}}(HHHHHH\rangle - VVVVVV\rangle)$
$ \Psi_6^+\rangle$	$= \frac{1}{\sqrt{2}} GHZ_6^-\rangle + \frac{1}{2}(\bar{W}_3\rangle \otimes \bar{W}_3\rangle - W_3\rangle \otimes W_3\rangle)$

We use the notation for polarization encoded qubits in different spatial modes, where $H(V)$ stands for horizontal (vertical) polarization and encodes a logical 0(1). The notation of, e.g., $|HHHH\rangle$ is an abbreviated form of $|HHHH\rangle = |H\rangle_s \otimes |H\rangle_r \otimes |H\rangle_s \otimes |H\rangle_r$, where the subscripts denote the spatial mode of each photon.

$$\begin{aligned}
 e_{bs} &= \frac{1}{2}(\sqrt{R_h R_v} - 3T_h \sqrt{R_h R_v} \\
 &\quad + 2\sqrt{T_h T_v} - 3T_h^{3/2} \sqrt{T_v}) \sin 4\gamma \\
 f_{bs} &= \frac{1}{2}(\sqrt{R_h R_v}(1 - 3T_v) + \sqrt{T_h T_v}(2 - 3T_v)) \sin 4\gamma.
 \end{aligned} \tag{3}$$

These states appear in several entanglement families of the four-qubit SLOCC classification introduced recently [2], [4]. To obtain a clearer insight into these states, we will discuss the following three particular BSs in more detail.

2) *Polarizing Beam Splitter*: By using a polarizing beam splitter (PBS) with $T_h = 1$ and $T_v = 0$, the family of states

$$|\Psi_4(\gamma)\rangle = a_4(\gamma)|GHZ_4\rangle + b_4(\gamma)|\psi^+\rangle \otimes |\psi^+\rangle \tag{4}$$

with

$$\begin{aligned}
 a_4(\gamma) &= \frac{\sqrt{2}(1 - \cos 4\gamma)}{\sqrt{5 - 4 \cos(4\gamma) + 3 \cos 8\gamma}} \\
 b_4(\gamma) &= \frac{(2 \cos 4\gamma)}{\sqrt{5 - 4 \cos(4\gamma) + 3 \cos 8\gamma}}
 \end{aligned} \tag{5}$$

and $a_4(\gamma)^2 + b_4(\gamma)^2 = 1$ is obtained [27] [Fig. 2(a)]. The states $|\Psi_4(\gamma)\rangle$ form a superposition of the well-known $|GHZ_4\rangle$ state, a highly entangled four-qubit state, and a product of two Bell states, a biseparable state. By using the SLOCC classification of [2], we can attribute the family $|\Psi_4(\gamma)\rangle$ to the generic entanglement class G_{abcd} of four-qubit entangled states. States of this class form a continuous set of SLOCC-inequivalent

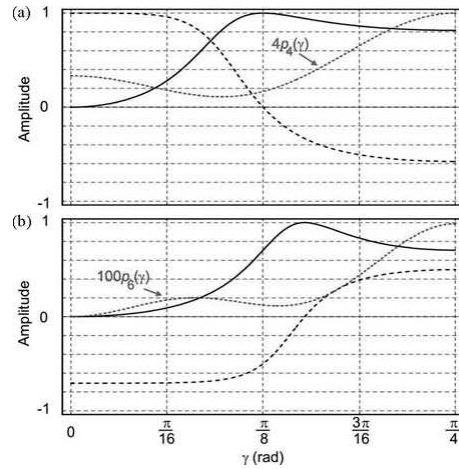


Fig. 2. Amplitudes. (a) $a_4(\gamma)$ (solid) and $b_4(\gamma)$ (dashed) for the family of states $|\Psi_4(\gamma)\rangle$. (b) $a_6(\gamma)$ (solid) and $b_6(\gamma)$ (dashed) for $|\Psi_6(\gamma)\rangle$. Further, (a) $p_4(\gamma)$ and (b) $p_6(\gamma)$ denote the probability of each state to be observed in the corresponding linear optical setup (dotted).

states, i.e., for each particular value of $\gamma \in [0, \pi/8]$, we obtain an SLOCC-inequivalent state [27] with a probability $p_4(\gamma) = (5 - 4 \cos(4\gamma) + 3 \cos(8\gamma))/48$ [Fig. 2(a)]. Recently, we accomplished the experimental realization of $|\Psi_4(\gamma)\rangle$ [27], which will be discussed in Section III in more detail.

At this point, let us highlight the well-known states of the family

$$\begin{aligned}\gamma = 0 &\rightarrow |\psi^+\rangle \otimes |\psi^+\rangle \\ \gamma = \frac{\pi}{12} &\rightarrow |D_4^{(2)'}\rangle \\ \gamma = \frac{1}{2} \arctan \frac{1}{\sqrt{2}} &\rightarrow |\Psi_4^+\rangle \\ \gamma = \frac{\pi}{8} &\rightarrow |GHZ_4\rangle \\ \gamma = \frac{\pi}{4} &\rightarrow |\Psi_4^{-'}\rangle.\end{aligned}\quad (6)$$

The states $|\psi^+\rangle \otimes |\psi^+\rangle$ and $|\Psi_4^+\rangle, |\Psi_4^{-'}\rangle$ are local unitary (LU) equivalent to $|\psi^-\rangle \otimes |\psi^-\rangle$ and $|\Psi_4^-\rangle$, respectively, which are the two basis states for decoherence-free communication of a qubit [32]. The state $|D_4^{(2)'}\rangle$ is LU equivalent to $|D_4^{(2)}\rangle$, which belongs to the family of Dicke states [33]. A remarkable property of $|D_4^{(2)}\rangle$ is that it allows to obtain by a single projective measurement states out of the two inequivalent three-qubit SLOCC entanglement classes [1], [34]. The state $|GHZ_4\rangle$ is a graph state [35] and can be used for numerous applications, e.g., for multiparty quantum secret sharing [36], dense coding [37], and simulating anyonic statistics [38]. While all of these states have been previously realized in dedicated linear optical setups [7], [34], [39]–[41], now, it is possible to observe all of them in a single setup only.

Finally, the usage of an additional HWP(δ) in mode b in front of the PBS adds another tuning parameter δ . However, it turns out that the angle dependence changes simply into $\gamma \rightarrow \gamma + \delta$, resulting in the same states as before.

3) *50:50 BS*: Another commonly used BS is given by $T_h = T_v = 1/2$. There, we obtain the states (up to normalization)

$$\begin{aligned}4\sqrt{2}(\cos \gamma)^2(\sin \gamma)^2 |GHZ_4\rangle \\ - (1 + 3 \cos 4\gamma)/\sqrt{2} |GHZ_4'\rangle \\ + 2(\cos 2\gamma)^2 |\psi^+\rangle \otimes |\psi^+\rangle.\end{aligned}\quad (7)$$

Let us mention particularly interesting states of this family

$$\begin{aligned}\gamma = 0 &\rightarrow |\Psi_4^-\rangle \\ \gamma = \frac{\pi}{8} &\rightarrow \frac{1}{\sqrt{2}}(|\phi^-\rangle \otimes |\phi^-\rangle + |\psi^+\rangle \otimes |\psi^+\rangle) \\ \gamma = \frac{1}{4} \arccos\left(-\frac{1}{3}\right) &\rightarrow |\Psi_4^+(\gamma)\rangle \\ \gamma = \frac{\pi}{6} &\rightarrow \sqrt{\frac{3}{4}} |GHZ_4\rangle + \sqrt{\frac{1}{4}} |D_4^{(2)}\rangle \\ \gamma = \frac{\pi}{4} &\rightarrow |\phi^+\rangle \otimes |\phi^+\rangle.\end{aligned}\quad (8)$$

The states given for $\gamma = 0$, $\gamma = (1/4) \arccos(-1/3)$, and $\gamma = \pi/4$ are LU equivalent to states of the family $|\Psi_4(\gamma)\rangle$. However, for other values of γ , we find different states, e.g., the state $1/\sqrt{2}(|\phi^-\rangle \otimes |\phi^-\rangle + |\psi^+\rangle \otimes |\psi^+\rangle)$ ($\gamma = \pi/8$) is a superposition of two biseparable states and $\sqrt{3/4} |GHZ_4\rangle +$

$\sqrt{1/4} |D_4^{(2)}\rangle$ ($\gamma = \pi/6$) is a superposition of all distinct permutations of an even number of vertically polarized photons.

When we additionally use an HWP(δ) in mode b in front of the 50:50 BS, the states

$$\begin{aligned}\propto \sqrt{2}(\sin 2(\gamma + \delta))^2 (|GHZ_4\rangle - |GHZ_4'\rangle) \\ + 2(\cos 2(\gamma + \delta))^2 |\psi^+\rangle \otimes |\psi^+\rangle \\ + (\sin 4(\gamma + \delta))(|\bar{W}_4\rangle - |W_4\rangle)\end{aligned}\quad (9)$$

are obtained. New states can be observed compared to using only one HWP. For example, terms with an odd number of vertically polarized photons ($|\bar{W}_4\rangle - |W_4\rangle$) also appear now.

4) *CPHASE BS*: Another well-known BS is given by $T_h = 1$ and $T_v = 1/3$. It was used in combination with two attenuation BSs of reversed splitting ratio ($T_h = 1/3$ and $T_v = 1$) to construct an all-optical controlled phase gate (CPHASE) [42]–[44]. When the CPHASE is used as the central overlap BS, one obtains the states

$$\begin{aligned}a_{cp} |GHZ_4'\rangle + b_{cp} |\psi^+\rangle \otimes |\psi^+\rangle \\ + c_{cp} (-|HHHH\rangle + 3|VVVV\rangle) \\ + d_{cp} (|VHVV\rangle + |HVVV\rangle \\ - |VVVH\rangle - |VHVH\rangle) \\ + \frac{d_{cp}}{3} (|VHHH\rangle + |HVHH\rangle \\ - |HHVH\rangle - |HHHV\rangle)\end{aligned}\quad (10)$$

with $a_{cp} = -\sqrt{2}(\cos 2\gamma)^2$, $b_{cp} = -(\cos 4\gamma)$, $c_{cp} = (\sin 2\gamma)^2$, and $d_{cp} = 3/2 \sin 4\gamma$. These states have a similar complexity to the states observed with an arbitrary BS.

An additional HWP(δ) in mode b leads to the states

$$\begin{aligned}a_{cp2} |GHZ_4'\rangle + b_{cp2} |\psi^+\rangle \otimes |\psi^+\rangle \\ + c_{cp2} (-|HHHH\rangle + 3|VVVV\rangle) \\ + d_{cp2} (|W_4\rangle + 3|\bar{W}_4\rangle)\end{aligned}\quad (11)$$

with $a_{cp2} = -\sqrt{2}(\cos 2(\gamma + \delta))^2$, $b_{cp2} = \cos 4(\gamma + \delta)$, $c_{cp2} = (\sin 2(\gamma + \delta))^2$, and $d_{cp2} = \sin 4(\gamma + \delta)$.

We can also directly use the four output modes of the attenuation BSs instead of distributing two of the four output modes via two 50:50 BSs. Then, we obtain

$$\begin{aligned}\cos 4\gamma |VHVV\rangle + 2(\sin 2\gamma)^2 |HHHH\rangle \\ + \sin 4\gamma (-|VHHH\rangle + |HHVH\rangle).\end{aligned}\quad (12)$$

Note that qubits in modes f and h can be factored from the aforementioned state

$$\begin{aligned}|HH\rangle \otimes (\cos 4\gamma |VV\rangle + 2(\sin 2\gamma)^2 |HH\rangle \\ + \sqrt{2} \sin 4\gamma |\psi^-\rangle)\end{aligned}\quad (13)$$

(we changed the qubit order into f, h, e, g). This comes from the fact that the attenuation BSs reflect only H polarized photons.

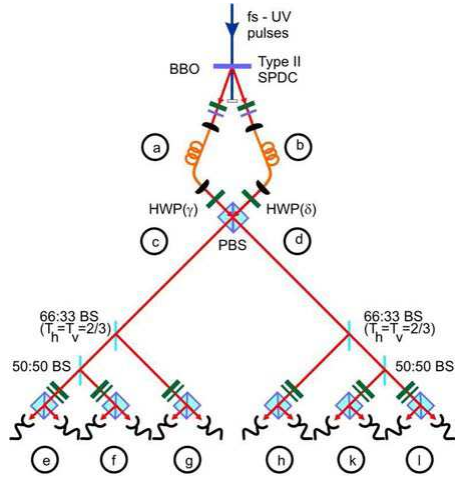


Fig. 3. Schematic experimental setup for using six-photon interference at a PBS to observe a family of entangled six-photon states in modes e, f, g, h, k, l .

B. Six-Photon Interference

Extending the level of interference further, let us consider six-photon interference. In Section II-A, the most successful approach to observe a family of states was to use interference at a *polarizing* BS [27]. Therefore, we will examine in the following the interference of the third-order SPDC with the photon state $(a_h^\dagger b_v^\dagger + a_v^\dagger b_h^\dagger)^3 |\text{vac}\rangle$ at a PBS too. Again, before the photons interfere, their polarization state is changed with an HWP(γ) in mode a (additionally, we also consider an HWP(δ) in mode b). The output modes of the PBS are split into six spatial modes by four polarization independent BSs (see Fig. 3).

Using the experimental layout described before, one obtains the family of states

$$|\Psi_6(\gamma)\rangle = a_6(\gamma) |GHZ_6^-\rangle + b_6(\gamma) (|\bar{W}_3\rangle \otimes |\bar{W}_3\rangle - |W_3\rangle \otimes |W_3\rangle) \quad (14)$$

where

$$a_6(\gamma) = \frac{2(\sin 2\gamma)^2}{\sqrt{7 + 4 \cos 4\gamma + 5 \cos 8\gamma}}$$

$$b_6(\gamma) = -\frac{1 + 3 \cos 4\gamma}{\sqrt{2}\sqrt{7 + 4 \cos 4\gamma + 5 \cos 8\gamma}} \quad (15)$$

and $a(\gamma)^2 + 2b(\gamma)^2 = 1$ [see Fig. 2(b)]. We observe these states with a probability of $p_6(\gamma) = (2/81)(\cos \gamma \sin \gamma)^2 (7 + 4 \cos 4\gamma + 5 \cos 8\gamma)$ [Fig. 2(b)]. Let us highlight two states that are well known to be useful for quantum information

$$\gamma = \arccos \sqrt{\frac{(3 + \sqrt{3})}{6}} \rightarrow |GHZ_6^-\rangle$$

$$\gamma = \frac{\pi}{4} \rightarrow |\Psi_6^+\rangle. \quad (16)$$

The state $|GHZ_6^-\rangle$ is a graph state and could be already observed experimentally in a dedicated linear optical setup [9]. With the described method, it is not only possible to observe this state but also the entire family $|\Psi_6(\gamma)\rangle$. For example, the state $|\Psi_6^+\rangle$ can be used for telecloning. It is LU equivalent (the necessary local transformation is $\sigma_z \otimes \sigma_z \otimes \sigma_z \otimes \mathbb{1} \otimes \mathbb{1} \otimes \mathbb{1}$) to the telecloning state described in [45] for $M = 3$ recipients, where $2M = 6$ qubits are necessary. An LU-equivalent state of $|\Psi_6^+\rangle$ was recently observed using a different configuration, without the central BS [46].

Finally, we note that the usage of an additional HWP(δ) in mode b in front of the PBS leads to the family of states

$$|\Psi'_6(\gamma)\rangle = a_6(\gamma) |GHZ_6\rangle + b_6(\gamma) (|\bar{W}_3\rangle \otimes |\bar{W}_3\rangle + |W_3\rangle \otimes |W_3\rangle) \quad (17)$$

which is LU equivalent to the family $|\Psi_6(\gamma)\rangle$.

III. EXPERIMENTAL REALIZATION OF A FAMILY OF FOUR-PHOTON ENTANGLED STATES

Let us now move to the experimental realization of one of the presented schemes. We implemented the interference of four photons at a PBS using as a photon source the second-order emission of a noncollinear type-II SPDC process. The general layout of the experiment was described in Section II-A and Fig. 1, which leads to the observation of the family of states [see Section II-A2 and Fig. 2(a)]

$$|\Psi_4(\gamma)\rangle = a_4(\gamma) |GHZ_4\rangle + b_4(\gamma) |\psi^+\rangle \otimes |\psi^+\rangle. \quad (18)$$

A. Experimental Setup

A frequency-doubled Ti:sapphire laser emits femtosecond UV pulses with a repetition rate of 81 MHz and a power of 600 mW at 390 nm. The UV pulses pump a 2-mm-thick β -barium borate (BBO) crystal, which is cut for type-II noncollinear SPDC (see Fig. 1). Its second-order emission yields the desired four photons necessary for the interference at the PBS. Walk-off effects in the BBO crystal due to birefringence are compensated by an HWP flipping the polarization state of each photon and a 1-mm-thick BBO crystal [47]. The spatial modes a and b are defined by coupling the SPDC emission into single-mode fibers. In mode a , an HWP(γ) is placed before the photons in modes a and b interfere at the PBS. Interference filters centered around the degenerate wavelength of 780 nm with a full-width at half-maximum of 3 nm are placed in output modes c and d (not shown in Fig. 1) to define the spectral modes of the SPDC photons. Further, in mode c , an additional HWP is placed (not shown in Fig. 1), which flips the polarization of the photons. Subsequently, each mode is split by a polarization independent BS, whose birefringence is compensated by a pair of birefringent, perpendicularly oriented yttrium vanadate crystals in each output mode (not shown in Fig. 1). Finally, the polarization state of each photon is analyzed with an HWP and quarter-wave plate (QWP) in front of a PBS. The outputs of the PBS are coupled into multimode fibers, which guide the photons to silicon avalanche photodiodes (APDs). The detection signals are fed into a coincidence unit capable

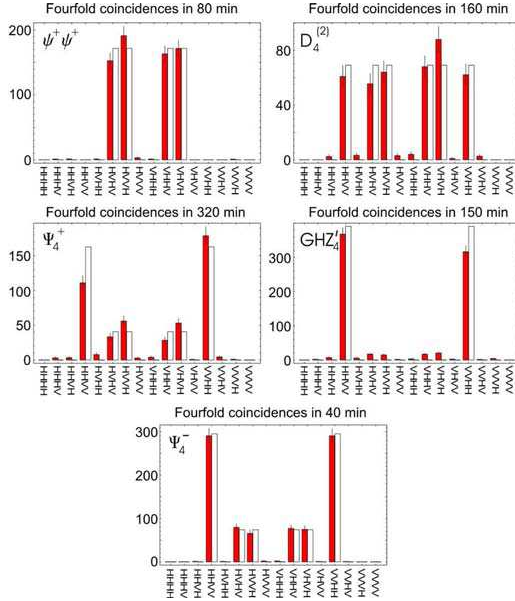


Fig. 4. Recorded counts in the computational basis for the states $|\psi^+\rangle \otimes |\psi^+\rangle$, $|D_4^{(2)}\rangle$, $|\Psi_4^+\rangle$, $|GHZ_4'\rangle$, and $|\Psi_4^-\rangle$. Clearly, the different contributions of the $|GHZ_4'\rangle$ and $|\psi^+\rangle \otimes |\psi^+\rangle$ terms are observable. Open bars without error show expected counts.

of registering all $2^8 = 256$ possible detection events between all eight detectors. The errors on following data are deduced from Poissonian counting statistics and errors on independently determined relative detection efficiencies.

Under the condition of detecting a single photon in each mode e, f, g, h , the family of states

$$|\Psi_4(\gamma')\rangle = a_4(\gamma) |GHZ_4'\rangle + b_4(\gamma) |\psi^+\rangle \otimes |\psi^+\rangle \quad (19)$$

is observed. Note that the family $|\Psi_4(\gamma')\rangle$ differs (by an LU operation) from $|\Psi_4(\gamma)\rangle$, i.e., by a polarization flip in modes e, f , which is performed by the additional HWP in mode c .

To show the power of the experimental setup, we choose five known states of the family $|\Psi_4(\gamma')\rangle$, namely $|\psi^+\rangle \otimes |\psi^+\rangle$, $|D_4^{(2)}\rangle$, $|\Psi_4^+\rangle$, $|GHZ_4'\rangle$, and $|\Psi_4^-\rangle$ (with $\gamma = 0$, $\gamma = \pi/12$, $\gamma = (1/2) \arctan(1/\sqrt{2})$, $\gamma = \pi/8$, and $\gamma = \pi/4$, respectively), and record for each state the counts in the computational basis. This demonstrates that we are able to observe different states in a single experimental setup simply by changing the angle setting of HWP(γ). Fig. 4 shows the 16 possible measurement outcomes for these five states. Open bars show the theoretically expected coincidences, with the scaling chosen such to give the same sum of counts. Clearly, a good agreement between experiment and theory is found. Deviations originate from higher order emissions of the SPDC that give undesired contributions. Additionally, an imperfect interference at the PBS

further adds noise. Nevertheless, a clear transition between the states $|\psi^+\rangle \otimes |\psi^+\rangle$ and $|GHZ_4'\rangle$ can be observed.

B. Detecting the Entanglement

Let us now discuss the detection of different degrees of entanglement for the observed states. First, we want to exclude that any of the states is separable. Further, we want to show that the expected four-partite entanglement is also found in the observed states.

A simple criterion to exclude separability was recently introduced in [48]. It is based on the correlations of a state. In our case, we have to consider the correlation tensor \hat{T} of a four-qubit state ρ with

$$\rho = \frac{1}{16} \sum_{\mu_1, \dots, \mu_4=0}^3 T_{\mu_1, \dots, \mu_4} (\sigma_{\mu_1} \otimes \sigma_{\mu_2} \otimes \sigma_{\mu_3} \otimes \sigma_{\mu_4}) \quad (20)$$

where $\sigma_{\mu_n} \in \{\mathbb{1}, \sigma_x, \sigma_y, \sigma_z\}$ is the σ_{μ_n} th Pauli matrix of the n th qubit (with $\sigma_0 = \mathbb{1}$) and $T_{\mu_1, \dots, \mu_4} \in [-1, 1]$ are the components of the correlation tensor \hat{T} . The values T_{μ_1, \dots, μ_4} are given by the expectation value $T_{\mu_1, \dots, \mu_4} = \text{Tr}[\rho(\sigma_{\mu_1} \otimes \sigma_{\mu_2} \otimes \sigma_{\mu_3} \otimes \sigma_{\mu_4})]$. For fully separable states, it holds that

$$T_4^{\max} \geq \sum_{j_1, \dots, j_4} T_{j_1, \dots, j_4}^2 \quad (21)$$

where T_4^{\max} is the maximal value of the four-qubit correlation function and is given by $T_4^{\max} = \max_{\vec{\sigma}_1 \otimes \vec{\sigma}_2 \otimes \vec{\sigma}_3 \otimes \vec{\sigma}_4} (\hat{T}, \vec{\sigma}_1 \otimes \vec{\sigma}_2 \otimes \vec{\sigma}_3 \otimes \vec{\sigma}_4)$, with $\vec{\sigma}_n = (T_x^{(n)}, T_y^{(n)}, T_z^{(n)})$ being a 3-D unit vector describing a pure state of the n th qubit [48].

The detection of entanglement can be very simple. As soon as the sum of squared correlations

$$\sum_{j_1, \dots, j_4} T_{j_1, \dots, j_4}^2 \quad (22)$$

exceeds unity, our experimental states are entangled [48]. Fig. 5 shows the correlations $T_{1,1,1,1} \equiv T_{x^{\otimes 4}}$, $T_{2,2,2,2} \equiv T_{y^{\otimes 4}}$, and $T_{3,3,3,3} \equiv T_{z^{\otimes 4}}$. When we sum the squares of, e.g., $T_{x^{\otimes 4}}$ and $T_{z^{\otimes 4}}$, we find that for all states, $(T_{x^{\otimes 4}})^2 + (T_{z^{\otimes 4}})^2 > 1$, and thus, all states are entangled. The same is found for $(T_{x^{\otimes 4}})^2 + (T_{y^{\otimes 4}})^2$. Hence, we conclude that the experimental states contain at least some entanglement.

Now, let us demonstrate that the experimental states exhibit the expected genuine four-partite entanglement. Note that the state $|\psi^+\rangle \otimes |\psi^+\rangle$ is a separable state, i.e., a product of two entangled pairs, and thus, is the only state that is not genuine four-partite entangled. To show genuine n -partite entanglement, we use the method of entanglement witnesses [49]. Generally, an entanglement witness that detects a genuine four-partite entangled state $|\xi\rangle$ is given by the operator $\mathcal{W}_{\xi, \alpha} = \alpha \mathbb{1}^{\otimes 4} - |\xi\rangle\langle\xi|$. Thereby, the constant α is the maximal overlap of $|\xi\rangle$ with all biseparable states (B-S), i.e., $\alpha = \max_{|\phi\rangle \in \text{B-S}} |\langle\phi|\xi\rangle|^2$. This construction guarantees that $\text{Tr}[(\mathcal{W}_{\xi, \alpha})\rho_{\text{B-S}}]$ is positive for all biseparable states $\rho_{\text{B-S}}$, but negative for $|\xi\rangle$. The power of entanglement witnesses stems from the fact that their expectation value is also negative for states close to $|\xi\rangle$. Hence, a negative expectation value $\text{Tr}[(\mathcal{W}_{\xi, \alpha})\rho_{\text{exp}}] = \text{Tr}[(\alpha \mathbb{1}^{\otimes 4} - |\xi\rangle\langle\xi|)\rho_{\text{exp}}] =$

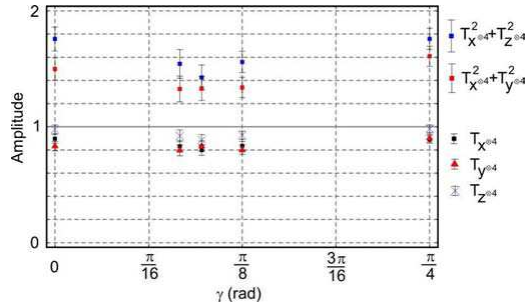


Fig. 5. Experimental correlations $T_{x^{\otimes 4}}$, $T_{y^{\otimes 4}}$, and $T_{z^{\otimes 4}}$ for the states $|\psi^+\rangle \otimes |\psi^+\rangle$, $|D_4^{(2)}\rangle$, $|\Psi_4^+\rangle$, $|GHZ_4'\rangle$, and $|\Psi_4^-\rangle$ (expected value is 1). From these, the values of $(T_{x^{\otimes 4}})^2 + (T_{y^{\otimes 4}})^2$ and $(T_{x^{\otimes 4}})^2 + (T_{z^{\otimes 4}})^2$ are deduced, which allow to demonstrate entanglement, if either of these values exceeds unity. All states fulfill this condition, and thus are entangled.

TABLE II
DETECTION OF GENUINE FOUR-PARTITE ENTANGLEMENT VIA ENTANGLEMENT WITNESSES

State	Entanglement Witness	Expectation value
$ D_4^{(2)}\rangle$	$\mathcal{W}_{D_4^{(2)}, 2/3}$	-0.142 ± 0.014
$ \Psi_4^+\rangle$	$\mathcal{W}_{\Psi_4^+, 3/4}$	-0.030 ± 0.013
$ GHZ_4'\rangle$	$\mathcal{W}_{GHZ_4', 1/2}$	-0.330 ± 0.008
$ \Psi_4^-\rangle$	$\mathcal{W}_{\Psi_4^-, 3/4}$	-0.182 ± 0.008

All experimental states yield negative expectation values, and thus, are genuine four-partite entangled.

$\alpha - \langle \xi | \rho_{\text{exp}} | \xi \rangle = \alpha - F_\xi(\rho_{\text{exp}}) < 0$ will signal genuine four-partite entanglement of the experimental state ρ_{exp} , where $F_\xi(\rho_{\text{exp}})$ is the fidelity of state ρ_{exp} with respect to $|\xi\rangle$. Hence, by measuring the fidelity, one can directly compute the expectation value of the corresponding entanglement witness.

Entanglement witnesses that detect the states $|D_4^{(2)}\rangle$, $|\Psi_4^+\rangle$, $|GHZ_4'\rangle$, and $|\Psi_4^-\rangle$ have already been constructed. The corresponding witnesses are given by $\mathcal{W}_{D_4^{(2)}, 2/3}$ in [34] and [50], $\mathcal{W}_{\Psi_4^+, 3/4}$ in [51], $\mathcal{W}_{GHZ_4', 1/2}$ in [52], and $\mathcal{W}_{\Psi_4^-, 3/4}$ in [51], respectively. To determine their expectation values, we measured the fidelity of the corresponding state (see [27] for details). The result is shown in Table II. We see that all experimental states are four-partite entangled as the expectation values of the corresponding witnesses are below zero.

Hence, we could indeed show that selected states of the family $|\Psi_4(\gamma)\rangle$ are not only entangled, but also genuine four-partite entangled. We again stress that all these states are SLOCC-inequivalent and that, so far, different experimental setups were necessary to observe each state.

IV. CONCLUSION

We have shown how multiphoton interference at different types of BSs can be used to observe different families of multi-

photon entangled states. The photons were generated by higher order emissions of an SPDC source. The combination of polarization rotations in the BS input modes with multiphoton interference at polarization-dependent BSs provides the necessary ingredients for the powerful scheme we presented. We implemented one particular case experimentally that allowed us to observe an entire family of four-photon entangled states. Our method opens the way for flexible linear optical experiments in the future and surely can also be applied in other areas of quantum information, e.g., for linear optical quantum computing.

ACKNOWLEDGMENT

The authors would like to thank O. Gühne and M. Bourenane for fruitful discussions. The work of W. Laskowski was supported by the Foundation for Polish Science.

REFERENCES

- [1] W. Dür, G. Vidal, and J. I. Cirac, "Three qubits can be entangled in two inequivalent ways," *Phys. Rev. A*, vol. 62, no. 6, pp. 062314-1–062314-12, 2000.
- [2] F. Verstraete, J. Dehaene, B. DeMoor, and H. Verschelde. (2002). Four qubits can be entangled in nine different ways. *Phys. Rev. A* [Online], 65(5), pp. 052112-1–052112-5. Available: <http://link.aps.org/abstract/PRA/v65/e052112>
- [3] L. Lamata, J. Leon, D. Salgado, and E. Solano. (2006). Inductive classification of multipartite entanglement under stochastic local operations and classical communication. *Phys. Rev. A* [Online], 74(5), pp. 052336-1–052336-10. Available: <http://link.aps.org/abstract/PRA/v74/e052336>
- [4] L. Lamata, J. Leon, D. Salgado, and E. Solano. (2007). Inductive entanglement classification of four qubits under stochastic local operations and classical communication. *Phys. Rev. A* [Online], 75(2), pp. 022318-1–022318-9. Available: <http://link.aps.org/abstract/PRA/v75/e022318>
- [5] M. Żukowski, A. Zeilinger, and H. Weinfurter. (1995). Entangling photons radiated by independent pulsed sources. *Ann. New York Acad. Sci.* [Online], 755, pp. 91–102. Available: <http://dx.doi.org/10.1111/j.1749-6632.1995.tb38959.x>
- [6] J. G. Rarity. (1995). Interference of single photons from separate sources. *Ann. New York Acad. Sci.* [Online], 755, pp. 624–631. Available: <http://dx.doi.org/10.1111/j.1749-6632.1995.tb39002.x>
- [7] J.-W. Pan, M. Daniell, S. Gasparoni, G. Weihs, and A. Zeilinger. (2001). Experimental demonstration of four-photon entanglement and high-fidelity teleportation. *Phys. Rev. Lett.* [Online], 86(20), pp. 4435–4438. Available: <http://link.aps.org/abstract/PRL/v86/p4435>
- [8] N. Kiesel, C. Schmid, U. Weber, G. Toth, O. Gühne, R. Ursin, and H. Weinfurter. (2005). Experimental analysis of a four-qubit photon cluster state. *Phys. Rev. Lett.* [Online], 95(21), pp. 210502-1–210502-4. Available: <http://link.aps.org/abstract/PRL/v95/e210502>
- [9] C.-Y. Lu, X.-Q. Zhou, O. Gühne, W.-B. Gao, J. Zhang, Z.-S. Yuan, A. Goebel, T. Yang, and J.-W. Pan. (2007, Feb.). Experimental entanglement of six photons in graph states. *Nature Phys.* [Online], 3, pp. 91–95. Available: <http://dx.doi.org/10.1038/nphys507>
- [10] C. Cabrillo, J. I. Cirac, P. García-Fernández, and P. Zoller, "Creation of entangled states of distant atoms by interference," *Phys. Rev. A*, vol. 59, no. 2, pp. 1025–1033, Feb. 1999.
- [11] S. Bose, P. L. Knight, M. B. Plenio, and V. Vedral, "Proposal for teleportation of an atomic state via cavity decay," *Phys. Rev. Lett.*, vol. 83, no. 24, pp. 5158–5161, Dec. 1999.
- [12] C. Skornia, J. vonZanthier, G. S. Agarwal, E. Werner, and H. Walther, "Nonclassical interference effects in the radiation from coherently driven uncorrelated atoms," *Phys. Rev. A*, vol. 64, no. 6, pp. 063801-1–063801-5, Nov. 2001.
- [13] L.-M. Duan, M. D. Lukin, J. I. Cirac, and P. Zoller. (2001, Nov.). Long-distance quantum communication with atomic ensembles and linear optics. *Nature* [Online], 414(6862), pp. 413–418. Available: <http://dx.doi.org/10.1038/35106500>
- [14] C. Simon and W. T. M. Irvine, "Robust long-distance entanglement and a loophole-free Bell test with ions and photons," *Phys. Rev. Lett.*, vol. 91, no. 11, pp. 110405-1–110405-4, Sep. 2003.

- [15] C. Thiel, J. von Zanthier, T. Bastin, E. Solano, and G. S. Agarwal. (2007). Generation of symmetric Dicke states of remote qubits with linear optics. *Phys. Rev. Lett.* [Online]. 99(19), pp. 193602-1-193602-4. Available: <http://link.aps.org/abstract/PRL/v99/e193602>
- [16] T. Bastin, C. Thiel, J. von Zanthier, L. Lamata, E. Solano, and G. S. Agarwal. (2009). Operational determination of multiqubit entanglement classes via tuning of local operations. *Phys. Rev. Lett.* [Online]. 102(5), pp. 053601-1-053601-4. Available: <http://link.aps.org/abstract/PRL/v102/e053601> 2009.
- [17] J. J. Bollinger, W. M. Itano, D. J. Wineland, and D. J. Heinzen. (1996). Optimal frequency measurements with maximally correlated states. *Phys. Rev. A* [Online]. 54(6), pp. R4649-R4652. Available: <http://link.aps.org/abstract/PRA/v54/pR4649>
- [18] M. J. Holland and K. Burnett, "Interferometric detection of optical phase shifts at the Heisenberg limit." *Phys. Rev. Lett.*, vol. 71, no. 9, pp. 1355-1358, Aug. 1993.
- [19] P. Walther, J.-W. Pan, M. Aspelmeyer, R. Ursin, S. Gasparoni, and A. Zeilinger. (2004, May). De Broglie wavelength of a non-local four-photon state. *Nature* [Online]. 429(6988), pp. 158-161. Available: <http://dx.doi.org/10.1038/nature02552>
- [20] M. W. Mitchell, J. S. Lundeen, and A. M. Steinberg. (2004, May). Super-resolving phase measurements with a multiphoton entangled state. *Nature* [Online]. 429(6988), pp. 161-164. Available: <http://dx.doi.org/10.1038/nature02493>
- [21] T. Nagata, R. Okamoto, J. L. O'Brien, K. Sasaki, and S. Takeuchi. (2007). Beating the standard quantum limit with four-entangled photons. *Science* [Online]. 316(5825), pp. 726-729. Available: <http://www.sciencemag.org/cgi/content/abstract/316/5825/726>
- [22] R. A. Campos, B. E. A. Saleh, and M. C. Teich, "Quantum-mechanical lossless beam splitter: Su(2) symmetry and photon statistics," *Phys. Rev. A*, vol. 40, no. 3, pp. 1371-1384, Aug. 1989.
- [23] Z. Y. Ou, J.-K. Rhee, and L. J. Wang. (1999). Observation of four-photon interference with a beam splitter by pulsed parametric down-conversion. *Phys. Rev. Lett.* [Online]. 83(5), pp. 959-962. Available: <http://link.aps.org/abstract/PRL/v83/p959>
- [24] Z. Y. Ou, J.-K. Rhee, and L. J. Wang. (1999). Photon bunching and multiphoton interference in parametric down-conversion. *Phys. Rev. A* [Online]. 60(1), pp. 593-604. Available: <http://link.aps.org/abstract/PRA/v60/p593>
- [25] B. H. Liu, F. W. Sun, Y. X. Gong, Y. F. Huang, G. C. Guo, and Z. Y. Ou. (2007). Four-photon interference with asymmetric beam splitters. *Opt. Lett.* [Online]. 32(10), pp. 1320-1322. Available: <http://www.opticsinfobase.org/abstract.cfm?URI=OL-32-10-1320>
- [26] C. K. Hong, Z. Y. Ou, and L. Mandel. (1987). Measurement of subpicosecond time intervals between two photons by interference. *Phys. Rev. Lett.* [Online]. 59(18), pp. 2044-2046. Available: <http://link.aps.org/abstract/PRL/v59/p2044>
- [27] W. Wieczorek, C. Schmid, N. Kiesel, R. Pohlner, O. Gühne, and H. Weinfurter. (2008). Experimental observation of an entire family of four-photon entangled states. *Phys. Rev. Lett.* [Online]. 101(1), pp. 010503-1-010503-4. Available: <http://link.aps.org/abstract/PRL/v101/e010503>
- [28] B. P. Lanyon, N. K. Langford. (2009). Experimentally generating and tuning robust entanglement between photonic qubits. *New J. Phys.* [Online]. 11(1), pp. 013008-1-013008-9. Available: <http://stacks.iop.org/1367-2630/11/013008>
- [29] H. Weinfurter, M. Żukowski. (2001). Four-photon entanglement from down-conversion. *Phys. Rev. A* [Online]. 64(1), pp. 010102-1-010102-4. Available: <http://link.aps.org/abstract/PRA/v64/e010102>
- [30] W. Wieczorek, N. Kiesel, C. Schmid, and H. Weinfurter. (2009). Multiqubit entanglement engineering via projective measurements. *Phys. Rev. A* [Online]. 79(2), pp. 022311-1-022311-8. Available: <http://link.aps.org/abstract/PRA/v79/e022311>
- [31] W. Laskowski, M. Wieśniak, M. Żukowski, M. Bourennane, and H. Weinfurter. (2009). Interference contrast in multisource few-photon optics. *J. Phys. B* [Online]. 42(11), pp. 114004-1-114004-12. Available: <http://stacks.iop.org/0953-4075/42/114004>
- [32] J. Kempe, D. Bacon, D. A. Lidar, and K. B. Whaley. (2001). Theory of decoherence-free fault-tolerant universal quantum computation. *Phys. Rev. A* [Online]. 63(4), pp. 042307-1-042307-29. Available: <http://link.aps.org/abstract/PRA/v63/e042307>
- [33] R. H. Dicke. (1954). Coherence in spontaneous radiation processes. *Phys. Rev.* [Online]. 93(1), pp. 99-110. Available: <http://link.aip.org/link?PR/93/99/1>
- [34] N. Kiesel, C. Schmid, G. Tóth, E. Solano, and H. Weinfurter. (2007). Experimental observation of four-photon entangled Dicke state with high fidelity. *Phys. Rev. Lett.* [Online]. 98(6), pp. 063604-1-063604-4. Available: <http://link.aps.org/abstract/PRL/v98/e063604>
- [35] M. Hein, J. Eisert, and H. J. Briegel. (2004). Multiparty entanglement in graph states. *Phys. Rev. A* [Online]. 69(6), pp. 062311-1-062311-20. Available: <http://link.aps.org/abstract/PRA/v69/e062311>
- [36] M. Hillery, V. Bužek, and A. Berthiaume. (1999). Quantum secret sharing. *Phys. Rev. A* [Online]. 59(3), pp. 1829-1834. Available: <http://link.aps.org/abstract/PRA/v59/p1829>
- [37] J.-C. Hao, C.-F. Li, and G.-C. Guo. (2001). Controlled dense coding using the Greenberger-Horne-Zeilinger state. *Phys. Rev. A* [Online]. 63(5), pp. 054301-1-054301-3. Available: <http://link.aps.org/abstract/PRA/v63/e054301>
- [38] J. K. Pachos, W. Wieczorek, C. Schmid, N. Kiesel, R. Pohlner, and H. Weinfurter. (2009). Revealing anyonic features in a toric code quantum simulation. *New J. Phys.* [Online]. 11, pp. 083010-1-083010-10. Available: <http://www.iop.org/EJ/abstract/1367-2630/11/8/083010>
- [39] M. Bourennane, M. Eibl, S. Gaertner, C. Kurtsiefer, A. Cabello, and H. Weinfurter. (2004). Decoherence-free quantum information processing with four-photon entangled states. *Phys. Rev. Lett.* [Online]. 92(10), pp. 107901-1-107901-4. Available: <http://link.aps.org/abstract/PRL/v92/e107901>
- [40] M. Eibl, S. Gaertner, M. Bourennane, C. Kurtsiefer, M. Żukowski, and H. Weinfurter. (2003). Experimental observation of four-photon entanglement from parametric down-conversion. *Phys. Rev. Lett.* [Online]. 90(20), pp. 200403-1-200403-4. Available: <http://link.aps.org/abstract/PRL/v90/e200403>
- [41] J.-S. Xu, C.-F. Li, and G.-C. Guo. (2006). Generation of a high-visibility four-photon entangled state and realization of a four-party quantum communication complexity scenario. *Phys. Rev. A* [Online]. 74(5), pp. 052311-1-052311-6. Available: <http://link.aps.org/abstract/PRA/v74/e052311>
- [42] N. Kiesel, C. Schmid, U. Weber, R. Ursin, and H. Weinfurter. (2005). Linear optics controlled-phase gate made simple. *Phys. Rev. Lett.* [Online]. 95(21), pp. 210505-1-210505-4. Available: <http://link.aps.org/abstract/PRL/v95/e210505>
- [43] N. K. Langford, T. J. Weinholt, R. Prevedel, K. J. Resch, A. Gilchrist, J. L. O'Brien, G. J. Pryde, and A. G. White. (2005). Demonstration of a simple entangling optical gate and its use in Bell-state analysis. *Phys. Rev. Lett.* [Online]. 95(21), pp. 210504-1-210504-4. Available: <http://link.aps.org/abstract/PRL/v95/e210504>
- [44] R. Okamoto, H. F. Hofmann, S. Takeuchi, and K. Sasaki. (2005). Demonstration of an optical quantum controlled-not gate without path interference. *Phys. Rev. Lett.* [Online]. 95(21), pp. 210506-1-210506-4. Available: <http://link.aps.org/abstract/PRL/v95/e210506>
- [45] M. Murao, D. Jonathan, M. B. Plenio, and V. Vedral. (1999). Quantum telecloning and multiparticle entanglement. *Phys. Rev. A* [Online]. 59(1), pp. 156-161. Available: <http://link.aps.org/abstract/PRA/v59/p156>
- [46] M. Rådmark, M. Żukowski, and M. Bourennane. (2009). Experimental test of rotational invariance and entanglement of photonic six-qubit singlet state. *arXiv:0903.3188 [quant-ph]* [Online]. Available: <http://arxiv.org/abs/0903.3188>
- [47] P. G. Kwiat, K. Mattle, H. Weinfurter, A. Zeilinger, A. V. Sergienko, and Y. Shih. (1995). New high-intensity source of polarization-entangled photon pairs. *Phys. Rev. Lett.* [Online]. 75(24), pp. 4337-4341. Available: <http://link.aps.org/abstract/PRL/v75/p4337>
- [48] P. Badziag, C. Brukner, W. Laskowski, T. Paterek, and M. Żukowski. (2008). Experimentally friendly geometrical criteria for entanglement. *Phys. Rev. Lett.* [Online]. 100(14), pp. 140403-1-140403-4. Available: <http://link.aps.org/abstract/PRL/v100/e140403>
- [49] O. Gühne and G. Tóth. (2009). Entanglement detection. *Phys. Rep.* [Online]. 474, pp. 1-75. Available: <http://www.sciencedirect.com/science/article/B6TVP-4VV2NGM-1/2/c9dbd012ebe762fd1e59139a3e064e60>
- [50] G. Tóth, "Detection of multipartite entanglement in the vicinity of symmetric Dicke states," *J. Opt. Soc. Amer. B*, vol. 24, no. 2, pp. 275-282, 2007.
- [51] M. Bourennane, M. Eibl, C. Kurtsiefer, S. Gaertner, H. Weinfurter, O. Gühne, P. Hyllus, D. Brub, M. Lewenstein, and A. Sanpera. (2004). Experimental detection of multipartite entanglement using witness operators. *Phys. Rev. Lett.* [Online]. 92(8), pp. 087902-087904. Available: <http://link.aps.org/abstract/PRL/v92/e087902>
- [52] G. Tóth, O. Gühne. (2005). Detecting genuine multipartite entanglement with two local measurements. *Phys. Rev. Lett.* [Online]. 94(6), pp. 060501-1-060501-4. Available: <http://link.aps.org/abstract/PRL/v94/e060501>



Witłef Wieczorek was born in Berlin, Germany, on January 20, 1979. He received the Diploma in physics from the Technische Universität Berlin, Berlin, in 2005. He is currently working toward the Ph.D. degree under the International Ph.D. Programme of Excellence "Quantum Computing, Control and Communication" of the Elite Network of Bavaria, Germany.

He was engaged in experimental studies on optical phenomena of self-assembled quantum dots during his Diploma studies. From 2006 to 2008, he was a Doctoral Fellow at the German National Academic Foundation (Studienstiftung des deutschen Volkes). Since 2006, he has been with the Max-Planck-Institute of Quantum Optics, Garching, Germany. He is also with the Department for Physics, LMU München. His current research interests include the experimental realization of quantum information and the study of entanglement.

Mr. Wieczorek is a member of the German Physical Society.



Nikolai Kiesel was born in Nürnberg, Germany, on February 8, 1977. He received the Diploma in physics and the Ph.D. degree from Ludwig-Maximilians-Universität (LMU) München, Munich, Germany, in 2002 and 2007, respectively.

During his Diploma studies he was engaged in the experimental analysis of photonic three-qubit entanglement. From 2003 to 2008, he was with the Max-Planck-Institute of Quantum Optics, Garching, Germany, where he was engaged in research on quantum information with multiphoton entanglement and tools for their efficient characterization. Since 2009, he has been a Postdoctoral Researcher at the Institute for Quantum Optics and Quantum Information, Austrian Academy of Sciences, Vienna, Austria. His current research interests include foundations of quantum mechanics and quantum information with optomechanical resonators.

Dr. Kiesel was nominated for the Dissertation Award of the German Physical Society. Since August 2009 he receives a Feodor-Lynen research fellowship by the Alexander von Humboldt foundation.



Christian Schmid was born in Landshut, Germany, on February 9, 1979. He received the Diploma and the Ph.D. degree in physics from Ludwig-Maximilians-Universität (LMU) München, Munich, Germany, in 2004 and 2008, respectively.

From 1998 to 2003, he studied physics at the LMU München. During 2001, he was a Summer Student at the European Organization for Nuclear Research (CERN). During his Diploma thesis he was engaged in the study of a source of polarization entangled photons and applications in quantum communication at the Max-Planck-Institute of Quantum Optics (MPQ), Garching, Germany. There he also carried out his research in the field of optical quantum information from 2004 until 2008, for which he received his Ph.D. Since 2008, he has been involved in the field of astronomical interferometry at the European Organisation for Astronomical Research in the Southern Hemisphere (ESO), Garching.



Wiesław Laskowski was born in Wejherowo, Poland, on February 24, 1978. He received the Ph.D. degree from the University of Gdańsk (UG), Gdansk, Poland, in 2007.

He was engaged in research on nonclassical properties of multiqubit quantum states during his Ph.D. studies. From 1997 to 2002, he studied physics at the UG, where he has been engaged in research since 2002 and has been a Postdoctoral Researcher since 2007. He is engaged in research on foundations of quantum mechanics, quantum information, and quantum communication.

Dr. Laskowski received a Young Researchers Fellowship of the Foundation for Polish Science from 2006 to 2007.



Marek Żukowski was born in Gdynia, Poland. He received the Master's and Doctoral degrees from the University of Gdańsk (UG), Gdansk, Poland, in 1976 and 1983, respectively, and the Doctor Habilitatus degree from Nicolaus Copernicus University, Torun, Poland, in 1995.

He is currently the Director of the Institute for Theoretical Physics and Astrophysics, UG, where he is also a Full Professor. During 1987, he started work on quantum foundations and quantum information. Since 1991, he intensively collaborates with Anton Zeilinger and Harald Weinfurter and their colleagues. His current research interests include entanglement, its production, detection, and applications.



Harald Weinfurter received the Diploma and the Ph.D. degree in neutron optics experiments from the Technical University of Vienna, Vienna, Austria, the latter in 1987.

He was a Postdoctoral Fellow at the Hahn-Meitner Institut, Berlin, Germany, and the RISØ-Laboratory, Roskilde, Denmark. In 1991, he started work on foundations of quantum physics and quantum information at the University of Innsbruck, Austria, in the group of Anton Zeilinger. In 1999, he became a member of the Faculty of Physics, University of Munich. He is currently with the Max-Planck-Institute of Quantum Optics (MPQ), Garching, Germany, and with the Department for Physics, Ludwig-Maximilians-Universität (LMU) München, Munich, Germany. His current research interests include experiments on studying and applying entanglement, e.g., in various demonstrations of quantum communication protocols, in free-space quantum cryptography over record distances of 144 km, or in atom-photon entanglement.

Chapter 4

Four-qubit entanglement for revealing anyonic features

It is well known that in the three-dimensional space only two types of indistinguishable particles can be observed, namely bosons and fermions. In two dimensions new types of particles can occur: anyons. These acquire upon particle exchange any possible statistical phase, in contrast to the behavior of bosons and fermions, which acquire a phase factor of $+1$ and -1 , respectively. In this chapter the observation of anyonic features is described based upon a quantum simulation of a minimal instance of the toric code [57] (see publ. P4.1). To this end, section 4.1 and 4.2 give an introduction to anyons and the toric code, while section 4.3 focuses on the experimental implementation presented in ref. [57] (see publ. P4.1).

The occurrence of anyons as new types of particles in the two-dimensional space [67, 68] is explained in section 4.1. The realization of anyons is only possible in two-dimensional systems. So far, systems in the fractional quantum Hall regime [260], an effect appearing in two dimensions, are the most likely candidates for the observation of anyons in a physical system, and thus deserve attention. Besides being interesting from a fundamental point of view anyons can find applications in topological quantum computing, which is also elaborated on. Another possibility to realize anyons is given by abstract two-dimensional spin lattice systems. One of these is the toric code [73], which is presented in section 4.2. A minimal subsystem thereof is sufficient to simulate basic anyonic features by studying the evolution of the anyonic wave function [261, 262]. In order to realize this instance of the toric code four-photon entanglement is used that has been observed with the experimental setup described in chapter 3. Basic anyonic features like creation and annihilation of anyonic quasiparticles as well as their mutual statistics can be demonstrated based on a four-qubit GHZ state [57] (see publ. P4.1), which is discussed in section 4.3.

4.1 Anyons, the quantum Hall effect, and topological quantum computation

Appearance of anyons in two-dimensional systems With the concept of indistinguishable particles quantum theory lays the basis for a fundamental understanding of physical phenomena such as metallic conduction, super fluidity, and Bose-Einstein condensation. Two types of indistinguishable particles are observed in three-dimensional space, bosons and fermions. Bosons and fermions are distinguished by their spin, bosons are integer spin particles and fermions are half-odd-integer spin particles. The spin of a single particle determines the statistics of an ensemble of indistinguishable particles, the so-called spin-statistics theorem [263, 264]. The statistical behavior is inferred from symmetry, namely the transformation of the wave function under exchange of particles. While the wave function of two bosons acquires a phase factor of $+1$ upon exchange, the one for two fermions obtains a phase factor of -1 . This exchange behavior can also be understood in terms of the topology of the space dimension [265]. A closed path in the three-dimensional rotation group $SO(3)$ that begins at the identity and ends at 4π can be smoothly contracted to a trivial path, see fig. 4.1 (even if it encloses a particle). Hence, a rotation by 4π can be represented by the identity and is equivalent to two successive particle exchanges. Consequently, a single particle exchange can have the eigenvalues $+1$ and -1 corresponding to bosonic and fermionic statistics, respectively. In contrast, a closed path in two dimensions is not necessarily contractible to a trivial path (fig. 4.1). Hence, *any* statistical phase factor θ can be acquired when exchanging two indistinguishable particles in two dimensions:

$$\psi(\mathbf{r}_1, \mathbf{r}_2) \rightarrow e^{i\theta} \psi(\mathbf{r}_2, \mathbf{r}_1). \quad (4.1)$$

A second exchange, which is equivalent to a loop of one particle around the other, leads to $\psi(\mathbf{r}_1, \mathbf{r}_2) \rightarrow e^{2i\theta} \psi(\mathbf{r}_1, \mathbf{r}_2)$. For bosons and fermions only the values $\theta = 0$ and $\theta = \pi$ would be possible. Particles with other values of θ are called *anyons* [67, 68]. Furthermore, special types of anyons can not only acquire any statistical phase factor but also a unitary transformation of their wave function upon exchange, which will be of importance for topological quantum computation discussed briefly later on. The former anyons are called Abelian, the latter non-Abelian anyons.

Anyons were first discussed as a theoretical concept appearing for composite particles made up from a particle with charge q and a magnetic flux tube with flux Φ_0 [67, 68] (labeled as e and m in fig. 4.1). When one of these composite particles circulates around another one, then it acquires a phase of $e^{iq\Phi_0}$ due to the Aharonov-Bohm effect [266]. Consequently, upon exchange they would acquire a statistical phase of $q\Phi_0/2$ and exhibit fractional statistics. The phase of $e^{iq\Phi_0/2}$ would be also acquired by simply moving a single electric charge around a magnetic flux, which corresponds to a rotation of the composite particle. This evolution emerges in the toric code, which will be described in section 4.2.

A system supporting anyons can be created by artificially confining particle movement from three to two dimensions. An example is the fractional quantum Hall effect (QHE), which will be discussed briefly in the following [267–270]. Alternatively, two-dimensionality

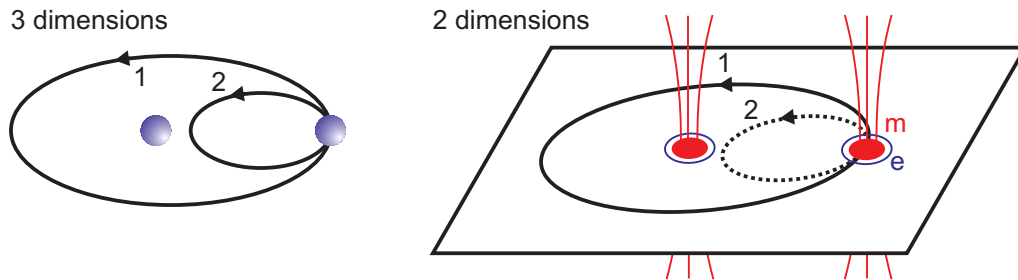


Figure 4.1: Schematic representations of the braiding of two indistinguishable particles. In a three-dimensional space a loop (1) of one particle around the other is contractible to a trivial loop (2). In contrast, in two dimensions this is not the case. Loops (1) and (2) are not topological equivalent, i.e., it is impossible to deform them continuously into each other (as one particle would cross the other one).

is also found in certain abstract spin lattice systems [73, 271], whereupon the implementation described in section 4.3 is based. For this purpose, the toric code will be discussed in section 4.2.

Quantum Hall effect and anyons The QHE [260, 272] is the quantum version of the classical Hall effect, whereby electrons accelerated in the x direction by an electric field are deflected in the y direction by a magnetic field applied perpendicular to the $x - y$ plane (fig. 4.2). Confining carrier movement in the z direction essentially leads to the QHE. It is observed in a layered heterostructure that forms an electron gas confined in the two-dimensional plane $x - y$ and appears at very low temperatures under high magnetic fields in samples of high electron mobility. Due to the high magnetic field, the electron is forced into circular orbits that are quantized into Landau levels separated by the cyclotron energy.

The QHE is characterized by vanishing longitudinal (R_{xx}) and constant transversal (Hall) resistance (R_{xy}) [267] (fig. 4.2). The Hall resistance shows pronounced steps at

$$R_{xy} = \frac{h}{e^2} \frac{1}{\nu}, \quad (4.2)$$

where $h/e^2 \approx 25.813 \text{ k}\Omega$ is the quantum of resistance and is used as a practical unit for resistance in calibrations [272, 273]. The dimensionless parameter ν is the Landau level filling factor: the ratio of the electron density to the magnetic flux density or, equivalently, the number of electrons per flux quantum ($\Phi_0 = h/e$). It can take integer values $\nu = 1, 2, 3, \dots$ describing the integer QHE [272], but also fractional values $\nu = p/q$ with p, q integer for the fractional QHE [260].

The integer QHE is a single particle effect of non-interacting electrons resulting from complete filling of Landau levels and additional pinning of electrons at defects. In contrast, the fractional QHE is a many-body effect resulting from the strong interaction of many electrons due to the magnetic field [267]. The interacting electrons have a charge smaller

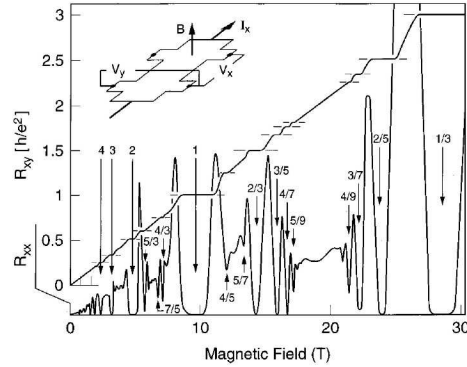


Figure 4.2: Hall resistance $R_{xy} = V_y/I_x$ and longitudinal resistance $R_{xx} = V_x/I_x$ for a two-dimensional electron system at a temperature of 85 mK as a function of the magnetic field B , taken from [267]. Numbers give the filling factor ν . The inset shows a schematic of the sample.

than that of the sum of individual electrons. This system can be described by the formation of composite quasiparticles with attached flux quanta. Excitations of the ground state are additional or missing flux quanta resulting in a missing or additional fractional charge; for $\nu = 1/3$ it is a third of the electron charge. Exactly such an excitation is an anyon [274–277] exhibiting fractional statistics. While the fractional charge was confirmed experimentally [278, 279], a clear-cut experimental evidence for the statistical properties of such an excitation is still missing. Such experiments would realize a closed path of a group of anyons around an island of anyons in an Aharonov-Bohm-like interferometer and yield interferometric oscillations [280, 281]. However, the difficulty in such a realization lies with the continuous presence of interactions in the samples and the unambiguous interpretation of the experimental results, which can originate from topology as well as dynamical interactions [70, 71].

Non-Abelian anyons are expected to appear as excitations in fractional Quantum Hall states, for example for $\nu = 5/2$. The first step in testing this theoretical expectation recently succeeded in confirming their fractional charge of $e/4$ [282]. However, the statistical nature of these anyons [283–285] has not been experimentally revealed so far. Other two-dimensional solid state systems realizing fractional charges and with that anyons consist of superconducting films on top of a two-dimensional electron gas [286]. In the following it is outlined why so much interest lies in the realization of anyons. To this end, a quantum information point of view will be taken again.

Topological quantum computation with anyons Anyons are on one hand interesting from a fundamental point of view. They are new types of particles in two spatial dimensions exhibiting fractional statistics. On the other hand, they also find powerful applications in the field of topological quantum computing [69, 73, 265, 271, 287, 288]. In the mathematical field of topology the properties of spatial configurations that are unaltered

by elastic deformations are studied. Hence, topological states of matter are intrinsically stable to local deformations. This results in a robustness against local errors as they are topologically protected, i.e., local perturbations do not change the topology of the system. It was shown that they can realize quantum computation that is intrinsically fault-tolerant [69, 265, 289]. This is in contrast to other schemes of quantum computation, for example the circuit model [1] or the one-way quantum computer [45], where additional quantum error correction [1] is required to compensate for intrinsic errors in the quantum hardware to reach fault tolerance.

Topological quantum computation on the basis of anyons is possible if at least three basic requirements of quantum computation are fulfilled: proper initialization of qubits, implementation of unitary evolution and measurement to read out the computational result [1]. Indeed, such schemes were developed using certain types of non-Abelian anyons [265, 289, 290]. Thereby, three anyons are necessary to encode one logical qubit. The unitary operations are implemented by braiding anyons, i.e., moving anyons around each other, which yields a unitary matrix. Finally, the computational result is read out by a non-Abelian anyon that acts as a test particle and circulates all other anyons that carry the information, or by fusing anyons. All these procedures take place in a subspace of the total Hilbert space, namely the degenerate ground state with a fixed number of quasiparticles. This subspace is separated from the excited states by an energy gap, and the computation is thus protected from errors. Topological quantum computing is based on non-local qubits (non-Abelian anyons) and non-local gates (braiding anyons), and is thus intrinsically protected from local errors.

The implementation of topological quantum computation is based on the realization of non-Abelian anyons. The fractional quantum Hall system is the most studied experimental system so far [69], but far from being used for that purpose yet. Alternative systems include spin lattice systems [73, 271]. The toric code [73] is one of these and will be discussed in the following section 4.2. While the toric code defined on a square lattice supports only Abelian anyons, a more complex version of the toric code is the honeycomb lattice [271] supporting also non-Abelian anyons.

4.2 Toric code

The toric code is a spin lattice system [72, 73]. It belongs to the broader class of surface codes mapped onto surfaces with different topologies. The following description follows mainly the seminal works of Alexei Kitaev (refs. [72, 73]). The toric code can be defined on a $k \times k$ two-dimensional lattice on a torus [fig. 4.3(a)]. Qubits are placed on the edges and are connected via two types of four-qubit interactions. A vertex, i.e., a star of four edges, is defined by the operator \hat{A}_s , while a plaquette, i.e., four edges facing each other, is defined by \hat{B}_p , with

$$\hat{A}_s = \otimes_{j \in s} \hat{\sigma}_x^{(j)}, \quad \hat{B}_p = \otimes_{j \in p} \hat{\sigma}_z^{(j)}. \quad (4.3)$$

The tensor product runs over all four qubits on the respective edges [fig. 4.3(b)]. Alternatively, one can regard the toric code as consisting of alternating s and p plaquettes arranged

in a chessboard manner with qubits placed at the vertices, which is depicted in fig. 4.3(b) as a gray lattice. This will be used in section 4.3, whereby a minimal subsystem of the toric code is considered. The operators \hat{A}_s and \hat{B}_p are Hermitian and commute with each other as they have zero or two qubits in common. Their eigenvalues are ± 1 . The sum taken over all plaquettes defines the Hamiltonian of the toric code

$$\hat{\mathcal{H}} = - \sum_s \hat{A}_s - \sum_p \hat{B}_p. \quad (4.4)$$

As the operators \hat{A}_s and \hat{B}_p commute with the Hamiltonian and also with each other, the system is exactly solvable with its ground state $|\xi\rangle$ given by [291]

$$|\xi\rangle \propto \otimes_s (\mathbb{1} + \hat{A}_s) |00\dots 0\rangle, \quad (4.5)$$

where $\hat{\sigma}_z |0\rangle = |0\rangle$. Thus, $\hat{A}_s |\xi\rangle = |\xi\rangle$ and $\hat{B}_p |\xi\rangle = |\xi\rangle$ for all s, p . In the context of quantum error correction these operators can therefore be regarded as commuting stabilizing operators (see eq. 2.15) of the toric code ground state as they simultaneously define it with eigenvalue +1.

Local excitations in the toric code are created by applying local operations on single qubits. By the application of a single $\hat{\sigma}_z$ operation, the eigenvalue of the neighboring two s vertices turns from ± 1 to ∓ 1 [fig. 4.3(c)], which can be checked by applying the corresponding \hat{A}_s operators on the respective vertices. Accordingly, applying $\hat{\sigma}_x$ on a qubit changes the eigenvalue of the neighboring two p plaquettes from ± 1 to ∓ 1 [fig. 4.3(c)]. These excitations are interpreted as quasiparticles. The former is called an e quasiparticle, whereas the latter is called an m quasiparticle, which can take the role of an electric charge and a magnetic flux, respectively. Finally, applying a $\hat{\sigma}_y$ operation simultaneously creates two e and two m particles on the neighboring vertices and plaquettes. The combination of e and m is labeled ϵ . Fusion rules determine the outcome of quasiparticles that are created at similar lattice sites. They are the following: $1 \times e = e$, $1 \times m = m$, $1 \times \epsilon = \epsilon$, $e \times e = 1$, $m \times m = 1$, $\epsilon \times \epsilon = 1$, $e \times m = \epsilon$, $e \times \epsilon = m$ and $m \times \epsilon = e$, where 1 is the vacuum state corresponding to no quasiparticle at the corresponding lattice site. For example, applying $\hat{\sigma}_z$ on a qubit and on a neighboring qubit creates two e quasiparticles on the same s plaquettes and two e quasiparticles at distant s plaquettes. The former two e quasiparticles annihilate due to the fusion rule $e \times e = 1$, while the latter ones can be envisaged to be connected by a string, see fig. 4.3(c).

More generally, quasiparticles can be moved on the lattice using string operators defined as

$$\hat{\mathcal{S}}_z(t) = \otimes_{j \in t} \hat{\sigma}_z^{(j)}, \quad \hat{\mathcal{S}}_x(t') = \otimes_{j \in t'} \hat{\sigma}_x^{(j)}, \quad (4.6)$$

which apply the corresponding local rotations on the qubits along path t or t' [fig. 4.3(c)]. The string operators $\hat{\mathcal{S}}_z(t)$ and $\hat{\mathcal{S}}_x(t')$ commute with all \hat{A}_s and \hat{B}_p , except for two lattice sites. These are the endpoints of a non-closed path, and thus create each a single quasiparticle [fig. 4.3(c)]. Hence, every combination of an even number of quasiparticles on the

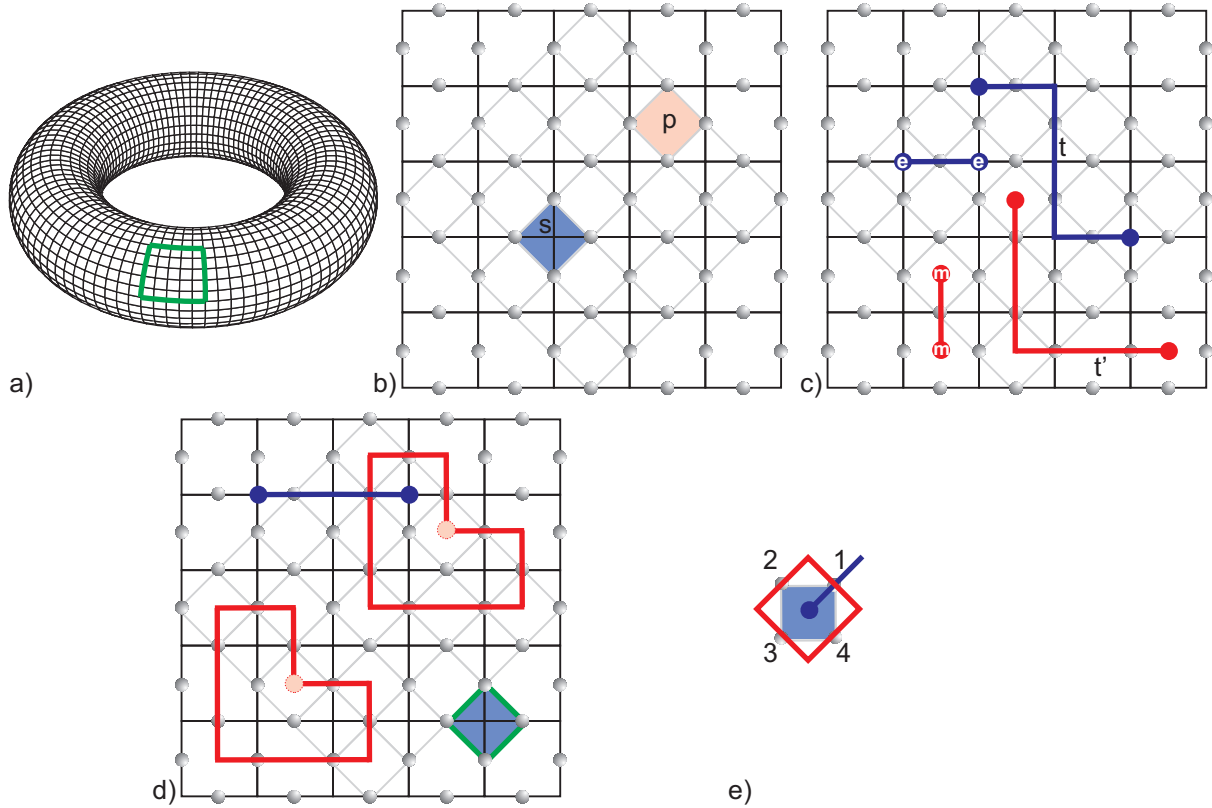


Figure 4.3: (a) The toric code defined on a torus. The green marked area is considered in (b)-(d). (b) Two types of interactions define s vertices and p plaquettes. Alternatively, one can consider alternating s and p plaquettes on the gray lattice. (c) Pairwise quasiparticles e and m are created via $\hat{\sigma}_z$ and $\hat{\sigma}_x$ operations on single qubits, respectively. Strings $\hat{S}_z(t)$ and $\hat{S}_x(t')$ move anyonic quasiparticles along the torus. (d) A loop around an unpopulated plaquette cancels. In contrast, a loop around a plaquette populated with an e quasiparticle yields a statistical phase factor of -1 revealing the anyonic phase factor of $\theta = \pi/2$ (eq. 4.1). For the experimental implementation a single s vertex (marked green) is considered. (e) A single s plaquette can host the circulation of a m around an e quasiparticle.

toric code is allowed¹. However, when a string forms a loop around unpopulated plaquettes or vertices the endpoints fall on the same lattice site, and thus two quasiparticles are annihilated due to the fusion rules [fig. 4.3(d)]. The loop is said to be contractible.

Having defined quasiparticles on the lattice, one can now consider their mutual statistical phase. Assuming the creation of an e quasiparticle at an s vertex with qubit labels 1, 2, 3, 4 by applying $\hat{\sigma}_z$ on the first qubit [fig. 4.3(d) and (e)] yields

$$|\Psi\rangle_{\text{initial}} = \hat{\sigma}_z^{(1)} |\xi\rangle. \quad (4.7)$$

¹This holds if one considers periodic boundary conditions occurring for example for the topology of a torus.

Now an m quasiparticle is transported around e , which is described by the string operator $\hat{\mathcal{S}}_x(4321) = \hat{\sigma}_x^{(4)} \hat{\sigma}_x^{(3)} \hat{\sigma}_x^{(2)} \hat{\sigma}_x^{(1)} = \hat{A}_s$,

$$\begin{aligned} |\Psi\rangle_{\text{final}} &= \hat{\mathcal{S}}_x(4321) |\Psi\rangle_{\text{initial}} = \hat{\mathcal{S}}_x(4321) \hat{\sigma}_z^{(1)} |\xi\rangle = -\hat{\sigma}_z^{(1)} \hat{\mathcal{S}}_x(4321) |\xi\rangle = -\hat{\sigma}_z^{(1)} \hat{A}_s |\xi\rangle \\ &= -|\Psi\rangle_{\text{initial}}. \end{aligned} \quad (4.8)$$

Hence, moving an m around an e quasiparticle, i.e., braiding these quasiparticles, results in a statistical phase of -1 acquired by the global wave function. As the phase for fermions or bosons would not change upon such a process, m and e behave as anyonic quasiparticles with respect to each other. Note, performing only an exchange of m and e yields no well defined statistical phase as the wave function describing that state is distinguishable, because the quasiparticles are distinguishable. In contrast, a full loop of one particle around the other results in indistinguishable initial and final spatial positions and therefore in the acquisition of a well-defined statistical phase. The statistical phase of an e quasiparticle with respect to another e quasiparticle is derived analogously and results in bosonic behavior, which also holds for m quasiparticles. However, an e quasiparticle exhibits a fermionic statistical phase as eq. 4.8 can also be interpreted in terms of rotating an e quasiparticle by 2π [292].

The interest in the toric code relies on the realization of anyonic quasiparticles. The fractional quantum Hall system is the only physical system known so far exhibiting a topological state of matter with anyonic particle excitations. However, due to the high experimental effort no conclusive result about the statistical nature of the expected anyonic quasiparticles could be stated so far. Hence, the toric code is an appealing alternative system realizing a topologically ordered state with anyonic quasiparticle excitations. In addition to this fundamental interest, its possible application as an error correcting code [73] is conceivable. An alternative to the toric code as a square lattice is the honeycomb lattice, which is a surface code with a hexagonal lattice and the additional benefit of supporting non-Abelian anyonic quasiparticles [271]. This allows the realization of topological quantum computation based on a surface code [271].

The experimental implementation of surface codes in general and the described minimal realization of an instance of the toric code in particular is the topic of the next section.

4.3 Minimal implementation

Recently, several theoretical proposals were put forward for the implementation of surface codes in real physical systems. Large scale schemes aiming at the implementation of the Hamiltonian were suggested based on the system of ultra cold atoms or molecules trapped in optical lattices [293]. A number of proposals for different experimental schemes have been developed – for example, trapped polar molecules with the spin represented by a single valence electron of the molecule [294], trapped ultra cold atoms with the effective spin given by two hyperfine atomic ground states [295], trapped atoms or molecules with a read-out of anyonic braiding through global operations [296] and, finally, trapped atoms or molecules with a read-out performed by another particle species [297]. Although none of

these schemes have been implemented experimentally to date, the necessary experimental techniques of trapping ultra cold atoms are available.

Other theoretical work was focusing on the study of minimal instances of surface codes [261, 262, 298], which is also the topic here. The aim of this work is to demonstrate anyonic features based on the evolution of the relevant wave functions. Such schemes avoid the experimental implementation of a surface code Hamiltonian as for example the necessary four-body interactions \hat{A}_s and \hat{B}_p in the toric code are difficult to realize. Rather, the relevant wave functions are created without the need of the toric code Hamiltonian. However, the lack of a Hamiltonian, which would provide the necessary energy gap to excited states not used for the actual computation, prevents the protection of the qubits from noise. Thus, such an implementation is not suitable for exploiting the topological nature of the code for fault-tolerant quantum computation.

In ref. [262] a single plaquette of the honeycomb lattice consisting of six qubits was considered to show basic anyonic features and also to reveal their mutual statistical phase via an interference experiment. In contrast, ref. [261] considered toric code states made up of N qubits created from graph states of $2N$ qubits via appropriate single qubit measurements. A system of six qubits was identified to show anyonic statistics and was recently implemented experimentally [37] simultaneously to the implementation described in this work [57] (publ. P4.1). A system of nine qubits was shown to be capable to demonstrate the robustness of the statistical phase for different braiding paths.

In this work, the implementation of a minimal instance of the toric code is pursued. Inspired by ref. [262] a single plaquette of the toric code made up of four qubits is considered. Basic anyonic features and also their mutual statistical phase can be demonstrated [57] (publ. P4.1) on a single s plaquette (now this nomenclature is chosen instead of s vertex).

Following eq. 4.5, the ground state of such a system is given by

$$|\xi\rangle = \frac{1}{\sqrt{2}}(\mathbb{1}^{\otimes 4} + \otimes_{j \in s} \hat{\sigma}_x^{(j)}) |0000\rangle = \frac{1}{\sqrt{2}}(|0000\rangle + |1111\rangle) = |\text{GHZ}_4\rangle, \quad (4.9)$$

where $j \in \{1, 2, 3, 4\}$ labels the qubits in a counterclockwise order. This state is the well known four-qubit GHZ state, which has already been implemented using photons [64] and atoms [299, 300]. Here this state is employed with the specific aim of simulating anyonic behavior in a minimal version of the toric code, which has not been done before. Note that the four-qubit GHZ state can be defined by a Hamiltonian that is the sum over the GHZ state's stabilizing operators, which are $\hat{\sigma}_x^{\otimes 4} = \hat{A}_s$ and $\hat{B}_{p'} = \hat{\sigma}_z^{(i)(j)}$ with $i \neq j \in \{1, 2, 3, 4\}$. The former stabilizer represents the s plaquette and the stabilizers $\hat{B}_{p'} \in \{\hat{\sigma}_z^{(1)(2)}, \hat{\sigma}_z^{(2)(3)}, \hat{\sigma}_z^{(3)(4)}, \hat{\sigma}_z^{(4)(1)}\}$ can be interpreted as neighboring four p plaquettes, which are only represented by links. Due to this non-periodic minimal instance of the toric code, this system is described by open boundary conditions. The presence of an e quasiparticle is detected by the plaquette operator \hat{A}_s , whereas the presence of m quasiparticles is detected by the eigenvalue of the four $\hat{B}_{p'} \in \{\hat{\sigma}_z^{(1)(2)}, \hat{\sigma}_z^{(2)(3)}, \hat{\sigma}_z^{(3)(4)}, \hat{\sigma}_z^{(4)(1)}\}$.

The experimental implementation is based on the setup described in chapter 3, whereby

for $\alpha = 0$ the four-qubit GHZ state is observed². The GHZ state and all other states obtained by local operations have to be analyzed. These states are of the form

$$|\text{GHZ}_4^\phi\rangle = \frac{1}{\sqrt{2}}(|HHHH\rangle + e^{i\phi}|VVVV\rangle), \quad (4.10)$$

in the notation of polarization encoded qubits. Specifically, one obtains, for example, $|\xi\rangle = |\text{GHZ}_4^0\rangle$, $\hat{\sigma}_z^{(i)}|\xi\rangle = |\text{GHZ}_4^\pi\rangle$ and $\hat{\mathcal{S}}_x(1234)|\xi\rangle = |\text{GHZ}_4^0\rangle$, which correspond to the ground state, an anyonic quasiparticle and a loop around an unpopulated plaquette, respectively. In order to determine the phase ϕ of $|\text{GHZ}_4^\phi\rangle$ a correlation function measurement is performed [299]:

$$\hat{c}_{xy}(\gamma) = \hat{\sigma}(\gamma)^{\otimes 4} \text{ with } \hat{\sigma}(\gamma) = (\cos \gamma)\hat{\sigma}_y + (\sin \gamma)\hat{\sigma}_x, \quad (4.11)$$

which corresponds to a measurement along the $x - y$ plane of the Bloch sphere (for the implemented measurement settings see appendix B). For $|\text{GHZ}_4^\phi\rangle$ its expectation value shows an oscillation, whose angular displacement depends on ϕ ,

$$\langle \hat{c}_{xy}(\gamma) \rangle = \mathcal{V} \cos(4\gamma + \phi), \quad (4.12)$$

with a period of one quarter of 2π , a unique signature of four-qubit GHZ entanglement. The visibility of this oscillation \mathcal{V} is 1 for pure GHZ states. For a general state it equals twice the element $\rho_{HHHH,VVVV} = \text{Tr}[[HHHH]\langle VVVV|\rho]$ of the corresponding density matrix ρ . The visibility is obtained from the experimental data by a weighted least squares fit to a Fourier decomposition of $\langle \hat{c}_{xy}(\gamma) \rangle$ considering only even components up to order 4 as only these components can originate from physical states [246]:

$$\langle \hat{c}_{xy}(\gamma) \rangle = \sum_{k=0}^2 a_k \cos(2k \cdot \gamma) + b_k \sin(2k \cdot \gamma). \quad (4.13)$$

The parameters a_k and b_k are in correspondence with elements of a physical density matrix, whereby a combination of a_2 and b_2 determines \mathcal{V} and ϕ [246]. Additionally, genuine four-qubit entanglement is proven by using an entanglement witness based on the fidelity, whereby a value larger than 0.5 is sufficient [138]. The fidelity can be derived from the visibility \mathcal{V} together with the populations P_{HHHH} and P_{VVVV} , which are determined from a measurement in the z basis. The fidelity is given by

$$F = \langle \text{GHZ}_4^\phi | \rho | \text{GHZ}_4^\phi \rangle = (\mathcal{V} + P_{HHHH} + P_{VVVV})/2. \quad (4.14)$$

For all measurements fidelity values in excess of 0.73 have been achieved, proving entanglement (see Table 1 of publ. P4.1).

In the following, several evolutions on the minimal toric code system consisting of a single s plaquette are described together with the results of the correlation measurements

²Here, the polarization-flip behind the PBS (step 4 in fig. 3.2) is not necessary. Hence, the HWP($\pi/4$) is left out.

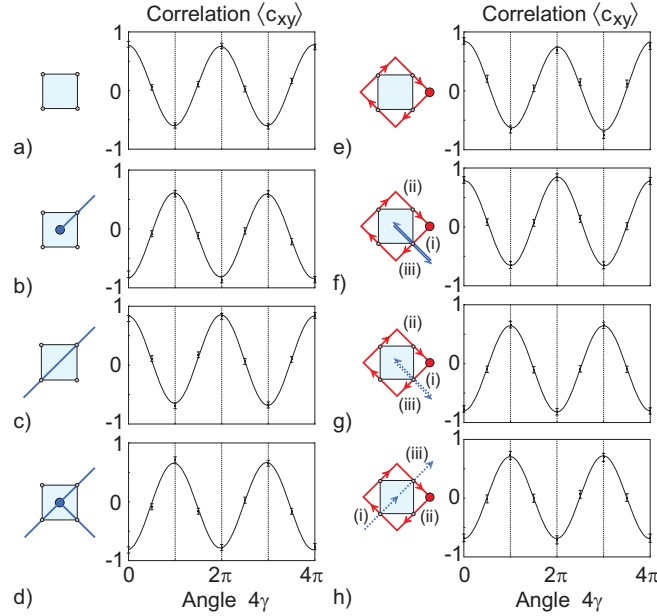


Figure 4.4: Pictorial representations of the s plaquette and measured correlation functions, whereby the phase ϕ of the state $|\text{GHZ}_4^\phi\rangle$ is determined by analyzing the correlation function $\langle \hat{c}_{xy}(\gamma) \rangle$ (see eq. 4.11 and eq. 4.13, the experimentally determined values of ϕ are given in Table 1 of publ. P4.1). (a) Ground state $|\xi\rangle$. (b) Generating an e -type anyonic state $|\text{GHZ}_4^\pi\rangle$ by a $\hat{\sigma}_z$ operation. (c) A second $\hat{\sigma}_z$ operation removes the anyon from the plaquette and elongates the string giving back the $|\text{GHZ}_4^0\rangle$ state. (d) A third $\hat{\sigma}_z$ operation creates an anyon, connected with the string already traversing the plaquette. (e) Performing an s plaquette loop on an empty plaquette and (f) first creating an anyon on the plaquette (i), performing the loop (ii), and removing the anyon from the plaquette again (iii) yield identical final states up to a global phase factor. (g) The global phase is revealed by superimposing the two aforementioned evolutions proving anyonic statistics as a $|\text{GHZ}_4^\phi\rangle$ state with $\phi = \pi$ is observed. (h) An alternative path for the anyon e that gives the same phase.

shown in fig. 4.4 (for details see publ. P4.1). Their aim is to show basic anyonic features and the mutual statistical phase of anyons. To this end, (a) the ground state has been verified, (b) the population of the plaquette with an e quasiparticle, (c) the fusion rule $e \times e = 1$, and (d) the creation of a string have been demonstrated, and (e) a loop around an unpopulated plaquette has been performed. Most importantly, the statistical phase between an e and m quasiparticle should be revealed. Although the loop around a populated plaquette (f) yields the statistical phase of -1 between e and m quasiparticles in theory, it is given as an unobservable global phase factor in the experiment. Hence, an interference measurement was performed for two different paths (g) and (h), superimposing the evolutions of a loop around (e) an unpopulated and (f) a populated plaquette. Thereby, the difference of the otherwise unobservable global phase shifts for these two evolutions becomes a relative phase

shift.

In particular, all evolutions are given by

- (a) ground state $[|\xi\rangle = |\text{GHZ}_4^0\rangle]$, fig. 4.4(a)],
- (b)-(d) creation of one anyonic quasiparticle $[\hat{\sigma}_z^{(1)}|\xi\rangle = |\text{GHZ}_4^\pi\rangle]$, fig. 4.4(b)], two anyonic quasiparticles that form a string $[\hat{\mathcal{S}}_z(31)|\xi\rangle = \hat{\sigma}_z^{(3)}\hat{\sigma}_z^{(1)}|\xi\rangle = |\text{GHZ}_4^0\rangle]$, fig. 4.4(c)] and a quasiparticle connected to the string $[\hat{\sigma}_z^{(4)}\hat{\mathcal{S}}_z(31)|\xi\rangle = |\text{GHZ}_4^\pi\rangle]$, fig. 4.4(d)],
- (e)-(f) loop around an unpopulated $[\hat{\mathcal{S}}_x(1234)|\xi\rangle = |\text{GHZ}_4^0\rangle]$, fig. 4.4(e)] and populated plaquette $[\hat{\sigma}_z^{(4)}\hat{\mathcal{S}}_x(1234)\hat{\sigma}_z^{(4)}|\xi\rangle = -|\text{GHZ}_4^0\rangle]$, fig. 4.4(f)],
- (g)-(h) two types of interference measurements $[(\hat{\sigma}_z^{(4)})^{1/2}\hat{\mathcal{S}}_x(1234)(\hat{\sigma}_z^{(4)})^{-1/2}|\xi\rangle = -i|\text{GHZ}_4^\pi\rangle]$, fig. 4.4(g) and $(\hat{\sigma}_z^{(1)})^{1/2}\hat{\mathcal{S}}_x(1234)(\hat{\sigma}_z^{(3)})^{-1/2}|\xi\rangle = -i|\text{GHZ}_4^\pi\rangle]$, fig. 4.4(h)].

Only the interference measurement transforms the global phase shift of -1 into a relative and observable phase factor resulting in the $|\text{GHZ}_4^\pi\rangle$ state. If the statistical phase shift of -1 had not occurred, $|\text{GHZ}_4^0\rangle$ would have been observed as final state.

To summarize, in the simulation of a single plaquette of the toric code system basic anyonic features as well as their mutual statistical phase have been demonstrated. An extension to scalable systems such as ultra cold atoms or molecules in optical lattices [293–297] is necessary to exploit the power of anyons for topological quantum computation in the future.

4.4 Publication

P4.1

New Journal of Physics

The open-access journal for physics

Revealing anyonic features in a toric code quantum simulation

J K Pachos¹, W Wieczorek^{2,3}, C Schmid^{2,3}, N Kiesel^{2,3},
R Pohlner^{2,3} and H Weinfurter^{2,3}

¹ School of Physics and Astronomy, University of Leeds, Leeds LS2 9JT, UK

² Max-Planck-Institute of Quantum Optics, D-85748 Garching, Germany

³ Department for Physics, Ludwig-Maximilians-Universität München, D-80799 München, Germany

E-mail: j.k.pachos@leeds.ac.uk

New Journal of Physics **11** (2009) 083010 (10pp)

Received 1 April 2009

Published 12 August 2009

Online at <http://www.njp.org/>

doi:10.1088/1367-2630/11/8/083010

Abstract. Anyons are quasiparticles in two-dimensional systems that show statistical properties very distinct from those of bosons or fermions. While their isolated observation has not yet been achieved, here we perform a quantum simulation of anyons on the toric code model. By encoding the model in the multi-partite entangled state of polarized photons, we are able to demonstrate various manipulations of anyonic states and, in particular, their characteristic fractional statistics.

Contents

1. Introduction	2
2. Toric code model	2
2.1. Hamiltonian and ground state	2
2.2. Anyonic quasiparticles	3
2.3. Anyonic statistics	4
3. Experimental implementation	4
3.1. Minimal instance of the toric code model	4
3.2. State implementation	5
3.3. Anyonic manipulations and detection of anyonic statistics	6
4. Conclusions	9
Acknowledgments	9
References	9

1. Introduction

In three spatial dimensions, only two types of statistical behaviors have been observed dividing particles into two groups: bosons and fermions. If one is restricted to two-dimensional systems the situation changes. There, anyons [1] can appear, which exhibit fractional statistics that ranges continuously from bosonic to fermionic. Anyons are responsible for the fractional quantum Hall effect [2] and it has been demonstrated that they could be realized as quasiparticles in highly entangled many-body systems. Formally, the properties of anyons are described by two-dimensional topological quantum field theories [3] that dictate their trivial dynamical, but complex statistical behavior. In general, it is expected that such topological quantum field theories come into effect at low energies of highly correlated many-body systems, such as quantum liquids [4]. However, the observation of anyonic features requires high population in the system's ground state, high purity samples and, above all, the ability to separate the anyonic effects from the dynamical background of the strongly interacting system. In spite of significant experimental progress [5], the fractional statistics of anyons has not yet been conclusively confirmed due to the complexity of these systems [6].

To demonstrate characteristic anyonic features, we employ here a different strategy. We simulate the toric code model [7] in a quantum system without the continuous presence of interactions [8]. The toric code is a two-dimensional topological lattice model, where anyons are spatially well localized. Recently, several proposals showed how the toric code could possibly be implemented on extended lattices of qubits enabling one to employ anyonic states for, e.g. protected quantum computation [9]. While such a quantum computational scheme requires large systems, here we show that a number of anyonic properties can be demonstrated by considering four-partite entangled Greenberger–Horne–Zeilinger (GHZ) states [10]. These states are dynamically encoded in the polarization of photons, rather than produced via cooling [8]. This provides the additional advantage of being subject to negligible decoherence due to the weak coupling of photons to the environment. Polarized photons as qubits are a well understood and controllable quantum optical system that has already allowed observation of the four-qubit GHZ state [11]. Here we employ this system to simulate anyonic behavior.

2. Toric code model

2.1. Hamiltonian and ground state

The anyonic model under consideration is based on the toric code proposed by Kitaev [7] and is described in detail in tutorial introductions [12]. This system can be defined on a two-dimensional square lattice with interacting qubits placed at its vertices. To facilitate the description of the interactions, let us split the lattice into two alternating types of plaquettes labeled by p and s , as in figure 1. The defining Hamiltonian is

$$\mathcal{H} = - \sum_p \sigma_{p,1}^z \sigma_{p,2}^z \sigma_{p,3}^z \sigma_{p,4}^z - \sum_s \sigma_{s,1}^x \sigma_{s,2}^x \sigma_{s,3}^x \sigma_{s,4}^x, \quad (1)$$

where the summations run over the corresponding plaquettes and the indices $1, \dots, 4$ of the Pauli operators, σ^z and σ^x , enumerate the vertices of each plaquette in a counter-clockwise fashion. Each of the s - or p -plaquette interaction terms commute with the Hamiltonian as well as with each other. Thus, the model is exactly solvable and its ground state is explicitly

3

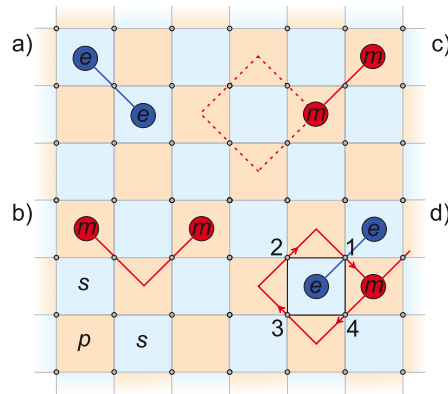
IOP Institute of Physics Φ DEUTSCHE PHYSIKALISCHE GESELLSCHAFT

Figure 1. The toric code lattice with qubits at the vertices of a square lattice with two types of plaquettes. Light blue and red plaquettes correspond to the s - and p -plaquettes, respectively. Qubit rotations enable manipulations of anyons on neighboring plaquettes. (a) Application of σ^z on a single qubit yields two e -type anyons placed at the neighboring s -plaquettes, where the string passes through the rotated qubits. Similarly, m anyons are created on p -plaquettes by σ^x rotations. (b) Two σ^x rotations create two pairs of m -type anyons. If one anyon from each pair is positioned on the same plaquette then they annihilate, thereby connecting their strings. (c) When a part of a string forms a loop around unpopulated plaquettes, the loop cancels (dashed). (d) Here we restrict to one s -plaquette and four neighboring p -plaquettes. Anyon e is produced by a σ^z on qubit 1 (blue), $|e\rangle = \sigma_1^z |\xi\rangle$. This system can support the circulation of an m around an e anyon.

given by [13]

$$|\xi\rangle = \prod_s \frac{1}{\sqrt{2}} (\mathbb{1} + \sigma_{s,1}^x \sigma_{s,2}^x \sigma_{s,3}^x \sigma_{s,4}^x) |00\dots 0\rangle, \quad (2)$$

with $\sigma^z|0\rangle = |0\rangle$. The state $|\xi\rangle$ represents the anyonic vacuum state and it is unique for systems with open boundary conditions.

2.2. Anyonic quasiparticles

Starting from this ground state one can excite pairs of anyons connected by a string on the lattice using single qubit operations. More specifically, by applying σ^z on some qubit of the lattice a pair of so-called e -type anyons is created on the two neighboring s -plaquettes (figure 1(a)) and the system is described by the state $|e\rangle = \sigma^z |\xi\rangle$. An m pair of anyons lives on the p -plaquettes and is obtained by a σ^x operation. The combination of both creates the composite quasiparticle ϵ with $|\epsilon\rangle = \sigma^z \sigma^x |\xi\rangle = i\sigma^y |\xi\rangle$. Two equal Pauli rotations applied on qubits of the same plaquette create two anyons on this plaquette. The fusion rules ($1 \times 1 = e \times e = m \times m = \epsilon \times \epsilon = 1$, $e \times m = \epsilon$, $1 \times e = e$, etc, where 1 is the vacuum state [12]) describe the outcome

from combining two anyons. In the above example, if two anyons are created on the same plaquette then they annihilate. This operation also glues two single strings of the same type together to form a new string, again with a pair of anyons at its ends (figure 1(b)). If the string forms a loop, the anyons at its end annihilate each other, thus removing the anyonic excitation. In the case that only a part of the string forms a loop, the string gets truncated (figure 1(c)). For non-compact finite systems, such as the one we consider here, a string may end up at the boundary describing a single anyon at its free endpoint.

2.3. Anyonic statistics

Anyonic statistics is revealed as a nontrivial phase factor acquired by the wavefunction of the lattice system after braiding anyons, i.e. after moving an m anyon around an e anyon (figure 1(d)) or vice versa. Consider the initial state $|\Psi_{\text{ini}}\rangle = \sigma_1^z |\xi\rangle = |e\rangle$. If an anyon of type m is assumed to be at a neighboring p -plaquette it can be moved around e along the path generated by successive applications of σ^x rotations on the four qubits of the s -plaquette. The final state is

$$|\Psi_{\text{fin}}\rangle = \sigma_1^x \sigma_2^x \sigma_3^x \sigma_4^x |\Psi_{\text{ini}}\rangle = -\sigma_1^z (\sigma_1^x \sigma_2^x \sigma_3^x \sigma_4^x |\xi\rangle) = -|\Psi_{\text{ini}}\rangle. \quad (3)$$

Such a minimal loop, which vanishes the moment it is closed, is analogous to the application of the respective interaction term $C_s = \sigma_{s,1}^x \sigma_{s,2}^x \sigma_{s,3}^x \sigma_{s,4}^x$ (or $C_p = \sigma_{p,1}^z \sigma_{p,2}^z \sigma_{p,3}^z \sigma_{p,4}^z$) of the Hamiltonian. This operator has eigenvalue $+1$ for all plaquettes of the ground state $|\xi\rangle$, whereas it signals an excitation, e.g. $|\Psi_{\text{ini}}\rangle$, with eigenvalue -1 , when applied to the plaquette where an anyon resides. However, equation (3) is much more general, as the actual path of the loop is irrelevant. It is the topological phase factor of -1 , which reveals the presence of the enclosed anyon. Alternatively, we can interpret (3) as a description of twisting ϵ , the combination of an e and an m -type anyon, by 2π . The phase factor of -1 thereby reveals its 4π -symmetry, characteristic for half spin, fermionic particles [14]. Note that the $e(m)$ anyons exhibit bosonic statistics with respect to themselves [7].

3. Experimental implementation

3.1. Minimal instance of the toric code model

As this two-dimensional system is well suited for demonstrating characteristic anyonic features, the question arises how big the lattice has to be. It turns out that four qubits of a single s -plaquette represent the minimal unit of the toric code model [15]. In this case, the four neighboring p -plaquettes are represented only by their corresponding links. Hence, while the presence of an e anyon is detected by the plaquette operator C_s , the presence of m anyons is detected by the eigenvalue of the four $C'_p = \sigma_{p,i}^z \sigma_{p,j}^z$ operators that correspond to the adjacent links of the p -plaquettes. Consequently, the product determining the ground state (equation (2)) reduces to only one factor for the single s -plaquette resulting in a four-qubit GHZ state, $|\xi\rangle = (|0000\rangle + |1111\rangle)/\sqrt{2}$. This is an eigenstate of the relevant C_s and C'_p operators with eigenvalue $+1$. An eigenvalue -1 for any of these operators denotes the presence of the corresponding anyon.

to the second-order interference at the PBS the polarization of two of the photons is rotated by a half-wave plate (HWP). Under the condition of detecting one photon in each spatial mode we observe the desired states.

As we are interested in the vacuum $|\xi\rangle = |\text{GHZ}^0\rangle$ and the anyonic state $|e\rangle = \sigma_i^z |\xi\rangle = |\text{GHZ}^\pi\rangle$, the successful simulation and demonstration of anyonic features relies on a careful distinction and characterization of these two orthogonal GHZ states. This comprises the confirmation of genuine four-partite entanglement and a method to reveal the phase ϕ . For this purpose, state analysis is performed by measuring the correlation, c_z , in the σ_i^z basis for each qubit and the correlation function $c_{xy}(\gamma) = \sigma_1(\gamma) \otimes \sigma_2(\gamma) \otimes \sigma_3(\gamma) \otimes \sigma_4(\gamma)$ with $\sigma_i(\gamma) = [(\cos\gamma)\sigma_i^y + (\sin\gamma)\sigma_i^x]$ [19]. This measurement is ideally suited to prove the coherent superposition of the terms $|\text{HHHH}\rangle$ and $|\text{VVVV}\rangle$ and to determine their relative phase ϕ . It is obtained from a measurement of all qubits along the same direction in the x - y -plane of the Bloch sphere. For a GHZ^ϕ state, its expectation value shows an oscillation, $\langle c_{xy}(\gamma) \rangle = \mathcal{V} \cos(4\gamma + \phi)$, with a period of one-quarter of 2π . This is a unique signature of four-qubit GHZ entanglement. The visibility of this oscillation \mathcal{V} is 1 for pure GHZ states. For a general state it equals twice the element $\rho_{\text{HHHH}, \text{VVVV}} = \text{Tr}(|\text{HHHH}\rangle\langle \text{VVVV}| \rho)$ of the corresponding density matrix ρ .

To analyze the performance of the set-up, first, the observation of the state $|\xi\rangle = |\text{GHZ}^0\rangle$ is confirmed. Figure 2(b) shows all possible measurement outcomes on the $\sigma_1^z \sigma_2^z \sigma_3^z \sigma_4^z$ basis, where the expected populations of $|\text{HHHH}\rangle$ and $|\text{VVVV}\rangle$ are clearly predominant with probabilities of $P_{\text{HHHH}} = (41.2 \pm 3.4)\%$ and $P_{\text{VVVV}} = (39.6 \pm 2.7)\%$, respectively, close to the expected $P_{\text{HHHH}} = P_{\text{VVVV}} = 50\%$. We find a correlation of $\langle c_z \rangle = 0.908 \pm 0.047$. The population of other terms is caused by noise arising from higher-order emissions of the down conversion and a remaining degree of distinguishability of photons at the PBS. The dependence of $\langle c_{xy}(\gamma) \rangle$ for the state $|\xi\rangle$ is displayed in figure 3(a) from which we infer a visibility \mathcal{V} of $(68.3 \pm 1.1)\%$. This value is obtained from a weighted least squares fit to a Fourier decomposition of $\langle c_{xy}(\gamma) \rangle$ considering only even components up to order 4: $\langle c_{xy}(\gamma) \rangle = \sum_{k=0}^2 a_k \cos(2k \cdot \gamma) + b_k \sin(2k \cdot \gamma)$. Only these components can originate from physical states. From the phase of the correlation function we deduce the phase of the GHZ^0 state to be $\phi = (0.02 \pm 0.01)\pi$, close to the expected value of 0.

The visibility \mathcal{V} together with the populations P_{HHHH} and P_{VVVV} allow further to determine the fidelity $F = \langle \text{GHZ} | \rho | \text{GHZ} \rangle = (\mathcal{V} + P_{\text{HHHH}} + P_{\text{VVVV}})/2$. We obtain a value of $(74.5 \pm 2.2)\%$ (for measurement data see also table 1). The fidelity is not only important for an estimation of state quality but also can be applied to verify genuine four-partite entanglement, an essential element in the presented toric code model. With a proper entanglement witness a fidelity greater than 50% is sufficient [20]. The experimentally observed fidelity is clearly above this bound, i.e. it is of high enough quality to allow for the demonstration of the anyonic properties.

3.3. Anyonic manipulations and detection of anyonic statistics

We start by analyzing the state change under the creation (and annihilation) of anyons, thereby demonstrating the characteristic fusion rules. Applying σ_1^z in mode 1 creates an e -type anyon on the s -plaquette resulting in a GHZ^π state, figure 3(b). This is clearly proven by the phase $\phi = 1.02\pi$ of the correlation function. A further application of σ_j^z on any other mode, say $j = 3$, changes the state of the plaquette according to $e \times e = 1$, and the anyon is moved away from the s -plaquette under investigation. These two σ^z rotations represent a string connecting two anyons, which traverses the particular plaquette without influencing its state, as confirmed by the

7

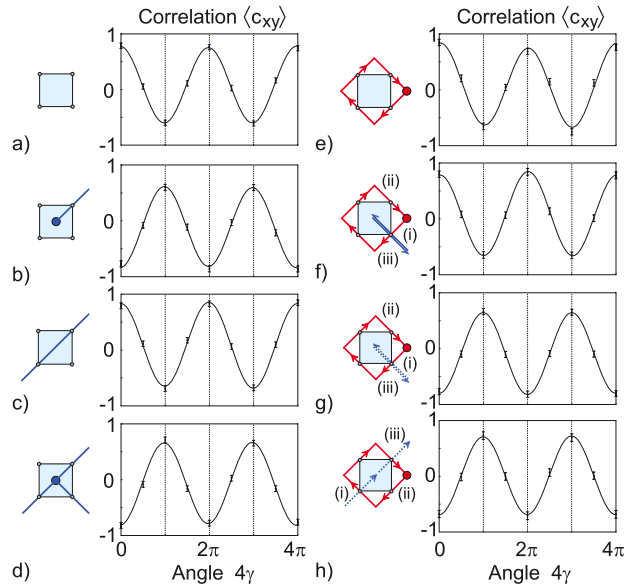
IOP Institute of Physics Φ DEUTSCHE PHYSIKALISCHE GESELLSCHAFT

Figure 3. Pictorial representations of various evolutions of anyons, together with the correlation function $\langle c_{xy} \rangle$. The phase of $\langle c_{xy} \rangle$ directly gives the phase ϕ of $|\text{GHZ}^\phi\rangle$. (a) The vacuum state, $|\xi\rangle$. (b) Generating an e -type anyonic state $|e\rangle = |\text{GHZ}^\pi\rangle$ by a σ^z operator. (c) A second σ^z removes the anyon from the plaquette and elongates the string resulting in the GHZ^0 state. (d) A third σ^z creates another pair of anyons, connected with the string already traversing the plaquette. (e) Moving an m anyon around an empty s -plaquette or (f) first creating an e anyon on the plaquette (i), performing the loop (ii), and removing the e anyon from the plaquette again (iii) give identical final states up to a global phase factor. (g) The global phase, π , is revealed by superimposing the two above evolutions, thereby clearly proving anyonic statistics. (h) An alternative path for the anyon e that gives the same fractional statistical phase, π .

observation of the initial GHZ^0 state ($\phi = 0.01\pi$, figure 3(c)). A further σ_j^z rotation on one of the remaining vertices, e.g. $j = 4$, creates an e occupation on the plaquette. Thus, the observation of GHZ^π ($\phi = 1.03\pi$, figure 3(d)) demonstrates the nontrivial version of the $1 \times e = e$ fusion rule. Alternatively, this can be seen as demonstrating the invariance of an anyonic state, when a string traverses the plaquette.

To detect the major feature of anyons, their nontrivial statistical phase acquired when moving one anyon around the other, we employed an interference measurement, which makes their *overall* phase factor visible (see (3) and figure 1(d)). Let us study the two evolutions separately. The first is to create a pair of two m anyons, move one of them around the empty s -plaquette and then annihilate them. This evolution is equivalent to having a string ending up at a p -plaquette with an m anyon at its endpoint and circulating that anyon around the s -plaquette.

Table 1. Experimental measurement data of the anyonic states.

	Phase ϕ	Fidelity F
Vacuum state		
$ \xi\rangle$	$(0.02 \pm 0.01) \cdot \pi$	$(74.5 \pm 2.2)\%$
Creation of a single e -type anyon		
$\sigma_1^z \xi\rangle$	$(1.02 \pm 0.01) \cdot \pi$	$(74.9 \pm 2.8)\%$
$\sigma_2^z \xi\rangle$	$(1.00 \pm 0.01) \cdot \pi$	$(74.2 \pm 2.7)\%$
$\sigma_3^z \xi\rangle$	$(1.01 \pm 0.01) \cdot \pi$	$(76.5 \pm 3.2)\%$
$\sigma_4^z \xi\rangle$	$(0.97 \pm 0.02) \cdot \pi$	$(76.2 \pm 3.7)\%$
String passing through the s -plaquette		
$\sigma_1^z \sigma_2^z \xi\rangle$	$(0.02 \pm 0.01) \cdot \pi$	$(77.4 \pm 2.8)\%$
$\sigma_1^z \sigma_3^z \xi\rangle$	$(0.01 \pm 0.01) \cdot \pi$	$(77.3 \pm 2.5)\%$
$\sigma_1^z \sigma_4^z \xi\rangle$	$(-0.01 \pm 0.01) \cdot \pi$	$(76.3 \pm 2.6)\%$
String passing through the s -plaquette populated with an anyon		
$\sigma_2^z \sigma_4^z e\rangle$	$(1.02 \pm 0.01) \cdot \pi$	$(75.2 \pm 2.4)\%$
$\sigma_3^z \sigma_4^z e\rangle$	$(1.03 \pm 0.01) \cdot \pi$	$(76.7 \pm 2.7)\%$
$\sigma_1^z \sigma_4^z e\rangle$	$(1.02 \pm 0.02) \cdot \pi$	$(74.5 \pm 3.1)\%$
Loop around an unpopulated s -plaquette		
$C_s \xi\rangle$	$(-0.02 \pm 0.02) \cdot \pi$	$(76.6 \pm 3.4)\%$
Loop around a populated s -plaquette followed by annihilation of the anyon		
$(\sigma_4^z C_s (\sigma_4^z) \xi\rangle)$	$(-0.01 \pm 0.01) \cdot \pi$	$(76.8 \pm 2.8)\%$
Interference procedure to reveal anyonic statistics		
$(\sigma_1^z)^{1/2} C_s (\sigma_1^z)^{-1/2} \xi\rangle$	$(1.03 \pm 0.01) \cdot \pi$	$(76.1 \pm 3.0)\%$
$(\sigma_2^z)^{1/2} C_s (\sigma_2^z)^{-1/2} \xi\rangle$	$(0.99 \pm 0.01) \cdot \pi$	$(73.5 \pm 3.6)\%$
$(\sigma_3^z)^{1/2} C_s (\sigma_3^z)^{-1/2} \xi\rangle$	$(1.01 \pm 0.01) \cdot \pi$	$(75.2 \pm 3.0)\%$
$(\sigma_4^z)^{1/2} C_s (\sigma_4^z)^{-1/2} \xi\rangle$	$(1.00 \pm 0.01) \cdot \pi$	$(75.8 \pm 2.5)\%$
$(\sigma_1^z)^{1/2} C_s (\sigma_1^z)^{-1/2} \xi\rangle$	$(1.00 \pm 0.01) \cdot \pi$	$(78.7 \pm 3.2)\%$

The obtained loop operator C_s , obviously, does not change the vacuum state and, thus, results in GHZ^0 ($\phi = -0.02\pi$, figure 3(e)). Alternatively, we (i) create an e anyon on the plaquette, (ii) encompass it with the loop of an m anyon and (iii) remove it again (figure 3(f)). The whole evolution is, in analogy to (3), described by $\sigma_4^z (\sigma_1^x \sigma_2^x \sigma_3^x \sigma_4^x) \sigma_4^z |\xi\rangle = -|\xi\rangle = -|\text{GHZ}^0\rangle$. The correlation function determines faithfully the angle $\phi = -0.01\pi$ (figure 3(f)), but is blind to the characteristic overall phase factor. This, finally, can be observed by (i) first generating the *superposition* $e^{-i\pi/4}(|\xi\rangle + i|e\rangle)/\sqrt{2}$ of having an anyon e on the plaquette or not by the unitary operation $(\sigma_i^z)^{-1/2}$; (ii) moving the m anyon around this superposition gives $e^{-i\pi/4}(|\xi\rangle - i|e\rangle)/\sqrt{2}$, the superposition of the above evolutions and (iii) the application of the inverse rotation $(\sigma_i^z)^{1/2}$ makes the phase difference visible resulting in $-i|e\rangle = -i|\text{GHZ}^\pi\rangle$. The observed value of $\phi = 1.00\pi$ (figure 3(g)) clearly proves the phase acquired by the braiding and therefore the anyonic statistics⁴. To reinforce the observation of the obtained fractional phase, we perform an additional interference experiment with an alternative path. Now, the

⁴ Note that during the braiding evolution no dynamical phases are generated as there is no Hamiltonian present and the Pauli rotations are performed with zero order wave plates, thus, adding insignificant erroneous phases.

superposition of an e anyonic state and the ground state is generated in the s -plaquette by rotating one qubit and it is removed by rotating another qubit, as seen in figure 3(h). If we move an m anyon around the plaquette in between the two steps, we observe *again* the characteristic phase shift of -1 .

4. Conclusions

Our results show that we can create, manipulate and detect the toric code states by encoding them in a simple physical system. In our quantum simulation, we demonstrated several of the fusion rules and we provided supporting evidence for the fractional statistics of the toric code anyons. Multiqubit toric code states are known to be useful for novel types of quantum error correction [21]. Extending our experimental results presented here to larger, scalable quantum systems [22, 23] will enable the application of the toric code for quantum information processing in the future [24].

Note added. With the completion of this work we became aware of a similar experimental implementation, closely resembling [8], that was simultaneously performed [25].

Acknowledgments

We would like to thank Phillipe Grangier, Peter Zoller and Robert Raussendorf for inspiring conversations. We acknowledge the support of this work by EPSRC, the Royal Society, the DFG-Cluster of Excellence MAP and the EU Projects QAP, EMALI and SCALA. WW acknowledges support by QCCC of the Elite Network of Bavaria and the Studienstiftung des dt. Volkes.

References

- [1] Wilczek F 1982 *Phys. Rev. Lett.* **48** 1144
- [2] Tsui D C, Stormer H L and Gossard A C 1982 *Phys. Rev. Lett.* **48** 1559
- [3] Witten E 1989 *Commun. Math. Phys.* **121** 351
- [4] Anderson P W 1987 *Science* **235** 1196
- [5] Camino F E, Zhou W and Goldman V J 2007 *Phys. Rev. Lett.* **98** 076805
- [6] Kim E-A 2006 *Phys. Rev. Lett.* **97** 216404
- [7] Kitaev A 2003 *Ann. Phys., NY* **303** 2
- [8] Han Y-J, Raussendorf R and Duan L-M 2007 *Phys. Rev. Lett.* **98** 150404
- [9] Jiang L *et al* 2008 *Nat. Phys.* **4** 482
- [10] Greenberger D M, Horne M A and Zeilinger A 1989 *Bell's Theorem, Quantum Theory and Conceptions of the Universe* ed M Kafatos (Dordrecht: Kluwer Academic) pp 73–6
- [11] Pan J W *et al* 2001 *Phys. Rev. Lett.* **86** 4435
- [12] Preskill J 2004 *Lecture Notes for Physics 219: Quantum Computation* <http://www.theory.caltech.edu/~preskill/>
- [13] Verstraete F *et al* 2006 *Phys. Rev. Lett.* **96** 220601
- [14] Rauch H *et al* 1975 *Phys. Lett. A* **54** 425
- [15] Pachos J K 2007 *Ann. Phys.* **322** 1254
- [16] Eibl M *et al* 2003 *Phys. Rev. Lett.* **90** 200403
- [17] Kwiat P G *et al* 1995 *Phys. Rev. Lett.* **75** 4337
- [18] Wieczorek W *et al* 2008 *Phys. Rev. Lett.* **101** 010503

10

IOP Institute of Physics Φ DEUTSCHE PHYSIKALISCHE GESELLSCHAFT

- [19] Sackett C A *et al* 2000 *Nature* **404** 256
- [20] Toth G and Gühne O 2005 *Phys. Rev. Lett.* **94** 060501
- [21] Kitaev A 1997 *Russ. Math. Surv.* **52** 1191
- [22] Raussendorf R, Bravyi S and Harrington J 2005 *Phys. Rev. A* **71** 062313
- [23] Micheli A, Brennen G K and Zoller P 2006 *Nat. Phys.* **2** 341
- [24] Freedman M H, Kitaev A, Larsen M J and Wang Z 2003 *Bull. Am. Math. Soc.* **40** 31
- [25] Lu C-Y *et al* 2009 *Phys. Rev. Lett.* **102** 030502

Chapter 5

Symmetric entangled Dicke states of up to six photons

Dicke states [77, 83] are an important group of states in quantum information. They have recently appeared in the context of SLOCC classifications [107, 109] in the form of the W ($|D_N^{(1)}\rangle$) states, whose entanglement was identified as highly persistent against photon loss [77, 107, 256]: a property that applies to other Dicke states as well. Such other important members are symmetric Dicke states of N qubits with $N/2$ excitations ($|D_N^{(N/2)}\rangle$) which have recently been the focus of experimental implementations [38, 39, 65] (see publ. P5.1). In particular, these states allow one to obtain SLOCC inequivalent states of a lower qubit number via projective measurements [55] (see publ. P5.2). This method makes them a resource for quantum information applications. In the following the implementation of a six-photon symmetric Dicke state with three excitations ($|D_6^{(3)}\rangle$) and Dicke states derived thereof are described.

To obtain a sufficiently high rate of multi-photon events a new SPDC photon source has been developed based on a femtosecond ultraviolet (UV) enhancement cavity [56] (see publ. P5.4). The cavity enhances the femtosecond UV pump pulses necessary for the SPDC process to achieve a sufficiently high six-photon count rate and is described in section 5.1. The photons generated in a type II collinear SPDC process are distributed by polarization-independent beam splitters (BSs) into six spatial modes. A simultaneous six-fold detection event in these modes signals in principle the observation of the state $|D_6^{(3)}\rangle$. In section 5.2 the detection of entanglement and properties of the state $|D_6^{(3)}\rangle$ are described focusing on qubit projections and qubit loss. This description reflects the results obtained in publ. P5.1, P5.2 and P5.3. General results for arbitrary Dicke states $|D_N^{(m)}\rangle$ are also given. It is shown that these properties are connected with applications of Dicke states in quantum information. Phase estimation in particular is described in section 5.3 as it plays an important role for precision measurements [19, 301]. Here, phase estimation relies on characteristic correlation functions of the state $|D_6^{(3)}\rangle$. This analysis goes beyond the mentioned publications.

5.1 High power SPDC photon source based on a femtosecond UV cavity

In the following the photon source and linear optical setup required for the observation of the six-photon entangled Dicke state $|D_6^{(3)}\rangle$ are described. The experimental setup follows one of the general schemes of SPDC experiments, namely the one of symmetric photon distribution [see section 3.1 and fig. 3.1(c)]. In addition, a UV enhancement cavity has been implemented to increase the power of the femtosecond UV pump pulses for the SPDC process. This was necessary to achieve reasonable six-photon count rates as the following estimation will show.

The count rate c_ψ of a desired N -partite photonic state $|\psi\rangle$ is proportional to the photon generation rate for N photons (for low pump powers given as $\tau^N f_r$ with $f_r = 80.8 \cdot 10^6 \text{ s}^{-1}$ the laser repetition rate, see eq. 2.58, eq. 2.56 and appendix A), the overall detection efficiency¹ for N photons (η_{det}^N) and the probability of observing the state in the linear optical setup (p_ψ):

$$c_\psi \sim \tau^N f_r \eta_{\text{det}}^N p_\psi. \quad (5.1)$$

The four-photon $|D_4^{(2)}\rangle$ experiment described in refs. [65, 104] has employed a typical laser system (see section 2.3) without enhancing the UV pump power by using additional means. Following values have been achieved: $\tau^2 = 0.034$, $\eta_{\text{det}} = 0.1$ and $p_{D_4^{(2)}} = 0.08$, yielding a four-photon count rate of $c_{D_4^{(2)}} \approx \tau^4 f_r \eta_{\text{det}}^4 p_{D_4^{(2)}} = 0.75 \text{ s}^{-1}$, which is in good agreement with the measured rate of 1 s^{-1} . To observe the six-photon Dicke state $|D_6^{(3)}\rangle$ with the same pump laser system a rate of $c_{D_6^{(3)}} = \tau^6 f_r \eta_{\text{det}}^6 p_{D_6^{(3)}} = 0.00005 \text{ s}^{-1}$ would be expected (with $p_{D_6^{(3)}} = 0.0154$, see below) corresponding to approximately 5 counts per day, which is much too low a count rate for acquiring sufficient statistical data. Increasing the pump power by a factor of 10 increases the six-photon rate by a factor of $10^3 = 1000$ (as $\tau^N \propto (P_{0,p})^{N/2}$ with $N = 6$, see section 2.3 eq. 2.58), which would result in 3 counts per minute yielding a sensible count rate for performing six-photon entanglement studies. This has motivated the design of a new SPDC photon source.

Theoretical considerations A suitable pump source for multi-photon SPDC experiments provides a high average pump power, which means in other words a high energy per pulse at high repetition rates (compare eq. 5.1). For enhancing the UV pump power different approaches are possible (for further approaches see [302]):

- (i) an external UV enhancement cavity operating with the same repetition rate as the laser source [74, 75, 303–305] (this has resulted in a maximal average UV power of about 7 W [56] and is described in the following),
- (ii) a frequency doubled, amplified Ti:Sa laser system working in the kHz regime [306] (average UV power of about 0.1 W) or

¹This includes the coupling efficiency η_c and the efficiency of the photon detectors η_d , thus $\eta_{\text{det}} = \eta_c \eta_d$.

- (iii) a frequency doubled, chirped-pulse Ti:Sa oscillator system with subsequent pulse compression with repetition rates up to 10 MHz [307] (average UV power of about 1 W).

Here, the implementation of an external cavity resonant for the UV around a BBO crystal is described. This has the advantage of keeping the repetition rate of the original pulses of the Ti:Sa laser compared to using, for example an amplified Ti:Sa laser system. Further, using the cavity the highest average pump power for the stated approaches has been achieved. An alternative approach to the aforementioned cases would be to increase the repetition rate of the pump source, which will not be discussed here.

Enhancement cavities are commonly utilized in the continuous wave regime, where they find many applications, for example to increase the conversion efficiency of second harmonic generation in non-linear crystals. For the ultrashort pulsed regime (< 200 fs) enhancement cavities have also been used for non-linear frequency conversion [303] and more recently have been applied for generating higher harmonics in a gas jet [74, 75, 304]. However, the implementation of an enhancement cavity for ultrashort pulses is more demanding. This can be illustrated by considering the frequency domain picture of a coherent train of ultrashort pulses (fig. 5.1), which is described by a frequency comb $\omega_n = n\omega_r + \omega_{ceo}$, where $\omega_r = 2\pi f_r$ is the repetition angular frequency and ω_{ceo} is the carrier envelope offset angular frequency. Both frequencies lie in the radio-frequency regime (~ 100 MHz), and thus for visible light, the mode number n is of order $10^5 \dots 10^7$.

The internal mode spectrum of the cavity has to match the external frequency comb of the laser pulses, i.e., the pulses have to be in phase after each cavity round trip to add up coherently. For continuous wave lasers this condition would be much simpler as only a single frequency mode has to match. If the following conditions are fulfilled phase coherent addition of pulses is guaranteed:

- (i) the inverse cavity round trip time c/L_{cav} corresponds to the repetition frequency f_r of the laser pulses,
- (ii) the offset frequency ω_{ceo} of the laser frequency comb is appropriately set to match the resonance frequencies of the cavity,
- (iii) the pulse shape inside the cavity is preserved, which means that dispersion² inside the cavity has to be minimized in order to obtain equidistant modes.

Conditions (i) and (ii) can be set during the experiment, for example, by changing the cavity length and the amount of dispersion inside the Ti:Sa oscillator, respectively. Condition (iii) can be realized by using, for example, chirped mirrors [309] to compensate for dispersion effects caused by media inside the cavity and the cavity mirrors.

The overall power enhancement $P_E(\omega)$ relating the intra-cavity power to the external power is given by [310, 311]

$$P_E(\omega) = \frac{|t_{IC}(\omega)|^2}{1 + |r(\omega)|^2 - 2|r(\omega)| \cos \phi(\omega)}, \quad (5.2)$$

²Dispersion results in the acquaintance of a frequency dependent phase.

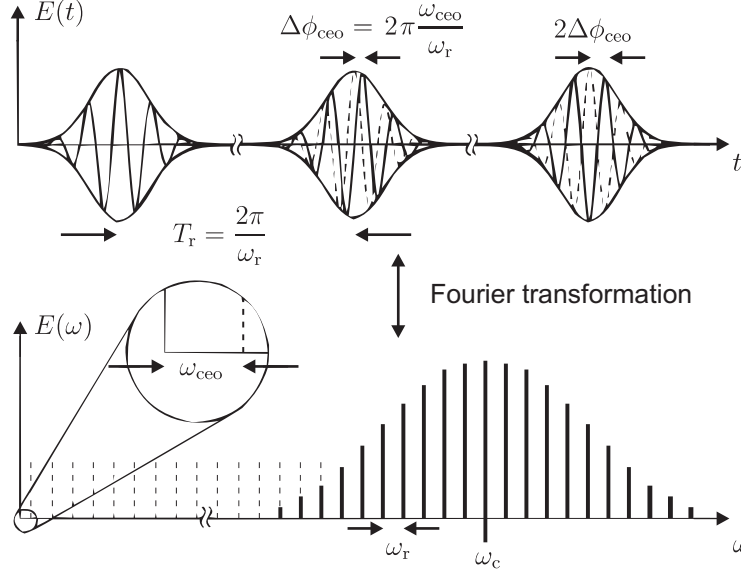


Figure 5.1: Schematic representation of the time and frequency domain picture of ultrashort pulses, associated by a Fourier transformation (adapted from [308]). A train of ultrashort pulses corresponds to a frequency comb. The pulse separation T_r and the carrier envelope offset phase $\Delta\phi_{\text{ceo}}$ in the time domain correspond in the frequency domain to the repetition angular frequency ω_r and the carrier envelope offset angular frequency ω_{ceo} . The angular frequency ω_c denotes the center of the frequency comb.

where $t_{\text{IC}}(\omega)$ denotes the frequency-dependent transmittance (for the field) of the input coupling mirror, $r(\omega) = r_{\text{IC}}(\omega)r_{\text{cavity}}(\omega)$ the overall reflectance of all optical components inside the cavity [given as $r_{\text{IC}}(\omega)$ of the input coupling mirror and $r_{\text{cavity}}(\omega)$ incorporates all other cavity mirrors and loss through air or a non-linear crystal] and $\phi(\omega)$ the frequency dependent round-trip phase. Assuming a certain intrinsic intra-cavity loss $[1 - |r_{\text{cavity}}(\omega)|^2]$ and neglecting absorption the so-called impedance matching condition $[T_{\text{IC,max}} = |t_{\text{IC}}(\omega)|^2 = 1 - |r_{\text{cavity}}(\omega)|^2]$ has to be fulfilled in order to achieve the maximal possible power enhancement $P_{\text{E,max}}(\omega) = 1/T_{\text{IC,max}}$ (for the cosine taking multiples of 2π) [311].

In general, the phase $\phi(\omega_n)$ can be written for the n th component of the frequency comb as a Taylor series around a fixed frequency ω_c as

$$\phi(\omega_n) = \phi(\omega_c) + \phi'(\omega_c)(\omega_n - \omega_c) + \Delta\phi(\omega_n), \quad (5.3)$$

where $\Delta\phi(\omega_n)$ includes group delay dispersion (GDD) and higher order dispersion effects. The terms $\phi(\omega_c)$ and $\phi'(\omega_c)(\omega_n - \omega_c)$ can be set experimentally by the cavity length and the offset frequency of the driving laser, and thus fulfill conditions (i) and (ii). Then, $\Delta\phi(\omega_n)$ determines the maximal achievable enhancement corresponding to condition (iii). Different contributions add to the phase $\phi(\omega_n)$, for example air, mirrors and a crystal inside the cavity: $\phi(\omega_n) = k_{\text{air}}(\omega_n)L_{\text{cav,air}} + \phi_{\text{mirror}}(\omega_n) + k_{\text{crystal}}(\omega_n)l_{\text{crystal}}$.

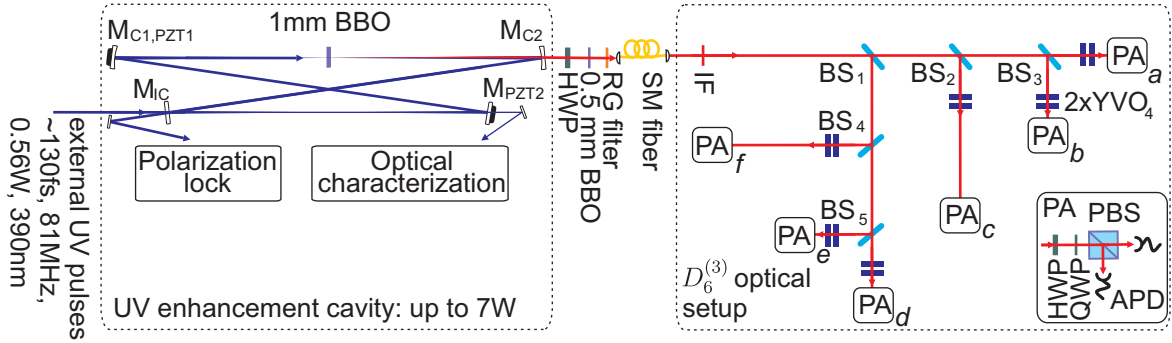


Figure 5.2: Schematic experimental setup of the UV enhancement cavity and the observation of the symmetric, six-photon entangled Dicke state $|D_6^{(3)}\rangle$. The cavity consists of four mirrors: the input coupler (M_{IC}), two curved mirrors [$M_{C1,PZT1}$ mounted on a piezoelectric transducer (PZT) and a dichroic mirror M_{C2}] and a mirror mounted on another PZT (M_{PZT2}). The reflected signal is spectrally dispersed (not shown) and directed to a polarization lock. The feedback signal is fed to PZT1 and PZT2. The optical characterization of the cavity consists of a spectrometer, a CCD camera and a photo diode. The generated SPDC photons are behind walk-off compensation (HWP and additional BBO crystal) coupled into a single mode fiber (SM) and guided to the linear optical setup for the observation of the state $|D_6^{(3)}\rangle$. The setup consists of five BSs (BS_{1-5}) distributing the photons equally into six spatial modes a, b, c, d, e , and f . Finally, polarization analysis (PA) is performed in each of the modes [bandpass filter (RG), interference filter of 3 nm FWHM (IF), YVO_4 -crystals for compensation of phase shifts introduced by BSs].

Experimental implementation The cavity has been implemented as a four mirror bow-tie ring cavity with a total length of $L_{cav} = c/f_r \approx 3.7$ m (fig. 5.2). Its input coupler has a transmission³ of $|t_{IC}(\omega)|^2 = 0.025$, which closely corresponds to the impedance-matching condition. The remaining three mirrors are highly reflective³ at 390 nm (> 0.9998), of which two mirrors are curved with a radius of curvature of -800 mm (concave). The curved mirrors have a separation of 0.98 m fulfilling the condition of a stable cavity [312] and create at their mid point a $100 \mu\text{m}$ waist, where the BBO crystal is placed. One curved mirror is dichroic: it transmits 780 nm light in order to be transparent for the generated SPDC photons.

Here, the GDD of air⁴ is $\sim 190 \text{ fs}^2$, of a 1 mm thick BBO crystal⁵ $\sim 190 \text{ fs}^2$ and of all mirrors³ in total $< 20 \text{ fs}^2$. The expected loss for air⁶ is 0.001 , for the BBO crystal⁷ 0.025 and for the three mirrors³ 0.0006 , yielding a total loss of 0.0266 , and thus a maximal power enhancement of $P_{E,max} = 1/0.0266 = 38$ neglecting dispersion. Considering dispersion⁸

³Specification of mirror manufacturer (Layertec).

⁴Calculated from the Sellmeier equation taken from [313, 314].

⁵Calculated from the Sellmeier equation taken from [315].

⁶Estimated from [316].

⁷Experimentally measured, including losses due to reflection.

⁸The mirror dispersion has been neglected. Including mirror dispersion changes the calculated power

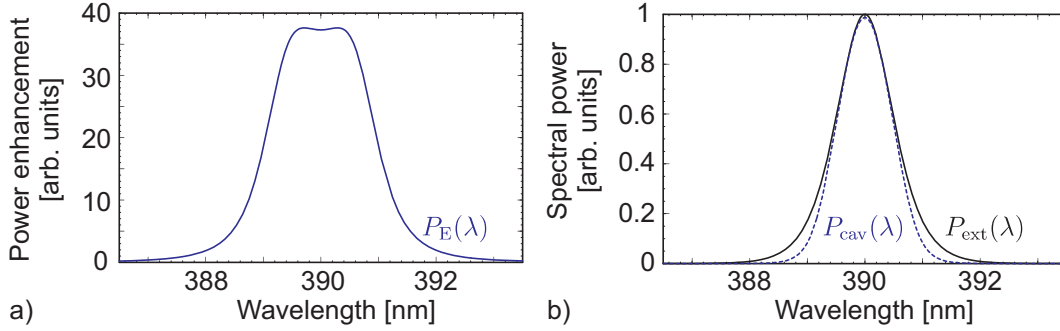


Figure 5.3: (a) Shown is the calculated power enhancement for the experimental parameters given in the text as a function of the wavelength. (b) The intra-cavity UV spectrum (dashed, blue) is slightly smaller than the external UV spectrum (solid, black) due to intra-cavity dispersion.

according to eq. 5.2 yields the spectrally resolved power enhancement shown in fig. 5.3(a) along with the external UV spectrum $P_{\text{ext}}(\lambda)$ and the calculated intra-cavity spectrum $P_{\text{cav}}(\lambda) = P_{\text{ext}}(\lambda) \cdot P_E(\lambda)$ [fig. 5.3(b)]. Then, a wavelength-averaged power enhancement of 33 is obtained.

Experimentally, a power enhancement of up to 13 has been reached giving a maximal intra-cavity power of 7 W [56]. The reduced value compared to the expected power enhancement can be attributed to spatial and spectral mode filtering of the cavity. Only a part of the original UV beam matches the cavity mode and can contribute to the intra-cavity field. For continuous operation of the cavity its length is actively stabilized by a polarization lock [317, 318]. The drift of ω_{ceo} of the Ti:Sa laser occurs on long time scales (hours). For achieving maximal intra-cavity power over this time scale, the prism insertion inside the Ti:Sa laser (changing ω_{ceo}) has been adjusted by a servo motor to equalize it with the offset frequency of the cavity.

The BBO crystal is placed at the intra-cavity focus and arranged in collinear type II configuration. The generated SPDC photons are emitted collinearly with the UV pump beam and coupled out of the cavity by the dichroic mirror into a single mode fiber. To observe the Dicke state $|D_6^{(3)}\rangle$ the photons are symmetrically distributed into six spatial modes (fig. 5.2). Under the condition of detecting a single photon of the third order SPDC emission in each spatial mode the state $|D_6^{(3)}\rangle$ is observed. This occurs with a probability 0.0126 (slightly lower than the expected value of $p_{D_6^{(3)}} = 5/324 \approx 0.0154$ due to asymmetries in the BS splitting ratios). Further, by conditioning the detection on two or four photons the states $|D_2^{(1)}\rangle$ or $|D_4^{(2)}\rangle$ can also be observed, respectively. For the following measurements a UV pump power of at most 5.3 W has been used in order to reduce the contribution of higher order SPDC noise (see appendix C). With this UV intra-cavity pump power we achieved a six-photon count rate of about 3.6 min^{-1} .

enhancement by less than 1%.

5.2 Entanglement detection, properties, and applications

In section 3.2 various methods to exclude full-separability and to detect genuine four-qubit entanglement for states of the family $|\Psi_4(\alpha)\rangle$ (eq. 3.3) have been examined. Here the focus is on the detection of genuine N -qubit entanglement of the state $|D_6^{(3)}\rangle$ and states derived thereof (see publ. P5.1 and P5.3). Further, properties of arbitrary Dicke states $|D_N^{(m)}\rangle$ are elucidated by considering the projection of photons or the loss of photons (see publ. P5.1 and P5.2). In particular, these properties are analyzed for the state $|D_6^{(3)}\rangle$ and are associated with possible applications, whereby telecloning and open destination teleportation will be described. The application of the state $|D_6^{(3)}\rangle$ for phase estimation based on correlation functions is discussed in section 5.3.

Entanglement detection To detect genuine N -qubit entanglement of the state $|D_6^{(3)}\rangle$ and the states derived thereof the methods of entanglement witnesses and Bell inequalities are used (for the implemented measurement settings see appendix B). Note, the recently developed density matrix element criterion [155] can also be constructed to detect six-qubit entanglement for $|D_6^{(3)}\rangle$ [319], but will not be applied here.

Entanglement witnesses In section 3.2 the projector-based witness has been applied (for its definition see section 2.2) to detect entanglement. For the Dicke states $|D_N^{(N/2)}\rangle$ and $|D_N^{(1)}\rangle$ general expressions for the projector-based witnesses have been found [41, 121, 135]:

$$\hat{\mathcal{W}} = \frac{N}{2(N-1)} \mathbb{1}^{\otimes N} - |D_N^{(N/2)}\rangle \langle D_N^{(N/2)}|, \text{ and} \quad (5.4)$$

$$\hat{\mathcal{W}} = \frac{N-1}{N} \mathbb{1}^{\otimes N} - |D_N^{(1)}\rangle \langle D_N^{(1)}|, \quad (5.5)$$

respectively. Hence, as the condition $F_{D_N^{(N/2)}}(\rho) > N/(2(N-1))$ (see section 3.2) has to hold in order to prove genuine N -qubit entanglement for $|D_N^{(N/2)}\rangle$, for the case $N = 6$ the fidelity of the experimental state has to be larger than 0.6. Experimentally a value of 0.654 ± 0.024 has been achieved, thus proving entanglement for the experimental realization of $|D_6^{(3)}\rangle$ (tab. 5.1). However, the determination of the fidelity would require 183 measurement settings. By exploiting the permutation symmetry of $|D_6^{(3)}\rangle$ 21 measurement settings are already sufficient, for details see refs. [38, 81] (publ. P5.1 and publ. P5.3).

From the projector-based witnesses $\hat{\mathcal{W}}$ one can derive other witnesses $\hat{\mathcal{W}}'$ that require less measurement setting [81] (publ. P5.3). The new witnesses $\hat{\mathcal{W}}'$ have to fulfill the condition $\hat{\mathcal{W}}' - \beta \hat{\mathcal{W}} \geq 0$ meaning that the expectation value for all bi-separable states remains positive. A useful ansatz for Dicke states is to design witnesses based on the

state $ \Psi\rangle$	fidelity $F_\Psi(\rho)$	minimal $F_\Psi(\rho)$ to prove N -qubit entanglement
$ D_6^{(3)}\rangle$	0.654 ± 0.024	0.6 [38]
$ D_4^{(1)}\rangle$	0.619 ± 0.043	0.75 [41]
$ D_4^{(2)}\rangle$	0.682 ± 0.022	$0.6\bar{6}$ [65, 121]
$(D_4^{(1)}\rangle + D_4^{(2)}\rangle)/\sqrt{2}$	0.528 ± 0.042	0.5 [138]

Table 5.1: Fidelity of the state $|D_6^{(3)}\rangle$ and the states derived thereof. The minimal fidelity to prove genuine N -qubit entanglement is also stated.

spin operators $\hat{J}_{N,l}$, of which Dicke states are eigenvectors:

$$\hat{\mathcal{W}}' = c_0 \mathbb{1}^{\otimes N} + \sum_{l=x,y,z} \sum_{n=1}^N c_{ln} (\hat{J}_{N,l})^n. \quad (5.6)$$

The definition of the spin operators $\hat{J}_{N,l}$ given in eq. 2.17 is used. The parameters c_0 and c_{ln} can be found by numerical optimization with respect to the aforementioned condition and, for example, maximal robustness against a particular form of noise on top of the expected state $|D_N^{(m)}\rangle$. The advantage of this type of witness is that it requires maximally only three measurement settings, namely all qubits measured along $\hat{\sigma}_x$, $\hat{\sigma}_y$ and $\hat{\sigma}_z$ and it can be used to estimate the fidelity [81] (publ. P5.3). For the state $|D_6^{(3)}\rangle$ particular witnesses are given in refs. [38, 81] (publ. P5.1 and P5.3), which have also been successfully used to detect entanglement of the experimentally observed states.

The simplest form of a witness operator for the states $|D_N^{(N/2)}\rangle$ (N even) and for $|D_N^{((N\pm 1)/2)}\rangle$ (N odd) is

$$\hat{\mathcal{W}}'' = \alpha_{\text{bi-sep},N} \mathbb{1}^{\otimes N} - \hat{O}_N \quad \text{with} \quad \hat{O}_N = (\hat{J}_{N,x})^2 + (\hat{J}_{N,y})^2, \quad (5.7)$$

where $\alpha_{\text{bi-sep},N}$ is the maximal value for N -qubit bi-separable states (see tab. 5.2). This witness requires only two measurement settings and has been applied in the experiments of refs. [38, 65].

Bell inequalities For the states $|D_N^{(N/2)}\rangle$ characteristic Bell inequalities (see section 3.2) have been found for the cases $N = 4$ and $N = 6$ [172, 255, 320]. They have the form

$$\hat{\mathcal{B}}_{D_N^{(N/2)}} = b_{D_N^{(N/2)}} (\hat{\sigma}_x \otimes \hat{M}_{N-1,xz} + \hat{\sigma}_y \otimes \hat{M}_{N-1,yz}), \quad (5.8)$$

with $\hat{M}_{N-1,ij}$ being $(N-1)$ -qubit Mermin operators [10]. For $N = 6$ one has

$$b_{D_N^{(N/2)}} = \frac{4}{5},$$

state $ \Psi\rangle$	$\alpha_\rho = \text{Tr}[\hat{O}_N \rho]$	minimal $\alpha_{\text{bi-sep},N}$ to prove N -qubit entanglement
$ D_6^{(3)}\rangle$	11.440 ± 0.148	11.0179 [38, 81]
$ D_5^{(3)}\rangle$	8.213 ± 0.143	7.87235 [38, 81]
$(D_5^{(2)}\rangle - D_5^{(3)}\rangle)/\sqrt{2}$	8.221 ± 0.188	”
ρ_5	8.219 ± 0.073	”
$ D_4^{(2)}\rangle$	5.696 ± 0.199	5.232 [65, 121]
ρ_4	5.423 ± 0.043	”

Table 5.2: Experimentally determined values for the operator \hat{O}_N . A value above $\alpha_{\text{bi-sep},N}$ is sufficient to prove genuine N -qubit entanglement for the state $|D_6^{(3)}\rangle$ and states derived thereof, see eq. 5.7. Note, for the state $|D_4^{(1)}\rangle$ a witness according to eq. 5.6 has been used: $\hat{\mathcal{W}}'_{D_4^{(1)}} = 5.5934 \cdot \mathbb{1}^{\otimes 4} - \hat{O}_4 + 1.47(\hat{J}_{4,z}^2 - 2\hat{J}_{4,z})$. The experimentally obtained value was $\langle \hat{\mathcal{W}}'_{D_4^{(1)}} \rangle = -0.624 \pm 0.170$. For details see refs. [38, 81, 121] (publ. P5.1 and P5.3).

$$\begin{aligned} \hat{M}_{5,ij} = & \frac{1}{16} \left(- \sum_l \mathcal{P}_l(\sigma_j \otimes \sigma_j \otimes \sigma_i \otimes \sigma_i \otimes \sigma_i) \right. \\ & \left. + \sum_l \mathcal{P}_l(\sigma_j \otimes \sigma_j \otimes \sigma_j \otimes \sigma_j \otimes \sigma_i) + \sigma_i^{\otimes 5} \right), \end{aligned} \quad (5.9)$$

and the maximal value $\langle \hat{\mathcal{B}}_{D_6^{(3)}} \rangle = 1$ is obtained for $|D_6^{(3)}\rangle$. In contrast, the maximal value for any LHV model is 0.4. For any SLOCC equivalent state to a six-qubit GHZ state the maximal value would be 0.85. Experimentally, a value of 0.43 ± 0.02 has been determined, which is sufficient to exclude an LHV model, but insufficient to exclude GHZ-type entanglement of the experimentally observed state.

Projective measurements and loss In section 3.3 entangled states have been characterized with respect to projective measurements and qubit loss. Here the same lines are followed as these properties are connected with particular applications of Dicke states.

Projective measurements In order to analyze the states obtained from projective measurements a Dicke state $|D_N^{(m)}\rangle$ is rewritten in the following way [77, 321]

$$|D_N^{(m)}\rangle = (C_N^m)^{-1/2} \left[(C_{N-1}^m)^{1/2} |H\rangle \otimes |D_{N-1}^{(m)}\rangle + (C_{N-1}^{m-1})^{1/2} |V\rangle \otimes |D_{N-1}^{(m-1)}\rangle \right] \quad (5.10)$$

with the binomial coefficient $C_N^m = \binom{N}{m}$ (for $m = 0$ and $N = m$ the coefficients are set to 0). In particular for $|D_N^{(N/2)}\rangle$ (N even) one obtains

$$|D_N^{(N/2)}\rangle = (|H\rangle \otimes |D_{N-1}^{(N/2)}\rangle + |V\rangle \otimes |D_{N-1}^{(N/2-1)}\rangle)/\sqrt{2}. \quad (5.11)$$

Hence, by projective measurements one can obtain superpositions of Dicke states [55] (for details of the following discussion see section IIb in publ. P5.2). Focusing on the state $|D_6^{(3)}\rangle = (|H\rangle \otimes |D_5^{(3)}\rangle + |V\rangle \otimes |D_5^{(2)}\rangle)/\sqrt{2}$ and a single projective measurement the SLOCC inequivalent states $|D_5^{(3)}\rangle$ (projection onto $|H\rangle$) and $(|D_5^{(2)}\rangle - |D_5^{(3)}\rangle)/\sqrt{2}$ (projection onto $|-\rangle$) can be obtained. By a subsequent projective measurement, for example, the genuinely four-qubit SLOCC inequivalent entangled states $|D_4^{(1)}\rangle$ (projection onto $|VV\rangle$), $|D_4^{(2)}\rangle$ (projection onto $|HV\rangle$) and $(|D_4^{(1)}\rangle + |D_4^{(3)}\rangle)/\sqrt{2}$ (projection onto $|LR\rangle$) can be realized. Surprisingly, the latter state, a superposition of two Dicke states, is LU equivalent to the four-qubit $|\text{GHZ}_4\rangle$ state. The result of a further projective measurement is outlined in detail in ref. [55] (see section IIb in publ. P5.2). Projective measurements have been performed to obtain the aforementioned states with the aim to prove genuine N -qubit entanglement and determine the achieved fidelity [38] (see tab. 5.1 and publ. P5.1). Note that projector-based witnesses are for the current experimental parameters not sufficient to prove N -qubit entanglement. For proving this, the witnesses in eq. 5.6 and eq. 5.7 can be applied (see tab. 5.2 and publ. P5.1).

It is likely that generally the states $|D_N^{(N/2)}\rangle$ for arbitrary even N are a rich resource of SLOCC inequivalent states of a lower qubit number, as has been demonstrated for $N = 4$ [65] and in this work for $N = 6$ [38, 55] (publ. P5.1 and P5.2). This opens up the opportunity of obtaining a state $|D_{N'}^{(m)}\rangle$ required for a particular application by projecting qubits of a suitable state $|D_N^{(N/2)}\rangle$ (with $N' < N$). This method is appealing as it requires no gate operations.

Photon loss A loss of k qubits of the state $|D_N^{(m)}\rangle$ results in the mixed state [77]

$$\rho_{N-k} = (C_N^m)^{-1} \sum_{j=0}^k C_k^j C_{N-k}^{m-j} \rho_{D_{N-k}^{(m-j)}}, \quad (5.12)$$

with $\rho_{D_{N-k}^{(m-j)}} = |D_{N-k}^{(m-j)}\rangle \langle D_{N-k}^{(m-j)}|$. The coefficients have to be set to zero for the cases $N < k$, $m < j$ and $N - k < m - j$. In comparison to states obtained after projection of qubits from $|D_N^{(m)}\rangle$, a loss of qubits results in mixtures of Dicke states with fixed coefficients. For example, losing $k = N - 2$ qubits of the state $|D_N^{(N/2)}\rangle$ (N even) results in the two-qubit mixed state

$$\rho_2 = \frac{N}{2(N-1)} \rho_{D_2^{(1)}} + \frac{N-2}{4(N-1)} (\rho_{D_2^{(0)}} + \rho_{D_2^{(2)}}). \quad (5.13)$$

The coefficient of $\rho_{D_2^{(1)}}$ turns out to be equal to the maximal singlet fraction (see section 2.2), which is closely related to a state's application for quantum telecloning as described below. Focusing on the state $|D_6^{(3)}\rangle$ one obtains after loss of photons the states

$$\rho_5 = (\rho_{D_5^{(2)}} + \rho_{D_5^{(3)}})/2,$$

$$\begin{aligned}
\rho_4 &= 3/5\rho_{D_4^{(2)}} + (\rho_{D_4^{(1)}} + \rho_{D_4^{(3)}})/5, \\
\rho_3 &= 9/20(\rho_{D_3^{(1)}} + \rho_{D_3^{(2)}}) + (\rho_{D_3^{(0)}} + \rho_{D_3^{(3)}})/20, \\
\rho_2 &= 3/5\rho_{D_2^{(1)}} + (\rho_{D_2^{(0)}} + \rho_{D_2^{(2)}})/5.
\end{aligned} \tag{5.14}$$

It is a remarkable property of $|D_6^{(3)}\rangle$ that all of these states are genuinely N -qubit entangled as can be proven by the witnesses of eq. 5.7, which is also found for experimentally observed states (tab. 5.2). Hence, loss of qubits from the states $|D_N^{(N/2)}\rangle$ results still in entangled states, a property that has also been found for the states $|D_N^{(1)}\rangle$ [76, 77, 107, 256] reflecting their high entanglement persistency against qubit loss. This is in sharp contrast to the GHZ states, which do not exhibit such entanglement persistency and result in a separable state upon loss of only a single qubit.

The communication protocol for telecloning [249] can be performed with $|D_6^{(3)}\rangle$ relying on the particular structure of the reduced two-qubit state of eq. 5.13. Telecloning, whereby a single state is teleported to N receivers [fig. 5.4(a)], can be seen as the generalization of teleportation ($N = 1$). N receivers and one sender share a genuinely $(N + 1)$ multi-partite entangled state. Similar to teleportation, the sender performs a Bell state measurement on one qubit of the shared resource state and the state to be teleported. The result is communicated to all receivers. In contrast to teleportation, the fidelity cannot be unity as the no-cloning theorem [322] forbids cloning with unit fidelity for $N > 1$. The maximal achievable fidelity of N symmetric output states with one input state is limited to $f_{\text{tele}} = (2N + 1)/(3N)$ [323]. It can be reformulated in terms of the maximal singlet fraction as $f_{\text{tele}} = (2\text{MSF}(\rho) + 1)/3$ (see eq. 2.33) [160]. Hence, a high value of $\text{MSF}(\rho)$ results in a high value of the telecloning fidelity.

The states $|D_{N+1}^{((N+1)/2)}\rangle$ [with $(N + 1)$ even] have a maximal singlet fraction of $\text{MSF}(D_{N+1}^{((N+1)/2)}) = (N + 1)/(2N)$ (see eq. 5.13 and [39]), resulting in the maximal possible cloning fidelity. The state $|D_6^{(3)}\rangle$ allows to perform $1 \rightarrow 5$ telecloning. For the experimentally observed state a $\text{MSF}(\rho) = 0.57 \pm 0.01$ averaged over all possible loss channels has been determined, which is close to the expected 0.6. This would yield a telecloning fidelity of $f_{\text{tele,expt}} = 0.71 \pm 0.01$ (compared to the theoretical value of $0.7\bar{3}$) when using the experimental state as telecloning channel still yielding a value above the classical threshold of $2/3$ [17].

However, in a closer examination for the resource states $|D_{N+1}^{((N+1)/2)}\rangle$ telecloning depends on the input state [65]. This is due to the fact that the two-qubit mixed state of eq. 5.13 is composed of a Bell state and a non-white noise fraction. Only the admixture of white noise would allow state-independent cloning. This can be circumvented when restricting the set of possible input states to the $x - y$ plane of the Bloch sphere, namely to $|\psi(\phi)\rangle_{\text{in}} = (|H\rangle + e^{i\phi}|V\rangle)/\sqrt{2}$ [fig. 5.4(b)]. This type of cloning is called phase-covariant. Theoretically, the maximal phase-covariant cloning fidelity is $f_{\text{tele,phase}} = [1 + (N + 1)/(2N)]/2$ [324, 325], which is higher than

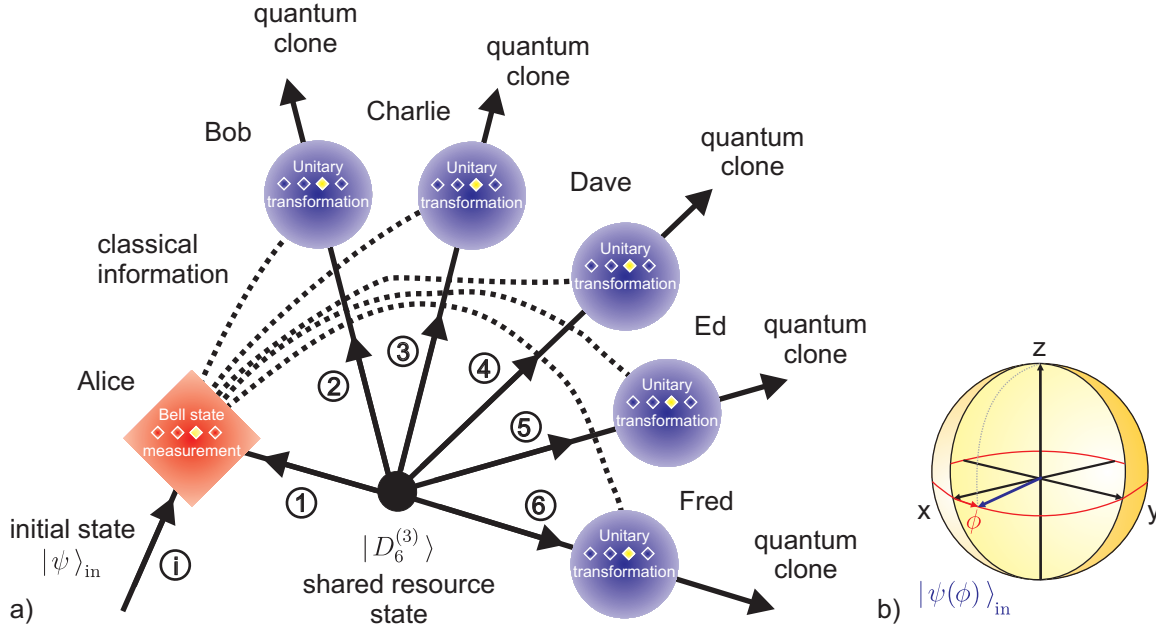


Figure 5.4: (a) Schematic representation of telecloning using the state $|D_6^{(3)}\rangle$ as resource. The sender (Alice) receives one photon of $|D_6^{(3)}\rangle$ and performs a Bell state measurement with the initial state $|\psi\rangle_{\text{in}}$. She communicates the result to the five receivers (Bob, Charlie, Dave, Ed, Fred), who perform a unitary transformation on their respective photons of $|D_6^{(3)}\rangle$ to retrieve an optimal phase-covariantly or averaged cloned state. (b) For phase-covariant telecloning the input state $|\psi(\phi)\rangle_{\text{in}}$ is restricted to the $x - y$ plane of the Bloch sphere.

f_{tele} . The states $|D_4^{(2)}\rangle$ and $|D_6^{(3)}\rangle$ reach this maximal value.

A perfect teleportation channel (i.e. the Bell state $|\psi^+\rangle = |D_2^{(1)}\rangle$) for a single receiver and the sender can be obtained if the remaining $(N - 1)$ receivers agree to project the state $|D_{N+1}^{((N+1)/2)}\rangle$ onto $(N - 1)/2$ times $|H\rangle$ and $(N - 1)/2$ times $|V\rangle$. Then, the state $|D_2^{(1)}\rangle$ is obtained with a probability of $\text{MSF}(D_{N+1}^{((N+1)/2)}) = (N + 1)/(2N)$ and can be used as a resource for perfect teleportation. As any of the receivers can be the chosen one, the application is called open destination teleportation [188]. The choice can even be made after the Bell state measurement for state teleportation has been performed.

5.3 Phase estimation

Phase estimation is a topic of quantum metrology [19]. One major goal is to beat the shot noise limit (SNL) limiting the precise determination of a phase in an interferometer to $1/\sqrt{N}$ with N as the utilized number of photons in the measurement [19]. An improvement in phase precision would be of additional benefit for, e.g., the sensitivity of gravitational

wave detectors [326]. To this end, optimized measurement strategies can be devised as well as particular correlated states turn out to be more powerful than uncorrelated, classical resources such as coherent light. Here, the applicability of the states $|D_{2N}^{(N)}\rangle$ (the notation is now changed to $|D_{2N}^{(N)}\rangle$ instead of writing $|D_N^{(N/2)}\rangle$ with N even) for phase estimation is discussed. To this end, correlation functions along great circles on the Bloch sphere are characterized as these turn out to be connected with phase estimation. Finally, the phase sensitivity is estimated for the experimentally observed state $|D_6^{(3)}\rangle$. This goes beyond the author's publications of this chapter.

Correlation function Correlation functions along arbitrary directions on the Bloch sphere reveal characteristic properties of the states $|D_{2N}^{(N)}\rangle$. To this end, the $2N$ -qubit correlation functions defined as

$$\hat{c}_{ij}(\gamma)^{\otimes 2N} = [(\cos \gamma)\hat{\sigma}_i + (\sin \gamma)\hat{\sigma}_j]^{\otimes 2N}, \quad (5.15)$$

with i, j taking all distinct permutations of x, y, z are considered (see also eq. 4.11 of section 4.3). They correspond to a simultaneous measurement of each qubit along the $i - j$ great circle of the Bloch sphere. One obtains for the states $|D_{2N}^{(N)}\rangle$ [85, 321]

$$\langle \hat{c}_{xz}(\gamma)^{\otimes 2N} \rangle_{D_{2N}^{(N)}} = \langle \hat{c}_{yz}(\gamma)^{\otimes 2N} \rangle_{D_{2N}^{(N)}} = \sum_{k=0}^N (-1)^k (C_N^k)^2 (\cos \gamma)^{2N-2k} (\sin \gamma)^{2k}, \quad (5.16)$$

$$\langle \hat{c}_{xy}(\gamma)^{\otimes 2N} \rangle_{D_{2N}^{(N)}} = 1. \quad (5.17)$$

The former result is simply the Legendre polynomial $P_N(\cos 2\gamma)$.

It turns out that the correlation functions along the $x - z$ and $y - z$ planes are useful for phase estimation, which is discussed below. The constant value of unity obtained for the plane $x - y$ indicates the applicability of the states $|D_{2N}^{(N)}\rangle$ for secret-sharing [38, 39, 118]. Secret sharing is a task where a message is split to several subsystems (receivers) and all subsystems have to cooperate to retrieve this common message, for details see ref. [118].

In general, the correlation function along any direction on the Bloch sphere is given as

$$\langle (\sin \theta \cos \phi \hat{\sigma}_x + \sin \theta \sin \phi \hat{\sigma}_y + \cos \theta \hat{\sigma}_z)^{\otimes 2N} \rangle_{D_{2N}^{(N)}} = -1^N P_N(\cos 2\theta), \quad (5.18)$$

where $\theta \in [0, \pi]$ is the polar angle with the z axis and $\phi \in [0, 2\pi)$ is the azimuthal angle in the $x - y$ plane. Thus, the value of the general correlation function is independent of ϕ . Note, here the usual spherical coordinates with angles θ, ϕ are used. Thus, a direct comparison with the definition of the correlation function of eq. 5.16 is possible if the replacement $i \leftrightarrow j$ for $\theta \leftrightarrow \gamma$ is done. Now, the notation is again switched back to the angle γ .

For $N = 3$ corresponding to the state $|D_6^{(3)}\rangle$ the general correlation function on the Bloch sphere is displayed in fig. 5.5(a). One obtains from eq. 5.16 (see fig. 5.6)

$$\langle \hat{c}_{xz}(\gamma)^{\otimes 6} \rangle_{D_6^{(3)}} = P_3(\cos 2\gamma) = \frac{1}{8}(3 \cos 2\gamma + 5 \cos 6\gamma), \quad (5.19)$$

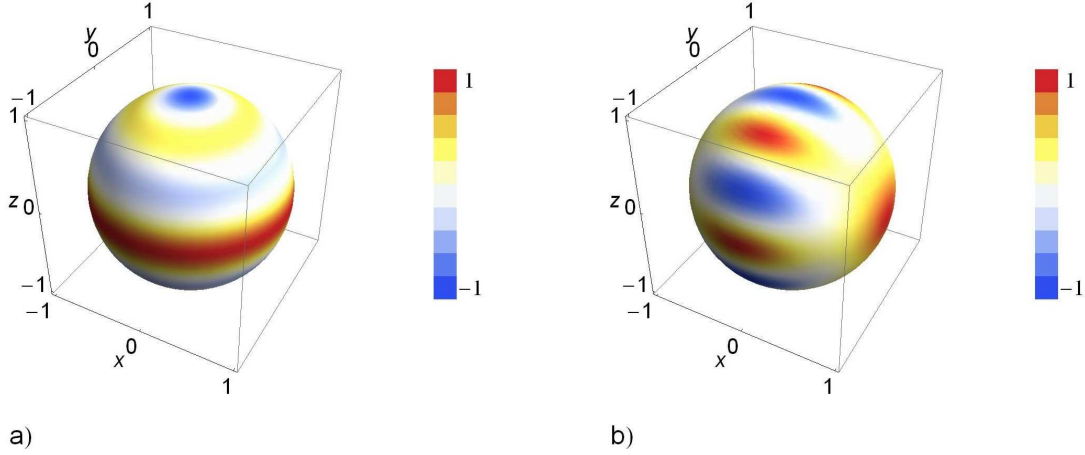


Figure 5.5: Correlation function $\langle (\sin \theta \cos \phi \hat{\sigma}_x + \sin \theta \sin \phi \hat{\sigma}_y + \cos \theta \hat{\sigma}_z)^{\otimes 6} \rangle$ for the states (a) $|D_6^{(3)}\rangle$ and (b) $|\text{GHZ}_6\rangle^+$. While for the state $|D_6^{(3)}\rangle$ the correlation function exhibits the same dependence on θ for any great circle parallel to the $\hat{\sigma}_z$ axis, this symmetry is not found for the state $|\text{GHZ}_6\rangle^+$. However, the $|\text{GHZ}_6\rangle^+$ state shows a $\cos 6\theta$ dependence with unit visibility along the $y-z$ plane of the Bloch sphere, whereas $|D_6^{(3)}\rangle$ has a reduced visibility of $5/8$.

which is according to eq. 5.18 found for any longitude, i.e. for any great circle parallel to the z axis. The term proportional to $\cos 6\gamma$ is known to be characteristic for the state $|\text{GHZ}_6\rangle$ [299] (see fig. 5.6 and eq. 5.26 below). For $|D_6^{(3)}\rangle$ the oscillation with 6γ has a reduced visibility of $5/8$. In general, correlation functions along great circles parallel to the z axis of $|D_{2N}^{(N)}\rangle$ possess this $2N$ -fold periodicity. This can be seen by examining the states $|D_{2N}^{(N)}\rangle$ in, for example, the \pm -basis [85]:

$$\hat{T}_{xz}^{\otimes 2N} |D_{2N}^{(N)}\rangle = \sum_{k=0}^N (-1)^{N-k} \sqrt{C_{2k}^k C_{2N-2k}^{N-k}} \left(\frac{1}{2}\right)^{2N} |D_{2N}^{(2k)}\rangle, \quad (5.20)$$

with $\hat{T}_{xz} = (\hat{\sigma}_x + \hat{\sigma}_z)/\sqrt{2}$. The sum contains the superposition

$$(|D_{2N}^{(0)}\rangle + |D_{2N}^{(2N)}\rangle)/\sqrt{2} \equiv |\text{GHZ}_{2N}\rangle, \quad (5.21)$$

i.e., the $2N$ -qubit GHZ state with a probability of $C_{2N}^N/2^{2N}$. For example, for $N = 3$ it occurs with a probability of $5/8$ corresponding exactly to the prefactor of $\cos 6\gamma$. Generally, the GHZ fraction decreases with increasing N and yields the $2N$ -fold periodicity.

Experimentally, the correlation functions $\langle \hat{c}_{xz}(\gamma)^{\otimes 6} \rangle$ and $\langle \hat{c}_{yz}(\gamma)^{\otimes 6} \rangle$ have been measured and are depicted in fig. 5.6(a) and (b) (for the implemented measurement settings see appendix B). The expected oscillation is observed with a reduced visibility. This can be attributed mainly to the influence of higher order SPDC emissions (as described in appendix C.3). A fit considering this noise can account for the reduced visibility (see

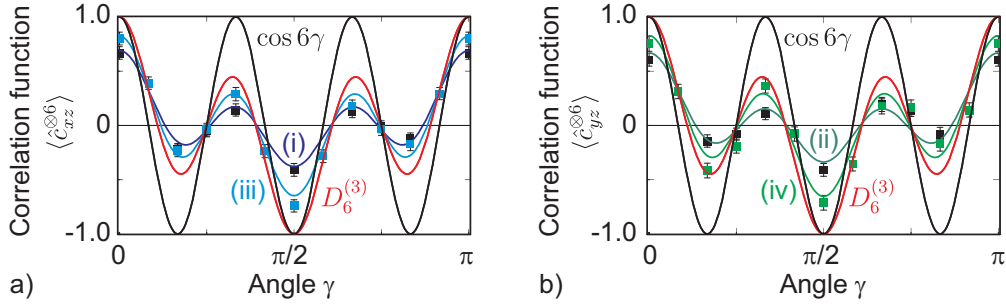


Figure 5.6: Experimentally determined correlation functions for (a) $\langle \hat{c}_{xz}(\gamma)^{\otimes 6} \rangle$ and (b) $\langle \hat{c}_{yz}(\gamma)^{\otimes 6} \rangle$ (eq. 5.15). For comparison, as red curve the expected correlation function for the ideal state $|D_6^{(3)}\rangle$ and as black curve the function $\cos 6\gamma$ are shown. The colored curves are functions fitted to the data points assuming a mixture of the ideal state with higher order SPDC noise, for details see appendix C.3. Two sets of measurements have been performed: (i) (black dots, blue curve), (ii) (black dots, green curve) are data points which have been recorded with a UV pump power of 5.3 W as has been done for all data in this chapter so far. The other data set (iii) (light blue dots, light blue curve), (iv) (light green dots, light green curve) has been recorded with a decreased UV pump power of 2 – 2.3 W. It is clearly visible that the negative influence of higher order emissions is smaller for the latter measurements.

fig. 5.6). Two sets of measurements have been performed. One data set has been recorded with a pump power of 5.3 W, and another one with a pump power of 2–2.3 W. The increase in visibility for the latter data set is clearly seen in fig. 5.6 and can be attributed to lower noise contribution of higher order emissions.

Phase estimation Different proposals for phase estimation in a Mach-Zehnder interferometer have been put forward to beat the SNL and reach the ultimate Heisenberg limit of $1/N$ in precision spectroscopy: phase squeezed coherent states of light at both input ports of a standard Mach-Zehnder interferometer [326, 327], Fock states with an equal number of photons at both inputs (so-called twin-Fock state) [84, 85], correlated fermion beams at both inputs [328], and a general treatment of fermions and bosons entering the interferometer [329, 330]. Other studies focused onto particular states useful for interferometry in general: spin squeezed atomic states [331], so-called NooN states [237], and robust states against noise [332, 333].

Generally, a phase γ is determined from the measurement of an observable \hat{O} . Then, the standard deviation $\Delta\gamma$ on γ can be calculated via error propagation [328]

$$\Delta\gamma = \frac{\Delta O}{\left| \frac{\partial \langle \hat{O} \rangle}{\partial \gamma} \right|}, \quad (5.22)$$

with the variance $(\Delta O)^2 = \langle \hat{O}^2 \rangle - \langle \hat{O} \rangle^2$. One can define the improved sensitivity \mathcal{S} com-

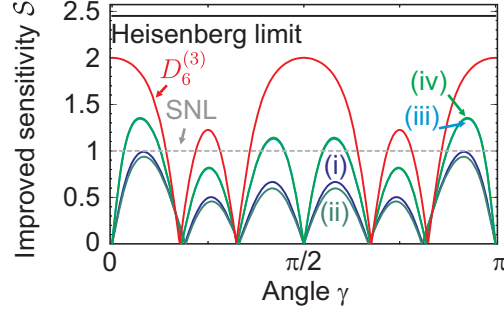


Figure 5.7: Improved phase sensitivity using the state $|D_6^{(3)}\rangle$. The black line marks the Heisenberg limit, the dashed gray line the SNL and the red curve is the expected improved sensitivity \mathcal{S} when using $|D_6^{(3)}\rangle$, see eq. 5.28. The blue and green curves are sensitivity curves from experimental, fitted data (compare fig. 5.6). The set of measurements (i) and (ii) do not surpass the SNL limit. However, the light blue and green curves for the set of measurements (iii) and (iv) surpass this limit. This has been achieved by decreasing noise from higher order SPDC emissions.

pared to the shot noise limit $\text{SNL} = 1/\sqrt{N}$ as [334]

$$\mathcal{S}^2 = (\text{SNL}/\Delta\gamma)^2. \quad (5.23)$$

Here, the observable \hat{O} is given by the $2N$ -qubit correlation function $\hat{c}_{ij}(\gamma)^{\otimes 2N}$ as defined in eq. 5.15. One obtains for the variance with $N = 1$

$$(\Delta c_{ij}(\gamma))^2 = \langle \hat{c}_{ij}(\gamma)^2 \rangle - \langle \hat{c}_{ij}(\gamma) \rangle^2 = 1 - \langle \hat{c}_{ij}(\gamma) \rangle^2, \quad (5.24)$$

as $\hat{c}_{ij}(\gamma)^2 = [((\cos \gamma)^2 + (\sin \gamma)^2)\mathbf{1} + \cos \gamma \sin \gamma (i\hat{\sigma}_k - i\hat{\sigma}_k)] = \mathbf{1}$. The same holds for arbitrary N . Hence, the improved sensitivity for $2N$ particles is given as

$$\mathcal{S}^2 = \frac{1}{2N} \frac{1}{1 - \langle \hat{c}_{ij}(\gamma)^{\otimes 2N} \rangle^2} \left| \frac{\partial \langle \hat{c}_{ij}(\gamma)^{\otimes 2N} \rangle}{\partial \gamma} \right|^2. \quad (5.25)$$

It is known that the Heisenberg limit can be reached using GHZ states [237], which with respect to interferometry applications are also often called NooN states. NooN states are a superposition of N photons occupying one mode and another one, whereby the mode could be given in the polarization or spatial degree of freedom [335]. For an illustration, the phase shift between $|\pm\rangle$ polarization is considered. The correlation function of a $2N$ -qubit GHZ state

$$|\text{GHZ}_{2N}\rangle^\pm = (|+\rangle^{\otimes 2N} \pm |-\rangle^{\otimes 2N})/\sqrt{2} \quad (5.26)$$

along the $y - z$ plane is $\langle \hat{c}_{yz}(\gamma)^{\otimes 2N} \rangle_{\text{GHZ}_{2N}^\pm} = \mp \cos(2N\gamma)$. For the standard deviation one obtains $\Delta\gamma = \sin 2N\gamma / (2N \sin 2N\gamma) = 1/(2N)$. Thus, the improved sensitivity evaluates to $\mathcal{S} = 1/\sqrt{2N} \cdot 2N = \sqrt{2N}$ and yields a $\sqrt{2N}$ fold improvement for a GHZ state corresponding exactly to the Heisenberg limit. However, phase estimation along other basis

directions, for example $\langle \hat{c}_{xz}(\gamma)^{\otimes 2N} \rangle$ and $\langle \hat{c}_{xy}(\gamma)^{\otimes 2N} \rangle$, does not reach the Heisenberg limit, see fig. 5.5(b).

For the calculation of the improved sensitivity \mathcal{S} for the states $|D_{2N}^{(N)}\rangle$ the derivative

$$\frac{\partial \langle \hat{c}_{ij}(\gamma)^{\otimes 2N} \rangle_{D_{2N}^{(N)}}}{\partial \gamma} = \sum_{k=0}^N \frac{4k - 2N + 2N \cos 2\gamma}{\sin 2\gamma} (-1)^k \cdot (C_N^k)^2 (\cos \gamma)^{2N-2k} (\sin \gamma)^{2k} \quad (5.27)$$

is required. For the case $N = 3$ one obtains an improved sensitivity for phase estimation along any great circle parallel to the z axis of the Bloch sphere of

$$(\mathcal{S}_{D_6^{(3)}})^2 = \frac{12(3 + 5 \cos 4\gamma)^2}{87 + 80 \cos 4\gamma + 25 \cos 8\gamma}. \quad (5.28)$$

This function is depicted in fig. 5.7. For particular values of γ the SNL can be beaten, but the Heisenberg limit is not reached. Using the fit of the experimental values (see fig. 5.6), the expected phase sensitivity can be calculated. However, this value is even lower than the SNL for the first set of measurements (i) and (ii). This can be attributed to higher order SPDC noise (see appendix C), which can be reduced by decreasing the UV pump power on the cost of a lower six-photon count rate. The result is displayed in fig. 5.7 as the set (iii) and (iv) of measurements, which clearly surpass the SNL.

Finally, it is worth recalling that the states $|D_{2N}^{(N)}\rangle$ have been obtained from a symmetric distribution of N horizontally and N vertically polarized photons initially in a single spatial mode m , i.e., of the state $|N_H, N_V\rangle_m$ from the N th order collinear type II SPDC emission. This state is equal to the twin-Fock state $|N, N\rangle_{a,b}$, which can be used as input state of modes a and b of a Mach-Zehnder interferometer. Its usefulness for phase estimation has been discussed in refs. [84, 85], where the derivation of eq. 5.16 and eq. 5.20 can be found.

To conclude, symmetric Dicke states of N qubits with $N/2$ excitations are straightforward to observe using collinear type II SPDC and subsequent symmetric photon distribution. The entanglement of these states has a high robustness against qubit loss and is an ideal resource for obtaining other interesting quantum states. Further, many applications can be performed with symmetric Dicke states making them an ideal object for future experimental investigations.

5.4 Publications

P5.1

PRL 103, 020504 (2009)

PHYSICAL REVIEW LETTERS

week ending
10 JULY 2009**Experimental Entanglement of a Six-Photon Symmetric Dicke State**Witlef Wieczorek,^{1,2,*} Roland Krischek,^{1,2} Nikolai Kiesel,^{1,2} Patrick Michelberger,^{1,2}
Géza Tóth,^{3,4} and Harald Weinfurter^{1,2}¹Max-Planck-Institut für Quantenoptik, Hans-Kopfermann-Strasse 1, D-85748 Garching, Germany²Department für Physik, Ludwig-Maximilians-Universität, D-80797 München, Germany³IKERBASQUE and Department of Theoretical Physics, The University of the Basque Country,
Post Office Box 644, E-48080 Bilbao, Spain⁴Research Institute for Solid State Physics and Optics, Hungarian Academy of Sciences,
Post Office Box 49, H-1525 Budapest, Hungary

(Received 12 March 2009; published 10 July 2009)

We report on the experimental observation and characterization of a six-photon entangled Dicke state. We obtain a fidelity as high as 0.654 ± 0.024 and prove genuine six-photon entanglement by, amongst others, a two-setting witness yielding -0.422 ± 0.148 . This state has remarkable properties; e.g., it allows obtaining inequivalent entangled states of a lower qubit number via projective measurements, and it possesses a high entanglement persistency against qubit loss. We characterize the properties of the six-photon Dicke state experimentally by detecting and analyzing the entanglement of a variety of multipartite entangled states.

DOI: 10.1103/PhysRevLett.103.020504

PACS numbers: 03.67.Bg, 03.65.Ud, 03.67.Mn, 42.50.Ex

Multipartite entangled states have been intensively studied during recent years. Still, the experimental realization of entangled states of more than four particles imposes a considerable challenge, and only a few experiments have yet demonstrated such states [1,2]. So far, many experiments have focused on the observation of graph states [3] like the Greenberger-Horne-Zeilinger (GHZ) states or the cluster states [1], which are, e.g., useful for one-way quantum computation [4]. Dicke states form another important group of states, which were first investigated with respect to light emission from a cloud of atoms [5] and have now come into the focus of both experimental realizations [2,6–8] and theoretical studies [9–12]. W states [13], a subgroup of the Dicke states, first received attention triggered by the seminal work on three-qubit classification based on stochastic local operations and classical communication (SLOCC) by Dür, Vidal, and Cirac [13]. Recently it turned out that other symmetric Dicke states also offer important features. Particularly, by applying projective measurements on a few of their qubits, states of different SLOCC entanglement classes are obtained [8,12]. These Dicke states can act as a rich resource of multipartite entanglement as required for quantum information applications.

In our Letter we experimentally implement and analyze a symmetric six-qubit entangled Dicke state. The entanglement of the Dicke state results from symmetrization and cannot be achieved in a simple way by pairwise interaction, in contrast to, e.g., GHZ states. In order to efficiently characterize the experimentally observed state, we developed optimized methods to determine the fidelity, detect entanglement, and characterize further properties. In particular, we analyze representatives from the variety of

multipartite entangled states obtained after projection or loss of qubits.

Generally, Dicke states are simultaneous eigenstates of the total angular momentum, $J_N^2 = J_{N,x}^2 + J_{N,y}^2 + J_{N,z}^2$, and the angular momentum component in the z direction, $J_{N,z}$, where $J_{N,i} = \frac{1}{2} \sum_k \sigma_i^k$ with, e.g., $\sigma_i^3 = \mathbb{1} \otimes \mathbb{1} \otimes \sigma_i \otimes \mathbb{1} \otimes \mathbb{1} \otimes \mathbb{1}$ for $N = 6$ qubits, $i \in \{x, y, z\}$ and σ_i the Pauli spin matrices. A subgroup of the Dicke states is symmetric under permutation of particles and given by

$$|D_N^{(l)}\rangle = \binom{N}{l}^{-1/2} \sum_i \mathcal{P}_i(|H^{\otimes(N-l)}V^{\otimes l}\rangle), \quad (1)$$

where $\sum_i \mathcal{P}_i(\dots)$ means the sum over all distinct symmetric permutations and l is the number of excitations in the usual notation of polarization encoded photonic qubits. In our experiment we focus on the symmetric six-qubit Dicke state with three excitations,

$$|D_6^{(3)}\rangle = (1/\sqrt{20}) \sum_i \mathcal{P}_i(|HHHVVV\rangle). \quad (2)$$

To realize the necessary 20 permutations, three horizontally and three vertically polarized photons in a single spatial mode are distributed by polarization-independent beam splitters into six modes, where $|D_6^{(3)}\rangle$ is observed under the condition of detecting a single photon in each of these modes. This scheme can be seen as a continuation of experiments on $D_2^{(1)}$ [6] and $D_4^{(2)}$ [8] and obviously can be extended to higher even photon numbers.

The experimental observation of $|D_6^{(3)}\rangle$ (Fig. 1) is achieved by utilizing a novel source of collinear type II spontaneous parametric down-conversion (SPDC) based on a femtosecond UV-enhancement resonator [14]. The

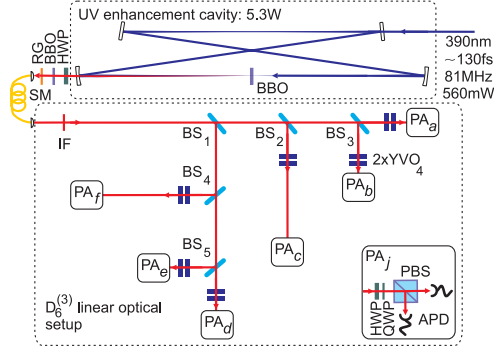


FIG. 1 (color online). Schematic experimental setup for the observation of the Dicke state $|D_6^{(3)}\rangle$. SPDC photons generated in the 1 mm thick β -barium borate (BBO) crystal inside the UV-enhancement cavity pass a half-wave plate (HWP) and a 0.5 mm thick BBO crystal to compensate beam walk-off effects. Their spatial mode is defined by coupling into a single-mode (SM) fiber. Spectral selection is achieved by a band-pass filter (RG) and a 3 nm interference filter (IF) at 780 nm. Birefringence of beam splitters BS_1 – BS_5 (BS_1 – BS_4 have a splitting ratio of 0.58:0.42 and BS_5 of 0.52:0.48) is compensated for by pairs of birefringent Yttrium-vanadate (YVO_4) crystals in the six output modes a, b, c, d, e, f . Polarization analysis (PA_j) in each mode is performed via a HWP and a quarter-wave plate (QWP) in front of a polarizing beam splitter (PBS). The photons are detected by single-photon avalanche photodiodes (APDs). The detection signals of the 12 detectors are fed into a FPGA controlled coincidence logic allowing histogramming of the 2^{12} possible detection events between the 12 detectors.

resonator allows pumping of the SPDC crystal with femto-second pulses with an average UV power of 5.3 W at a repetition rate of 81 MHz [14]. The SPDC photons are coupled out of the cavity by a dichroic mirror transparent at 780 nm, are spatially filtered by a single-mode fiber, and are subsequently distributed in free space by polarization-independent beam splitters. Asymmetry in the splitting ratios of the beam splitters reduces the probability of registering $|D_6^{(3)}\rangle$ (0.0126 compared to the optimal value of $5/324 \approx 0.0154$, yielding a six-photon count rate of 3.7

events per minute), but does not influence the state quality. For all data the errors are deduced from Poissonian counting statistics and errors of independently determined relative detector efficiencies.

The first characteristic feature of the state $|D_6^{(3)}\rangle$ is its structure in the z , x , and y bases (Fig. 2); i.e., when analyzing the photons in the six outputs all either along $|H$ or $V\rangle$, $|\pm\rangle = (1/\sqrt{2})(|H\rangle \pm |V\rangle)$ (linear polarization under 45°) and $|L$ or $R\rangle = (1/\sqrt{2})(|H\rangle \pm i|V\rangle)$ (left or right circular polarization), which, in our notation, are the eigenvectors of σ_z , σ_x , and σ_y , respectively. For the z basis [Fig. 2(a)] we find the pronounced 20 terms that are expected for $|D_6^{(3)}\rangle$. However, we also detect coincidences for $HHVVVV$, $HHHHVV$, and permutations thereof. These originate from higher orders of the SPDC process, in particular, from the fourth order emission, where, due to the finite detection efficiency, two of these photons can get lost and the remaining six photons will be registered as a sixfold detector click in the output modes. Thus, $|D_6^{(3)}\rangle$ is mixed with highly colored noise, which exhibits different types of entanglement itself depending on the loss type. Insight into the coherence between the observed coincidences can be obtained from measurements in the x [Fig. 2(b)] and y [Fig. 2(c)] bases. The state $|D_6^{(3)}\rangle$ transforms in these bases to $\sqrt{5/8}|GHZ_6^\mp\rangle + \sqrt{3/16}(|D_6^{(4)}\rangle \mp |D_6^{(2)}\rangle)$ with $|GHZ_N^\mp\rangle = (1/\sqrt{2}) \times (|0\rangle^{\otimes N} \mp |1\rangle^{\otimes N})$ and $0 = \{+, L\}$, $1 = \{-, R\}$. We observe the GHZ contribution as pronounced coincidence counts for the left- and rightmost projector. The residual counts from other terms [insets of Figs. 2(b) and 2(c)] make the decisive difference to a GHZ state as they are in a superposition with the GHZ terms. Apart from this, noise on top of all counts is also apparent. Most importantly, while the GHZ state shows its two terms only in a single basis, we observe these features now for two bases, which is directly related to the symmetry of $|D_6^{(3)}\rangle$.

A quantitative measure, indicating how well we prepared $|D_6^{(3)}\rangle$ experimentally, is given by the fidelity $F_{D_6^{(3)}}(\rho) = \text{Tr}(|D_6^{(3)}\rangle\langle D_6^{(3)}|\rho)$. Its determination would require 183 correlation measurements in the standard Pauli bases. However, employing the permutational symmetry of

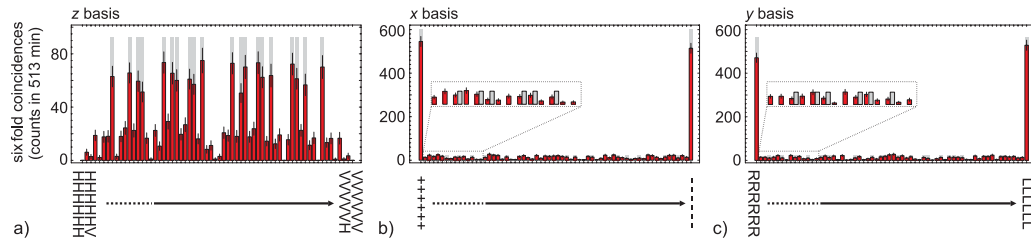


FIG. 2 (color online). Experimentally measured coincidences for the bases (a) z , (b) x , and (c) y with eigenvectors $|H$ or $V\rangle$, $|\pm\rangle$, and $|L$ or $R\rangle$, respectively. Theoretical predictions are shown as pale gray bars normalized to the total number of coincidences. The insets in (b) and (c) are magnified views of a part of all coincidences, where for clarity expected counts are shown next to experimental ones.

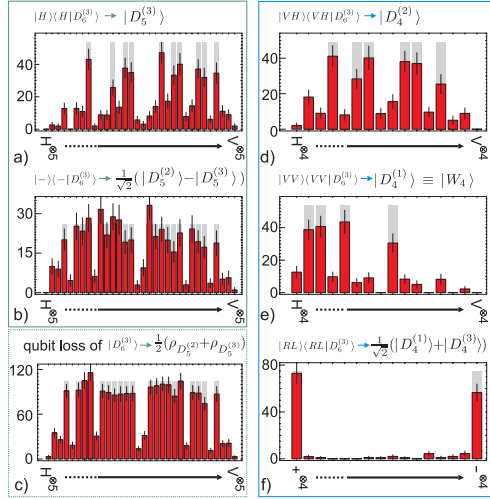


FIG. 3 (color online). Experimentally measured coincidence counts in the z basis [(a)–(e)] and x basis (f) for projections of $|D_6^{(3)}\rangle$ to obtain (a)–(b) five- and (d)–(f) four-qubit entangled states. (c) ρ_s obtained after a loss of a qubit from $|D_6^{(3)}\rangle$. Each measurement took 279 min. Theoretical predictions are shown as pale gray bars normalized to the total number of coincidences.

the state $|D_6^{(3)}\rangle$ leads to a reduction to only 21 measurement settings [15,16]. We have determined $F_{D_6^{(3)}} = 0.654 \pm 0.024$ with a measurement time of 31.5 h. This allows the application of the generic entanglement witness [10] $\langle \mathcal{W}_g \rangle = 0.6 - F_{D_6^{(3)}} = -0.054 \pm 0.024$ and thus proves genuine six-qubit entanglement of the observed state with a significance of 2 standard deviations (Fig. 4).

Proving entanglement based on witness operators can be much simpler in terms of the number of measurement settings, as due to the symmetry of $|D_6^{(3)}\rangle$ already the two measurements x and y are sufficient [8,10,18]. The generic form of such a witness is given by $\mathcal{W}_N(\alpha) = \alpha \cdot \mathbb{1}^{\otimes N} - (J_{N,x}^2 + J_{N,y}^2)$, where α is obtained by numerical optimization over all biseparable states. For the state $|D_6^{(3)}\rangle$ $\mathcal{W}_6(11.0179)$ [15] has a minimal value of -0.9821 . In our experiment we have obtained with the data shown in Figs. 2(b) and 2(c) $\langle \mathcal{W}_6(11.0179) \rangle = -0.422 \pm 0.148$, i.e., after a measurement time of only 17.1 h a higher significance for proving six-qubit entanglement compared to the generic witness (Fig. 4). A different witness, allowing additionally to estimate the fidelity and requiring three measurement settings only, can be obtained by considering higher moments of the $J_{6,i}$ operators and is given as $\mathcal{W} = 1.5 \cdot \mathbb{1}^{\otimes 6} - \sum_{i=x,y,z} \sum_{j=1}^3 c_{ij} J_{6,i}^{2j}$ [15], with $c_{ij} = (-1/45, 1/36, -1/180; -1/45, 1/36, -1/180; 1007/360, -31/36, 23/360)$. Experimentally, using the three measurements of Fig. 2 we obtain $\langle \mathcal{W} \rangle = -0.105 \pm 0.040$

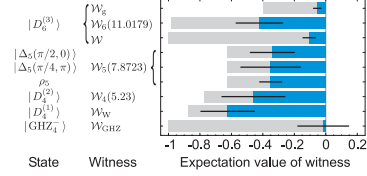


FIG. 4 (color online). Experimental results [dark gray (blue)] and theoretical predictions (pale gray) are shown for the various entanglement witnesses for different states (see text). Negative values prove genuine N -partite entanglement.

yielding also a quite accurate bound on the fidelity [15] of $F_{D_6^{(3)}} \geq 0.6 - \langle \mathcal{W} \rangle / 2.5 = 0.642 \pm 0.016$ (Fig. 4).

Another method to reveal entanglement and additionally the nonclassical nature of a quantum state are Bell inequalities. Introduced with the aim to exclude a local-realistic description of measurement results [19,20], they recently became important tools in quantum information processing, e.g., for security analysis [21] or for state discrimination [22,23]. A Bell operator well suited for the latter task is given by $\hat{\mathcal{B}}_{D_6^{(3)}} = \frac{1}{5}(\sigma_x \otimes M_5 + \sigma_y \otimes M_5')$, where M_5 and M_5' are five-qubit Mermin operators [20,23,24]. The associated Bell inequality, $|\langle \hat{\mathcal{B}}_{D_6^{(3)}} \rangle| \leq 0.4$, is maximally violated by the six-photon Dicke state ($\langle \hat{\mathcal{B}}_{D_6^{(3)}} \rangle_{D_6^{(3)}} = 1$) and much less, e.g., by any six-qubit GHZ state ($\langle \hat{\mathcal{B}}_{D_6^{(3)}} \rangle_{\text{GHZ, max}} = 0.85$). This again is a consequence of the symmetry of $|D_6^{(3)}\rangle$. While an inequality based on any of the two Mermin terms is maximally violated by a GHZ state, the violation of their sum is only maximal for $|D_6^{(3)}\rangle$ due to its symmetry and equal form in the x and y bases. The experimental value of $\langle \hat{\mathcal{B}}_{D_6^{(3)}} \rangle_{\text{expt}} = 0.43 \pm 0.02$ shows that there is no local-realistic model describing this state, yet due to the higher order SPDC noise, it is not sufficient to discriminate against GHZ states.

The characteristic symmetry and entanglement of $|D_6^{(3)}\rangle$ enables one to observe a wealth of five- and four-qubit entangled states that can be obtained by projective measurements or qubit loss [12]. When we project one of the qubits onto $\cos\theta|V\rangle + \sin\theta e^{-i\phi}|H\rangle$, we first obtain superpositions of five-qubit Dicke states, $|\Delta_5(\theta, \phi)\rangle = \cos\theta|D_5^{(2)}\rangle + \sin\theta e^{i\phi}|D_5^{(3)}\rangle$ with θ, ϕ real. These states belong to two different SLOCC classes, one for the values $\theta = 0$ or $\theta = \pi/2$ and the other one for the remaining value range [12]. Figures 3(a) and 3(b) show measurements in the z basis for a representative state of the two classes, obtained by projecting a qubit either onto $|H\rangle$ [$|\Delta_5(\pi/2, 0)\rangle = |D_5^{(3)}\rangle$] or onto $|-\rangle$ [$|\Delta_5(\pi/4, \pi)\rangle = (1/\sqrt{2})(|D_5^{(2)}\rangle - |D_5^{(3)}\rangle)$]. Figure 4 shows measured expectation values of optimized entanglement witnesses for detecting genuine N -qubit entanglement of these and the following states. When a qubit of $|D_6^{(3)}\rangle$ is lost, one obtains

$\rho_5 = \frac{1}{2}(\rho_{D_5^{(2)}} + \rho_{D_5^{(3)}})$, i.e., an equal mixture of $|D_5^{(2)}\rangle$ and $|D_5^{(3)}\rangle$ [Fig. 3(c)]. Remarkably and in sharp contrast to the case of losing a qubit from a GHZ₆ state, this mixed state is also genuine five-qubit entangled (Fig. 4). This fact now clearly provides, after all, a criterion to definitely distinguish these two prominent states and demonstrates the entanglement persistency [25] of $|D_6^{(3)}\rangle$.

By means of a second projective measurement we obtain a variety of SLOCC-inequivalent four-qubit states. In Fig. 3 we exemplarily show coincidences for three of those states. The state $|D_4^{(2)}\rangle$ [8] [Fig. 3(d)] is obtained by projection of one qubit onto $|V\rangle$ and another one onto $|H\rangle$. By projecting two qubits onto the same polarization (here $|V\rangle$) for the first time the four-photon W state [11,26], i.e., $|D_4^{(1)}\rangle$, could be observed in a linear optics experiment [Fig. 3(e)]. Both states are clearly genuine four-partite entangled [8,27] as depicted in Fig. 4. We have determined fidelities of $F_{D_4^{(2)}} = 0.682 \pm 0.022$ and $F_{D_4^{(1)}} = 0.619 \pm 0.043$ using optimized measurement settings [15,17]. Possible applications of $|D_4^{(1)}\rangle$ and $|D_4^{(2)}\rangle$ comprise, for example, quantum teleportation, teleportation, and secret sharing [8,9,28,29]. Most remarkably, one can also obtain a four-qubit GHZ state, which is suitable for, e.g., secret sharing [29]. As mentioned before, there is a strong GHZ component in the state $|D_6^{(3)}\rangle$. Considering the representation in the y basis [Fig. 2(c)], a projection of one photon onto $|R\rangle$ and another one onto $|L\rangle$ filters out just this GHZ component, but the remaining terms coherently superimpose to a four-qubit GHZ state, $|\text{GHZ}_4^-\rangle = (1/\sqrt{2}) \times (|D_4^{(1)}\rangle + |D_4^{(3)}\rangle) = (1/\sqrt{2})(|+\rangle^{\otimes 4} - |-\rangle^{\otimes 4})$. The fourfold coincidence counts shown in Fig. 3(f) reveal the characteristic GHZ structure. However, for this state a two-setting witness measurement [30] resulted in a value of $\langle W_{\text{GHZ}} \rangle = -0.016 \pm 0.162$, which is not sufficient to prove entanglement with the relevant significance and can be attributed to the low fidelity of $F_{\text{GHZ}} = 0.528 \pm 0.042$ and the asymmetric GHZ structure [Fig. 3(f)].

Altogether, we have experimentally demonstrated in this Letter remarkable entanglement properties of the Dicke state $|D_6^{(3)}\rangle$. It exhibits a high symmetry with characteristic correlations in various bases. As shown, this makes it a perfect resource for observing a wealth of different SLOCC-inequivalent states of a lower qubit number. The novel setup presented here allows experiments with a sufficient count rate and lays the foundations for demonstrations of important applications of $|D_6^{(3)}\rangle$, e.g., for phase-covariant teleportation, multipartite quantum communication, or entanglement enhanced phase measurements.

We would like to thank Christian Schmid, Wiesław Laskowski, Akira Ozawa, and Thomas Udem for helpful discussions. We acknowledge the support of this work by the DFG-Cluster of Excellence MAP, the EU Project QAP, and the DAAD/MNiSW exchange program. W.W. acknowledges the support of QCCC of the Elite Network

of Bavaria and the Studienstiftung des dt. Volkes. G. T. is thankful for the support of the National Research Fund of Hungary OTKA (T049234).

*witlef.wieczorek@mpq.mpg.de

- [1] D. Leibfried *et al.*, Nature (London) **438**, 639 (2005); C.-Y. Lu *et al.*, Nature Phys. **3**, 91 (2007); Phys. Rev. Lett. **102**, 030502 (2009).
- [2] H. Häffner *et al.*, Nature (London) **438**, 643 (2005).
- [3] M. Hein, J. Eisert, and H.J. Briegel, Phys. Rev. A **69**, 062311 (2004).
- [4] R. Raussendorf and H.J. Briegel, Phys. Rev. Lett. **86**, 5188 (2001); P. Walther *et al.*, Nature (London) **434**, 169 (2005).
- [5] R. H. Dicke, Phys. Rev. **93**, 99 (1954).
- [6] T. E. Kiess *et al.*, Phys. Rev. Lett. **71**, 3893 (1993).
- [7] M. Eibl *et al.*, Phys. Rev. Lett. **92**, 077901 (2004); H. Mikami *et al.*, Phys. Rev. Lett. **95**, 150404 (2005).
- [8] N. Kiesel *et al.*, Phys. Rev. Lett. **98**, 063604 (2007).
- [9] A. Sen(De) *et al.*, Phys. Rev. A **68**, 062306 (2003); P. Agrawal and A. Pati, Phys. Rev. A **74**, 062320 (2006); C. Thiel *et al.*, Phys. Rev. Lett. **99**, 193602 (2007); O. Gühne, F. Bodoky, and M. Blaauboer, Phys. Rev. A **78**, 060301(R) (2008).
- [10] G. Tóth, J. Opt. Soc. Am. B **24**, 275 (2007).
- [11] T. Tashima *et al.*, Phys. Rev. A **77**, 030302(R) (2008).
- [12] W. Wieczorek *et al.*, Phys. Rev. A **79**, 022311 (2009).
- [13] W. Dür, G. Vidal, and J.I. Cirac, Phys. Rev. A **62**, 062314 (2000); A. Zeilinger, M. A. Horne, and D. M. Greenberger, NASA Conf. Publ. No. 3135, 1997.
- [14] R. Krischek *et al.* (unpublished).
- [15] G. Tóth *et al.*, arXiv:0903.3910.
- [16] $|D_6^{(3)}\rangle\langle D_6^{(3)}| = \{-0.6[|\mathbb{1}\rangle + 0.05(|x \pm y \pm \mathbb{1}\rangle - |x \pm z \pm \mathbb{1}\rangle - |y \pm z \pm \mathbb{1}\rangle - |x \pm y \pm z\rangle) + 0.2(|x \pm z\rangle + |y \pm z\rangle) + 0.1(|x \pm y\rangle + 0.3(|x \pm \mathbb{1}\rangle + |y \pm \mathbb{1}\rangle) - 0.6(|x\rangle + |y\rangle) + 0.2(|z \pm \mathbb{1}\rangle - 0.1(|z \pm i\mathbb{1}\rangle - 0.2|z\rangle + 0.6(M_{x,z} + M_{y,z}))/64$ with $M_{i,j} = \frac{16}{3} \sum_{k=1}^6 [\cos(k\pi/6)\sigma_i + \sin(k\pi/6)\sigma_j]$, $|x \pm y\rangle = (\sigma_x + \sigma_y)^{\otimes 6}$, and $|x \pm y\rangle = |x + y\rangle + |x - y\rangle$, etc. For decomposition of $M_{i,j}$ see [17].
- [17] O. Gühne *et al.*, Phys. Rev. A **76**, 030305(R) (2007).
- [18] G. Tóth *et al.*, Phys. Rev. Lett. **99**, 250405 (2007).
- [19] J. S. Bell, Physics **1**, 195 (1964).
- [20] N. D. Mermin, Phys. Rev. Lett. **65**, 1838 (1990).
- [21] P. W. Shor and J. Preskill, Phys. Rev. Lett. **85**, 441 (2000); A. Acin, N. Gisin, and L. Masanes, Phys. Rev. Lett. **97**, 120405 (2006).
- [22] C. Schmid *et al.*, Phys. Rev. Lett. **100**, 200407 (2008).
- [23] C. Schmid *et al.*, arXiv:0804.3154.
- [24] $M_5 = [-\sum_i \mathcal{P}_i(\sigma_z \otimes \sigma_z \otimes \sigma_x \otimes \sigma_x \otimes \sigma_x) + \sum_i \mathcal{P}_i(\sigma_z \otimes \sigma_z \otimes \sigma_z \otimes \sigma_x \otimes \sigma_x) + \sigma_x^{\otimes 5}]/16$; M'_5 , exchange σ_x with σ_y .
- [25] M. Bourennane *et al.*, Phys. Rev. Lett. **96**, 100502 (2006).
- [26] X. B. Zou, K. Pahlke, and W. Mathis, Phys. Rev. A **66**, 044302 (2002); Y. Li and T. Kobayashi, Phys. Rev. A **70**, 014301 (2004).
- [27] $W_W = W_4(5.5934) + 1.47(J_{4,z}^2 - 2J_{4,z})$ [15].
- [28] M. Murao *et al.*, Phys. Rev. A **59**, 156 (1999).
- [29] M. Hillery, V. Bužek, and A. Berthiaume, Phys. Rev. A **59**, 1829 (1999).
- [30] G. Tóth and O. Gühne, Phys. Rev. Lett. **94**, 060501 (2005).

P5.2

PHYSICAL REVIEW A 79, 022311 (2009)

Multiqubit entanglement engineering via projective measurements

Witłef Wieczorek,^{1,2,*} Nikolai Kiesel,^{1,2} Christian Schmid,^{1,2} and Harald Weinfurter^{1,2}
¹Max-Planck-Institut für Quantenoptik, Hans-Kopfermann-Strasse 1, D-85748 Garching, Germany
²Department für Physik, Ludwig-Maximilians-Universität, D-80797 München, Germany
 (Received 8 October 2008; published 9 February 2009)

So far, various multiphoton entangled states have been observed experimentally by using different experimental setups. We present a scheme to realize many stochastic local operations and classical communication (SLOCC) inequivalent states of three and four qubits via projective measurements on suitable entangled states. We demonstrate how these states can be observed experimentally in a single setup and study the feasibility of implementation with present-day technology.

DOI: 10.1103/PhysRevA.79.022311

PACS number(s): 03.67.Bg, 03.65.Ud, 03.67.Mn, 42.50.Ex

I. INTRODUCTION

Entangled states are an essential resource for quantum information applications. Recently, the equivalence under stochastic local operations and classical communication (SLOCC) was successfully used to classify multipartite entanglement [1–4]. This classification is particularly relevant for evaluating the use of states for multiparty quantum communication as states of the same SLOCC class can be employed for the same applications. Therefore, the experimental realization of different SLOCC-inequivalent states is highly desirable.

So far, several SLOCC-inequivalent states have been realized in various physical systems. The largest variety of states was observed in experiments that rely on photonic qubits (e.g., Ref. [5]). However, typical for this experimental approach is its inherent inflexibility. The design of the necessary optical network is especially tailored to the particular state that should be observed. Consequently, once a particular network is built, it will not offer, in general, the choice between different SLOCC-inequivalent states. Recently, a linear optics experiment was performed that broke with this inflexibility [6] by allowing the observation of an entire family of SLOCC-inequivalent four-photon entangled states. Essentially, this was achieved by multiphoton interference.

Here we show that projective measurements on subsystems can provide another means of preparing SLOCC-inequivalent classes of entangled states [7]. It is well known that atomic entangled states, even from different SLOCC classes, can be remotely prepared by projective measurements on photons [8,9], which previously have been entangled with the atoms—i.e., by a measurement of typically half of the total multipartite entangled state. Here, in contrast, we focus on the property of certain symmetric multipartite entangled states that allow a more flexible preparation of families of SLOCC-inequivalent types of entanglement by projective measurements on small subsystems. The initial n -qubit symmetric states can be observed in linear optics setups that distribute n photons of a single spatial mode to n different output modes. Subsequent projective measurements on these n -qubit states will yield states belonging to different

SLOCC classes. We focus in the following on the case of $n=4$ and 5 and demonstrate that our approach can be realized by using a single linear optical setup only.

The paper is structured as follows. In Sec. II we discuss the effect of projective measurements on particular symmetric states. We begin our investigations with SLOCC-inequivalent three-qubit states obtained from the four-qubit symmetric Dicke state with two excitations $|D_4^{(2)}\rangle$ [10–12]. Further, we show how to obtain SLOCC-inequivalent four-qubit entangled states like, e.g., the Greenberger-Horne-Zeilinger (GHZ) state $|\text{GHZ}_4\rangle$, W state $|W_4\rangle$, and even $|D_4^{(2)}\rangle$, via projective measurements on five-qubit states, which are given by superpositions of two symmetric Dicke states [13]. In Sec. III we will discuss the experimental implementation of the proposed schemes. We recapitulate the experiment of Ref. [11], which lead to the observation of $|D_4^{(2)}\rangle$ and discuss the feasibility of an extension in order to observe the five-qubit states.

II. PROJECTIVE MEASUREMENTS ON PARTICULAR SYMMETRIC STATES

In their seminal work, Dür *et al.* [2] discovered that only two SLOCC-inequivalent classes of genuine tripartite entanglement exist: the GHZ and W classes. Well-known representatives of these classes are the states $|\text{GHZ}_3\rangle = 1/\sqrt{2}(|HHH\rangle + |VVV\rangle)$ and $|W_3\rangle = 1/\sqrt{3}(|HHV\rangle + |HVH\rangle + |VHH\rangle)$, respectively. We utilize the notation for polarization encoded qubits throughout this work—e.g., $|HHV\rangle = |H\rangle_a \otimes |H\rangle_b \otimes |V\rangle_c$ and $|H\rangle$ or $|V\rangle$ mean linear horizontal (H) or vertical (V) polarization of photons, respectively—and the subscript denotes the spatial mode of each photon. In contrast to the three-qubit case, the SLOCC classification of four-partite entangled states is much richer, containing infinitely many SLOCC-inequivalent four-partite entangled states [3,14].

In the following we show that via projective measurements on particular symmetric states, SLOCC-inequivalent entangled states of a lower qubit number can be obtained. To this end, we consider particular members of the family of symmetric Dicke states [10]. Generally, a symmetric N -qubit Dicke state with m excitations, denoted as $|D_N^{(m)}\rangle$, is, again in the notation of polarization encoded photonic qubits, the equally weighted superposition of all possible permutations

*witl.wieczorek@mpq.mpg.de

WIECZOREK *et al.*PHYSICAL REVIEW A **79**, 022311 (2009)TABLE I. Three-qubit states obtained by a single projective measurement on the state $|D_4^{(2)}\rangle$; cf. Eq. (1).

α'	β'	ϵ'	State
$\cos \theta'$	$\sin \theta'$	ϵ'	$\cos \theta' D_3^{(2)}\rangle + e^{-i\epsilon'} \sin \theta' D_3^{(1)}\rangle$
1	0		$ D_3^{(2)}\rangle \equiv \bar{W}_3\rangle$
0	1		$ D_3^{(1)}\rangle \equiv W_3\rangle$
$\frac{1}{\sqrt{2}}$	$\frac{1}{\sqrt{2}}$	0	$(D_3^{(1)}\rangle + D_3^{(2)}\rangle) / \sqrt{2} \equiv G_3^+\rangle$
$\frac{1}{\sqrt{2}}$	$\frac{1}{\sqrt{2}}$	π	$(D_3^{(1)}\rangle - D_3^{(2)}\rangle) / \sqrt{2} \equiv G_3^-\rangle$

of N -qubit product states with m vertically and $N-m$ horizontally polarized photons.

A. Projections of the four-qubit Dicke state $|D_4^{(2)}\rangle$

First, we aim at obtaining states from the two inequivalent tripartite entanglement classes by applying projective measurements on a four-qubit entangled state. The symmetric Dicke state

$$|D_4^{(2)}\rangle = \frac{1}{\sqrt{6}}(|HHVV\rangle + |HVHV\rangle + |VHHV\rangle + |HVVH\rangle + |VHVH\rangle + |VVHH\rangle)$$

turned out to be useful for this purpose [11]. Here, we will analyze in more detail which three-qubit states can be obtained.

Generally, an arbitrary projective measurement can be expressed by $P(\alpha', \epsilon') := |\alpha', \epsilon'\rangle\langle\alpha', \epsilon'|$, with $|\alpha', \epsilon'\rangle = \alpha'|H\rangle + \beta'e^{i\epsilon'}|V\rangle$ (all parameters real and $\alpha'^2 + \beta'^2 = 1$). The projection $P(\alpha', \epsilon')$ applied on $|D_4^{(2)}\rangle$ leads to the three-qubit states

$$\alpha' |D_3^{(2)}\rangle + \beta' e^{-i\epsilon'} |D_3^{(1)}\rangle, \quad (1)$$

which are arbitrary superpositions of the two entangled, symmetric three-qubit Dicke states (Table I).

To analyze the entanglement of the states, we choose as a suitable entanglement measure the three-tangle τ_3 [15], which distinguishes the W and GHZ class as only for GHZ-type entangled states is τ_3 nonzero [2]. The solid line in Fig. 1 shows τ_3 for the states of Eq. (1) in dependence of θ'

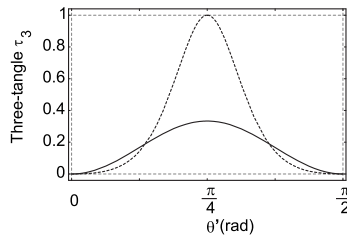


FIG. 1. Three-tangle τ_3 for the states of Eq. (1) without (solid line) and with (dashed line) application of the transformation $T_+ \otimes T_+ \otimes T_+$ (where $\alpha' = \cos \theta'$ and $\epsilon' = 0$).

($\alpha' = \cos \theta'$). It is found that the three-tangle is zero for $\theta' = 0, \pi/2$ ($\alpha' = 0, 1$), which corresponds to a measurement in the computational basis. There, we obtain states from the W class: namely, $|W_3\rangle \equiv |D_3^{(1)}\rangle$ and $|\bar{W}_3\rangle = 1/\sqrt{3}(|VVH\rangle + |VHV\rangle + |HVV\rangle) \equiv |D_3^{(2)}\rangle$, respectively. For all other values of θ' , $\tau_3 \neq 0$, implying that these states belong to the GHZ class. The maximal value of $\tau_3 = 1/3$ is obtained for $\theta' = \pi/4$, corresponding to a measurement in the (\pm) basis, where $|\pm\rangle = 1/\sqrt{2}(|H\rangle \pm |V\rangle)$. For $\theta' = \pi/4$ and $\epsilon' = 0, \pi$, one obtains the G_3 states [16] with $|G_3^+\rangle = \frac{1}{\sqrt{2}}(|\bar{W}_3\rangle + |W_3\rangle)$ and $|G_3^-\rangle = \frac{1}{\sqrt{2}}(|\bar{W}_3\rangle - |W_3\rangle)$, respectively.

The G_3 states can be transformed directly into the GHZ₃ state, which has the maximal possible three-tangle $\tau_3 = 1$, via the stochastic local operations (local filtering)

$$T_+ = \mathcal{H} \left\{ \frac{1}{2} \left[\left(\frac{1}{\sqrt{3}} + i \right) 1 + \left(\frac{1}{\sqrt{3}} - i \right) \sigma_z \right] \right\} \mathcal{H},$$

$$T_- = \mathcal{H} \left\{ \frac{1}{2} \left[\left(\frac{1}{\sqrt{3}} + i \right) \sigma_x + i \left(\frac{1}{\sqrt{3}} - i \right) \sigma_y \right] \right\} \mathcal{H},$$

where σ_x , σ_y , and σ_z are the Pauli spin matrices and \mathcal{H} is the Hadamard transformation, in the following way:

$$(T_+ \otimes T_+ \otimes T_+) |G_3^+\rangle = \frac{1}{3} |\text{GHZ}_3\rangle,$$

$$(T_- \otimes T_- \otimes T_-) |G_3^-\rangle = \frac{1}{3} |\text{GHZ}_3\rangle. \quad (2)$$

Though these operations perform the desired transformation, they only do so with a success probability of $1/9$. Figure 1 shows the three-tangle when the operation $T_+ \otimes T_+ \otimes T_+$ is applied successfully to all states of Eq. (1). For $\theta' = \pi/4$ the three-tangle is indeed increased to its maximal value of $\tau_3 = 1$.

B. Projections of superpositions of five-qubit Dicke states

Extending the idea described before, SLOCC-inequivalent four-partite entangled states can be obtained from suitable five-qubit symmetric states via projective measurements. Here we consider an arbitrary superposition of the two symmetric five-qubit Dicke states $|D_5^{(2)}\rangle$ and $|D_5^{(3)}\rangle$:

$$|\Delta_5\rangle = \alpha |D_5^{(2)}\rangle + \beta e^{i\epsilon} |D_5^{(3)}\rangle. \quad (3)$$

We note that these states can also be seen as a natural choice as they are obtained via a single projective measurement on the six-qubit Dicke state $|D_6^{(3)}\rangle$. The states $|\Delta_5\rangle$ belong to two different SLOCC classes. The first class occurs for $\alpha = 0$ or $\beta = 0$, as the states $|D_5^{(2)}\rangle$ and $|D_5^{(3)}\rangle$ can be transformed into each other by spin-flipping all qubits. The second class is given for $\alpha \neq 0$ and $\beta \neq 0$. The weighting and phase between the terms of $|\Delta_5\rangle$ can be changed easily via the SLOCC operations $T_r^{\otimes 5} = T_r \otimes T_r \otimes T_r \otimes T_r \otimes T_r$, with $T_r = [(1+1/r)1 + (1-1/r)\sigma_z]/2$ and $r \neq 0$ complex. To obtain a new ratio of parameters $\bar{\alpha}/(\bar{\beta}e^{i\bar{\epsilon}})$, r needs to be chosen as $\beta\bar{\alpha}e^{i\epsilon}/(\bar{\beta}\alpha e^{i\bar{\epsilon}})$. Note that this reasoning could also be applied for the states of Eq. (1).

A single projective measurement $P(\alpha', \epsilon')$ applied on $|\Delta_5\rangle$ yields the four-qubit entangled states

TABLE II. Four-qubit entangled states obtained from the states $|\Delta_5\rangle$ by a single projective measurement; cf. Eq. (4). In analogy to Eq. (3), the states $\cos^2 \theta |D_4^{(1)}\rangle - \sin^2 \theta e^{2i\epsilon} |D_4^{(3)}\rangle$ belong to two SLOCC classes given by (i) $\theta=0$ or $\theta=\pi/2$ and (ii) $\theta \in (0, \pi/2)$ with ϵ arbitrary.

α	β	ϵ	α'	β'	ϵ'	State
1	0		1	0		$ D_4^{(2)}\rangle$
0	1		0	1		$ D_4^{(2)}\rangle$
1	0		0	1		$ W_4\rangle = D_4^{(1)}\rangle$
0	1		1	0		$ \bar{W}_4\rangle = D_4^{(3)}\rangle$
$\frac{1}{\sqrt{2}}$	$\frac{1}{\sqrt{2}}$	$\frac{\pi}{2}$	$\frac{1}{\sqrt{2}}$	$\frac{1}{\sqrt{2}}$	$-\frac{\pi}{2}$	$ \text{GHZ}_4^+\rangle$
$\cos \theta$	$\sin \theta$	ϵ	$\sin \theta$	$\cos \theta$	$\epsilon - \pi$	$\cos^2 \theta D_4^{(1)}\rangle - \sin^2 \theta e^{2i\epsilon} D_4^{(3)}\rangle$

$$|\Delta_4\rangle \propto \alpha\beta' e^{-i\epsilon'} |D_4^{(1)}\rangle + \alpha'\beta e^{i\epsilon} |D_4^{(3)}\rangle + (\alpha\alpha' + \beta\beta' e^{i(\epsilon-\epsilon')}) \sqrt{6/4} |D_4^{(2)}\rangle. \quad (4)$$

These states are superpositions of all symmetric four-qubit entangled Dicke states. In particular, these superpositions contain the SLOCC-inequivalent family of states $\mu(\alpha, \alpha', \epsilon, \epsilon') |\text{GHZ}_4\rangle + \nu(\alpha, \alpha', \epsilon, \epsilon') |D_4^{(2)}\rangle$ (for details, see [17]), which forms according to the SLOCC classification by Verstraete *et al.* [3] a subset of the four-qubit entangled generic family G_{abcd} . In the following we discuss prominent SLOCC-inequivalent states of the family of Eq. (4) (see also Table II).

Remarkably, we obtain a four-qubit GHZ_4 state. This can be easily seen when we consider the state $|\text{GHZ}_4^+\rangle = 1/\sqrt{2}(|HHHH\rangle - |VVVV\rangle)$ under a Hadamard transformation \mathcal{H} acting on each qubit:

$$|\text{GHZ}_4^+\rangle \equiv (\mathcal{H} \otimes \mathcal{H} \otimes \mathcal{H} \otimes \mathcal{H}) |\text{GHZ}_4^-\rangle = \frac{1}{\sqrt{2}}(|D_4^{(1)}\rangle + |D_4^{(3)}\rangle).$$

We get $|\text{GHZ}_4^+\rangle$ when the amplitude of $|D_4^{(2)}\rangle$ is zero and the two remaining terms in Eq. (4) are equally balanced; i.e., the conditions (i) $\alpha\alpha' = -\beta\beta' e^{i(\epsilon-\epsilon')}$ and (ii) $\alpha\beta' e^{-i\epsilon'} = \alpha'\beta e^{i\epsilon}$ are fulfilled. This holds only for $\alpha = \beta = \alpha' = \beta' = 1/\sqrt{2}$ and $\epsilon = -\epsilon' = \pi/2$ or $-\epsilon = \epsilon' = \pi/2$. When we impose only condition (i)—i.e., the amplitude of $|D_4^{(2)}\rangle$ is zero [which holds for $\alpha = \sqrt{1-\alpha'^2}$ and $\Delta\epsilon = \epsilon - \epsilon' = (2n+1)\pi$ for $n \in \{0, 1, 2, \dots\}$ —a continuous transition between the states $|W_4\rangle$ ($\alpha=1$), $|\text{GHZ}_4^+\rangle$ ($\alpha = \sqrt{1/2}$ and $\Delta\epsilon = \pi$), and $|\bar{W}_4\rangle$ ($\alpha=0$) can be achieved.

Further, three-qubit states are obtained by performing a projective measurement $P(\alpha'', \epsilon'')$ on $|\Delta_4\rangle$:

$$\begin{aligned} |\Delta_3\rangle &\propto \alpha\beta'\beta'' e^{-i(\epsilon'+\epsilon'')} |D_3^{(0)}\rangle + \alpha'\beta\alpha'' e^{i\epsilon} |D_3^{(3)}\rangle \\ &+ \left((\alpha\beta'\alpha'' e^{-i\epsilon'} + \sqrt{\frac{6}{4}} (\alpha\alpha' + \beta\beta' e^{i(\epsilon-\epsilon')}) \beta'' e^{-i\epsilon''} \right) \\ &\times \sqrt{3} |D_3^{(1)}\rangle + \left((\alpha'\beta\beta'' e^{i(\epsilon-\epsilon'')} + \sqrt{\frac{6}{4}} (\alpha\alpha' + \beta\beta' e^{i(\epsilon-\epsilon')}) \alpha'' \right) \sqrt{3} |D_3^{(2)}\rangle. \end{aligned} \quad (5)$$

All permutation symmetric three-qubit states are included in the states $|\Delta_3\rangle$ [18]. In particular, we note that a GHZ_3 state can be obtained directly without the need for local operations. To show this, we consider $|\text{GHZ}_3^-\rangle = 1/\sqrt{2}(|HHH\rangle - |VVV\rangle)$ under a Hadamard transformation \mathcal{H} acting on each qubit:

$$|\text{GHZ}_3^+\rangle \equiv (\mathcal{H} \otimes \mathcal{H} \otimes \mathcal{H}) |\text{GHZ}_3^-\rangle = \sqrt{\frac{3}{4}} |D_3^{(1)}\rangle + \sqrt{\frac{1}{4}} |D_3^{(3)}\rangle.$$

The state $|\text{GHZ}_3^+\rangle$ is obtained for $\alpha = \beta = \alpha' = \beta' = 1/\sqrt{2}$, $\alpha'' = 1$, and $\epsilon = -\epsilon' = \pi/2$.

III. EXPERIMENTAL IMPLEMENTATION

The states $|D_4^{(2)}\rangle$ and $|\Delta_5\rangle$ are permutation symmetric. Hence, their experimental implementation can be achieved via a symmetric distribution of photons. For the observation of the state $|D_4^{(2)}\rangle$ the necessary four photons originate from the second-order emission of a collinear, type-II spontaneous parametric down-conversion (SPDC). For observing the states $|\Delta_5\rangle$, we will consider different experimental implementations, which are extensions of the $|D_4^{(2)}\rangle$ setup.

A. Dicke state $|D_4^{(2)}\rangle$

Figure 2 shows one of the possible setups for the states $|\Delta_5\rangle$. As can be seen, the setup for observing the state $|D_4^{(2)}\rangle$ is at the core of it. The state $|D_4^{(2)}\rangle$ was observed after a symmetric distribution of two horizontally and two vertically polarized photons, initially in a single spatial mode s , onto four spatial modes (a, b, c, d) via three polarization-independent beam splitters (BS). The photons originate from a β -barium borate (BBO) crystal in a type-II, collinear SPDC process, which emits the state [19,20]

$$|\Psi_{\text{dc}}\rangle = \sqrt{1 - |z_{\text{dc}}|^2} \sum_{n=0}^{\infty} \frac{(iz_{\text{dc}})^n}{n!} (s_H^\dagger s_V^\dagger)^n |\text{vac}\rangle, \quad (6)$$

where s_i^\dagger is the creation operator for a photon in mode s having polarization $i \in \{H, V\}$, $|\text{vac}\rangle$ is the vacuum state, $z_{\text{dc}} = |z_{\text{dc}}| e^{i2\phi_{\text{dc}}}$ with $|z_{\text{dc}}| = \tanh \tau$, and τ depends on the pump amplitude and the coupling between the electromagnetic

WIECZOREK *et al.*

PHYSICAL REVIEW A 79, 022311 (2009)

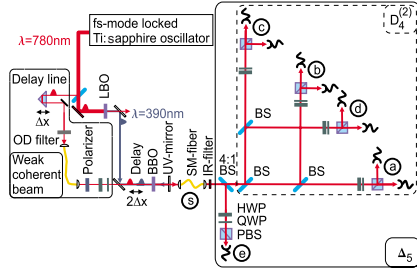


FIG. 2. (Color online) Schematic experimental setup for the observation of the state $|D_4^{(2)}\rangle$ (innermost section, dashed frame). The weak coherent beam, the 4:1 beam splitter as well as the detection in an additional mode e are needed for the proposed experimental implementation of the five photon states $|\Delta_5\rangle$ (details see text).

field and the crystal ($\tau \ll 1$). The probability to create a single pair is $(1 - |z_{dc}|^2)|z_{dc}|^2$. Here, we are interested in the second-order emission $\propto (s_H^{\dagger} s_V^{\dagger})^2 |\text{vac}\rangle$.

The BBO crystal was pumped by a frequency-doubled, femtosecond, mode-locked Ti:sapphire laser. The spatial mode s of the photons is defined by coupling into a single-mode (SM) fiber. The photons pass an interference filter (IR), reducing their spectral distinguishability. The polarization state of each photon is analyzed via a polarizing beam splitter (PBS) preceded by a half-wave plate (HWP) and quarter-wave plate (QWP). Finally, the photons are detected by fiber-coupled single-photon detectors. The experimental state was observed under the condition of detecting a photon in each of the four spatial modes (a, b, c, d).

We found a fidelity of $F_{\text{expt}} = \langle D_4^{(2)} | \rho_{\text{expt}} | D_4^{(2)} \rangle = 0.844 \pm 0.008$ to the state $|D_4^{(2)}\rangle$. Using a generic entanglement witness \mathcal{W} [21], where we use the shorthand notation $\mathcal{W}(|\Psi\rangle, \alpha) = \alpha \mathbb{1} - |\Psi\rangle\langle\Psi|$, with $\alpha = \frac{2}{3}$ and $|\Psi\rangle = |D_4^{(2)}\rangle$, genuine four-partite entanglement of ρ_{expt} was verified: $\text{Tr}[\mathcal{W}(D_4^{(2)}, \frac{2}{3}) \rho_{\text{expt}}] = \frac{2}{3} - F_{\text{expt}} = -0.177 \pm 0.008$. A value < 0 is sufficient to prove genuine four-partite entanglement [21]. Further, by using the state-discrimination method described in [22], we were able to exclude W - and cluster-type entanglement for the experimentally observed state.

For demonstrating that we can experimentally access states from both inequivalent tri-partite entanglement classes, we performed a full-state tomography to reconstruct the density matrices of the respective states. A projection measurement of the photon in mode d in the computational basis yields the W_3 states characterized by the density matrices shown in Figs. 3(a) and 3(b). We calculated fidelities of 0.882 ± 0.015 and 0.835 ± 0.015 to the theoretical states $|W_3\rangle$ and $|\bar{W}_3\rangle$, respectively. Their genuine tripartite entanglement is verified via the entanglement witnesses $\mathcal{W}(W_3, \frac{2}{3})$ and $\mathcal{W}(\bar{W}_3, \frac{2}{3})$ [21], where we determined values of -0.215 ± 0.015 and -0.168 ± 0.015 , respectively.

A measurement in the (\pm) basis yields G_3 states, which belong to the GHZ class. If we apply the corresponding transformations [see Eq. (2)] on the measured density matrices, we indeed obtain GHZ₃ states; see Figs. 3(c) and 3(d).

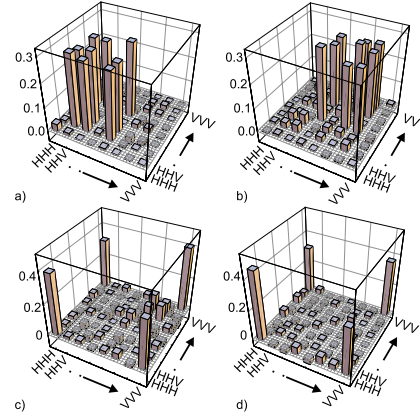


FIG. 3. (Color online) Experimental density matrices for the measured W_3 (a) and \bar{W}_3 (b) states. The density matrices for the GHZ₃ states of (c) and (d) are calculated from the measured G_3^+ and G_3^- states. Displayed is the real part of the corresponding density matrix.

We determined fidelities of 0.719 ± 0.022 and 0.733 ± 0.024 to a GHZ₃ state, respectively. An entanglement witness detecting genuine tripartite entanglement of these states is $\mathcal{W}(\text{GHZ}_3, \frac{1}{2})$ [21]. We find the negative values of -0.219 ± 0.022 and -0.233 ± 0.024 , respectively. A witness that further excludes W -type entanglement is given by $\mathcal{W}(\text{GHZ}_3, \frac{3}{4})$ [23]. The transformed GHZ₃ states do not fulfill the witness's entanglement condition. However, by applying local filtering operations on this witness [24], we obtain values of -0.033 ± 0.026 and -0.029 ± 0.023 , respectively, which finally proves GHZ-type entanglement with a significance of one standard deviation.

B. Towards $|\Delta_5\rangle$

1. Implementation

For observing the states $|\Delta_5\rangle$, different implementations are possible. One possibility is given by the application of a projective measurement on the state $|D_6^{(3)}\rangle$ (see Sec. II B), where the necessary six photons originate from the third-order SPDC emission. However, when implementing the state $|\Delta_5\rangle$ directly, only five photons are necessary and, thus, a higher count rate should be possible. These five photons can be obtained by superimposing the four photons from the second-order SPDC emission with an additional photon. The polarization of the additional photon determines the parameters α , β , and ϵ in Eq. (3). In the ideal case, the additional photon is obtained from a single-photon source (see, e.g., [25,26]) that acts on demand and matches the SPDC photons spectrally, temporally, and spatially. However, to our knowledge, no such source exists. Alternatively, a heralded SPDC source [27] can be employed, which results in low count rates, since again six photons have to be detected in total. Instead, we investigate whether the single-photon

MULTIQUBIT ENTANGLEMENT ENGINEERING VIA ...

PHYSICAL REVIEW A 79, 022311 (2009)

source can be substituted by a weak coherent beam (WCB) [28]—i.e., whether this simplification influences the state quality.

This implementation is based on the setup used for observing the state $|D_4^{(2)}\rangle$ described in Sec. III A (Fig. 2). The WCB can be derived via a beam splitter [and additional attenuation via optical density (OD) filters] from the Ti:sapphire laser, which also pumps the BBO crystal for the SPDC process after a frequency-doubling stage. The polarization of the WCB can be set arbitrarily via a polarizer, followed by a HWP and QWP. These settings determine the parameters α , β , and ϵ in Eq. (3). A delay line in the WCB allows one to adjust the temporal overlap with the SPDC emission. The photons of both sources are overlapped collinearly in the BBO crystal and coupled in the same single-mode fiber. They are symmetrically distributed onto the modes (a, b, c, d, e) via a beam splitter with 4:1 splitting ratio and further splitting as described in Sec. III A.

2. Weak coherent beam: Effects

The state of the WCB that substitutes the single-photon source is [29]

$$|\Psi_w\rangle = e^{-|z_w|^2/2} \sum_{n=0}^{\infty} \frac{(z_w)^n}{n!} (w_j^\dagger)^n |\text{vac}\rangle, \quad (7)$$

where w_j^\dagger is the creation operator of a photon with polarization j in mode w , $z_w = |z_w| e^{i\phi_w}$, $|z_w|^2$ is the mean photon number, and $|z_w|^2 e^{-|z_w|^2}$ is the probability for the photon state $|1\rangle$. The photons of the WCB and SPDC originate from the same laser—i.e., the Ti:sapphire laser—but travel different paths before they are coupled into the same single-mode fiber. As only their relative phase is relevant, we set for the following considerations $\phi_{dc}=0$, without loss of generality. In the experiment the relative phase fluctuates without an active stabilization of the relative delay of the WCB and SPDC photons. Further, the WCB compared to a real single-photon source exhibits higher-order terms, resulting in multiple photons per pulse. We note that the phase dependence and the higher-order terms have a much smaller influence if a heralded source is employed, of course, with the disadvantage of requiring, effectively, a six-photon down-conversion experiment.

We will now demonstrate effects caused by using the WCB. First, we observe quantum interference, which occurs when there are at least two indistinguishable possibilities that lead to the same detection event. In our case this becomes already observable when we consider only two photons. There, the following two possibilities exist: Two photons originate either from the SPDC emission *or* the WCB. To show the interference let us assume a left circularly polarized WCB, whose two-photon term is

$$\begin{aligned} \propto e^{2i\phi_w} (w_H^\dagger)^2 &= e^{2i\phi_w} (w_H^\dagger - iw_V^\dagger)^2/2 \\ &= e^{2i\phi_w} [(w_H^\dagger)^2 - (w_V^\dagger)^2 - 2i(w_H^\dagger w_V^\dagger)]/2. \end{aligned} \quad (8)$$

For a coherent overlap—i.e., $w_j^\dagger \rightarrow s_j^\dagger$ —the last term of Eq. (8) is identical with the first-order SPDC emission ($\propto s_H^\dagger s_V^\dagger$). Hence, for the twofold coincidence detection event *HV*, both

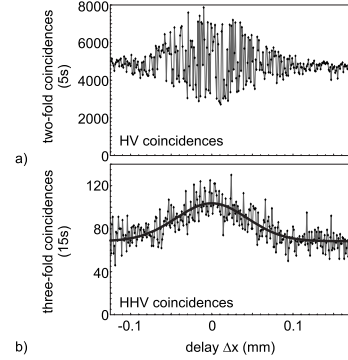


FIG. 4. Coherence between the weak coherent beam and the SPDC photons. (a) Interference of the two possibilities how to obtain an *HV* coincidence. (b) Enhanced emission (cloning) due to the bosonic nature of photons. The solid line shows a Gaussian fit to the data points, giving an enhancement of 1.52 ± 0.03 .

possibilities contribute and interfere in dependence on ϕ_w . This is shown in Fig. 4(a). When we change the path difference between the photons of both sources, we observe an oscillation in the coincidence count rate on the order of the wavelength ($< \mu\text{m}$), which is due to the change of ϕ_w . The exact modulation is unresolved as ϕ_w was not actively stabilized. The width of the envelope of that interference is on the order of the coherence length of the photons ($\approx 100 \mu\text{m}$). It indicates the spatial region for which the mode overlap is different from zero.

Furthermore, we can observe bosonic enhancement (cloning [30–32])—i.e., stimulation of the SPDC emission—which appears independent of the employed single-photon source and enhances the total count rate. This enhancement is visible for, e.g., a horizontally polarized WCB as input and registration of a threefold coincidence of *HHV*, Fig. 4(b). The single-photon term of the WCB ($\propto w_H^\dagger$) and the first-order emission of the SPDC ($\propto s_H^\dagger s_V^\dagger$) lead incoherently overlapped to $\propto w_H^\dagger s_H^\dagger s_V^\dagger |\text{vac}\rangle = |H\rangle_w |HV\rangle_s$. In contrast, a coherent superposition yields $\propto (s_H^\dagger)^2 s_V^\dagger |\text{vac}\rangle = \sqrt{2} |HHV\rangle_s$ —hence, an increase by a factor of 2 in the count rate due to the bosonic enhancement [33]. This effect occurs on the order of the coherence length of the photons ($\approx 100 \mu\text{m}$). In the experiment we observe an enhancement of 1.52 ± 0.03 . We attribute the deviation from the expected value of 2 to higher-order emissions of the WCB and SPDC, which add an offset to the three-photon count rate.

3. Fidelity of the states $|GHZ_4^+\rangle$ and $|W_4\rangle$

In the following we give a quantitative estimate of the influence on the quality of the desired four-photon states when a WCB is used instead of a single-photon source. To this end two effects have to be considered leading to the observation of imperfect states. First, the coherent superposition of different emission orders leads, in dependence on ϕ_w , to the observation of a different *pure* state. Second, higher-order emissions cause an *admixture* of correlated

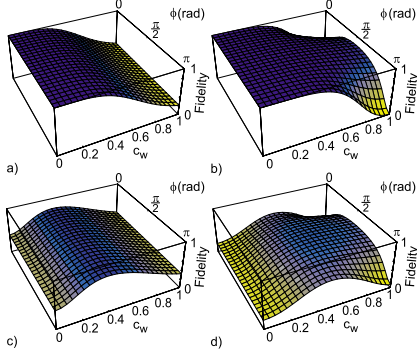
WIECZOREK *et al.*PHYSICAL REVIEW A **79**, 022311 (2009)

FIG. 5. (Color online) Calculated fidelity of W_4 (a) and GHZ_4^+ (b) states when considering only five-photon contributions [Eq. (9)]. Calculated fidelity of W_4 (c) and GHZ_4^+ (d) states when considering also six-photon contributions. All calculations assume a strength of the SPDC source of $|z_{\text{dc}}|=0.17$, which we experimentally observed for our setup.

noise. The first effect can be analyzed when considering all terms from Eqs. (6) and (7) that contribute directly to five photons (yielding the state on which a projective measurement is applied):

$$\propto -|z_{\text{dc}}|^2|z_w|e^{i\phi_w}W_j^\dagger(s_H^\dagger s_V^\dagger)^2/2 + i|z_{\text{dc}}||z_w|^3e^{i3\phi_w}W_j^\dagger(s_H^\dagger s_V^\dagger)/6 + |z_w|^5e^{i5\phi_w}W_j^\dagger/120. \quad (9)$$

Only the first term is necessary to observe the state $|\Delta_5\rangle$. The other terms significantly modify the desired state.

Exemplarily, we calculate the fidelity to the ideal GHZ_4^+ and W_4 states when the photons from Eq. (9) are symmetrically distributed onto five spatial modes and the respective projective measurement is performed. We obtain

$$F_{W_4} = 1/[1 + |z_w|^4/(9|z_{\text{dc}}|^2)],$$

$$F_{\text{GHZ}_4^+} = 1 - \frac{1}{2 + 36\frac{|z_{\text{dc}}|^2}{|z_w|^4} - 12\frac{|z_{\text{dc}}|}{|z_w|^2}\cos(2\phi_w)};$$

see Figs. 5(a) and 5(b). Both fidelities are better than >0.99 for $|z_w| < 0.2$, whereas for higher $|z_w|$ the fidelity decreases rapidly. This is the case as with increasing $|z_w|$ the second term of Eq. (9) grows relatively stronger than the first term and, thus, spoils the state quality. Obviously the relative phase ϕ_w becomes only relevant for $F_{\text{GHZ}_4^+}$. There, the highest fidelity values are found for $\phi_w = \pi/2$.

A second effect causes the admixture of correlated noise, which reduces the fidelity. This admixture is produced by the detection of additional fivefold coincidences that originate from six or more photons (higher-order emissions from both the SPDC and WCB), where multiple photons are registered by the same detector or some photons are not registered at all. As this leads to additional noise, the quality of the observed states is dependent on the photon detection efficiency.

For our setup we determined an efficiency for the photon coupling to the single-mode fiber of $\eta_c \approx \frac{1}{3}$ and a detection efficiency of $\eta_d \approx \frac{1}{3}$. For calculating the fidelity in that case, these loss channels are accounted for by additional beam splitters with ancillary output modes [19], where reflected photons are lost and transmitted photons (with probability η_t) correspond to detectable photons. We consider for this calculation all photon terms of five photons [see Eq. (9)] and the next higher-order contribution from six photons, which are obtained from the multiplication of Eqs. (6) with (7). The numerical results are shown in Figs. 5(c) and 5(d). The fidelity of the state $|W_4\rangle$ reaches its maximum of 0.776 for $|z_w| = 0.39$ independent of ϕ_w . For larger $|z_w|$ the fidelity decreases due to the increase of the multiple-photon terms of the WCB. For lower $|z_w|$ the fidelity decreases as the contribution from the third-order SPDC emission constitutes the major source of noise. The fidelity of the state $|\text{GHZ}_4^+\rangle$ reaches its maximum of 0.701 for $|z_w| = 0.6$. Again, it is phase dependent with maximal values for $\phi_w = \pi/2$. The dependence on $|z_w|$ follows the same arguments as given for the W_4 state.

The calculations show that the fidelity of each state is still high enough to demonstrate, e.g., four-photon entanglement via an entanglement witness, as for the state $|W_4\rangle$ ($|\text{GHZ}_4^+\rangle$) a fidelity larger than 0.75 (0.5) is sufficient for this purpose [24,34]. However, in the considerations so far, we neglected other experimental imperfections, like spectral distinguishability of photons. For pulsed type-II SPDC it is known that the broad pump spectrum results in the generation of photons with partial spectral distinguishability [35,36], which leads to an additional reduction in state fidelity. For example, the state $|D_4^{(2)}\rangle$ described in Sec. III A was observed with a fidelity of $F_{\text{expt}} = 0.844 \pm 0.008$ [11]. This fidelity value can be partly ascribed to higher-order contributions of the SPDC emission, which give a reduction in fidelity of about 9% [37]. However, the missing 7% can be attributed to a remaining degree of distinguishability of the SPDC photons and nonideal optical components. It is reasonable to expect that at least the same additional reduction of the fidelity in the proposed implementation occurs. Then, the fidelity for the state $|W_4\rangle$ is below the threshold for proving four-partite entanglement directly.

For this reason we suggest to use a (heralded) single-photon source instead of a WCB in order to achieve higher fidelity values. The utilization of a single-photon source avoids, on the one hand, noise from higher-order contributions of the WCB and therefore also phase dependence of the state. On the other hand, even noise from the SPDC alone would become negligible as the heralding signal from the single-photon source serves as a trigger for a valid detection event, and thus, the SPDC noise is suppressed. Alternatively, one could realize the state $|D_6^{(3)}\rangle$ with photons coming from the third-order SPDC emission, however at the cost of introducing again SPDC higher-order noise. Both alternative implementations demand new and stronger photon sources, which are currently being developed.

IV. CONCLUSION

We have demonstrated possibilities for the observation of SLOCC-inequivalent families of three- and four-qubit en-

tangled states. They are based on the property of the states $|D_4^{(2)}\rangle$ and $|\Delta_5\rangle$ to allow access to different classes of quantum states via projective measurements on single qubits.

We experimentally demonstrated that indeed all types of three-qubit entangled states can be obtained from $|D_4^{(2)}\rangle$. We presented a scheme how the states $|\Delta_5\rangle$ can be observed experimentally. As this requires the use of an additional photon, it still poses a considerable challenge when reasonable count rates are to be achieved. We could demonstrate that the most simple approach—i.e., substituting the single photon by a weak coherent beam—leads to a drastic reduction of the state quality. Yet we identified two alternative possibilities to realize the powerful scheme we presented, which both seem achievable in the near future.

Altogether, our scheme is an alternative method [6,9] for the observation of many different multipartite entangled states. We are optimistic that sources for the observation of the presented states will soon be available and that schemes relying on the same kind of approach will allow the observation of many other interesting quantum states in the future.

ACKNOWLEDGMENTS

We would like to thank Enrique Solano for stimulating discussions. We acknowledge the support of this work by the DFG-Cluster of Excellence MAP, the EU Project QAP, and the DAAD exchange program. W.W. acknowledges support by QCCC of the Elite Network of Bavaria and the Studienstiftung des dt. Volkes.

- [1] C. H. Bennett and D. P. DiVincenzo, *Nature (London)* **404**, 247 (2000).
- [2] W. Dür, G. Vidal, and J. I. Cirac, *Phys. Rev. A* **62**, 062314 (2000).
- [3] F. Verstraete, J. Dehaene, B. DeMoor, and H. Verschelde, *Phys. Rev. A* **65**, 052112 (2002).
- [4] L. Lamata, J. Leon, D. Salgado, and E. Solano, *Phys. Rev. A* **74**, 052336 (2006).
- [5] D. Bouwmeester, J.-W. Pan, M. Daniell, H. Weinfurter, and A. Zeilinger, *Phys. Rev. Lett.* **82**, 1345 (1999); J.-W. Pan, M. Daniell, S. Gasparoni, G. Weihs, and A. Zeilinger, *ibid.* **86**, 4435 (2001); M. Eibl, S. Gaertner, M. Bourennane, C. Kurtsiefer, M. Zukowski, and H. Weinfurter, *ibid.* **90**, 200403 (2003); M. Eibl, N. Kiesel, M. Bourennane, C. Kurtsiefer, and H. Weinfurter, *ibid.* **92**, 077901 (2004); Z. Zhao *et al.*, *Nature (London)* **430**, 54 (2004); H. Mikami, Y. Li, K. Fukuoka, and T. Kobayashi, *Phys. Rev. Lett.* **95**, 150404 (2005); N. Kiesel, C. Schmid, U. Weber, G. Toth, O. Guhne, R. Ursin, and H. Weinfurter, *Phys. Rev. Lett.* **95**, 210502 (2005); P. Walther *et al.*, *Nature (London)* **434**, 169 (2005); C.-Y. Lu *et al.*, *Nat. Phys.* **3**, 91 (2007).
- [6] W. Wieczorek, C. Schmid, N. Kiesel, R. Pohlner, O. Guhne, and H. Weinfurter, *Phys. Rev. Lett.* **101**, 010503 (2008).
- [7] R. Ionicioiu, A. E. Popescu, W. J. Munro, and T. P. Spiller, *Phys. Rev. A* **78**, 052326 (2008).
- [8] C. Cabrillo, J. I. Cirac, P. García-Fernández, and P. Zoller, *Phys. Rev. A* **59**, 1025 (1999); S. Bose, P. L. Knight, M. B. Plenio, and V. Vedral, *Phys. Rev. Lett.* **83**, 5158 (1999); C. Skornia, J. vonZanthier, G. S. Agarwal, E. Werner, and H. Walther, *Phys. Rev. A* **64**, 063801 (2001); L.-M. Duan, M. D. Lukin, J. I. Cirac, and P. Zoller, *Nature (London)* **414**, 413 (2001); L.-M. Duan and H. J. Kimble, *Phys. Rev. Lett.* **90**, 253601 (2003); C. Simon and W. T. M. Irvine, *ibid.* **91**, 110405 (2003); C. Thiel, J. von Zanthier, T. Bastin, E. Solano, and G. S. Agarwal, *ibid.* **99**, 193602 (2007).
- [9] T. Bastin *et al.*, e-print arXiv:0710.3720.
- [10] R. H. Dicke, *Phys. Rev.* **93**, 99 (1954).
- [11] N. Kiesel, C. Schmid, G. Toth, E. Solano, and H. Weinfurter, *Phys. Rev. Lett.* **98**, 063604 (2007).
- [12] C. Schmid *et al.*, in *Quantum Communication and Security*, edited by M. Żukowski, S. Kilin, and J. Kowalik, p. 113 (IOS Press, Amsterdam, 2007).
- [13] C. Schmid, N. Kiesel, W. Wieczorek, R. Pohlner, and H. Weinfurter, *Proc. SPIE* **6780**, 67800E (2007).
- [14] L. Lamata, J. Leon, D. Salgado, and E. Solano, *Phys. Rev. A* **75**, 022318 (2007).
- [15] V. Coffman, J. Kundu, and W. K. Wootters, *Phys. Rev. A* **61**, 052306 (2000).
- [16] A. Sen(De), U. Sen, and M. Żukowski, *Phys. Rev. A* **68**, 032309 (2003).
- [17] In order to obtain the family of states $\mu(\alpha, \alpha', \epsilon, \epsilon')|\text{GHZ}_4\rangle + \nu(\alpha, \alpha', \epsilon, \epsilon')|D_4^{(2)}\rangle$, we need to apply the local transformations $(T_2 T_1)^{\otimes 4}$ on the states of Eq. (4), where
- $$T_1 = \begin{pmatrix} x & y \\ x & -y \end{pmatrix}$$
- and $T_2 = (z1 - \sigma_z)^{0.25}$ with $x = \exp(i\epsilon/2)\sqrt{\alpha'\beta/2}$, $y = \exp(-i\epsilon'/2)\sqrt{\alpha\beta'/2}$, and $z = 0.75\{\exp[i(\epsilon' - \epsilon)/2]\alpha\alpha' + \exp[-i(\epsilon' - \epsilon)/2]\beta\beta'\}/\sqrt{\alpha\alpha'\beta\beta'}$. A simple calculation shows that the absolute value of μ (and accordingly ν) can take all values between 0 and 1. For particular parameters other types of states can be obtained; e.g., if only the local transformations $T_1^{\otimes 4}$ are applied on the states of Eq. (4) we can obtain, for example, the state $\sqrt{6/7}|HHHH\rangle - \sqrt{1/7}|D_4^2\rangle$ [$\alpha = \alpha' = 1/\sqrt{2}$ and $\epsilon = 2 \arccos(2/3) + \epsilon'$].
- [18] T. Bastin *et al.* (unpublished).
- [19] P. Kok and S. L. Braunstein, *Phys. Rev. A* **61**, 042304 (2000).
- [20] H. Weinfurter and M. Żukowski, *Phys. Rev. A* **64**, 010102(R) (2001).
- [21] M. Bourennane, M. Eibl, C. Kurtsiefer, S. Gaertner, H. Weinfurter, O. Guhne, P. Hyllus, D. Bruss, M. Lewenstein, and A. Sanpera, *Phys. Rev. Lett.* **92**, 087902 (2004).
- [22] C. Schmid, N. Kiesel, W. Laskowski, W. Wieczorek, M. Żukowski, and H. Weinfurter, *Phys. Rev. Lett.* **100**, 200407 (2008).
- [23] A. Acin, D. Bruß, M. Lewenstein, and A. Sanpera, *Phys. Rev. Lett.* **87**, 040401 (2001).
- [24] H. Häffner *et al.*, *Nature (London)* **438**, 643 (2005).
- [25] M. Oxborrow and A. G. Sinclair, *Contemp. Phys.* **46**, 173

WIECZOREK *et al.*

- (2005).
- [26] B. Lounis and M. Orrit, *Rep. Prog. Phys.* **68**, 1129 (2005).
- [27] P. P. Rohde, T. C. Ralph, and M. A. Nielsen, *Phys. Rev. A* **72**, 052332 (2005).
- [28] J. G. Rarity and P. R. Tapster, *Phys. Rev. A* **59**, R35 (1999).
- [29] L. Mandel and E. Wolf, *Optical Coherence and Quantum Optics* (Cambridge University Press, Cambridge, England, 1995).
- [30] A. Lamas-Linares, C. Simon, J. C. Howell, and D. Bouwmeester, *Science* **296**, 712 (2002).
- [31] F. Sciarrino and F. DeMartini, *Phys. Rev. A* **72**, 062313 (2005).
- PHYSICAL REVIEW A **79**, 022311 (2009)
- [32] F. DeMartini, F. Sciarrino, and V. Secondi, *Phys. Rev. Lett.* **95**, 240401 (2005).
- [33] F. W. Sun, B. H. Liu, Y. X. Gong, Y. F. Huang, Z. Y. Ou, and G. C. Guo, *Phys. Rev. Lett.* **99**, 043601 (2007).
- [34] G. Tóth and O. Gühne, *Phys. Rev. A* **72**, 022340 (2005).
- [35] W. P. Grice and I. A. Walmsley, *Phys. Rev. A* **56**, 1627 (1997).
- [36] T. E. Keller and M. H. Rubin, *Phys. Rev. A* **56**, 1534 (1997).
- [37] N. Kiesel, Ph.D. thesis, Ludwig-Maximilians-Universität München, 2007.

P5.3

New Journal of Physics

The open-access journal for physics

Practical methods for witnessing genuine multi-qubit entanglement in the vicinity of symmetric states

Géza Tóth^{1,2,3,7}, Witlef Wieczorek^{4,5}, Roland Krischek^{4,5},
Nikolai Kiesel^{4,5,6}, Patrick Michelberger^{4,5}
and Harald Weinfurter^{4,5}

¹ Department of Theoretical Physics, The University of the Basque Country, PO Box 644, E-48080 Bilbao, Spain

² Ikerbasque–Basque Foundation for Science, Alameda Urquijo 36, E-48011 Bilbao, Spain

³ Research Institute for Solid State Physics and Optics, Hungarian Academy of Sciences, PO Box 49, H-1525 Budapest, Hungary

⁴ Max-Planck-Institut für Quantenoptik, Hans-Kopfermann-Strasse 1, D-85748 Garching, Germany

⁵ Fakultät für Physik, Ludwig-Maximilians-Universität, D-80799 Garching, Germany

⁶ Institute for Quantum Optics and Quantum Information (IQOQI), Austrian Academy of Sciences, Boltzmannngasse 3, A-1090 Vienna, Austria

E-mail: toth@alumni.nd.edu

New Journal of Physics **11** (2009) 083002 (18pp)

Received 26 March 2009

Published 4 August 2009

Online at <http://www.njp.org/>

doi:10.1088/1367-2630/11/8/083002

Abstract. We present general numerical methods to construct witness operators for entanglement detection and estimation of the fidelity. Our methods are applied to detecting entanglement in the vicinity of a six-qubit Dicke state with three excitations and also to further entangled symmetric states. All our witnesses are designed to keep the measurement effort small. We also present general results on the efficient local decomposition of permutationally invariant operators, which makes it possible to measure projectors to symmetric states efficiently.

⁷ Author to whom any correspondence should be addressed.

Contents

1. Introduction	2
2. Basic definitions and general methods	4
2.1. Projector witness	5
2.2. Witnesses based on the projector witness	7
2.3. Witnesses independent from the projector witness	8
3. Witnesses for a six-qubit Dicke state with three excitations	9
3.1. Witnesses based on the projector witness	9
3.2. Witness independent from the projector witness	11
4. Witnesses for states derived from $D_6^{(3)}\rangle$ via projections	13
4.1. Witnesses for the superposition of five-qubit Dicke states	13
4.2. Witness for the four-qubit W state	13
4.3. Three-setting witness for the four-qubit Dicke state	13
4.4. Measuring the projector witness for the four-qubit Dicke state	14
5. Conclusions	14
Acknowledgments	15
Appendix A. Semidefinite programming used for obtaining witnesses	15
Appendix B. List of MATLAB subroutines	15
Appendix C. Witnesses for systems with 5–10 qubits	16
References	16

1. Introduction

Entanglement plays a central role in quantum mechanics and in quantum information processing applications [1]. Moreover, it is also the main goal in today's quantum physics experiments aiming to create various quantum states [2]. For example, entanglement has been realized with photonic systems using parametric down-conversion and conditional detection [3]–[9], with trapped cold ions [10]–[12], in cold atomic ensembles [13], in cold atoms in optical lattices [14] and in diamond between the electron and nuclear spins [15]. These experiments aimed at creating entangled states. Entanglement makes it possible for some quantum algorithms (e.g. prime factoring, searching in a database) to outperform their classical counterparts. Entangled particles are needed for quantum teleportation and other quantum communication protocols. Moreover, the creation of large entangled states might lead to new insights about how a classical macroworld emerges from a quantum microworld.

In a multi-qubit experiment, typically the full density matrix is not known, and only few measurements can be made, yet one would still like to ensure that the prepared state is entangled. One possibility is applying entanglement witnesses [16, 17]. These are observables that have a positive expectation value for separable states, while for some entangled states their expectation value is negative. Since these witness operators are multi-qubit operators, they typically cannot be measured directly and must be decomposed into the sum of locally measurable operators, which are just products of single-qubit operators [4, 18, 19].

For many quantum states, like the Greenberger–Horne–Zeilinger (GHZ, [20]) states and the cluster states [21] such a decomposition of projector-based witness operators seems to be

very difficult: the number of terms in a decomposition to a sum of products of Pauli matrices increases rapidly with the number of qubits. However, practically useful entanglement witnesses with two measurement settings can be constructed for such states [5, 22]. It also turned out that there are decompositions of the projector for GHZ and W states in which the increase with the number of qubits is linear [23].

However, optimal decomposition of an operator is a very difficult, unsolved problem. Moreover, in general, it is still a difficult task to construct efficient entanglement witnesses for a given quantum state. For that, typically we need to obtain the maximum of some operators for product states. In most of the cases, we would like to detect genuine multipartite entanglement. For that, we need to obtain the maximum of these operators for biseparable states, which is again a very hard problem.

In this paper, our goal is to design witnesses that make it possible to detect genuine multipartite entanglement with few measurements, and also to estimate the fidelity of an experimentally prepared state with respect to the target state. Here three strategies are applied to find an experimentally realizable witness. (i) The first strategy is based on measuring the projector-based witness

$$\mathcal{W}^{(P)} = \text{const.} \cdot \mathbb{1} - |\Psi\rangle\langle\Psi| \quad (1)$$

for the detection of genuine multipartite entanglement. $|\Psi\rangle$ is the target state of the experiment. For reducing experimental effort, the aim is to find an efficient decomposition of the projector. (ii) The second strategy is to find a witness that needs fewer measurements than the projector witness, but the price for that might be a lower robustness against noise. The search for such a witness can be simplified if we look for a witness \mathcal{W} such that

$$\mathcal{W} - \alpha\mathcal{W}^{(P)} \geq 0 \quad (2)$$

for some $\alpha > 0$. Such a witness is guaranteed to detect genuine multi-qubit entanglement. The advantage of this approach is that the expectation value of \mathcal{W} can be used to find a lower bound on the fidelity. (iii) The third strategy is to find a witness independent from the projector witness. In this case, one has to find an easily measurable operator whose expectation value takes its maximum for the target state. Then, one has to find the maximum of this operator for biseparable states. Any state that has an operator expectation value larger than that is genuine multipartite entangled.

For the optimization of entanglement witnesses for small experimental effort and large robustness to noise, we use semidefinite programming [24]–[29]. Our methods can efficiently be used for multi-qubit systems with up to about 10 qubits. This is important, since there are many situations where semidefinite programming could help theoretically, but in practice the calculations cannot be carried out even for systems of modest size.

We use our methods to design witnesses detecting entanglement in the vicinity of symmetric Dicke states. An N -qubit symmetric Dicke state with m excitations is defined as [30, 31]

$$|D_N^{(m)}\rangle := \binom{N}{m}^{-1/2} \sum_k \mathcal{P}_k(|1_1, 1_2, \dots, 1_m, 0_{m+1}, \dots, 0_N\rangle), \quad (3)$$

where $\sum_k \mathcal{P}_k(\cdot)$ denotes summation over all distinct permutations of the spins. $|D_N^{(1)}\rangle$ is the well-known N -qubit W state. The witnesses we will introduce in the following have already been used in the photonic experiment described in [32], aiming to observe a $|D_6^{(3)}\rangle$

4

IOP Institute of Physics Φ DEUTSCHE PHYSIKALISCHE GESELLSCHAFT

state [32]⁸. We show that genuine multi-qubit entanglement can be detected and the fidelity with respect to the above highly entangled state can efficiently be estimated with two and three measurement settings, respectively. As a byproduct, we will also derive an upper bound for the number of settings needed to measure any permutationally invariant operator. We show that such operators can be efficiently measured even for large systems.

The structure of our paper is as follows. In section 2, we present the basic methods for constructing witnesses. In section 3, we use these methods for constructing witnesses to detect entanglement in the vicinity of a six-qubit symmetric Dicke state with three excitations. In section 4, we present witnesses for states obtained from the above state by measuring some of the qubits. In appendix A, we summarize the tasks that can be solved by semidefinite programming, when looking for suitable entanglement witnesses. In appendix B, we summarize some of the relevant numerical routines of the QUBIT4MATLAB 3.0 program package [34]. In appendix C, we present entanglement conditions for systems with 5–10 qubits that will be relevant in future experiments.

2. Basic definitions and general methods

A multi-qubit quantum state is entangled if it cannot be written as a convex combination of product states. However, in a multi-qubit experiment we would like to detect genuine multi-qubit entanglement [35]: the presence of such entanglement indicates that all the qubits are entangled with each other, not only some of them. We will now need the following definitions:

Definition 1. A pure multi-qubit quantum state is called **biseparable** if it can be written as the tensor product of two, possibly entangled, multi-qubit states

$$|\Psi\rangle = |\Psi_1\rangle \otimes |\Psi_2\rangle. \quad (4)$$

A mixed state is called biseparable, if it can be obtained by mixing pure biseparable states. If a state is not biseparable then it is called **genuine multi-partite entangled**. In this paper, we will consider witness operators that detect genuine multipartite entanglement.

Definition 2. While an entanglement witness is an observable, typically it cannot be measured directly. This is because in most experiments only local measurements are possible. At each qubit k we are able to measure a single-qubit operator M_k , which we can do simultaneously at all the qubits. If we repeat such measurements, then we obtain the expectation values of $2^N - 1$ multi-qubit operators. For example, for $N = 3$ these are $M_1 \otimes \mathbb{1} \otimes \mathbb{1}$, $\mathbb{1} \otimes M_2 \otimes \mathbb{1}$, $\mathbb{1} \otimes \mathbb{1} \otimes M_3$, $M_1 \otimes M_2 \otimes \mathbb{1}$, $M_1 \otimes \mathbb{1} \otimes M_3$, $\mathbb{1} \otimes M_2 \otimes M_3$, $M_1 \otimes M_2 \otimes M_3$. The set of single-qubit operators measured is called the **measurement setting** [4] and it can be given as $\{M_1, M_2, M_3, \dots, M_N\}$. When we consider an entanglement condition, it is important to know how many measurement settings are needed for its evaluation.

Definition 3. Many experiments aim at preparing some, typically pure quantum state ρ . An entanglement witness is then designed to detect the entanglement of this state. However, in real experiments such a state is never produced perfectly, and the realized state is mixed with noise as given by the following formula:

$$\rho_{\text{noisy}}(p_{\text{noise}}) = (1 - p_{\text{noise}})\rho + p_{\text{noise}}\rho_{\text{noise}}. \quad (5)$$

⁸ For another experiment aiming to observe a six-qubit Dicke state see Prevedel *et al* [33]. See also the related theoretical work of Campbell *et al* [33].

where p_{noise} is the ratio of noise and ϱ_{noise} is the noise. If we consider white noise then $\varrho_{\text{noise}} = \mathbb{1}/2^N$. The **noise tolerance** of a witness \mathcal{W} is characterized by the largest p_{noise} for which we still have $\text{Tr}(\mathcal{W}\varrho_{\text{noisy}}) < 0$.

In this paper, we will consider three possibilities for detecting genuine multi-qubit entanglement, explained in the following subsections. Later, we will use these ideas to construct various entanglement witnesses.

2.1. Projector witness

A witness detecting genuine multi-qubit entanglement in the vicinity of a pure state $|\Psi\rangle$ can be constructed with the projector as

$$\mathcal{W}_{\Psi}^{(P)} := \lambda_{\Psi}^2 \mathbb{1} - |\Psi\rangle\langle\Psi|, \quad (6)$$

where λ is the maximum of the Schmidt coefficients for $|\Psi\rangle$, when all bipartitions are considered [4]. For the states considered in this paper, projector-based witnesses are given by [4, 12, 37]

$$\mathcal{W}_{D(N,N/2)}^{(P)} := \frac{1}{2} \frac{N}{N-1} \mathbb{1} - |D_N^{(N/2)}\rangle\langle D_N^{(N/2)}|, \quad (7)$$

$$\mathcal{W}_{D(N,1)}^{(P)} := \frac{N-1}{N} \mathbb{1} - |D_N^{(1)}\rangle\langle D_N^{(1)}|. \quad (8)$$

These witnesses must be decomposed into the sum of locally measurable terms. For this decomposition, the following observations will turn out to be very important.

Observation 1. A permutationally invariant operator A can always be decomposed as [45]

$$A = \sum_n c_n a_n^{\otimes N}, \quad (9)$$

where a_n are single-qubit operators, and such a decomposition can be straightforwardly obtained.

Proof. Any permutationally invariant multi-qubit operator A can be decomposed as

$$A = \sum_n c_n \sum_k P_k (B_{n,1} \otimes B_{n,2} \otimes B_{n,3} \otimes \cdots \otimes B_{n,N}) P_k, \quad (10)$$

where $B_{n,m}$ are single-qubit operators, c_n are constants, and P_k are the full set of operators permuting the qubits. For odd N , we can use the identity

$$\begin{aligned} \sum_k P_k (B_{n,1} \otimes B_{n,2} \otimes B_{n,3} \otimes \cdots \otimes B_{n,N}) P_k \\ = 2^{-(N-1)} \sum_{\substack{s_1, s_2, \dots, s_N = \pm 1, \\ s_1 s_2 s_3 \cdots s_N = +1}} (s_1 B_{n,1} + s_2 B_{n,2} + s_3 B_{n,3} + \cdots)^{\otimes N}. \end{aligned} \quad (11)$$

6

IOP Institute of Physics Φ DEUTSCHE PHYSIKALISCHE GESELLSCHAFT

Substituting (11) into (10), we obtain a decomposition of the form (9). Equation (11) can be proved by carrying out the summation and expanding the brackets. Due to the $s_1 s_2 s_3 \cdots s_N = +1$ condition, the coefficient of $B_{n,1} \otimes B_{n,2} \otimes B_{n,3} \otimes \cdots \otimes B_{n,N}$ is 1. The coefficient of terms like $B_{n,1} \otimes B_{n,1} \otimes B_{n,3} \otimes \cdots \otimes B_{n,N}$, that is, terms containing one of the variables more than once is zero. For even N , a similar proof can be carried out using⁹

$$\begin{aligned} \sum_k P_k(B_{n,1} \otimes B_{n,2} \otimes B_{n,3} \otimes \cdots \otimes B_{n,N}) P_k \\ = 2^{-(N-1)} \sum_{\substack{s_1, s_2, \dots, s_N = \pm 1, \\ s_1 s_2 s_3 \cdots s_N = +1}} s_1(B_{n,1} + s_2 B_{n,2} + s_3 B_{n,3} + \cdots)^{\otimes N}. \end{aligned} \quad (12)$$

Next, we give two examples for the application of (11) and (12) for the decomposition of simple expressions

$$\sum_k P_k(\sigma_x \otimes \sigma_y) P_k = \frac{1}{2} \left\{ (\sigma_x + \sigma_y)^{\otimes 2} - (\sigma_x - \sigma_y)^{\otimes 2} \right\}, \quad (13)$$

$$\begin{aligned} \sum_k P_k(\sigma_x \otimes \sigma_y \otimes \sigma_z) P_k = \frac{1}{4} \left\{ (\sigma_x + \sigma_y + \sigma_z)^{\otimes 3} + (\sigma_x - \sigma_y - \sigma_z)^{\otimes 3} + (-\sigma_x - \sigma_y + \sigma_z)^{\otimes 3} \right. \\ \left. + (-\sigma_x + \sigma_y - \sigma_z)^{\otimes 3} \right\}, \end{aligned} \quad (14)$$

where σ_k are the Pauli spin matrices. While the first example does not reduce the number of settings needed, the second example reduces the number of settings from 6 to 4. \square

Next, we present a method to get efficient decompositions for permutationally invariant operators.

Observation 2. Any N -qubit permutationally invariant operator A can be measured with at most

$$\mathcal{L}_N = \frac{2}{3}N^3 + N^2 + \frac{4}{3}N \quad (15)$$

local measurement settings, using (11) and (12).

Proof. We have to decompose first A into the sum of Pauli group elements as

$$A = \sum_{i, j, m: i+j+m \leq N} c_{ijm} \sum_k P_k(\sigma_x^{\otimes i} \otimes \sigma_y^{\otimes j} \otimes \sigma_z^{\otimes m} \otimes \mathbb{1}^{\otimes(N-i-j-m)}) P_k, \quad (16)$$

where c_{ijm} are some constants. Then, such a decomposition can be transformed into another one of the form (9), using (11) and (12). All of the settings needed are of the form $\{a, a, a, \dots, a\}$ where $a = n_x \sigma_x + n_y \sigma_y + n_z \sigma_z$, n_k are integer and $1 \leq \sum_k |n_k| \leq N$. Simple counting leads to an upper bound \mathcal{L}_N for the number of settings given in (15). Here we considered that (n_x, n_y, n_z) and $(-n_x, -n_y, -n_z)$ describe the same setting. An even better bound can be obtained using that (n_x, n_y, n_z) and (cn_x, cn_y, cn_z) for some $c \neq 0$ represent the same setting. An algorithm based

⁹ A similar decomposition with continuous number of terms is of the form $\sum_k P_k(B_1 \otimes B_2 \otimes \dots) P_k \propto \int_{\phi_i \in [0, 2\pi]} [e^{i\phi_1} B_1 + e^{i\phi_2} B_2 + \dots + e^{i\phi_{N-1}} B_{N-1} + e^{-i(\phi_1 + \phi_2 + \dots + \phi_{N-1})} B_N]^{\otimes N} d\phi_1 d\phi_2 \dots d\phi_{N-1}$. Such a construction has been used for the $N = 2$ case in [48].

7

IOP Institute of Physics Φ DEUTSCHE PHYSIKALISCHE GESELLSCHAFT

on this leads to the bounds $\mathcal{L}'_N = 9, 25, 49, 97, 145, 241, 337, 481, 625$ for $N = 2, 3, \dots, 10$ qubits, respectively.

For the projector $|D_N^{(N/2)}\rangle\langle D_N^{(N/2)}|$, the decomposition to Pauli group elements contain only terms in which each Pauli matrix appears an even number of times. Hence, all of the settings needed are of the form $\{a, a, a, \dots, a\}$ where $a = 2n_x\sigma_x + 2n_y\sigma_y + 2n_z\sigma_z$, n_k are integer and $1 \leq \sum_k |n_k| \leq N/2$. For this reason, $\mathcal{L}_{N/2}$ and $\mathcal{L}'_{N/2}$ are upper bounds for the number of settings needed to measure this operator.

Let us discuss the consequences of observations 1 and 2. They essentially state that the number of settings needed to measure a permutationally invariant operator scales only polynomially with the number of qubits. This is important since for operators that are not permutationally invariant, the scaling is known to be exponential [36]. Moreover, even if we can measure only correlation terms of the form $a^{\otimes N}$, we can measure any permutationally invariant operator. \square

2.2. Witnesses based on the projector witness

We can construct witnesses that are easier to measure than the projector witness, but they are still based on the projector witness. We use the idea mentioned in the introduction. If $\mathcal{W}^{(p)}$ is the projector witness and (2) is fulfilled for some $\alpha > 0$, then \mathcal{W} is also a witness. This is because \mathcal{W} has a negative expectation value only for states for which $\mathcal{W}^{(p)}$ also has a negative expectation value. The advantage of obtaining witnesses this way is that we can have a lower bound on the fidelity from the expectation value of the witness as

$$\mathrm{Tr}(\varrho|\Psi\rangle\langle\Psi|) \geq \lambda_{\Psi}^2 - \frac{1}{\alpha} \mathrm{Tr}(\mathcal{W}\varrho). \quad (17)$$

We will look for such witnesses numerically, such that the noise tolerance of the witness be the largest possible. This search can be simplified by the following observation.

Observation 3. Since we would like to construct a witness detecting genuine multi-qubit entanglement in the vicinity of a permutationally invariant state, it is enough to consider witness operators that are also permutationally invariant.

Proof. Let us consider a witness operator that detects entanglement in the vicinity of a permutationally invariant state ϱ and its expectation value takes its minimum for ϱ . Then, based on (5), the witness \mathcal{W} detects entanglement if

$$p_{\text{noise}} > \frac{\mathrm{Tr}(\mathcal{W}\varrho)}{\mathrm{Tr}(\mathcal{W}\varrho) - \mathrm{Tr}(\mathcal{W}\varrho_{\text{noise}})}. \quad (18)$$

For a permutationally invariant state ϱ , we have $\varrho = \frac{1}{N_p} \sum_k P_k \varrho P_k$, where N_p is the number of different permutation operators P_k . We assume that the same holds also for ϱ_{noise} . Let us define the permutationally invariant operator $\mathcal{W}' = \frac{1}{N_p} \sum_k P_k \mathcal{W} P_k$. The operator \mathcal{W}' is non-negative on all biseparable states since

$$\inf_{\varrho \in \mathcal{B}} \mathrm{Tr}(\mathcal{W}\varrho) = \frac{1}{N_p} \sum_k \inf_{\varrho \in \mathcal{B}} \mathrm{Tr}(\mathcal{W} P_k \varrho P_k) \leq \inf_{\varrho \in \mathcal{B}} \mathrm{Tr}(\mathcal{W}'\varrho), \quad (19)$$

where \mathcal{B} is the set of biseparable states. Hence, \mathcal{W}' is a witness detecting genuine multipartite entanglement. Since we have $\mathrm{Tr}(\mathcal{W}\varrho) = \mathrm{Tr}(\mathcal{W}'\varrho)$, and $\mathrm{Tr}(\mathcal{W}\varrho_{\text{noise}}) = \mathrm{Tr}(\mathcal{W}'\varrho_{\text{noise}})$,

the robustness to noise of \mathcal{W}' is identical to that of \mathcal{W} . Hence, it is sufficient to look for witnesses that are permutationally invariant.

We will first consider measuring the $\{\sigma_x, \sigma_x, \sigma_x, \sigma_x, \sigma_x, \sigma_x\}$ and $\{\sigma_y, \sigma_y, \sigma_y, \sigma_y, \sigma_y, \sigma_y\}$ settings, where σ_l are the Pauli spin matrices. This we call the two-setting case. Then we will consider measuring also the $\{\sigma_z, \sigma_z, \sigma_z, \sigma_z, \sigma_z, \sigma_z\}$ setting, which we call the three-setting case. Due to observation 3, we consider only permutationally invariant witnesses. Such witnesses can be written as

$$\mathcal{W}(\alpha_0, \{\alpha_{ln}\}) := \alpha_0 \cdot \mathbb{1} + \sum_{l=x,y,z} \sum_{n=1}^N \alpha_{ln} \sum_k \mathcal{P}_k[\sigma_l^{\otimes n} \otimes \mathbb{1}^{\otimes(N-n)}], \quad (20)$$

where the summation is over all distinct permutations, and α_0 and α_{ln} are some constants. We will consider a simpler but equivalent formulation

$$\mathcal{W}(c_0, \{c_{ln}\}) := c_0 \cdot \mathbb{1} + \sum_{l=x,y,z} \sum_{n=1}^N c_{ln} J_l^n, \quad (21)$$

where c_0, c_{ln} are the coefficients of the linear combination defining the witness and J_l are the components of the total angular momentum given as

$$J_l = \frac{1}{2} \sum_{k=1}^N \sigma_l^{(k)}. \quad (22)$$

Here $\sigma_l^{(k)}$ denotes a Pauli spin matrix acting on qubit (k) .

Finally, if we consider detecting entanglement in the vicinity of $|D_N^{(N/2)}\rangle$ states, then further simplifications can be made. For this state and also for the completely mixed state all odd moments of J_l have a zero expectation value. For any witness of the form (21), the maximum for biseparable states does not change if we flip the sign of c_{ln} for all odd n . Hence, following from an argument similar to the one in observation 3 concerning permutational symmetry, it is enough to consider only even powers of J_l in our witnesses. \square

2.3. Witnesses independent from the projector witness

In general, we can also design witnesses without any relation to the projector witness. We can use an easily measurable operator M to make a witness of the form

$$\mathcal{W} := c\mathbb{1} - M, \quad (23)$$

where c is some constant. To make sure that (23) is a witness for genuine multipartite entanglement, i.e. $\langle \mathcal{W} \rangle$ is positive on all biseparable states, we have to set c to

$$c = \max_{|\psi\rangle \in \mathcal{B}} \langle M \rangle_{|\psi\rangle}, \quad (24)$$

where \mathcal{B} is the set of biseparable states. The optimization needed for (24) can be done analytically. For example, for the $|D_4^{(2)}\rangle$ state a witness has been presented that detects genuine four-qubit entanglement by measuring second moments of angular momentum operators [37]. However, analytical calculations become exceedingly difficult as the number of qubits increases.

The optimization can also be done numerically, but one cannot be sure that simple numerical optimization finds the global maximum. (See appendix B for a reference to such a MATLAB program.) Semidefinite programming is known to find the global optimum, but

the optimization task (24) cannot be solved directly by semidefinite programming. Instead of looking for the maximum for biseparable states, using semidefinite programming, we can look for the maximum for states that have a positive partial transpose (PPT) [24, 38] (see appendices A and B). This way we can obtain

$$c' := \max_I \max_{\rho \geq 0, \rho^{T_I} \geq 0} \langle M \rangle_{\rho}, \quad (25)$$

for which $c' \geq c$. The first maximization is over all bipartitions I . Thus, when putting c' into the place of c in (23), we obtain a witness that detects only genuine multipartite entanglement. In many cases simple numerics show that $c = c'$. In this case, our witnesses are optimal in the sense that some biseparable state gives a zero expectation value for these witnesses.

Finally, let us discuss how to find the operator M in (23) for a two- or a three-setting witness, in particular, for detecting entanglement in the vicinity of $|D_N^{(N/2)}\rangle$. Based on section 2.2, we have to look for an operator that contains only even powers of J_I . Hence, the general form of a two-setting witness with moments up to second order is

$$\mathcal{W}_{D(N,N/2)}^{(I2)} := c_{DN} - (J_x^2 + J_y^2), \quad (26)$$

where c_{DN} is a constant¹⁰. The coefficients of J_x^2 and J_y^2 could still be different, however, this would not lead to witnesses with a better robustness to noise.

For other symmetric Dicke states, based on similar arguments, a general form of a witness containing moments of J_I up to second order such that it takes its minimum for $|D_N^{(m)}\rangle$ is of the form

$$\mathcal{W}_{D(N,m)}^{(I3)} := c_q - (J_x^2 + J_y^2) + q(J_z - \langle J_z \rangle_{|D_N^{(m)}\rangle})^2, \quad (27)$$

where c_q and q are constants. For the witnesses described in this section, the optimization process is more time-consuming than for the witnesses related to the projector witness. Because of that we presented witnesses of the above type that are constructed only with the first and second moments of the angular momentum operators, and thus contain a few free parameters.

3. Witnesses for a six-qubit Dicke state with three excitations

In this section, we will consider entanglement detection close to a six-qubit symmetric Dicke state with three excitations, denoted as $|D_6^{(3)}\rangle$. There are several proposals for creating Dicke states in various physical systems [40]–[43].

3.1. Witnesses based on the projector witness

3.1.1. Two-setting witness. Let us consider the two-setting case and define first the optimization problem we want to solve. We would like to look for the witness \mathcal{W} with the largest noise tolerance that fulfills the following requirements:

1. \mathcal{W} is a linear combination of certain basis operators B_k , that is, $\mathcal{W} = \sum_k c_k B_k$,
2. $\mathcal{W} - \alpha \mathcal{W}_{D(6,3)}^{(P)} \geq 0$ with some $\alpha > 0$.

¹⁰ Witnesses for the state $|D_6^{(3)}\rangle$ are presented with the structure factor in [39]. In a sense, these witnesses are written with collective quantities, after a site-dependent phase shift is applied.

10

IOP Institute of Physics Φ DEUTSCHE PHYSIKALISCHE GESELLSCHAFT

For the two-setting case we set $\{B_k\} = \{\mathbb{1}, J_x^2, J_y^2, J_x^4, J_y^4, J_x^6, J_y^6\}$. The second condition makes sure that \mathcal{W} is also a witness detecting genuine multipartite entanglement.

Note that *any* optimization algorithm can be used for looking for \mathcal{W} . Even if we do not find the global optimum, that is, the witness with the largest possible robustness to white noise, \mathcal{W} is still a witness detecting genuine multipartite entanglement. However, semidefinite programming can be used to find the global optimum (see appendix A). The two-setting witness obtained this way is

$$\mathcal{W}_{D(6,3)}^{(P2)} := 7.75 \cdot \mathbb{1} - \frac{35}{18}(J_x^2 + J_y^2) + \frac{55}{72}(J_x^4 + J_y^4) - \frac{5}{72}(J_x^6 + J_y^6), \quad (28)$$

which tolerates white noise if $p_{\text{noise}} < 0.1391$. Straightforward calculation shows that $\mathcal{W}_{D(6,3)}^{(P2)} - 2.5\mathcal{W}^{(P)} \geq 0$. Based on (17), $(0.6 - \langle \mathcal{W}_{D(6,3)}^{(P2)} \rangle) / 2.5$ bounds the fidelity from below.

3.1.2. Three-setting witness. Similarly we can look for the optimal witness for the three-setting case. The result is

$$\mathcal{W}_{D(6,3)}^{(P3)} := 1.5 \cdot \mathbb{1} - \frac{1}{45}(J_x^2 + J_y^2) + \frac{1}{36}(J_x^4 + J_y^4) - \frac{1}{180}(J_x^6 + J_y^6) + \frac{1007}{360}J_z^2 - \frac{31}{36}J_z^4 + \frac{23}{360}J_z^6. \quad (29)$$

White noise is tolerated if $p_{\text{noise}} < 0.2735$. It is easy to check that \mathcal{W} is a witness as $\mathcal{W}_{D(6,3)}^{(P3)} - 2.5\mathcal{W}^{(P)} \geq 0$.

Based on (17), the expectation value of this witness can be used to bound the fidelity as $F \geq 0.6 - \langle \mathcal{W}_{D(6,3)}^{(P3)} \rangle / 2.5 =: F'$. Here we will demonstrate how well the fidelity estimation works for our witness for noisy states. We consider first white noise, then non-white noise of the form

$$\rho_{\text{noisy}}^{(\text{NW})} := p_{D63} |D_6^{(3)}\rangle \langle D_6^{(3)}| + \frac{1 - p_{D63}}{2} (|D_6^{(2)}\rangle \langle D_6^{(2)}| + |D_6^{(4)}\rangle \langle D_6^{(4)}|), \quad (30)$$

with $p_{D63} = 4/7$, which is one of the relevant types of noise for the experiment of [32]. Note that the noise contains the original state $|D_6^{(3)}\rangle \langle D_6^{(3)}|$. The results are shown in figure 1. For the non-white noise (30), the fidelity estimate based on the witness yields a very good estimate.

Note that it is also possible to design a witness for the largest possible tolerance to the noise in (30). Due to the special form of the noise, the fidelity estimate turns out to be equal to the fidelity. This is remarkable: the fidelity can be obtained exactly with only three local measurements.

3.1.3. Measuring the projector-based witness. For measuring the projector-based witness (7) for $N = 6$, one has to decompose the projector in an efficient way. The straightforward decomposition into the weighted sum of products of Pauli spin matrices leads to a scheme that needs 183 settings, since for all local operators all the permutations have to be measured. The number of settings needed can be dramatically decreased if one is looking for a decomposition of the form (9). Observation 1 makes it possible to decompose the projector in this way such that only 25 settings are needed. We could further decrease the number of settings needed and found the following decomposition:

$$\begin{aligned} 64 |D_6^{(3)}\rangle \langle D_6^{(3)}| = & -0.6[\mathbb{1}] + 0.3[x \pm \mathbb{1}] - 0.6[x] + 0.3[y \pm \mathbb{1}] - 0.6[y] + 0.2[z \pm \mathbb{1}] - 0.2[z] \\ & + 0.2\text{Mermin}_{0,z} + 0.05[x \pm y \pm \mathbb{1}] - 0.05[x \pm z \pm \mathbb{1}] - 0.05[y \pm z \pm \mathbb{1}] \\ & - 0.05[x \pm y \pm z] + 0.2[x \pm z] + 0.2[y \pm z] + 0.1[x \pm y] \\ & + 0.6\text{Mermin}_{x,z} + 0.6\text{Mermin}_{y,z}. \end{aligned} \quad (31)$$

11

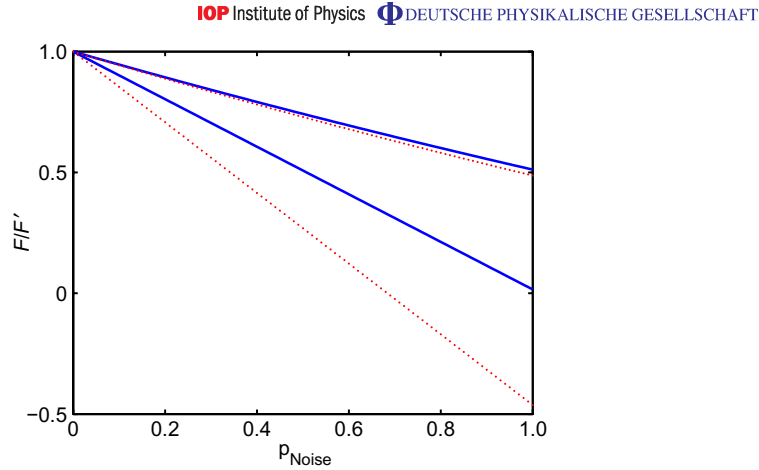


Figure 1. The fidelity F versus noise (solid) and the fidelity estimate F' versus noise (dotted), for the white noise (bottom two curves) and for the non-white noise (30) (top two curves). For the fidelity estimate, the three-setting witness (29) was used.

Here we use the notation $[x + y] = (\sigma_x + \sigma_y)^{\otimes 6}$, $[x + y + \mathbb{1}] = (\sigma_x + \sigma_y + \mathbb{1})^{\otimes 6}$, etc. The \pm sign denotes a summation over the two signs, i.e., $[x \pm y] = [x + y] + [x - y]$. The Mermin operators are defined as

$$\text{Mermin}_{a,b} := \sum_{k \text{ even}} (-1)^{k/2} \sum_k \mathcal{P}_k (\otimes_{i=1}^k \sigma_a \otimes_{i=k+1}^N \sigma_b), \quad (32)$$

where $\sigma_0 = \mathbb{1}$. That is, it is the sum of terms with even number of σ_a 's and σ_b 's, with the sign of the terms depending on the number of σ_a 's. The expectation value of the operators $\text{Mermin}_{a,b}$ can be measured based on the decomposition [23]

$$\text{Mermin}_{a,b} = \frac{2^{N-1}}{N} \sum_{k=1}^N (-1)^k \left[\cos\left(\frac{k\pi}{N}\right) a + \sin\left(\frac{k\pi}{N}\right) b \right]^{\otimes N}. \quad (33)$$

Hence, $\text{Mermin}_{x,z}$ and $\text{Mermin}_{y,z}$ can be measured with six settings. $\text{Mermin}_{0,z}$, on the other hand, needs only the measurement of the $\{\sigma_z, \sigma_z, \sigma_z, \sigma_z, \sigma_z, \sigma_z\}$ setting. Knowing that $[A]$, $[A + \mathbb{1}]$ and $[A - \mathbb{1}]$ can be measured with a single setting $\{A, A, A, \dots, A\}$, we find that 21 measurement settings are needed to measure $|D_6^{(3)}\rangle\langle D_6^{(3)}|$: $x, y, z, x \pm y, x \pm z, y \pm z, \sqrt{3}x \pm z, \sqrt{3}z \pm x, \sqrt{3}y \pm z, \sqrt{3}z \pm y$, and $x \pm y \pm z$. The settings are also shown in figure 2(a)¹¹.

3.2. Witness independent from the projector witness

So far we constructed witnesses that detected fewer states than the projector-based witness, in return, they were easier to measure. When proving that they were witnesses, we used the

¹¹ Note that [33] presents another decomposition that needs also 21 settings.

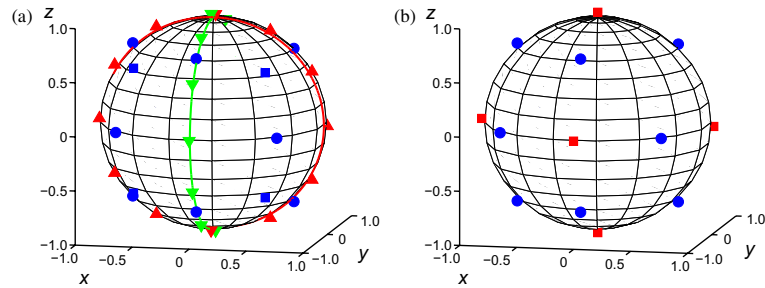


Figure 2. (a) The measurement settings needed to measure the projector to the six-qubit symmetric Dicke state with three excitations based on the decomposition (31). A point at (x, y, z) indicates measuring $x\sigma_x + y\sigma_y + z\sigma_z$ on all qubits. (\blacktriangle) Settings for Mermin $_{x,z}$, (\blacktriangledown) settings for Mermin $_{y,z}$, (\blacksquare) $\sigma_x \pm \sigma_y \pm \sigma_z$, and (\bullet) rest of the settings. (b) Settings for the four-qubit Dicke state with two excitations based on (37). (\blacksquare) $\pm\sigma_x, \pm\sigma_y, \pm\sigma_z$, and (\bullet) $\sigma_x \pm \sigma_y, \sigma_x \pm \sigma_z$, and $\sigma_y \pm \sigma_z$.

Table 1. The list of entanglement witnesses presented in this paper, together with the number of measurement settings needed to measure them and their robustness to white noise. Top four lines: six-qubit witnesses. Bottom five lines: four- and five-qubit witnesses.

Witness	Number of settings	Noise tolerance
$\mathcal{W}_{D(6,3)}^{(P)}$	21	0.4063
$\mathcal{W}_{D(6,3)}^{(P3)}$	3	0.2735
$\mathcal{W}_{D(6,3)}^{(P2)}$	2	0.1391
$\mathcal{W}_{D(6,3)}^{(I2)}$	2	0.1091
$\mathcal{W}_{D(5,2)}^{(I2)}$	2	0.1046
$\mathcal{W}_{D(4,1)}^{(P)}$	7	0.2667
$\mathcal{W}_{D(4,1)}^{(I2)} (q = 1.47)$	3	0.1476
$\mathcal{W}_{D(4,2)}^{(P)}$	9	0.3556
$\mathcal{W}_{D(4,2)}^{(P3)}$	2	0.2759

simple relation (2). Following the example of [37], we now look for a two-setting witness of the form (26) for $N = 6$ that is independent from the projector witness. For determining c_{D6} , we need to compute the maximum of $J_x^2 + J_y^2$ for biseparable states for all the possible bipartitions. As we have discussed in section 2.3, instead of looking for the maximum for states that are

separable with respect to a certain bipartition, we can also look for the maximum for PPT states (see appendix A). We obtain

$$c_{D6} := 11.0179. \quad (34)$$

$\mathcal{W}_{D(6,3)}^{(J2)}$ detects genuine multipartite entanglement if for white noise $p_{\text{noise}} < 0.1091$. Simple numerical optimization leads to the same value for the maximum for biseparable states¹². Hence we find that our witness is optimal. Finally, the list of witnesses presented in this section are shown in the top part of table 1.

4. Witnesses for states derived from $|D_6^{(3)}\rangle$ via projections

By projective measurements of one or two of the qubits we can obtain several states that are inequivalent under stochastic local operations and classical communication (SLOCC). Surprisingly, these states still possess genuine multipartite entanglement [32, 44]. Next, we discuss how to detect the entanglement of these states.

4.1. Witnesses for the superposition of five-qubit Dicke states

After measuring one of the qubits in some basis and post-selecting for one of the two outcomes, one can obtain states of the form

$$\varrho_{D5} := c_1 |D_5^{(2)}\rangle + c_2 |D_5^{(3)}\rangle, \quad (35)$$

where $|c_1|^2 + |c_2|^2 = 1$. For such states, the expectation value of $J_x^2 + J_y^2$ is maximal, thus a witness of the form (26) for $N = 5$ is used to detect their entanglement. Both semidefinite programming and simple numerical optimization leads to $c_{D5} := 7.8723$. Naturally, $\langle \mathcal{W}_{D5}^{(J2)} \rangle$ is minimal not only for states of the form (35), but for any mixture of such states.

4.2. Witness for the four-qubit W state

Now we will construct witnesses for a four-qubit W state, which is obtained from $|D_6^{(3)}\rangle$ if two qubits are measured in the σ_z basis, and the measurement result is +1 in both cases. We consider a witness of the form (27) for $N = 4$ and $m = 1$. We try several values for q and determine c_q for the witness $\mathcal{W}_{D(4,1)}(q)$ as a function of q using semidefinite programming. For each witness we also compute the noise tolerance. The results of these computations can be seen in figure 3. It turns out, that the best witness is obtained for $q = 1.47$ and $c_q = 4.1234$. It tolerates white noise if $p_{\text{noise}} < 0.1476$.

4.3. Three-setting witness for the four-qubit Dicke state

A $|D_4^{(2)}\rangle$ state can also be obtained from $|D_6^{(3)}\rangle$, namely if the measurement outcomes are +1 and -1 for two consecutive σ_z measurements. For that case, we look for a three-setting witness, based on the projector witness. For white noise, the result is

$$\mathcal{W}_{D(4,2)}^{(P3)} := 2 \cdot \mathbb{1} + \frac{1}{6}(J_x^2 + J_y^2 - J_x^4 - J_y^4) + \frac{31}{12}J_z^2 - \frac{7}{12}J_z^4. \quad (36)$$

¹² We used the `maxbiseq` routine of the QUBIT4MATLAB V3.0 package [34] with parameters for accuracy [30 000, 100 000, 0.0005]. See also appendix B.

14

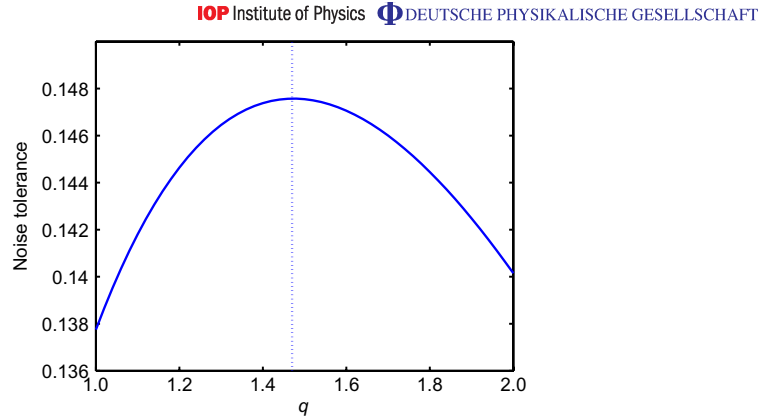


Figure 3. The noise tolerance of the witness $\mathcal{W}_{D(1,4)}^{(I3)}$ given in (27) as a function of the parameter q . The maximum is in the vicinity of $q = 1.47$.

The witness tolerates white noise if $p_{\text{noise}} < 0.2759$. It is easy to check that \mathcal{W} is a witness: one has to notice that $\mathcal{W}_{D(4,2)}^{(P3)} - 3\mathcal{W}_{D(4,2)}^{(P)} \geq 0$, where $\mathcal{W}_{D(4,2)}^{(P)}$ is defined in (7). Thus, the fidelity can be estimated from the measurement of the witness as $F \geq 2/9 - \langle \mathcal{W}_{D(4,2)}^{(P3)} \rangle / 3$.

4.4. Measuring the projector witness for the four-qubit Dicke state

We can also measure the projector witness $\mathcal{W}_{D(4,2)}^{(P)} = \frac{2}{3}\mathbb{1} - |D_4^{(2)}\rangle\langle D_4^{(2)}|$. The method in observation 1 gives the following decomposition for the projector

$$16|D_4^{(2)}\rangle\langle D_4^{(2)}| = \frac{2}{3}([x] + [x \pm \mathbb{1}] + [y] + [y \pm \mathbb{1}]) + \frac{1}{3}(8[z] - [z \pm \mathbb{1}] - [x \pm z] - [y \pm z]) + \frac{1}{6}[x \pm y]. \quad (37)$$

The nine measurement settings are $x, y, z, x \pm y, x \pm z$ and $y \pm z$, shown also in figure 2(b). The list of witnesses presented in this section are given in the bottom part of table 1.

5. Conclusions

In summary, we presented general methods for constructing entanglement witnesses for detecting genuine multipartite entanglement in experiments. In particular, we considered projector-based witnesses and found efficient decompositions for them. Then, we constructed two- and three-setting witnesses for symmetric Dicke states that were based on the projector witness, as well as independent of the projector witness. We applied our methods to design witnesses for the recent experiment observing a six-qubit symmetric Dicke state with three excitations [32]. Our methods can be generalized for future experiments. As a first step, in appendix C we list some entanglement witnesses for systems with 5–10 qubits. Moreover, recent results on the symmetric tensor rank problem suggest that decompositions more efficient than the one in observation 1 are possible, however, they involve complex algorithms [45]. Thus, it would be interesting to look for better upper bounds for the number of settings used for symmetric operators.

Acknowledgments

We thank A Doherty, O Gühne, D Hayes and S Pironio for fruitful discussions. We are grateful for the support of the DFG-Cluster of Excellence MAP, and the EU (QAP, SCALA). WW acknowledges the support by QCCC of the Elite Network of Bavaria and the Studientiftung des dt. Volkes. GT thanks the National Research Fund of Hungary OTKA (contract no. T049234), the Hungarian Academy of Sciences (Bolyai Programme), and the Spanish MEC (Ramon y Cajal Programme, Consolider-Ingenio 2010 project ‘QOIT’).

Appendix A. Semidefinite programming used for obtaining witnesses

Here we summarize two optimization problems that are useful for designing entanglement witnesses and can be solved with semidefinite programming. Both tasks are related to designing witnesses that are easy to measure.

1. Semi-definite programming can be used to find the witness \mathcal{W} with the largest noise tolerance as explained in the beginning of section 3.1.1. The corresponding task can be formulated as

$$\begin{aligned}
 & \text{minimize} && \sum_k c_k \text{Tr}(B_k \varrho_{\text{noise}}), \\
 & \text{subject to} && \sum_k c_k \text{Tr}(B_k \varrho) = -1, \\
 & && \sum_k c_k B_k - \alpha \mathcal{W}^{(P)} \geq 0, \\
 & && \alpha > 0.
 \end{aligned} \tag{A.1}$$

Here ϱ is the state around which we detect entanglement. ϱ_{noise} is the noise, not necessarily white. The optimization is over α and the c_k 's.

2. Semi-definite programming can be used to look for the maximum for PPT bipartite states. This gives an upper bound on the maximum for biseparable states. In many cases, the two coincide. The corresponding task can be formulated as a standard semidefinite program as

$$\begin{aligned}
 & \text{minimize} && -\text{Tr}(M\varrho), \\
 & \text{subject to} && \varrho \geq 0, \\
 & && \text{Tr}(\varrho) = 1, \\
 & && \varrho^{T_A} \geq 0.
 \end{aligned} \tag{A.2}$$

Here T_A means partial transpose according to some groups of the qubits.

Appendix B. List of MATLAB subroutines

We summarize some of the MATLAB routines of the QUBIT4MATLAB 3.0 package that can be used for the calculations necessary for designing entanglement witnesses. A full list of the commands is given in [34].

The command `decompose` can be used to obtain a decomposition of a Hermitian operator into the sum of products of Pauli spin matrices. Moreover, `maxsep` and `maxsymsep` can be

used for getting the maximum for separable multi-qudit states and symmetric product states for a Hermitian operator, respectively. The command `maxbiseq` gives the maximum for states that are biseparable with respect to some partitioning of the qubits. The command `maxb` gives the maximum for all possible bipartitions. All these commands look for the maximum with a simple optimization algorithm that is not guaranteed to find the global maximum, nevertheless, it typically does find it. `overlapb` gives the maximum overlap of a state $|\Psi\rangle$ and biseparable states. It can be used to construct entanglement witnesses of the type (6).

For semidefinite programming, we used SeDuMi [46] and YALMIP [47]. Two subroutines based on them are now in QUBIT4MATLAB 4.0¹³. The command `optwitness` looks for the best witness that can be composed linearly from a set of operators, while `maxppt` determines the maximum of an operator expectation value for states with a PPT for some bipartitioning of the qubits.

Appendix C. Witnesses for systems with 5–10 qubits

A three-setting witness based on the projector witness for the state $|D_8^{(4)}\rangle$ is given by

$$\mathcal{W}_{D(8,4)}^{(P3)} := 1.3652 \cdot \mathbb{1} + \sum_{l=x,y,z} \sum_{n=1}^4 c_{ln} J_l^{2n}, \quad (\text{C.1})$$

with

$$\{c_{ln}\} = \begin{pmatrix} 0.0038612 & -0.0052555 & 0.0015016 & -0.00010726 \\ 0.0038612 & -0.0052555 & 0.0015016 & -0.00010726 \\ 3.124 & -1.07699 & 0.11916 & -0.0038992 \end{pmatrix}. \quad (\text{C.2})$$

The noise tolerance for white noise is $p_{\text{noise}} < 0.2578$. For larger N , we can use the ansatz

$$\mathcal{W}_{D(N,N/2)}^{(P3)} := c_1 \cdot \mathbb{1} + c_{xy} \{(\sigma_x + \mathbb{1})^{\otimes N} + (\sigma_x - \mathbb{1})^{\otimes N} + (\sigma_y + \mathbb{1})^{\otimes N} + (\sigma_y - \mathbb{1})^{\otimes N}\} + \sum_{n=1}^{N/2} c_{zn} J_z^{2n}. \quad (\text{C.3})$$

For $N = 10$, the optimal coefficients are $c_1 = 1.3115$, $c_{xy} = -0.0023069$, and $c_z = \{3.4681, -1.2624, 0.16494, -0.0084574, 0.000146551\}$. White noise is tolerated if $p_{\text{noise}} < 0.2404$. The large noise-tolerance for the $N = 10$ case suggests that a robust three-setting witness for $|D_N^{(N/2)}\rangle$ might be constructed even for large N .

A three-setting witness independent of the projector witness for the N -qubit W state is given by (27) for $m = 1$. For $N = 5$, we have $c_5 = 5.6242$, $q_5 = 2.22$, and the witness tolerates white noise if $p_{\text{noise}} < 0.0744$. For $N = 6$, we have $c_6 = 7.1095$, $q_6 = 3.13$, and noise is tolerated if $p_{\text{noise}} < 0.0401$.

References

- [1] For reviews see Horodecki R, Horodecki P, Horodecki M and Horodecki K 2009 *Rev. Mod. Phys.* **81** 865
Plenio M and Virmani S 2007 *Quantum Inf. Comput.* **7** 1
- [2] Gühne O and Tóth G 2009 *Phys. Rep.* **474** 1
- [3] Pan J W, Bouwmeester D, Daniell M, Weinfurter H and Zeilinger A 2000 *Nature* **403** 515

¹³ <http://www.mathworks.com/matlabcentral/fileexchange/8433>.

- [4] Bourennane M, Eibl M, Kurtsiefer C, Gaertner S, Weinfurter H, Gühne O, Hyllus Ph, Bruß D, Lewenstein M and Sanpera A 2004 *Phys. Rev. Lett.* **92** 087902
- [5] Kiesel N, Schmid C, Weber U, Tóth G, Gühne O, Ursin R and Weinfurter H 2005 *Phys. Rev. Lett.* **95** 210502
- [6] Kiesel N, Schmid C, Tóth G, Solano E and Weinfurter H 2007 *Phys. Rev. Lett.* **98** 063604
- [7] Wieczorek W, Schmid C, Kiesel N, Pohlner R, Gühne O and Weinfurter H 2008 *Phys. Rev. Lett.* **101** 010503
- [8] Lu C Y, Zhou X Q, Gühne O, Gao W B, Zhang J, Yuan Z S, Goebel A, Yang T and Pan J W 2007 *Nat. Phys.* **3** 91
- [9] Gao W B, Lu C Y, Yao X C, Xu P, Gühne O, Goebel A, Chen Y A, Peng C Z, Chen Z B and Pan J W 2008 arXiv:0809.4277
- [10] Sackett C A *et al* 2000 *Nature* **404** 256
- [11] Leibfried D *et al* 2005 *Nature* **438** 639
- [12] Häffner H *et al* 2005 *Nature* **438** 643
- [13] Hald J, Sørensen J L, Schori C and Polzik E S 1999 *Phys. Rev. Lett.* **83** 1319
- [14] Mandel O, Greiner M, Widera A, Rom T, Hänsch T and Bloch I 2003 *Nature* **425** 937
- [15] Neumann P, Mizuochi N, Rempp F, Hemmer P, Watanabe H, Yamasaki S, Jacques V, Gaebel T, Jelezko F and Wrachtrup J 2008 *Science* **320** 1326
- [16] Terhal B M 2002 *Theor. Comput. Sci.* **287** 313
- [17] Lewenstein M, Kraus B, Cirac J I and Horodecki P 2000 *Phys. Rev. A* **62** 052310
- [18] Gühne O, Hyllus P, Bruß D, Ekert A, Lewenstein M, Macchiavello C and Sanpera A 2002 *Phys. Rev. A* **66** 062305
- [19] Gühne O, Hyllus P, Bruss D, Ekert A, Lewenstein M, Macchiavello C and Sanpera A 2003 *J. Mod. Opt.* **50** 1079
- [20] Greenberger D M, Horne M A, Shimony A and Zeilinger A 1990 *Am. J. Phys.* **58** 1131
- [21] Briegel H J and Raussendorf R 2001 *Phys. Rev. Lett.* **86** 910
- [22] Tóth G and Gühne O 2005 *Phys. Rev. Lett.* **94** 060501
- [23] Gühne O, Lu C Y, Gao W B and Pan J W 2007 *Phys. Rev. A* **76** 030305
- [24] Doherty A C, Parrilo P A and Spedalieri F M 2002 *Phys. Rev. Lett.* **88** 187904
- [24] Doherty A C, Parrilo P A and Spedalieri F M 2004 *Phys. Rev. A* **69** 022308
- [25] Brandão F G S L and Vianna R O 2004 *Phys. Rev. Lett.* **93** 220503
- [26] Eisert J, Hyllus P, Gühne O and Curty M 2004 *Phys. Rev. A* **70** 062317
- [27] Jafarizadeh M A, Najarbashi G and Habibian H 2007 *Phys. Rev. A* **75** 052326
- [28] Hyllus P and Eisert J 2006 *New J. Phys.* **8** 51
- [29] Wunderlich H and Plenio M B 2009 arXiv:0902.2093
- [30] Dicke R H 1954 *Phys. Rev.* **93** 99
- [31] Stockton J K, Geremia J M, Doherty A C and Mabuchi H 2003 *Phys. Rev. A* **67** 022112
- [32] Wieczorek W, Krischek R, Kiesel N, Michelberger P, Tóth G and Weinfurter H 2009 *Phys. Rev. Lett.* **103** 020504
- [33] Prevedel R, Cronenberg G, Tame M S, Paternostro M, Walther P, Kim M S and Zeilinger A 2009 *Phys. Rev. Lett.* **103** 020503
- [33] Campbell S, Tame M S and Paternostro M 2009 *New J. Phys.* **11** 073039
- [34] Tóth G 2008 *Comput. Phys. Commun.* **179** 430
- [35] Acín A, Bruß D, Lewenstein M and Sanpera A 2001 *Phys. Rev. Lett.* **87** 040401
- [36] Gühne O 2004 *PhD Thesis* University of Hannover
- [37] Tóth G 2007 *J. Opt. Soc. Am. B* **24** 275
- [38] Peres A 1996 *Phys. Rev. Lett.* **77** 1413
- [38] Horodecki M, Horodecki P and Horodecki R 1996 *Phys. Lett. A* **223** 1
- [39] Krammer P, Kampermann H, Bruss D, Bertlmann R A, Kwek L C and Macchiavello C 2009 arXiv:0904.3860
- [40] Unanyan R G and Fleischhauer M 2003 *Phys. Rev. Lett.* **90** 133601
- [41] Duan L M and Kimble H J 2003 *Phys. Rev. Lett.* **90** 253601

18

IOP Institute of Physics Φ DEUTSCHE PHYSIKALISCHE GESELLSCHAFT

- [42] Thiel C, von Zanthier J, Bastin T, Solano E and Agarwal G S 2007 *Phys. Rev. Lett.* **99** 193602
- [43] Stockton J K, van Handel R and Mabuchi H 2004 *Phys. Rev. A* **70** 022106
- [44] Wieczorek W, Kiesel N, Schmid C and Weinfurter H 2009 *Phys. Rev. A* **79** 022311
- [45] P Golub G, Lim L H and Murrain B 2008 *SIAM J. Matrix Anal. Appl.* **30** 1254
- [46] Sturm J *SeDuMi, a MATLAB Toolbox for Optimization Over Symmetric Cones* <http://sedumi.mcmaster.ca>.
- [47] Löfberg J *Yalmip: A Toolbox for Modeling and Optimization in MATLAB* <http://control.ee.ethz.ch/~joloef/yalmip.php>.
- [48] Keilmann T and Garcia-Ripoll J J 2008 *Phys. Rev. Lett.* **100** 110406

P5.4

Ultraviolet enhancement cavity for ultrafast nonlinear optics

Roland Krischek,^{1,2,*} Witlef Wiczorek,^{1,2} Akira Ozawa,¹ Nikolai Kiesel,^{1,2,3}
 Patrick Michelberger,^{1,2} Thomas Udem,¹ and Harald Weinfurter^{1,2}

¹*Max-Planck-Institut für Quantenoptik, D-85748 Garching, Germany*

²*Fakultät für Physik, Ludwig-Maximilians-Universität München, D-80799 München, Germany*

³*Present address: Institute for Quantum Optics and Quantum Information, A-1090 Vienna, Austria*

Ultrafast ultraviolet light pulses became a key tool for spectroscopic studies, for example, of molecular formation[1, 2], of carrier dynamics in semiconductors[3] and as source for nonclassical states of light[4–13]. The power required for many nonlinear processes makes the use of amplifier systems mandatory, a fact, which significantly reduces the available repetition rate and often lengthens the experimental acquisition time. Here we adopt techniques, recently developed for the infrared[14–16], to design an enhancement cavity for femtosecond ultraviolet pulses. More than 7 W average ultraviolet power at 81 MHz repetition rate are now available to pump a nonlinear crystal inside the cavity. We have characterised the cavity and demonstrated its applicability as powerful source for entangled multi-photon states. This field-enhancement enables a new scale of experiments in photonic quantum logic and in other areas of research, for example, to operate optical parametric amplifiers at high repetition rates or to create high harmonic frequency combs[14–16].

PACS numbers:

Keywords:

Recent developments for generating infrared (IR) frequency combs show that spectrally broad ultra-short pulses can be enhanced in narrowband resonators, provided that they are phase coherent with each other[14–17]. Then, in the time domain picture, a laser pulse can add to the circulating field inside the resonator. In the frequency domain this corresponds to the condition, that the frequency-comb characterising a series of mode-locked pulses[18] has sufficient overlap with the mode spectrum of the cavity. The transfer of these methods to the ultraviolet (UV), a frequency regime not yet tested for femtosecond pulse enhancement, needs special care due to the significantly higher dispersion of nonlinear crystals and air, and due to higher demands on the quality of the optical components and the stability of the setup.

An example for a nonlinear optics process in constant need for higher pump powers is spontaneous parametric down conversion (SPDC), whereas n photon pairs are available in its n th order emission, which is widely applied for multi-photon entanglement experiments. With typical systems using a frequency doubled titanium-sapphire (Ti:Sa) mode-locked laser, with an average pump power of 0.6 W at about 80 MHz repetition rate, a wavelength of around 400 nm and a pulse duration between 100 and 150 fs, a series of experiments on four-photon entangled states have been performed[5, 7, 10, 12]. More recently, high-power oscillators providing about 1 W UV pump power allowed six-photon experiments, but the count rates are rather low and limit state analysis due to long measurement times[6, 8, 13]. In contrast, increasing the pulse energy

by several orders of magnitude, e.g., realised in amplified femtosecond laser sources working in the kHz regime[19], leads, at the expense of the repetition rate, to a very high number of generated photon pairs per pulse. Yet, due to the limited detection efficiency of the single photon detectors, noise originating from higher order emissions fully dominates and renders this approach unsuitable for studies of multi-partite entangled states. Other developments in alternative sources are promising but not yet mature enough for multi-photon entanglement generation[20–23] (see supplementary information). In our work, we employ for the first time a femtosecond UV enhancement cavity with a nonlinear crystal inside to address a regime, in which high multi-photon count rates allow an in-depth state characterisation[9] and the observation of genuine six-partite entanglement.

In the experiment, the output of a Ti:Sa laser, delivering 130 fs pulses centred at 780 nm with an average power of 2 W and a repetition rate of $f_r = 81$ MHz, is frequency doubled by a 3 mm lithium triborate (LBO) crystal, yielding an average power of 0.54 W at 390 nm. Crucial for multi-photon experiments is the stability of the system on a time scale of days due to the long measurement times necessary even with increased pump power. We thus implement a pointing stabilisation, in which two mirrors on piezoelectric transducers (PZTs) are controlled by the error signals deduced from two quadrant photodiodes and correct for position and direction fluctuations originating in the laser and frequency doubling unit. The femtosecond UV enhancement cavity is designed as a bow-tie resonator with an input coupler of 97.5% reflectivity and a dichroic mirror to couple the SPDC photons out of the cavity (see Fig.1 for details).

The cavity has to be stabilised to continuously match the free running modes of the Ti:Sa laser. The characteristic frequency comb spectrum $f_m = mf_r + f_{CE}$ de-

*roland.krischek@mpq.mpg.de

depends on two parameters: the repetition frequency of the pulses f_r and the carrier-envelope offset f_{CE} . First, we equalise f_r between the laser oscillator and the enhancement cavity by actively adjusting the cavity length. To this end, an error signal is generated via the Hänsch-Couillaud-method[24]. This signal, resulting from interference between the cavity field leaking through the input coupler and a component reflected directly thereof, is spectrally selected to reduce the impact of the laser's spectral envelope instabilities. The error signal controls two PZT driven mirror mounts, whereby the mirror on PZT 1 compensates short term (max. $2\ \mu\text{m}$ travel-range, bandwidth $< 10\ \text{kHz}$) and the mirror on PZT 2 long term drifts ($12\ \mu\text{m}$, $< 3\ \text{Hz}$). Second, additional servo motors steer the Ti:Sa laser wavelength and prism insertion to keep its central wavelength at $780\ \text{nm}$ and to optimise the offset frequency f_{CE} for maximising the intra cavity power on a long-time scale (typical locking time of 24 h). Hence, no feedback signal, as, e.g., generated by an $f/2f$ interferometer[18], is required to control f_{CE} of the Ti:Sa laser. With this configuration we achieve during long-time operation a UV power of $P_{UV} = 7.2 \pm 0.2\ \text{W}$ inside the cavity (see Fig. 1b), which corresponds to an overall power enhancement of 13.3 ± 0.5 . We estimate the intra cavity pulse length to approximately $175\ \text{fs}$ from an interferometric autocorrelation measurement (see Fig. 1c and methods).

Air and the nonlinear crystal, here β -barium borate (BBO), cause dispersion inside the cavity, which distort the resonant cavity modes away from being equidistant in frequency and consequently change the resonant spectrum. The influence of dispersion is estimated by the spectrally resolved power enhancement (Fig. 2a, blue line), which results from dividing the intra-cavity spectrum (orange) by the external one in front of the resonator (black). The two spectra are similar, indicated by the flat dependence of the power enhancement around the centre wavelength, even without dispersion compensation. Removing the crystal and consequently choosing an input-coupler of 99% reflectivity decreases loss yielding a UV power of $21 \pm 1\ \text{W}$, i.e., a power enhancement of almost a factor of 40, again with flat spectral dependence (Fig. 2a, inset) due to the lower dispersion inside the cavity. The similarity of both power enhancement curves can be attributed to an increase in acceptance bandwidth of the resonator for the case with a BBO crystal inside, since the finesse decreases for higher loss. These measurements are in good agreement with calculations[16] (Fig. 2b orange and black line, respectively). Additionally, Fig. 2b shows the expected cavity spectra for an evacuated cavity and for a reduced crystal thickness with a broadband spectrum as cavity input. Remarkably, in an evacuated cavity with a $0.5\ \text{mm}$ thick crystal, pulses of a duration down to $40\ \text{fs}$ (corresponding to $\Delta\lambda = 3.9\ \text{nm}$) can be enhanced without the need of dispersion compensation.

To illustrate the potential of this enhancement cavity we use it as a new source for experiments on linear optics quantum logic. To evaluate its performance, we analyse

the statistics of multi-photon events and the achieved entanglement of two-, four-, and six-photon Dicke[25] states (see supplementary information) depending on the intra cavity UV pump power. For this purpose IR-photons created inside the cavity are coupled into a single mode fibre and a linear optics setup is used to distribute them to six polarisation analysers (see methods). To evaluate photon detection statistics and contributions from higher order emissions we use this setup merely as a polarisation sensitive photon number detector[26]. In the employed type-II collinear SPDC process, which generates an equal number of horizontally (H) and vertically (V) polarised photons, the emission rate of n photon pairs for typical pump powers is proportional to $(P_{UV})^n$ (see methods). The experimentally measured count rates are shown in Fig. 3 and divided up into two groups: the first one are coincidences with an equal number of H and V polarised photons (\square) and thus, to a good approximation, proportional to $(P_{UV})^n$ (solid lines in Fig. 3). All other possible coincidences with an unequal number of H and V polarised photons (\diamond) form the second group and can only be due to an emission of $(n+1)$ photon pairs followed by photon loss (dashed lines in Fig. 3). Consequently, this rate is proportional to $(P_{UV})^{n+1}$. The decreasing distance between solid and dashed lines in Fig. 3 for higher n shows clearly the increasing influence of higher order emissions. In order to compare our count rates with other state-of-the-art experiments we evaluate the yield of the cavity source by estimating the number of six- and eight-photon events at the output of the fibre (see methods). For the pump power of $P_{UV} = 7.2\ \text{W}$ we obtain an effective six- and eight-photon count rate of 527 ± 6 and 3.9 ± 1.0 coincidences per minute, respectively. The six-photon count rate is almost 2 orders of magnitude higher than in any other state of the art experiment[6, 8], also due to an improved collection efficiency caused by the additional mode filtering of the cavity (Fig. 1d; see supplementary information analysing the entanglement of the observed quantum states depending on the pump power).

In this letter we have introduced a femtosecond UV enhancement cavity as a novel device in ultrafast nonlinear optics. For the particular case of a $1\ \text{mm}$ BBO crystal inside the cavity, we have demonstrated its benefits by significantly increasing the yield in multi-photon experiments. UV pulses with an approximate duration of $175\ \text{fs}$ have been enhanced by an overall factor of 13 (or even 40 for the case without a crystal), which has resulted in an improvement of the six-photon count rate by almost two orders of magnitude. With an average circulating UV power of more than $7\ \text{W}$ and a pulse energy of about $100\ \text{nJ}$ at a repetition frequency of $81\ \text{MHz}$ this long-time stable enhancement cavity is well suited for a series of different applications in nonlinear optics for example as an efficient source generating squeezed light inside the cavity[27, 28], as a pump source for optical parametric amplifiers used, e.g., to study molecular dynamics[1, 2], or as a possible extension of recent developments for generating high harmonic far-UV light in a gas jet[14–16].

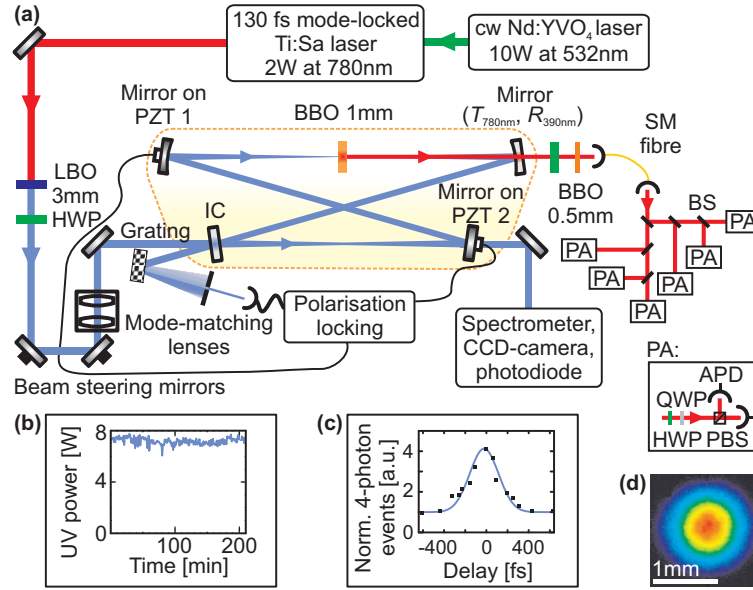


FIG. 1: Schematic experimental setup. (a) A mode-locked titanium-sapphire (Ti:Sa) oscillator is pumped by a 10 W cw laser at 532 nm generating laser pulses of 130 fs duration with an output spectrum centred at 780 nm and an average power of 2 W. After frequency doubling by a lithium triborate (LBO) crystal the UV beam has an average power of 540 mW at 390 nm. A beam steering unit and mode matching optics prepare the input beam for the bow-tie cavity (inside orange dotted line) with two focusing mirrors with a radius of curvature of ~ 800 mm, generating two beam waists of $100 \mu\text{m}$ and $330 \mu\text{m}$, respectively. A 1 mm thick β barium borate (BBO) crystal is placed at the smaller waist. Except for the input coupler ($R_{390\text{nm}} = 97.5\%$), all resonator mirrors are highly reflective ($R_{390\text{nm}} > 99.9\%$) at 390 nm and one is additionally highly transmissive ($T_{780\text{nm}} > 99.5\%$) for the SPDC photons at 780 nm, which are analysed in a linear optics setup. Inset (b) shows the long-term stability of the cavity over several hours. In (c) the envelope of an interferometric auto-correlation signal is shown. It is obtained by counting the number of four-photon coincidences in dependence on the delay between split UV pulses. Inset (d) shows the transversal mode of the cavity, where we determined a beam quality of $M^2 = 1.15 \pm 0.03$. HWP, half wave plate; QWP, quarter wave plate; PZT, piezoelectric transducer; IC, input coupler; SM, single mode fibre; BS, non-polarising beam splitter cube; PBS, polarising beam splitter cube; PA, polarisation analysis; APD, avalanche photo diode

APPENDIX A: SPDC PHOTON PREPARATION AND ANALYSIS.

Photons collinearly emitted by the cavity pumped SPDC are transmitted through a dichroic mirror with $R_{390\text{nm}} > 99.9\%$ and $T_{780\text{nm}} > 99.5\%$. To compensate for walk-off effects between the horizontally and vertically polarised photons emitted from the SPDC BBO crystal, a half-wave plate together with another 0.5 mm thick BBO crystal are positioned outside the cavity. The SPDC photons are subsequently focused into a single mode fibre to define their spatial mode. To achieve spectral selection, a narrowband interference filter ($\Delta\lambda = 3\text{ nm}$) is placed at the output of the fibre. After distributing the photons into six modes by polarisation independent beam splitters the birefringence of these beam splitters is compensated by pairs of perpendicularly orientated $200 \mu\text{m}$

thick birefringent yttrium-vanadate crystals (YVO₄) (not shown in Fig. 1). For each mode we choose the direction of the polarisation analysis with half- and quarter-wave plates and detect photons in the outputs of polarising beam splitters using single photon avalanche photodiodes. The detection signals are evaluated by an FPGA controlled coincidence logic which allows to simultaneously register any possible coincidence. To detect the $2n$ -fold coincidences we consider all possible combinations between the twelve detectors. In order to compare our count rates with other experiments we evaluate the effective number of six- or eight-photon coincidences at the output of the fibre taking all possible combinations between the twelve detectors into account. For this purpose, we divide the experimental count rates by the probability to observe such events, which is calculated to be 0.284 for six- and 0.065 for eight-photon events,

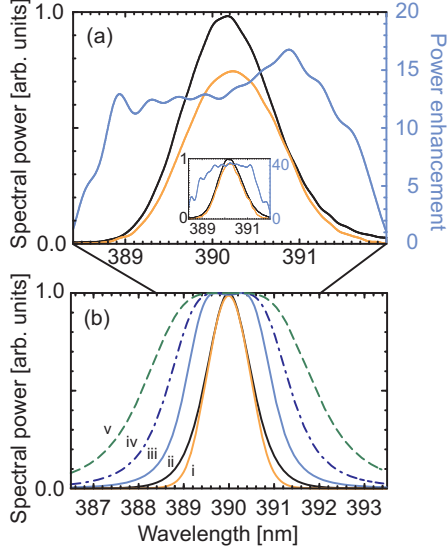


FIG. 2: UV spectra and power enhancement. (a) Measured intra cavity and external UV spectra with corresponding spectral power enhancement for the case of a 1 mm BBO crystal inside the cavity and an input-coupler of 97.5% reflectivity. The spectrally resolved power enhancement is calculated by scaling the cavity spectrum according to the power inside the resonator and the external spectrum according to the power measured in front of the input-coupler. The inset shows the data for the empty cavity without a BBO crystal and an input-coupler of 99% reflectivity. (b) Calculated cavity UV spectra for different dispersion scenarios (using the specifications of the mirrors provided by the manufacturer). The first curves correspond to our experiment: (i) orange, 1 mm BBO crystal and air inside the cavity compared to (ii) black, the external UV spectrum. The others are calculated for a broadband input spectrum and thus show the dependence of the achievable power enhancement: (iii) azure, 1 mm BBO crystal and air inside the cavity, (iv) dash-dotted blue, evacuated cavity with a 1 mm BBO crystal, (v) dashed green, evacuated cavity with a 0.5 mm BBO crystal. We assumed for these calculations a total loss of 2.66% inside the cavity and an input coupler of 2.5% transmittivity. The full-width-half-maximum of the cavity spectrum increases for these cases from 1.1 nm to 3.9 nm corresponding to sech-shaped pulse widths of 140 fs down to 40 fs.

deviating slightly from the theoretical probabilities for optimal beam splitters of $\frac{25}{81}$ and $\frac{25}{324}$, respectively, due to small asymmetries of the beam splitting ratios. The coincidences for the calculation of the entanglement witness are corrected for the different relative detector efficiencies. The total error is determined from errors on the independently measured relative detector efficiencies and Poissonian counting statistics.

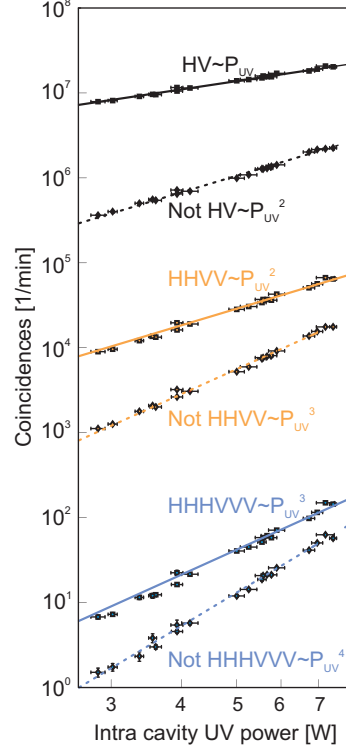


FIG. 3: Count rate statistics depending on the average SPDC pump power circulating in the cavity. The data shows the role of $2n$ -detection events either with n horizontally (H) and n vertically (V) detected photons (squares) originating predominantly from a $2n$ -photon emission, or with unequal number of H and V detections (diamonds) essentially due to a $2n+2$ -photon emission with two photons lost. The solid and dashed curves for $n=1$ (black), $n=2$ (orange) and $n=3$ (blue) are fits, which are proportional to $(P_{UV})^n$ or $(P_{UV})^{n+1}$ (according to the approximation of Eq. B1) for the rates with equal or unequal number of H and V detections, respectively.

APPENDIX B: SPDC PHOTON STATISTICS.

For a type-II collinear SPDC process we obtain the state[19]

$$|\Psi_{\text{SPDC}}\rangle = \sqrt{1 - \tanh^2 \tau} \sum_{n=0}^{\infty} (\tanh \tau)^n |V^{\otimes n} H^{\otimes n}\rangle, \quad (\text{B1})$$

where $|V^{\otimes n} H^{\otimes n}\rangle$ represents n horizontally (H) and n vertically (V) polarised photons emitted by the source, and τ the coupling between in- and output fields, which

depends linearly on the pump field amplitude, on the nonlinearity of the crystal and on its length. From this state one obtains the probability to create n photon pairs per pulse with $p_n = (1 - \tanh^2 \tau)(\tanh \tau)^{2n}$ and thus the rate of emission of n pairs, c_n , as $c_n = p_n f_r$. For $\tau \ll 1$, i.e., for low pump powers, we can approximate $\tanh \tau \approx \tau$, $(1 - \tanh^2 \tau) \approx 1$ and thus $p_n \approx \tau^{2n}$. Hence, increasing the pump power P_{UV} , increases the rate of n photon pairs according to $c_n \propto (P_{UV})^n$. For high pump powers the observed rate of the n th order emission is contaminated by photons originating from higher order emissions due to the limited detection efficiency, predominantly from the $(n + 1)$ th order emission and the loss of two photons. In our case, we have $\tau \in [0.26, 0.46]$ and an overall detection efficiency of about 14%. We apply the simple model $c_n \propto (P_{UV})^n$ in order to illustrate the trend for growing pump powers. A more elaborate analysis is, e.g., described in Ref. [29].

APPENDIX C: PULSE LENGTH MEASUREMENT OF THE INTRA CAVITY UV PULSES

Estimating the length of ultra short pulses can be done by interferometric autocorrelation. The general idea is to overlap two pulses with different time delays and subsequently measure the intensity of a signal derived from a nonlinear process, e.g., second harmonic generation (SHG). As applying SHG is quite problematic for UV pulses, we instead profit from the nonlinear intensity dependence of the second order SPDC emission. Therefore, a Michelson interferometer is used in front of the cavity to create two delayed pulses and measure the count rates of four photon events as a function of the pulse delay. The interferometric autocorrelation envelope provides an approximate pulse duration of 175 fs, when assuming a sech-shaped pulse. This value is slightly above the one deduced from the spectrum (Fig. 2) as the setup has been optimised for high entanglement visibility in the latter case. The contrast of the signal, being approximately 4 : 1 (compared to ideally 8 : 1), can be attributed to a reduced interference visibility. We would also like to note that there is no background noise on the offset outside the interference region as random four-fold coincidences have not been registered.

APPENDIX D: SUPPLEMENTARY INFORMATION: ULTRAVIOLET ENHANCEMENT CAVITY FOR ULTRAFAST NONLINEAR OPTICS

1. Alternative multi-photon sources

Recently, promising methods have been developed to generate multi-photon states. These methods are well suited regarding the number of generated photons as

a function of the pump power, but the observation of multi-photon polarisation entangled states imposes further requirements, namely spectral, spatial and temporal indistinguishability[30, 31]. So far, the highest number of photon pairs for pulsed sources was obtained using spontaneous processes in waveguide structures[20] and photonic crystal fibres (PCF)[21–23]. Though these sources are promising, their application for multi-photon entanglement studies has still to be proven. For example, the PCF sources are usually operating in the non-degenerate mode, resulting in different wavelengths for the signal and idler photons. This prevents the use of signal and idler photons for the same linear optics logic gates. Alternatively, working at telecom wavelengths for down converted photons might simplify their generation due to high available pump powers. However, in this case the detection efficiency of about 10% for InGaAs-avalanche diodes is still too low for multi-photon experiments. In the future, these systems might profit from the development of high-efficient cryogenic single photon detectors or more elaborate waveguide and PCF structures. To date, sources based on our approach are still the workhorses for multi-photon entanglement studies.

2. Multipartite entanglement depending on the intra-cavity UV pump power

In general, distributing $2n$ photons from the n th order emission of a type II collinear SPDC process symmetrically into $2n$ spatial modes allows to observe polarisation-entangled multi-photon Dicke[25] states. Formally, these states are described by

$$D_{2n}^{(n)} = \binom{2n}{n}^{-\frac{1}{2}} \sum_i \mathcal{P}_i(|V^{\otimes n} H^{\otimes n}\rangle_{1,\dots,2n}), \quad (\text{D1})$$

where $\sum_i \mathcal{P}_i(\dots)$ represents the sum over all distinct symmetric permutations of distributing $2n$ photons one in each of $2n$ different output modes $(1, \dots, 2n)$. Here, we are able to observe the states $D_2^{(1)}$, $D_4^{(2)}$ and $D_6^{(3)}$, whose genuine $2n$ -partite entanglement has been shown recently experimentally[5, 8, 9, 32]. The high symmetry of the Dicke states enables one to formulate entanglement witnesses, which use the collective spin-component in the x - and y -direction[33], $\mathcal{W}_{2n} = J_{x,2n}^2 + J_{y,2n}^2$, where $J_{x/y,2n} = \frac{1}{2} \sum_k \sigma_{x/y}^k$ with $\sigma_{x,y}$ being the Pauli matrices $\sigma_x^3 = \mathbb{1}^{\otimes 2} \otimes \sigma_x \otimes \mathbb{1}^{\otimes (2n-3)}$. The expectation value $\langle \mathcal{W}_{2n} \rangle$ is determined from a measurement of all photons in the σ_x and all in the σ_y basis, which corresponds to polarisation analysis along $\pm 45^\circ$ linear and left/right circular polarisation, respectively.

We evaluate the multipartite entanglement, which is achieved with the cavity enhanced SPDC source using \mathcal{W}_{2n} [33]. Two-, four- and six-photon polarisation-entangled Dicke states can be observed with the same linear optics setup used to determine the photon statis-

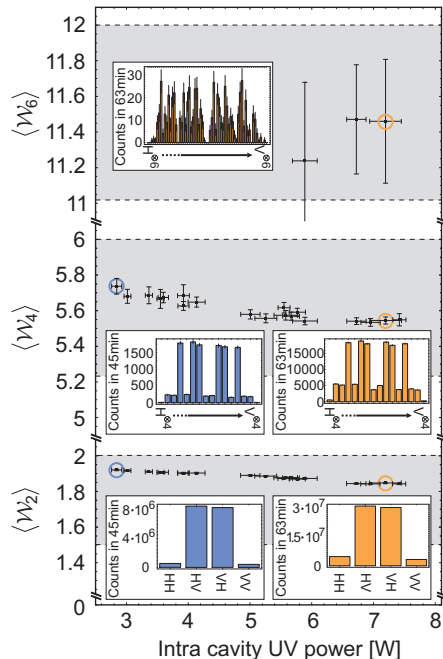


FIG. 4: Verification of multipartite entanglement. The experimental value $\langle W_{2n} \rangle$ of the entanglement witness is plotted as function of the UV pump power for the experimentally observed two-, four- and six photon Dicke states. Genuine $2n$ -partite entanglement is confirmed for $\langle W_2 \rangle$ larger than 1.5 [33], $\langle W_4 \rangle$ larger than 5.23 [5] and $\langle W_6 \rangle$ larger than 11.0175 [9], respectively, indicated by the shading. The five insets show the experimentally measured coincidences for polarisation analysis along the H/V linear polarisation for the data indicated by the orange and blue circles. Reduction of the entanglement for higher pump powers is caused by increased noise from higher order emissions.

tics. Extending previous measurements on the six-photon Dicke state [8, 9], here we focus on the change of the observed entanglement depending on the pump power (Fig. 4). All observed values are within the required bound (shaded region) proving genuine multipartite entanglement. However, for increasing pump power $\langle W_{2n} \rangle$ decreases as the state is contaminated by coloured noise from higher order contributions. The effect of this noise can also be recognised by comparing the rates for analysis along H/V-direction for low and high pump powers (insets in Fig. 4).

ACKNOWLEDGMENTS

We acknowledge the support of this work by the DFG-Cluster of Excellence MAP, the EU Project QAP and the DAAD/MNiSW exchange program. W.W. acknowledges support by QCCC of the Elite Network of Bavaria and the Studienstiftung des dt. Volkes.

- [1] Schrader, T. E., Schreier, W. J., Cordes, T., Koller, F. O., Babitzki, G., Denschlag, R., Renner, C., Löweneck, M., Dong, S.-L., Moroder, L., Tavan, P. & Zinth, W. Light-triggered β -hairpin folding and unfolding. *Proc. Nat. Acad. Sci.* **104**, 15729–15734 (2007).
- [2] Schrieber, C., Lochbrunner, S., Riedle, E. & Nesbitt, D. J. Ultrasensitive ultraviolet-visible 20 fs absorption spectroscopy of low vapor pressure molecules in the gas phase. *Rev. Sci. Instrum.* **79**, 013107 (2008).
- [3] Choi, C. K., Kwon, Y. H., Krasinski, J. S., Setlur, G. & Song, J. J. Ultrafast carrier dynamics in a highly excited GaN epilayer. *Phys. Rev. B* **63**, 115315 (2001).
- [4] Bouwmeester, D., Pan, J.-W., Daniell, M., Weinfurter, H. & Zeilinger, A. Observation of three-photon Greenberger-Horne-Zeilinger entanglement. *Phys. Rev. Lett.* **82**, 1345–1349 (1999).
- [5] Kiesel, N., Schmid, C., Tóth, G., Solano, E. & Weinfurter, H. Experimental observation of four-photon entangled Dicke state with high fidelity. *Phys. Rev. Lett.* **98**, 063604 (2007).
- [6] Lu, C.-Y., Zhou, X.-Q., Gühne, O., Gao, W.-B., Zhang, J., Yuan, Z.-S., Goebel, A., Yang, T. & Pan, J.-W. Experimental entanglement of six photons in graph states. *Nature Physics* **3**, 91 – 95 (2007).
- [7] Wieczorek, W., Schmid, C., Kiesel, N., Pohlner, R., Gühne, O. & Weinfurter, H. Experimental observation of an entire family of four-photon entangled states. *Phys. Rev. Lett.* **101**, 010503 (2008).

- [8] Prevedel, R., Cronenberg, G., Tame, M. S., Paternostro, M., Walther, P., Kim, M. S. & Zeilinger, A. Experimental Realization of Dicke States of up to Six Qubits for Multiparty Quantum Networking. *Phys. Rev. Lett.* **103**, 020503 (2009).
- [9] Wieczorek, W., Krischek, R., Kiesel, N., Michelberger, P., Tóth, G. & Weinfurter, H. Experimental entanglement of a six-photon symmetric Dicke state. *Phys. Rev. Lett.* **103**, 020504 (2009).
- [10] Walther, P., Resch, K. J., Rudolph, T., Schenck, E., Weinfurter, H., Vedral, V., Aspelmeyer, M. & Zeilinger, A. Experimental one-way quantum computing. *Nature* **434**, 169–176 (2005).
- [11] Zhao, Z., Chen, Y.-A., Zhang, A.-N., Yang, T., Briegel, H. J. & Pan, J.-W. Experimental demonstration of five-photon entanglement and open-destination teleportation. *Nature* **430**, 54–58 (2004).
- [12] Lanyon, B. P., Weinhold, T. J., Langford, N. K., Barbieri, M., James, D. F. V., Gilchrist, A. & White, A. G. Experimental demonstration of Shor's algorithm with quantum entanglement. *Phys. Rev. Lett.* **99**, 250505 (2007).
- [13] Rådmark, M., Żukowski, M. & Bourennane, M. Experimental test of rotational invariance and entanglement of photonic six-qubit singlet state. *arXiv: 0903.3188 [quant-ph]* (2009).
- [14] Jones, J. R., Moll, K. D., Thorpe, M. J. & Ye, J. Phase-coherent frequency combs in the vacuum ultraviolet via high-harmonic generation inside a femtosecond enhancement cavity. *Phys. Rev. Lett.* **94**, 193201 (2005).
- [15] Gohle, C., Udem, T., Herrmann, M., Rauschenberger, J., Holzwarth, R., Schuessler, H. A., Krausz, F. & Hänsch, T. W. A frequency comb in the extreme ultraviolet. *Nature* **436**, 234–237 (2005).
- [16] Ozawa, A., Rauschenberger, J., Gohle, C., Herrmann, M., Walker, D. R., Pervak, V., Fernandez, A., Graf, R., Apolonski, A., Holzwarth, R., Krausz, F., Hänsch, T. W. & Udem, T. High harmonic frequency combs for high resolution spectroscopy. *Phys. Rev. Lett.* **100**, 253901 (2008).
- [17] Yanovsky, V. P. & Wise, F. W. Frequency doubling of 100-fs pulses with 50% efficiency by use of a resonant enhancement cavity. *Opt. Lett.* **19**, 1952 (1994).
- [18] Udem, T., Holzwarth, R. & Hänsch, T. W. Optical frequency metrology. *Nature* **416**, 233 (2002).
- [19] Eisenberg, H. S., Khoury, G., Durkin, G. A., Simon, C. & Bouwmeester, D. Quantum entanglement of a large number of photons. *Phys. Rev. Lett.* **93**, 193901 (2004).
- [20] U'Ren, A. B., Silberhorn, C., Banaszek, K. & Walmsley, I. A. Efficient conditional preparation of high-fidelity single photon states for fiber-optic quantum networks. *Phys. Rev. Lett.* **93**, 093601 (2004).
- [21] Fulconis, J., Alibart, O., O'Brien, J. L., Wadsworth, W. J. & Rarity, J. G. Nonclassical Interference and Entanglement Generation Using a Photonic Crystal Fiber Pair Photon Source. *Phys. Rev. Lett.* **99**, 120501 (2007).
- [22] Li, X., Voss, P. L., Sharping, J. E. & Kumar, P. Optical-Fiber Source of Polarization-Entangled Photons in the 1550 nm Telecom Band. *Phys. Rev. Lett.* **94**, 053601 (2005).
- [23] Fan, J., Migdall, A. & Wang, L. J. Efficient generation of correlated photon pairs in a microstructure fiber. *Opt. Lett.* **30**, 3368 (2005).
- [24] Hänsch, T. W. & Couillaud, B. Laser frequency stabilization by polarization spectroscopy of a reflecting reference cavity. *Opt. Comm.* **35**, 441–444 (1980).
- [25] Dicke, R. H. Coherence in spontaneous radiation processes. *Phys. Rev.* **93**, 99–110 (1954).
- [26] Achilles, D., Silberhorn, C., Śliwa, C., Banaszek, K. & Walmsley, I. A. Fiber-assisted detection with photon number resolution. *Opt. Lett.* **28**, 2387–2389 (2003).
- [27] Ou, Z. Y., Pereira, S. F., Kimble, H. J. & Peng, K. C. Realization of the Einstein-Podolsky-Rosen paradox for continuous variables. *Phys. Rev. Lett.* **68**, 3663–3666 (1992).
- [28] Zavatta, A., Parigi, V. & Bellini, M. Toward quantum frequency combs: Boosting the generation of highly nonclassical light states by cavity-enhanced parametric down-conversion at high repetition rates. *Phys. Rev. A* **78**, 033809 (2008).
- [29] Wieczorek, W., Kiesel, N., Schmid, C. & Weinfurter, H. Multiqubit entanglement engineering via projective measurements. *Phys. Rev. A* **79**, 022311 (2009).
- [30] Żukowski, M., Zeilinger, A. & Weinfurter, H. Entangling photons radiated by independent pulsed sources. *Ann. N. Y.* **755**, 91 (2006).
- [31] Rarity, J. G. Interference of Single Photons from Separate Sources. *Ann. N. Y.* **755**, 624 (1995).
- [32] Kiess, T. E., Shih, Y. H., Sergienko, A. V. & Alley, C. O. Einstein-Podolsky-Rosen-Bohm experiment using pairs of light quanta produced by type-II parametric down-conversion. *Phys. Rev. Lett.* **71**, 3893–3897 (1993).
- [33] Tóth, G. Detection of multipartite entanglement in the vicinity of symmetric Dicke states. *J. Opt. Soc. Am. B* **24**, 275 (2007).

Chapter 6

Conclusions and outlook

This work introduced several new tools for quantum information experiments and applications using photonic qubits. A major focus has been the realization of flexible experimental schemes, setup-based and entanglement-based, that allow the observation of different types of entangled states in a single setup. In addition, a novel spontaneous parametric down conversion (SPDC) source has been designed based on an ultraviolet (UV) enhancement cavity to increase the number of photons available for photonic entanglement studies. The characterization of the entangled states has been performed with new theoretical tools that allow one to study characteristic entanglement properties with few measurement settings. Most importantly, two of the observed entangled states have been applied for proof-of-principle demonstrations of quantum information applications: the simulation of anyonic features and the estimation of a phase shift with a sensitivity better than the shot noise limit.

In general, the experimental implementation of multi-photon entanglement requires photon sources, subsequent photonic manipulations in an optical network and conditional detection [42]. This approach was successfully applied to the observation of a variety of entangled states and for proof-of-principle demonstrations of applications [23]. However, so far, for each and every application and quantum state a new experimental setup had to be designed. In this work two different approaches have been described to break with this inflexibility [38, 53–55] (see publ. P3.1, P3.2, P5.1 and P5.2). The first approach has relied on a particular experimental arrangement, namely on multi-photon interference of an entangled input state at a polarizing beam splitter with prior polarization manipulations [53, 54] (see publ. P3.1 and P3.2). This approach has allowed the observation of an important family of four photon, highly entangled states, all with a fidelity ranging between 0.762 ± 0.011 and 0.932 ± 0.008 . The second approach has been based on the properties of particular entangled states, namely the behavior of symmetric Dicke states under particle projections [55] (see publ. P5.2). It has been demonstrated that by using the six-qubit entangled Dicke state with three excitations (implemented with a fidelity of 0.654 ± 0.024) inequivalent types of entanglement of a lower qubit number can be achieved [38, 39] (see publ. P5.1).

These two approaches consequently have been utilized for a photonic implementation of

particular quantum information applications. The four-photon family of states mentioned above contains many well known states. One of these, namely the Greenberger Horne Zeilinger (GHZ) state [62–64], has been used for the simulation of anyonic statistics [57] (see publ. P4.1). Anyons are new types of particles that appear in two-dimensional systems besides the well known particle groups of fermions and bosons [67, 68]. In this work an instance of the toric code has been implemented to demonstrate anyonic features and their statistics [57] (see publ. P4.1). To this end, the evolution of the anyonic wave function upon local operations has been studied. This simulation paves the way for a future utilization of anyons in topological quantum information and has already stimulated many new proposals [296, 298, 336]. The six-qubit entangled Dicke state can be used for phase estimation [19]. It surpasses classical means of phase estimation by beating the shot noise limit, which has also been demonstrated experimentally. Remarkably, it has been found that the symmetric Dicke states $D_{2N}^{(N)}$ exhibit a phase sensitivity better than the shot noise limit along any great circle parallel to the z axis of the Bloch sphere. This is not found, for example, for GHZ states.

The multi-photon entangled states observed in this work have been characterized along two major directions. First, their entanglement has been proven by using different theoretical tools. Second, their properties have been analyzed focusing on particle projections and particle loss. The four-qubit family experiment has allowed the comparison of different entanglement detection methods. It has been found that the methods differed in the necessary measurement settings and their robustness against noise. Furthermore, for symmetric Dicke states new entanglement witnesses have been developed, which exploit their permutational symmetry [81] (see publ. P5.3). Some of these allow an estimation of the fidelity of the observed states with only three measurement settings. Further characterization has focused on particular properties of entangled states that turn out to be useful in quantum information: It has been found that symmetric entangled Dicke states [77, 83] allow one to obtain inequivalent types of entanglement of a lower qubit number by using projective measurements. These states also exhibit a high robustness against particle loss. All this clearly shows that Dicke states resemble another important group of states in quantum information besides the well known GHZ states, cluster states or, more generally, graph states [116].

In general, the observation of entanglement between an increasing number of photons is demanding. The widespread utilization of probabilistic photon sources based on the process of SPDC comes along with an exponentially decreasing amplitude for increasing photon numbers. Therefore, in this work a new SPDC source has been implemented with the goal to increase the UV pump power necessary for the production of SPDC photons [56] (see publ. P5.4). Though the probabilistic nature of photon production still remains, the available photon rate has been significantly increased. To this end, a femtosecond UV enhancement cavity has been implemented increasing the available UV pump power from ~ 1 W for commercial laser systems to now up to ~ 7 W, which altogether has resulted in an increase of the six-photon count rate by up to two orders of magnitude.

However, in spite of this dramatic increase in photon rate, for future implementations of multiple photonic qubits further improvements have to be made. Two main technological

issues are a challenge to current multi-photon experiments, the probabilistic production of photons and the low detection efficiency. The development of reliable, deterministic single photon sources is desirable: they are a major ingredient for scalable, linear optical quantum computation [42]. To date, single photon sources still lack the suitability for multi-photon entanglement implementations and, thus, probabilistic sources will still be the workhorse for these studies. However, spontaneous sources always emit undesired higher order photons, which yield noise on top of the desired states [55, 337]. An increase in detection and coupling efficiency will drastically reduce measurement times and the effects of SPDC noise. Still, silicon-based avalanche photo diodes are the most efficient detectors in the visible to infrared wavelength regime. New developments can be expected from superconducting detectors in the future [338, 339].

The number of entangled, individually addressable particles in different physical systems can be regarded as a useful measure to compare the photonic implementation of multi-partite entanglement with other physical systems. At the same time this comparison reflects the current status of the control over entanglement. Atomic, molecular and optical systems lead, at the present time, with the achievements of entanglement between eight trapped ions [41] or six photons [36–39]. Recently, high gate fidelities of larger than 99% [340] have been realized and new trap geometries based on microfabricated surface-electrode traps [341] will surely increase the number of entangled ions in the near future. The progress in photonic based entanglement studies depends crucially on the development of efficient single photon sources and high efficiency detectors, as has been outlined before. Recently, multi-partite entanglement has also been achieved in solid state-based systems with microsecond long coherence times: three entangled carbon nuclear and electronic spins in diamond [32] or two entangled superconducting qubits [34, 35]. Increasing the number of entangled qubits in both systems will demand for longer coherence times and higher fidelities.

Which physical system will turn out to be the most appropriate for realizing entanglement between a huge number of individually addressable particles is still an open issue [33]. Potentially, however, a combination of systems uniting fast operation, long distance communication and long storage times, which are all important ingredients for a breakthrough in quantum information processing and related future technological applications, will be used.

Appendix A

SPDC photon state

In this appendix the photonic states for non-collinear and collinear type II SPDC (see eq. 2.57 and eq. 2.56) are explicitly derived. It begins with the Hamiltonians of eq. 2.53 and eq. 2.54 describing the SPDC process in a single mode treatment. The goal here is to deduce the complete photonic quantum state. The derivation for non-collinear type II SPDC can also be found in refs. [52, 206].

Commutation relations First, some rules and commutation relations for bosonic operators \hat{a} and \hat{b} are stated [50], where the indices i and j will take the role of the horizontal (H) and vertical (V) polarization modes. Further, $|\text{vac}\rangle$ denotes the vacuum state, $|n\rangle$ a state with n photons and $\hat{a}^\dagger\hat{a} = \hat{n}$ is the photon number operator:

$$\begin{aligned}\hat{a}^\dagger |n\rangle &= \sqrt{n+1} |n+1\rangle \\ (\hat{a}^\dagger)^n |\text{vac}\rangle &= \sqrt{n!} |n\rangle \\ \hat{a} |n\rangle &= \sqrt{n} |n-1\rangle \\ \hat{a} |\text{vac}\rangle &= 0 |\text{vac}\rangle = 0 \\ \hat{a}^\dagger\hat{a} |n\rangle &= n |n\rangle \\ [\hat{a}_i, \hat{a}_j^\dagger] &= \delta_{i,j} \\ [\hat{a}_i, \hat{a}_j] &= [\hat{a}_i^\dagger, \hat{a}_j^\dagger] = 0. \\ (\hat{a}^\dagger)^\dagger &= \hat{a} \\ (\hat{a}\hat{b})^\dagger &= \hat{b}^\dagger\hat{a}^\dagger.\end{aligned}\tag{A.1}$$

A.1 Non-collinear type II SPDC

Hamiltonian The following Hamiltonian is assumed for a single mode treatment of a non-collinear type II SPDC process (see eq. 2.54) [50, 206, 245]:

$$\hat{\mathcal{H}} = i\hbar\kappa(\hat{a}_H^\dagger\hat{b}_V^\dagger - \hat{a}_V^\dagger\hat{b}_H^\dagger) + h.c.\tag{A.2}$$

where κ describes the coupling between the crystal and the pump field and depends linearly on the latter and on the non-linearity $\chi^{(2)}$ of the crystal. Using the time evolution operator $\hat{U}(t) = \exp(-i\hat{\mathcal{H}}t/\hbar)$ the state vector $|\psi\rangle$ is given as

$$|\psi\rangle = \hat{U}(t)|\text{vac}\rangle = \exp(-i\hat{\mathcal{H}}t/\hbar)|\text{vac}\rangle, \quad (\text{A.3})$$

where t is the time the pump propagates through the crystal and $|\text{vac}\rangle$ is the vacuum state. It is useful to define the ladder operators \hat{L}_+ and \hat{L}_-

$$\hat{L}_+ := \hat{a}_H^\dagger \hat{b}_V^\dagger - \hat{a}_V^\dagger \hat{b}_H^\dagger = (\hat{L}_-)^\dagger \quad (\text{A.4})$$

that describe the creation and annihilation of a photon pair of orthogonal polarizations in two spatial modes a and b . The Hamiltonian and the time evolution operator can then be rewritten as

$$\hat{\mathcal{H}} = i\hbar\kappa\hat{L}_+ - i\hbar\kappa^*\hat{L}_-, \quad (\text{A.5})$$

$$\hat{U}(t) = \exp(\kappa t\hat{L}_+ - \kappa^* t\hat{L}_-). \quad (\text{A.6})$$

For the ladder operators \hat{L}_- and \hat{L}_+ the commutation relations and rules

$$\begin{aligned} [\hat{L}_-, \hat{L}_+] &= \hat{L}_-\hat{L}_+ - \hat{L}_+\hat{L}_- = \hat{a}_H^\dagger \hat{a}_H + \hat{a}_V^\dagger \hat{a}_V + \hat{b}_H^\dagger \hat{b}_H + \hat{b}_V^\dagger \hat{b}_V + 2 =: 2\hat{L}_0 \\ [\hat{L}_0, \hat{L}_\pm] &= \hat{L}_0\hat{L}_\pm - \hat{L}_\pm\hat{L}_0 = \pm\hat{L}_\pm \\ \hat{L}_- &= (\hat{L}_+)^\dagger \\ \hat{L}_0 &= (\hat{L}_0)^\dagger \end{aligned}$$

hold with the operator \hat{L}_0 defined as in eq. A.7. The commutation relations for the three operators \hat{L}_- , \hat{L}_+ , and \hat{L}_0 can be attributed to a $\text{SU}(1,1)$ algebra [342]. For this algebra a normal ordering of the operators can be used to rewrite eq. A.6 with the goal to order all annihilation operators to the right hand side:

$$\begin{aligned} \hat{U}(t) &= \exp(\kappa t\hat{L}_+ - \kappa^* t\hat{L}_-) \\ &= \exp(\hat{\tau} \tanh|\tau|\hat{L}_+) \cdot \exp(-2\ln(\cosh|\tau|)\hat{L}_0) \cdot \exp(-\hat{\tau}^* \tanh|\tau|\hat{L}_-), \quad (\text{A.7}) \end{aligned}$$

where $\tau := \kappa t$ can be interpreted as overall interaction parameter and $\hat{\tau} = \tau/(|\tau|)$. Here, $\hat{\tau} = \kappa t/(|\kappa t|) = 1$.

SPDC photon state Now the state $|\psi\rangle = \hat{U}(t)|\text{vac}\rangle$ can be calculated using eq. A.7 and the abbreviations $r := \tanh|\tau|$ and $q := 2\ln(\cosh|\tau|)$:

$$\begin{aligned} |\psi\rangle &= \exp(r\hat{L}_+) \cdot \exp(-q\hat{L}_0) \cdot \underbrace{\exp(-r\hat{L}_-)|\text{vac}\rangle}_{\exp(-q)|\text{vac}\rangle} \\ &= e^{-q} \sum_{l=0}^{\infty} \frac{r^l}{l!} (\hat{L}_+)^l |\text{vac}\rangle. \end{aligned}$$

Using

$$(\hat{L}_+)^l |\text{vac}\rangle = \sum_{m=0}^l l! (-1)^m |m_H, (l-m)_V\rangle_a |(l-m)_H, m_V\rangle_b, \quad (\text{A.8})$$

one finally obtains the photon state of a non-collinear type II SPDC process as

$$\begin{aligned} |\psi\rangle &= e^{-q} \sum_{l=0}^{\infty} \frac{r^l}{l!} (\hat{L}_+)^l |\text{vac}\rangle = e^{-q} \sum_{l=0}^{\infty} r^l \sum_{m=0}^l (-1)^m |m_H, (l-m)_V\rangle_a |(l-m)_H, m_V\rangle_b \\ &= \frac{1}{\cosh^2 |\tau|} \sum_{l=0}^{\infty} \tanh^l |\tau| \cdot (-1)^m |m_H, (l-m)_V\rangle_a |(l-m)_H, m_V\rangle_b. \end{aligned} \quad (\text{A.9})$$

This state corresponds to the one given in eq. 2.57. Assuming $|\tau| \ll 1$, which holds for example for low pump powers, the approximation $\tanh |\tau| \approx |\tau|$ is valid and one obtains as simplified SPDC photon state using also $(1 - |\tau|^2) \approx 1$

$$|\psi\rangle \approx \sum_{l=0}^{\infty} |\tau|^l \cdot (-1)^m |m_H, (l-m)_V\rangle_a |(l-m)_H, m_V\rangle_b. \quad (\text{A.10})$$

Normalization The state $|\psi\rangle$ is normalized for $|\tanh^2 |\tau|| < 1$:

$$\begin{aligned} \langle \psi | \psi \rangle &= e^{-2q} \sum_{l'=0}^{\infty} r^{l'} \sum_{m'=0}^{l'} (-1)^{m'} \sum_{l=0}^{\infty} r^l \sum_{m=0}^l (-1)^m \delta_{mm'} \\ &= e^{-2q} \sum_{l',l=0}^{\infty} \sum_{m',m=0}^{l',l} r^{l'+l} (-1)^{2m} \\ &\stackrel{\delta_{mm'} \rightarrow l'=l}{=} e^{-2q} \sum_{l=0}^{\infty} \sum_{m=0}^l r^{2l} (-1)^{2m} = e^{-2q} \sum_{l=0}^{\infty} r^{2l} (l+1) \\ &\text{using } \sum_{n=1}^{\infty} nq^{n-1} = \frac{1}{(1-q)^2}, \quad |q| < 1 \\ &= e^{-2q} \sum_{l=1}^{\infty} (r^2)^{l-1} l \stackrel{|r^2| < 1}{=} e^{-2q} \frac{1}{(1-r^2)^2} \\ &\stackrel{r=\tanh |\tau|, q=2 \ln(\cosh |\tau|)}{=} \frac{1}{\cosh^4 |\tau|} \frac{1}{(1 - \tanh^2 |\tau|)^2} \\ &= \frac{1}{\cosh^4 |\tau|} \frac{1}{(1/\cosh^2 |\tau|) (\underbrace{\cosh^2 |\tau| - \sinh^2 |\tau|}_{=1})^2} \\ &= 1. \end{aligned}$$

A.2 Collinear type II SPDC

Hamiltonian The following Hamiltonian is assumed for a collinear type II SPDC process (see eq. 2.53) [50]:

$$\hat{\mathcal{H}} = i\hbar\kappa\hat{a}_H^\dagger\hat{a}_V^\dagger + h.c. \quad (\text{A.11})$$

where κ describes the coupling between the crystal and the pump field. For collinear type II SPDC the ladder operators \hat{L}_+ and \hat{L}_- are given as

$$\hat{L}_+ := \hat{a}_H^\dagger\hat{a}_V^\dagger = (\hat{L}_-)^\dagger \quad (\text{A.12})$$

describing the creation and annihilation of a photon pair of orthogonal polarization in a single spatial mode a . For the ladder operators \hat{L}_- and \hat{L}_+ the commutation relations and rules

$$\begin{aligned} [\hat{L}_-, \hat{L}_+] &= \hat{L}_-\hat{L}_+ - \hat{L}_+\hat{L}_- = \hat{a}_H^\dagger\hat{a}_H + \hat{a}_V^\dagger\hat{a}_V + 1 =: 2\hat{L}_0 \\ [\hat{L}_0, \hat{L}_\pm] &= \hat{L}_0\hat{L}_\pm - \hat{L}_\pm\hat{L}_0 = \pm\hat{L}_\pm \\ \hat{L}_- &= (\hat{L}_+)^\dagger \\ \hat{L}_0 &= (\hat{L}_0)^\dagger \end{aligned}$$

hold. Again, the commutation relations for \hat{L}_- , \hat{L}_+ , and \hat{L}_0 can be attributed to a $SU(1,1)$ algebra [342], thus the time evolution operator can be rewritten as:

$$\begin{aligned} \hat{U}(t) &= \exp(\kappa t\hat{L}_+ - \kappa^* t\hat{L}_-) \\ &= \exp(\hat{\tau} \tanh|\tau|\hat{L}_+) \cdot \exp(-2\ln(\cosh|\tau|)\hat{L}_0) \cdot \exp(-\hat{\tau}^* \tanh|\tau|\hat{L}_-), \quad (\text{A.13}) \end{aligned}$$

where $\tau := \kappa t$ and $\hat{\tau} = \tau/|\tau|$. Here, $\hat{\tau} = \kappa t/|\kappa t| = 1$.

SPDC photon state The state $|\psi\rangle = \hat{U}(t)|\text{vac}\rangle$ can be calculated using eq. A.13 and the abbreviations $r := \tanh|\tau|$ and $q := 2\ln(\cosh|\tau|)$:

$$\begin{aligned} |\psi\rangle &= \exp(r\hat{L}_+) \cdot \exp(-q\hat{L}_0) \cdot \underbrace{\exp(-r\hat{L}_-)|\text{vac}\rangle}_{|\text{vac}\rangle} \\ &= e^{-q/2} \sum_{l=0}^{\infty} \frac{r^l}{l!} (\hat{L}_+)^l |\text{vac}\rangle. \end{aligned}$$

Using

$$(\hat{L}_+)^l |\text{vac}\rangle = l! |l_H, l_V\rangle_a, \quad (\text{A.14})$$

one obtains the photon state of a type II collinear SPDC process as

$$\begin{aligned}
 |\psi\rangle &= e^{-g/2} \sum_{l=0}^{\infty} \frac{r^l}{l!} (\hat{L}_+)^l |\text{vac}\rangle = e^{-g/2} \sum_{l=0}^{\infty} r^l |l_H, l_V\rangle_a \\
 &= \sqrt{1 - \tanh^2 |\tau|} \sum_{l=0}^{\infty} \tanh^l |\tau| \cdot |l_H, l_V\rangle_a.
 \end{aligned} \tag{A.15}$$

This state corresponds to the one given in eq. 2.56 and is normalized for $|\tanh^2 |\tau|| \ll 1$. Assuming $|\tau| \ll 1$ one can make the approximation $\tanh |\tau| \approx |\tau|$ and obtains as simplified SPDC photon state using also $\sqrt{1 - |\tau|^2} \approx 1$

$$|\psi\rangle \approx \sum_{l=0}^{\infty} |\tau|^l \cdot |l_H, l_V\rangle_a. \tag{A.16}$$

Appendix B

Measurement settings and counting statistics

B.1 Measurement settings

Local measurement settings The following abbreviations for the Pauli spin matrices

$$\begin{aligned}\hat{\sigma}_x &\rightarrow X \\ \hat{\sigma}_y &\rightarrow Y \\ \hat{\sigma}_z &\rightarrow Z\end{aligned}\tag{B.1}$$

are used. As has been described in section 2.1 a single tensor product of Pauli spin matrices $\hat{\sigma}_{\mu_1} \otimes \hat{\sigma}_{\mu_2} \otimes \dots \otimes \hat{\sigma}_{\mu_N}$ is called measurement setting, where $\hat{\sigma}_{\mu_n} \in \{\hat{\sigma}_0, \hat{\sigma}_x, \hat{\sigma}_y, \hat{\sigma}_z\}$ and $\hat{\sigma}_0 = \mathbb{1}$, or more generally $\hat{\sigma}_{\mu_n} = \hat{\sigma}(\theta, \phi)$ for any observable. This is abbreviated as, for example

$$\begin{aligned}\hat{\sigma}_{x_1} \otimes \hat{\sigma}_{x_2} \otimes \dots \otimes \hat{\sigma}_{x_N} &= \underbrace{XX \dots X}_{N\text{-times}} = X^{\otimes N} \text{ or,} \\ \hat{\sigma}_{z_1} \otimes \hat{\sigma}_{z_2} \otimes \hat{\sigma}_{y_3} \dots \otimes \hat{\sigma}_{y_N} &= ZZ \underbrace{Y \dots Y}_{(N-2)\text{times}} = ZZ Y^{\otimes N-2}\end{aligned}\tag{B.2}$$

Experimentally, a local observable $\hat{\sigma}_{\mu_n} = \hat{\sigma}(\theta, \phi)$ is measured with a polarization analysis consisting of a HWP(θ_1), a QWP(θ_2) and a PBS and has been described in section 2.3, see also fig. 2.6 (for the relation between θ, ϕ and θ_1, θ_2 see eq. 2.67). The angles given in tab. B.1 have to be set in order to measure particular observables.

Measurement setting	HWP(θ_1)	QWP(θ_2)
X	22.5°	0°
Y	0°	45°
Z	0°	0°
$(X + Z)/\sqrt{2}$	11.25°	0°
$(X - Z)/\sqrt{2}$	33.75°	0°
$(Y + Z)/\sqrt{2}$	11.25°	22.5°
$(Y - Z)/\sqrt{2}$	56.25°	22.5°
$(X + Y)/\sqrt{2}$	33.75°	22.5°
$(X - Y)/\sqrt{2}$	11.25°	-22.5°
$(X + Y + Z)/\sqrt{3}$	2.4339°	72.3678°
$(X + Y - Z)/\sqrt{3}$	24.9339°	72.3678°
$(X - Y + Z)/\sqrt{3}$	20.0661°	107.632°
$(X - Y - Z)/\sqrt{3}$	42.5661°	107.632°
$(\cos \frac{\pi}{8})Y + (\sin \frac{\pi}{8})X$	39.375°	33.75°
$(\cos \frac{3\pi}{8})Y + (\sin \frac{3\pi}{8})X$	28.125°	11.25°
$(\cos \frac{5\pi}{8})Y + (\sin \frac{5\pi}{8})X$	16.875°	-11.25°
$(\cos \frac{7\pi}{8})Y + (\sin \frac{7\pi}{8})X$	5.625°	-33.75°
$(Z + \sqrt{3}X)/2$	15°	0°
$(Z - \sqrt{3}X)/2$	75°	0°
$(\sqrt{3}Z + X)/2$	7.5°	0°
$(\sqrt{3}Z - X)/2$	82.5°	0°
$(Z + \sqrt{3}Y)/2$	-15°	60°
$(Z - \sqrt{3}Y)/2$	15°	120°
$(\sqrt{3}Z + Y)/2$	-7.5°	75°
$(\sqrt{3}Z - Y)/2$	7.5°	105°
$((1 + \sqrt{3})X + (-1 + \sqrt{3})Z)/(2\sqrt{2})$	18.75°	0°
$((-1 + \sqrt{3})X + (1 + \sqrt{3})Z)/(2\sqrt{2})$	3.75°	0°
$((1 - \sqrt{3})X + (1 + \sqrt{3})Z)/(2\sqrt{2})$	86.25°	0°
$-((1 + \sqrt{3})X + (1 - \sqrt{3})Z)/(2\sqrt{2})$	71.25°	0°
$((1 + \sqrt{3})Y + (-1 + \sqrt{3})Z)/(2\sqrt{2})$	-18.75°	52.5°
$((-1 + \sqrt{3})Y + (1 + \sqrt{3})Z)/(2\sqrt{2})$	-3.75°	82.5°
$((1 - \sqrt{3})Y + (1 + \sqrt{3})Z)/(2\sqrt{2})$	3.75°	97.5°
$-((1 + \sqrt{3})Y + (1 - \sqrt{3})Z)/(2\sqrt{2})$	18.75°	127.5°

Table B.1: Measurement settings and corresponding settings of a HWP(θ_1) and QWP(θ_2) in a polarization analysis (see fig. 2.6).

Measurement settings for the four-photon family experiment In tab. B.2 the measurement settings for the observables (for their definition see chapter 2) measured in the four-photon family experiment and the experiment for revealing anyonic features are summarized.

#	Measurement setting	Observable
1	$X^{\otimes 4}$	$F_{\Psi_4(\alpha)}(\rho), T_{x^{\otimes 4}}, \langle \hat{J}_x^2 \rangle, \langle \hat{c}_{xy}(\pi/2) \rangle$
2	$Y^{\otimes 4}$	$F_{\Psi_4(\alpha)}(\rho), T_{y^{\otimes 4}}, \langle \hat{J}_y^2 \rangle, \langle \hat{c}_{xy}(0) \rangle$
3	$Z^{\otimes 4}$	$F_{\Psi_4(\alpha)}(\rho), T_{z^{\otimes 4}}, \langle \hat{J}_z^2 \rangle$
4	YYXX	$F_{\Psi_4(\alpha)}(\rho)$
5	ZZXX	$F_{\Psi_4(\alpha)}(\rho)$
6	YXYX	$F_{\Psi_4(\alpha)}(\rho)$
7	XYXX	$F_{\Psi_4(\alpha)}(\rho)$
8	ZXZX	$F_{\Psi_4(\alpha)}(\rho)$
9	XZZX	$F_{\Psi_4(\alpha)}(\rho)$
10	YXXY	$F_{\Psi_4(\alpha)}(\rho)$
11	XYXY	$F_{\Psi_4(\alpha)}(\rho)$
12	XXYY	$F_{\Psi_4(\alpha)}(\rho)$
13	ZZYY	$F_{\Psi_4(\alpha)}(\rho)$
14	ZYZY	$F_{\Psi_4(\alpha)}(\rho)$
15	YZZY	$F_{\Psi_4(\alpha)}(\rho)$
16	ZXXZ	$F_{\Psi_4(\alpha)}(\rho)$
17	XZZZ	$F_{\Psi_4(\alpha)}(\rho)$
18	ZYYZ	$F_{\Psi_4(\alpha)}(\rho)$
19	YZYZ	$F_{\Psi_4(\alpha)}(\rho)$
20	XXZZ	$F_{\Psi_4(\alpha)}(\rho)$
21	YYZZ	$F_{\Psi_4(\alpha)}(\rho)$
22	$((\cos \frac{\pi}{8})Y + (\sin \frac{\pi}{8})X)^{\otimes 4}$	$\langle \hat{c}_{xy}(\pi/8) \rangle$
23	$((Y + X)/\sqrt{2})^{\otimes 4}$	$\langle \hat{c}_{xy}(\pi/4) \rangle$
24	$((\cos \frac{3\pi}{8})Y + (\sin \frac{3\pi}{8})X)^{\otimes 4}$	$\langle \hat{c}_{xy}(3\pi/8) \rangle$
25	$((\cos \frac{5\pi}{8})Y + (\sin \frac{5\pi}{8})X)^{\otimes 4}$	$\langle \hat{c}_{xy}(5\pi/8) \rangle$
26	$((Y - X)/\sqrt{2})^{\otimes 4}$	$\langle \hat{c}_{xy}(3\pi/4) \rangle$
27	$((\cos \frac{7\pi}{8})Y + (\sin \frac{7\pi}{8})X)^{\otimes 4}$	$\langle \hat{c}_{xy}(7\pi/8) \rangle$

Table B.2: Measurement settings for the four-photon family experiment and the experiment for revealing anyonic features. The measured observables have been the fidelity $F_{\Psi_4(\alpha)}(\rho)$, the correlations $T_{x^{\otimes 4}}, T_{y^{\otimes 4}}, T_{z^{\otimes 4}}$, the spin components $\langle \hat{J}_x^2 \rangle, \langle \hat{J}_y^2 \rangle, \langle \hat{J}_z^2 \rangle$ and the correlation function $\langle \hat{c}_{xy}(\gamma) \rangle$. Note, for a four-qubit tomography all $3^4 = 81$ possible combinations of the settings X, Y and Z for four qubits have to be measured.

Measurement settings for the six-photon Dicke experiment In tab. B.3, tab. B.4, and tab. B.5 the measurement settings for the observables measured in the six-photon Dicke experiment are summarized.

#	Measurement setting	Observable	#	Measurement setting	Observable
1	$X^{\otimes 6}$	$\langle \hat{\mathcal{B}}_{D_6^{(3)}} \rangle$	17	$XZZXXZ$	$\langle \hat{\mathcal{B}}_{D_6^{(3)}} \rangle$
2	$Y^{\otimes 6}$	$\langle \hat{\mathcal{B}}_{D_6^{(3)}} \rangle$	18	$XZXZXZ$	$\langle \hat{\mathcal{B}}_{D_6^{(3)}} \rangle$
3	$XZZZZX$	$\langle \hat{\mathcal{B}}_{D_6^{(3)}} \rangle$	19	$XXZZXZ$	$\langle \hat{\mathcal{B}}_{D_6^{(3)}} \rangle$
4	$XZZZXZ$	$\langle \hat{\mathcal{B}}_{D_6^{(3)}} \rangle$	20	$XZXXZZ$	$\langle \hat{\mathcal{B}}_{D_6^{(3)}} \rangle$
5	$XZZXZZ$	$\langle \hat{\mathcal{B}}_{D_6^{(3)}} \rangle$	21	$XXZXZZ$	$\langle \hat{\mathcal{B}}_{D_6^{(3)}} \rangle$
6	$XZXZZZ$	$\langle \hat{\mathcal{B}}_{D_6^{(3)}} \rangle$	22	$XXXZZZ$	$\langle \hat{\mathcal{B}}_{D_6^{(3)}} \rangle$
7	$XXZZZZ$	$\langle \hat{\mathcal{B}}_{D_6^{(3)}} \rangle$	23	$YZZZY Y$	$\langle \hat{\mathcal{B}}_{D_6^{(3)}} \rangle$
8	$YZZZY Y$	$\langle \hat{\mathcal{B}}_{D_6^{(3)}} \rangle$	24	$YZZYZ Y$	$\langle \hat{\mathcal{B}}_{D_6^{(3)}} \rangle$
9	$YZZZY Z$	$\langle \hat{\mathcal{B}}_{D_6^{(3)}} \rangle$	25	$YZYZZY$	$\langle \hat{\mathcal{B}}_{D_6^{(3)}} \rangle$
10	$YZZYZZ$	$\langle \hat{\mathcal{B}}_{D_6^{(3)}} \rangle$	26	$YYZZZY$	$\langle \hat{\mathcal{B}}_{D_6^{(3)}} \rangle$
11	$YZYZZZ$	$\langle \hat{\mathcal{B}}_{D_6^{(3)}} \rangle$	27	$YZZYYZ$	$\langle \hat{\mathcal{B}}_{D_6^{(3)}} \rangle$
12	$YYZZZZ$	$\langle \hat{\mathcal{B}}_{D_6^{(3)}} \rangle$	28	$YZYZYZ$	$\langle \hat{\mathcal{B}}_{D_6^{(3)}} \rangle$
13	$XZZZX X$	$\langle \hat{\mathcal{B}}_{D_6^{(3)}} \rangle$	29	$YYZZYZ$	$\langle \hat{\mathcal{B}}_{D_6^{(3)}} \rangle$
14	$XZZXZX$	$\langle \hat{\mathcal{B}}_{D_6^{(3)}} \rangle$	30	$YZYYZZ$	$\langle \hat{\mathcal{B}}_{D_6^{(3)}} \rangle$
15	$XZXZZX$	$\langle \hat{\mathcal{B}}_{D_6^{(3)}} \rangle$	31	$YYZYZZ$	$\langle \hat{\mathcal{B}}_{D_6^{(3)}} \rangle$
16	$XXZZZX$	$\langle \hat{\mathcal{B}}_{D_6^{(3)}} \rangle$	32	$YYYZZZ$	$\langle \hat{\mathcal{B}}_{D_6^{(3)}} \rangle$

Table B.3: Measurement settings for the six-photon Dicke experiment. The measured observable has been the Bell inequality $\langle \hat{\mathcal{B}}_{D_6^{(3)}} \rangle$.

#	Measurement setting	Observable
1	$X^{\otimes 6}$	$F_{D_6^{(3)}}(\rho), \langle \hat{J}_{6,x}^2 \rangle, \langle \hat{J}_{5,x}^2 \rangle, \langle \hat{c}_{xz}(0)^{\otimes 6} \rangle$
2	$Y^{\otimes 6}$	$F_{D_6^{(3)}}(\rho), \langle \hat{J}_{6,y}^2 \rangle, F_{(D_4^{(1)} + D_4^{(3)})/\sqrt{2}}(\rho), \langle \hat{c}_{yz}(0)^{\otimes 6} \rangle$
3	$Z^{\otimes 6}$	$F_{D_6^{(3)}}(\rho), \langle \hat{J}_{6,z}^2 \rangle, \langle \hat{J}_{5,z}^2 \rangle, \langle \hat{J}_{4,z}^2 \rangle, \langle \hat{c}_{xz}(\pi/2)^{\otimes 6} \rangle, \langle \hat{c}_{yz}(\pi/2)^{\otimes 6} \rangle$
		$F_{D_4^{(1)}}(\rho), F_{D_4^{(2)}}(\rho)$
4	$ZX^{\otimes 5}$	$\langle \hat{J}_{5,x}^2 \rangle$
5	$ZY^{\otimes 5}$	$\langle \hat{J}_{5,y}^2 \rangle$
6	$XZ^{\otimes 5}$	$\langle \hat{J}_{5,z}^2 \rangle$
7	$XY^{\otimes 5}$	$\langle \hat{J}_{5,y}^2 \rangle$
8	$ZZX^{\otimes 4}$	$\langle \hat{J}_{4,x}^2 \rangle$
9	$ZZY^{\otimes 4}$	$\langle \hat{J}_{4,y}^2 \rangle$
10	$ZZ((X + Z)/\sqrt{2})^{\otimes 4}$	$F_{D_4^{(1)}}(\rho), F_{D_4^{(2)}}(\rho)$
11	$ZZ((X - Z)/\sqrt{2})^{\otimes 4}$	$F_{D_4^{(1)}}(\rho), F_{D_4^{(2)}}(\rho)$
12	$ZZ((Y + Z)/\sqrt{2})^{\otimes 4}$	$F_{D_4^{(1)}}(\rho), F_{D_4^{(2)}}(\rho)$
13	$ZZ((Y - Z)/\sqrt{2})^{\otimes 4}$	$F_{D_4^{(1)}}(\rho), F_{D_4^{(2)}}(\rho)$
14	$ZZ((X + Y)/\sqrt{2})^{\otimes 4}$	$F_{D_4^{(2)}}(\rho)$
15	$ZZ((X - Y)/\sqrt{2})^{\otimes 4}$	$F_{D_4^{(2)}}(\rho)$
16	$YYZ^{\otimes 4}$	$\langle \hat{J}_{4,z}^2 \rangle, F_{(D_4^{(1)} + D_4^{(3)})/\sqrt{2}}(\rho)$
17	$YYX^{\otimes 4}$	$\langle \hat{J}_{4,x}^2 \rangle, F_{(D_4^{(1)} + D_4^{(3)})/\sqrt{2}}(\rho)$
18	$YY((Y + Z)/\sqrt{2})^{\otimes 4}$	$F_{(D_4^{(1)} + D_4^{(3)})/\sqrt{2}}(\rho)$
19	$YY((Y - Z)/\sqrt{2})^{\otimes 4}$	$F_{(D_4^{(1)} + D_4^{(3)})/\sqrt{2}}(\rho)$

Table B.4: Measurement settings for the six-photon Dicke experiment. The measured observables for the state $|D_6^{(3)}\rangle$ have been: the fidelity $F_{D_6^{(3)}}(\rho)$ (continued in tab. B.5), the correlation functions $\langle \hat{c}_{xz}(\gamma)^{\otimes 6} \rangle$ and $\langle \hat{c}_{yz}(\gamma)^{\otimes 6} \rangle$ (continued in tab. B.5), and different witnesses using $\langle \hat{J}_{6,x}^2 \rangle$, $\langle \hat{J}_{6,y}^2 \rangle$, and $\langle \hat{J}_{6,z}^2 \rangle$. For the five-qubit states $|D_5^{(3)}\rangle$ and $(|D_5^{(2)}\rangle - |D_5^{(3)}\rangle)/\sqrt{2}$ the observables $\langle \hat{J}_{5,x}^2 \rangle$, $\langle \hat{J}_{5,y}^2 \rangle$ and $\langle \hat{J}_{5,z}^2 \rangle$ for determining different witnesses have been measured. For the four-qubit states $|D_4^{(1)}\rangle$, $|D_4^{(2)}\rangle$ and $(D_4^{(1)} + D_4^{(3)})/\sqrt{2}$ the observables $\langle \hat{J}_{4,x}^2 \rangle$, $\langle \hat{J}_{4,y}^2 \rangle$ and $\langle \hat{J}_{4,z}^2 \rangle$ for determining different witnesses and their fidelities $F_{D_4^{(1)}}(\rho)$, $F_{D_4^{(2)}}(\rho)$ and $F_{(D_4^{(1)} + D_4^{(3)})/\sqrt{2}}(\rho)$, respectively, have been measured.

#	Measurement setting	Observable
1	$((X + Y)/\sqrt{2})^{\otimes 6}$	$F_{D_6^{(3)}}(\rho)$
2	$((X - Y)/\sqrt{2})^{\otimes 6}$	$F_{D_6^{(3)}}(\rho)$
3	$((X + Z)/\sqrt{2})^{\otimes 6}$	$F_{D_6^{(3)}}(\rho), \langle \hat{c}_{xz}(\pi/4)^{\otimes 6} \rangle$
4	$((X - Z)/\sqrt{2})^{\otimes 6}$	$F_{D_6^{(3)}}(\rho), \langle \hat{c}_{xz}(3\pi/4)^{\otimes 6} \rangle$
5	$((Y + Z)/\sqrt{2})^{\otimes 6}$	$F_{D_6^{(3)}}(\rho), \langle \hat{c}_{yz}(\pi/4)^{\otimes 6} \rangle$
6	$((Y - Z)/\sqrt{2})^{\otimes 6}$	$F_{D_6^{(3)}}(\rho), \langle \hat{c}_{yz}(3\pi/4)^{\otimes 6} \rangle$
7	$((X + Y + Z)/\sqrt{3})^{\otimes 6}$	$F_{D_6^{(3)}}(\rho)$
8	$((X + Y - Z)/\sqrt{3})^{\otimes 6}$	$F_{D_6^{(3)}}(\rho)$
9	$((X - Y + Z)/\sqrt{3})^{\otimes 6}$	$F_{D_6^{(3)}}(\rho)$
10	$((X - Y - Z)/\sqrt{3})^{\otimes 6}$	$F_{D_6^{(3)}}(\rho)$
11	$((\sqrt{3}Z + X)/2)^{\otimes 6}$	$F_{D_6^{(3)}}(\rho), \langle \hat{c}_{xz}(\pi/3)^{\otimes 6} \rangle$
12	$((\sqrt{3}Z - X)/2)^{\otimes 6}$	$F_{D_6^{(3)}}(\rho), \langle \hat{c}_{xz}(2\pi/3)^{\otimes 6} \rangle$
13	$((Z + \sqrt{3}X)/2)^{\otimes 6}$	$F_{D_6^{(3)}}(\rho), \langle \hat{c}_{xz}(\pi/6)^{\otimes 6} \rangle$
14	$((Z - \sqrt{3}X)/2)^{\otimes 6}$	$F_{D_6^{(3)}}(\rho), \langle \hat{c}_{xz}(5\pi/6)^{\otimes 6} \rangle$
15	$((\sqrt{3}Z + Y)/2)^{\otimes 6}$	$F_{D_6^{(3)}}(\rho), \langle \hat{c}_{yz}(\pi/3)^{\otimes 6} \rangle$
16	$((\sqrt{3}Z - Y)/2)^{\otimes 6}$	$F_{D_6^{(3)}}(\rho), \langle \hat{c}_{yz}(2\pi/3)^{\otimes 6} \rangle$
17	$((Z + \sqrt{3}Y)/2)^{\otimes 6}$	$F_{D_6^{(3)}}(\rho), \langle \hat{c}_{yz}(\pi/6)^{\otimes 6} \rangle$
18	$((Z - \sqrt{3}Y)/2)^{\otimes 6}$	$F_{D_6^{(3)}}(\rho), \langle \hat{c}_{yz}(5\pi/6)^{\otimes 6} \rangle$
19	$((1 + \sqrt{3})X + (-1 + \sqrt{3})Z)/(2\sqrt{2})$	$\langle \hat{c}_{xz}(\pi/12)^{\otimes 6} \rangle$
20	$((-1 + \sqrt{3})X + (1 + \sqrt{3})Z)/(2\sqrt{2})$	$\langle \hat{c}_{xz}(5\pi/12)^{\otimes 6} \rangle$
21	$((1 - \sqrt{3})X + (1 + \sqrt{3})Z)/(2\sqrt{2})$	$\langle \hat{c}_{xz}(7\pi/12)^{\otimes 6} \rangle$
22	$-((1 + \sqrt{3})X + (1 - \sqrt{3})Z)/(2\sqrt{2})$	$\langle \hat{c}_{xz}(11\pi/12)^{\otimes 6} \rangle$
23	$((1 + \sqrt{3})Y + (-1 + \sqrt{3})Z)/(2\sqrt{2})$	$\langle \hat{c}_{yz}(\pi/12)^{\otimes 6} \rangle$
24	$((-1 + \sqrt{3})Y + (1 + \sqrt{3})Z)/(2\sqrt{2})$	$\langle \hat{c}_{yz}(5\pi/12)^{\otimes 6} \rangle$
25	$((1 - \sqrt{3})Y + (1 + \sqrt{3})Z)/(2\sqrt{2})$	$\langle \hat{c}_{yz}(7\pi/12)^{\otimes 6} \rangle$
26	$-((1 + \sqrt{3})Y + (1 - \sqrt{3})Z)/(2\sqrt{2})$	$\langle \hat{c}_{yz}(11\pi/12)^{\otimes 6} \rangle$

Table B.5: Measurement settings for the six-photon Dicke experiment. The measured observables for the state $|D_6^{(3)}\rangle$ have been (continued from tab. B.4): the fidelity $F_{D_6^{(3)}}(\rho)$ and the correlation functions $\langle \hat{c}_{xz}(\gamma)^{\otimes 6} \rangle$ and $\langle \hat{c}_{yz}(\gamma)^{\otimes 6} \rangle$.

B.2 Counting statistics

The counting statistics of the experiments are summarized in tab. B.6 and tab. B.7. These consist of the achieved N -photon count rate, which is the sum of the rates obtained from all possible N -photon detections in different spatial modes (2^N possibilities). Further, the coincidence rate in the H/V -, \pm - and L/R -bases as well as the observed visibilities are given. The coincidence rate is calculated from all possible coincident detection events in different spatial modes, for example for four spatial modes and the coincidence $H : V$ 12 different possibilities contribute to the coincidence rate $c_{H:V}$ (the sign “:” means that it is summed over HV and VH coincidences). The visibility $\mathcal{V}_{H/V}$ is defined as

$$\mathcal{V}_{H/V} = \frac{c_{H:V} - (c_{HH} + c_{VV})}{c_{H:V} + (c_{HH} + c_{VV})} \quad (\text{B.3})$$

and accordingly for the bases \pm and L/R . Note, for the determination of the visibility the raw data is directly used without any background subtraction. The tab. B.6 summarizes the results obtained for the four-photon family $|\Psi_4(\alpha)\rangle$ experiment and tab. B.7 for the $|D_6^{(3)}\rangle$ experiment.

α	p_4	$c_4[\text{min}^{-1}]$	$c_{H:V} [\text{s}^{-1}]$	$\mathcal{V}_{H/V}$
$-\sqrt{\frac{1}{3}}$	$\frac{1}{4} = 0.25$	23.22	13500	0.982
$-\sqrt{\frac{1}{6}(3 - \sqrt{3})}$	0.131	14.63	12900	0.981
0	$\frac{1}{24} \approx 0.042$	4.91	10200	0.98
$\sqrt{\frac{1}{6}(3 - \sqrt{3})}$	0.028	3.61	9700	0.974
$\sqrt{\frac{1}{3}}$	$\frac{1}{36} \approx 0.028$	1.57	6300	0.976
$\sqrt{\frac{1}{2}}$	0.0286	3.45	8900	0.974
$\sqrt{\frac{2}{3}}$	$\frac{1}{32} \approx 0.031$	2.79	7500	0.974
$\sqrt{\frac{1}{6}(3 + \sqrt{3})}$	0.035	4.08	8600	0.972
1	$\frac{1}{12} \approx 0.083$	8.69	6900	0.969

Table B.6: Counting statistics for the four-photon family of states $|\Psi_4(\alpha)\rangle$. Thereby, p_4 denotes the theoretical probability to observe the state in the linear optical setup (eq. 3.5), c_4 is the averaged four-photon count rate, $c_{H:V}$ the coincidence rate for HV detections (rounded to full 100 counts) and $\mathcal{V}_{H/V}$ the observed visibility. Note, the \pm - and L/R -bases are not considered here as the two-photon states obtained for different α are different.

#	$c_6[\text{min}^{-1}]$	$c_{H:V} [\text{s}^{-1}]$	$\mathcal{V}_{H/V}$	$c_{+:+} + c_{-:-} [\text{s}^{-1}]$	\mathcal{V}_{\pm}	$c_{L:L} + c_{R:R} [\text{s}^{-1}]$	$\mathcal{V}_{L/R}$
1	3.63	210000	0.835	217000	-0.891	212000	-0.884
2	0.52	128000	0.932	130000	-0.948	130000	-0.946

Table B.7: Counting statistics for the state $|D_6^{(3)}\rangle$ (settings $X^{\otimes 6}$, $Y^{\otimes 6}$ and $Z^{\otimes 6}$ with #1: 5.3 W UV pump power and #2: 2.3 W UV pump power). Thereby, c_6 is the averaged six-photon count rate, $c_{H:V}$ the coincidence rate for HV detections (rounded to full 1000 counts), $\mathcal{V}_{H/V}$ the observed visibility and accordingly for the bases \pm and L/R . The probability to observe the state $|D_6^{(3)}\rangle$ in the linear optical setup was 0.0126.

Appendix C

SPDC higher order noise

In this appendix the higher order noise contribution that is observed on top of the desired states is calculated. This contribution is shown to reduce the fidelity of the expected state. Other known issues reducing the quality of photonic states are spatial, spectral and temporal mode mismatch. These are neglected here and the interested reader is referred to, for example, ref. [337].

The general scheme to observe multi-photon entangled states relies on conditional detection: $2N$ photon clicks have to be detected in $2N$ spatial modes. Ideally, the clicks originate only from the desired emission order of a SPDC process, i.e. the N th order emission yielding $2N$ photons. However, higher order emissions, though they occur with a lower generation rate, can also lead to detection patterns in $2N$ spatial modes when photons are lost or multiple photons are detected in the same detector. In particular, the highest contribution of undesired clicks originates from the $(N + 1)$ th order SPDC emission, creating $2N + 2$ photons. Upon loss of two photons, the remaining $2N$ photons can also be detected in $2N$ different spatial modes. Alternatively, multiple photons can be detected in the same detector leading also to a $2N$ photon detection. Combinations of loss and multiple detection events are also possible.

Generally, to reduce the influence of higher order noise the following technical issues have to be addressed. Loss can be minimized by using high efficient photon detectors, by optimizing the coupling efficiency of the SPDC photons into single mode fibers and by minimizing loss at all utilized optical components. To date the most efficient single photon detectors are silicon APDs, which have a quantum efficiency of up to 65%. Future developments will strongly improve the quality of the observed photonic states. Multiple detection events could be excluded by using photon number resolving detectors [343] in the future. Coupling could be circumvented at all by realising the full experimental setup consisting of the photon source, gates and the detection system in, for example, waveguide structures and/or photonic chips. So far, this has only been demonstrated separately for the SPDC photon source [344–346] and gates [347]. Such complete waveguide/photonic chip setups for multi-photon entanglement studies are foreseeable in the near future. Finally, for the experiments described in this work all optical components have been anti-reflection coated for the SPDC photon wavelength of 780 nm, which yields minimal losses.

C.1 Model

In this work, four- or six-photon entangled states have been observed in four or six spatial modes, respectively. The most relevant noise comes from the next higher order emission, i.e. the third or fourth order SPDC emission, respectively. To accurately calculate this higher order contribution on top of the expected counts one has to consider photon loss and multiple detection events. To take these into account, the experimental setup is divided into different building blocks, which together yield a model of the experimental setup. In each building block the photonic states are transformed by using optical elements. This can be calculated by transforming the photonic creation and annihilation operators appropriately. The required transformations of BSs, PBSs and wave plates have been given in section 2.3.

In the model, photon loss is simulated by additional BSs. The transmitted mode t of the BS gives useful photons and the reflected mode l contains lost photons [206] (see eq. 2.62):

$$\hat{a} \rightarrow \sqrt{\eta}\hat{t} + i\sqrt{1-\eta}\hat{l}, \quad (\text{C.1})$$

where η is the transmission probability modeling the non-unit efficiency and a is the input mode. The other input mode of the model BS is empty. In the experiment simple click detectors are used, i.e. non-photon number resolving detectors. For this type of detector the probability p to register a click if n photons are incident is given as [348]

$$p = \sum_{m=1}^n \binom{n}{m} \eta_d^m (1-\eta_d)^{n-m}, \quad (\text{C.2})$$

whereby η_d is the efficiency of the detector. To obtain this probability in the operator formalism, the amplitude for the operator \hat{t} in the final mode t is transformed according to the usual bosonic relation

$$\hat{t}^n |n\rangle \rightarrow \sqrt{n!} |\text{vac}\rangle. \quad (\text{C.3})$$

This applies to all modes, i.e., the final detection modes at the output of the PBSs of the polarization analysis and also to all loss modes.

The model of the experimental setup is divided into six building blocks (see fig. C.1):

- (1) The calculation starts with the normalized SPDC photon states given in eq. 2.56 and eq. 2.57, as derived in appendix A.
- (2) To incorporate the non-unit coupling efficiency η_c a single BS is placed into each emission mode of the SPDC process to model coupling loss into the loss mode l_c (for type II collinear SPDC: modes a_H and a_V , for type II non-collinear SPDC: modes a_H , a_V , b_H , b_V).
- (3) The linear optical network consisting of BSs, PBSs and phase shifters is implemented. It is assumed that the optical elements do not introduce loss. Naturally, this does not exactly correspond to the experimental situation. But this loss can be simply shifted to the efficiency of the detectors.

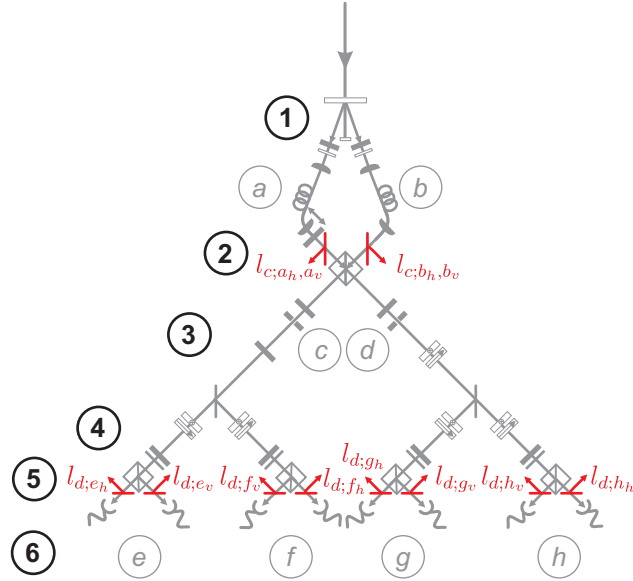


Figure C.1: Model of the setup for the family $|\Psi_4(\alpha(\gamma))\rangle$ experiment to calculate higher order contributions. The different building blocks are labeled with 1 to 6.

- (4) The polarization analysis consisting of a HWP(θ_1), a QWP(θ_2) and a PBS is implemented (see fig. 2.6). For each different analysis setting θ_1 and θ_2 (i.e. measurement setting) the noise calculation is rerun.
- (5) In each output of the PBS a BS is introduced accounting for the non-unit efficiency η_d of the detector. The transmitted mode is assumed to be detected with unit detection efficiency, whereas the reflected mode is the detector loss mode l_d . The transformation of eq. C.3 is applied.
- (6) Finally, loss modes are traced out. This means if multiple possibilities exist leading to the same detection event and if these possibilities can be distinguished by different loss modes $l_{d;i}$, their probabilities add incoherently. This accounts for the in principle distinguishability of the photon loss modes. However, if multiple possibilities exist leading to the same detection event and if these possibilities cannot be distinguished by different loss modes, then their amplitudes add coherently.

C.2 Higher order noise in the four-photon family experiment

The aforementioned model is now applied to the experiment described in chapter 3. The experimental parameters given in tab. C.1 have been determined¹. These values have been calculated from the observed count rates of coincidence $c_{i,j} = \eta_i \eta_j \tau' f_{\text{rep}}$ and single detection events $s_i = \eta_i (1 - \eta_j) \tau' f_{\text{rep}}$ of detectors i and j ($i, j \in \{a, b, c, d, \dots\}$) [349], whereby η_i denotes the total efficiency of detecting a photon², τ' the generation probability of a photon pair and f_{rep} the laser repetition rate. The parameters τ' and η_i can be calculated from

$$\tau' = \frac{1}{f_{\text{rep}}} \frac{(s_i + c_{i,j})(s_j + c_{i,j})}{c_{i,j}}, \quad (\text{C.4})$$

$$\eta_i = \frac{c_{i,j}}{s_j + c_{i,j}}. \quad (\text{C.5})$$

The probability to generate a photon pair τ' is obtained from the probability of the term with $n = 1$ of eq. 2.57, which allows to determine τ by solving

$$\tau' = \left(\frac{\tanh \tau}{\cosh^2 \tau} \right)^2. \quad (\text{C.6})$$

The rates s_i and $c_{i,j}$ are corrected by the independently measured detector dark counts. Note, this procedure for determining τ and η is only valid for small pump powers, where higher order events on top of the observed two- and single photon rates are negligible.

Now, the influence of higher order events on the desired four-photon states can be calculated. Here, only noise coming from the third order SPDC emission is considered, which yields the strongest influence. Further, it is assumed that³ $\eta_c = 1/3$ and η_d is calculated from the measured value of η . The result of the calculation⁴ is shown in fig. C.2(a) that depicts the fidelity as a function of the angle γ , which determines the state in the family $|\Psi_4(\alpha(\gamma))\rangle$ (see eq. 3.3 and eq. 3.4). Additionally, the experimentally observed fidelities are shown (see fig. 3.4). Further, fig. C.2(b) shows the calculated and the measured four-photon count rate.

¹These values have been determined after completion of the measurement for the state observed for $\alpha = \sqrt{(3 - \sqrt{3})}/6$.

²This includes the coupling efficiency η_c , the efficiency η_d of the detector and the probabilistic photon distribution using BSs p_{BS} . The latter can also be determined in an independent measurement. Each BS had a splitting ratio of 0.6:0.4, optimal would have been 0.5:0.5. Hence, the total efficiency is given as $\eta = \eta_c \eta_d p_{\text{BS}} = \eta_{\text{det}} p_{\text{BS}}$.

³This assumption is necessary as only two equations are used to yield η and τ' . One more equation is required to determine η_c and η_d separately. This is done in section C.3. The value of $\eta_c = 1/3$ is an estimate such that with the measured mean efficiency $\bar{\eta} = 0.084$ the efficiency of the detector of $\bar{\eta}_d = 0.5$ is obtained and, thus, $\bar{\eta}_{\text{det}} = \eta_c \bar{\eta}_d = 0.167$.

⁴The $2^4 = 16$ possible outcomes in each of the $3^4 = 81$ possible measurement bases dependent on τ and γ for fixed efficiencies are calculated with a Mathematica[®] 5.1 program. On a Intel[®]Core[™] 2 Duo CPU with 3 GHz and 8 GByte Ram this takes about 12 hours.

mode	e_V	e_H	f_V	f_H	g_V	g_H	h_V	h_H
η	0.139	0.105	0.091	0.075	0.057	0.057	0.071	0.079
$\bar{\eta}$					0.084			
$\bar{\eta}_{\text{det}}$					0.167			
τ					0.056			

Table C.1: Model parameters for the four-photon family experiment. The total efficiency η is given for each mode, $\bar{\eta}$ denotes the averaged total efficiency over all modes, $\bar{\eta}_{\text{det}}$ denotes the averaged total detection efficiency over all modes and τ is the pair creation amplitude.

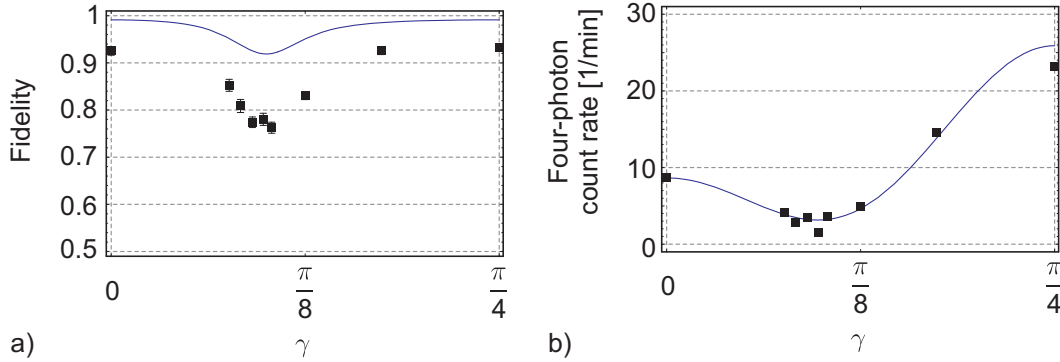


Figure C.2: The four-photon and six-photon higher order contribution influencing (a) the fidelity and (b) count rate are calculated and shown in comparison to the measured values for the family $|\Psi_4(\alpha(\gamma))\rangle$ experiment. The theoretical curves reflect the trend of the data points. The discrepancy for the fidelity curve is explained in the text.

Generally, the trend of the theoretical curves reflect the one of the experimental data points and very good agreement is found for the count rate. However, a higher fidelity value would be expected from the calculation. The gap can be attributed to four major effects:

- A non-perfect spatial and spectral overlap of SPDC photons at the central PBS (see fig. 3.2 and fig. 3.3) decreases the fidelity. The spectral mismatch is due to the difference in spectral bandwidth of signal and idler photons in pulsed pump SPDC [209–211], which is reduced by using narrow-band interference filters. Spatial distinguishability comes from non-perfect alignment. For the measured states a mean two-photon interference visibility of 0.97 ± 0.01 has been achieved.
- Pair distinguishability [212, 213], also reduced by using narrow-band interference filters, further decreases the fidelity.
- Higher order SPDC emissions in addition to the third one would yield a further reduction in fidelity.
- The determined parameters η and τ do not entirely reflect the real ones. This is due

to the assumption that higher order contributions to two- and single photon count rates have been neglected.

A more elaborate analysis could include these effects.

C.3 Higher order noise in the six-photon Dicke experiment

The calculation of the higher order contribution to the six-photon state $|D_6^{(3)}\rangle$ proceeds according to the steps given in section C.1. Here, focus is put on the next higher order emission consisting of eight photons (see eq. 2.56). The parameters η_c , η_d and τ have been determined by fitting the experimentally measured count rates to the theoretically calculated ones⁵. The simple model of determining η and τ as described in section C.2 is not applied. In contrast, three equations⁶ are used to determine η_c , η_d and τ : the two-photon count rate⁷ $c_{H:V}$ of modes a and b (summed over all possible events in different spatial modes), the four-photon count rate⁸ $c_{H:H:V:V}$ of modes a , b , c , and d (summed over all possible events in different spatial modes) and the four-photon count rates⁹ $c_{H:V:V:V}$ and $c_{V:H:H:H}$ of modes a , b , c , and d (summed over all possible events in different spatial modes). For each coincidence count rate the contribution of the desired order and of the next higher order emission has been calculated and fitted to the experimentally measured count rates. Beam splitting ratios for BS₁-BS₄ of 0.58:042 and for BS₅ of 0.52:048 have been experimentally measured and used for the calculation. Using this procedure the parameters given in tab. C.2 have been determined.

Using the determined parameters the expectation values given in tab. C.3 and the counts in fig. C.3 have been calculated¹⁰. In general, the agreement of the simulated with the measured data is quite well (by 10 – 20% difference, the six-photon count rate is underestimated). The simulation model gives for all operators slightly better results. This can be traced back to the following reasons:

- The main reason is the simplification to consider only the next higher order emission. Additional consideration of ten-photon production would decrease the values further and match the experimental data even better.

⁵Two simplifications are made: it is assumed that η_d is the same for all detectors and η_c is the same for both polarization modes.

⁶In principle, another choice of coincidence events could be considered as well. However, this set turned out to yield results resembling the experimental findings.

⁷ $c_{H:V} = c_{HV} + c_{VH}$

⁸ $c_{H:H:V:V} = c_{HHVV} + c_{HVHV} + c_{VHHV} + c_{VHVH} + c_{VVHH} + c_{HVVV}$

⁹ $c_{H:V:V:V} + c_{V:H:H:H} = c_{HVVV} + c_{VHVV} + c_{VHVH} + c_{VHVH} + c_{VHHH} + c_{HVVH} + c_{HHVH} + c_{HHHV}$

¹⁰The $2^6 = 64$ possible outcomes in each of the $3^6 = 729$ possible measurement bases dependent on τ , η_c and η_d are calculated with a Mathematica[®] 5.1 program. On a Intel[®]Core[™] 2 Duo CPU with 3 GHz and 8 GByte Ram this takes about 4 weeks!

- Pair distinguishability [212, 213] also influences the values and is not considered in the model.
- The efficiency η_d is different for each detector. Also, the coupling efficiency η_c could be different for each polarization mode. Both has been neglected for simplicity.

Compared to the noise calculation of the four-photon family experiment in section C.2, here the main noise component is definitely higher order SPDC noise as no interference between photons is present. Thus, spatial mismatch of photons is absent due to coupling into the same single mode fiber.

$c_6[\text{min}^{-1}]$	τ	η_c	η_d	$\eta_{\text{det}} = \eta_c \eta_d$	$c_{6,\text{model}} [\text{min}^{-1}]$
3.6	0.34	0.41	0.37	0.15	3.0

Table C.2: Model parameters for the $|D_6^{(3)}\rangle$ experiment. The count rates are only given for the $Z^{\otimes 6}$ basis.

operator	experimental value	simulation model value	noise model value
fidelity $F_{D_6^{(3)}}(\rho)$	0.654 ± 0.024	0.71	0.71
two-setting witness (eq. 5.7)	-0.422 ± 0.148	-0.75	-0.69
Bell inequality $\langle \hat{\mathcal{B}}_{D_6^{(3)}} \rangle$ (eq. 5.8)	0.43 ± 0.02	0.51	0.51

Table C.3: Modeled expectation values for the $|D_6^{(3)}\rangle$ experiment. The simulation model is the one described in section C.1, the noise model is the assumption of the state $\rho(p_{D_6^{(3)}})$ given in eq. C.9.

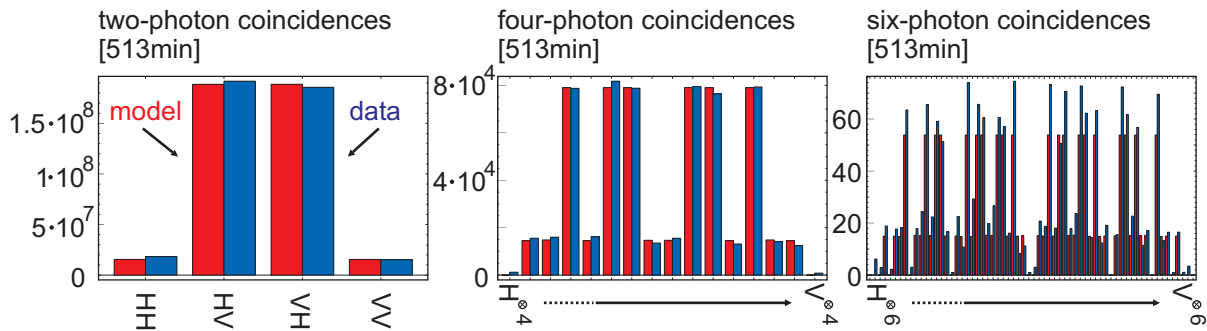


Figure C.3: Modeled and measured two-, four- and six-photon counts for the state $|D_6^{(3)}\rangle$ in the Z -basis. To calculate the parameters η_c , η_d and τ a fit of the model count rates has been made to the measured rates of all possible HV , $HHVV$ and $HVVV/VHHH$ coincidences.

Simple theoretical noise model

The main noise contribution to the desired state $|D_6^{(3)}\rangle$ comes from eight photons of the third order SPDC emission and subsequent loss of two photons, which yields detectable six-photon events. This situation is similar to loss of two photons of the state $|D_8^{(4)}\rangle$, which would be observed in a setup that splits the photons onto eight spatial modes. Hence, a simple theoretical noise model has already been indirectly given with eq. 5.12 and $m = N/2$ and $k = 2$:

$$\rho_{N-2} = (C_N^{N/2})^{-1} \sum_{j=0}^2 C_2^j C_{N-2}^{N/2-j} \rho_{D_{N-2}^{(N/2-j)}}, \quad (\text{C.7})$$

with $\rho_{D_{N-2}^{(N/2-j)}} = |D_{N-2}^{(N/2-j)}\rangle \langle D_{N-2}^{(N/2-j)}|$. For the state $|D_6^{(3)}\rangle$ one sets $N = 8$ in the above equation and obtains

$$\rho_6 = \frac{4}{7} \rho_{D_6^{(3)}} + \frac{3}{14} (\rho_{D_6^{(2)}} + \rho_{D_6^{(4)}}). \quad (\text{C.8})$$

This result can also be calculated by counting the possible ways how two photons can be lost from four horizontally and four vertically polarized photons. Then, the observed state is a mixture of that state and the desired state $|D_6^{(3)}\rangle$:

$$\rho(p_{D_6^{(3)}}) = p_{D_6^{(3)}} \rho_{D_6^{(3)}} + (1 - p_{D_6^{(3)}}) \rho_6. \quad (\text{C.9})$$

Using the parameters given in tab. C.2 a value of $p_{D_6^{(3)}} = 0.32$ has been determined. The model of eq. C.9 can also be used to calculate various expectation values, which are additionally stated in tab. C.3.

In section 5.3 this noise model has been applied to the correlation functions $\langle \hat{c}_{xz}(\gamma) \rangle$ and $\langle \hat{c}_{yz}(\gamma) \rangle$ [see fig. 5.6(a) and (b)]. The state of eq. C.9 yields the following correlation function

$$\begin{aligned} \langle \hat{c}_{xz}(\gamma)^{\otimes 6} \rangle &= \frac{1}{224} \left((45 + 39p_{D_6^{(3)}}) \cos 2\gamma \right. \\ &\quad \left. - 6(p_{D_6^{(3)}} - 1)(3 + 5 \cos 4\gamma) + 35(1 + 3p_{D_6^{(3)}}) \cos 6\gamma \right), \quad (\text{C.10}) \end{aligned}$$

and similarly for $\langle \hat{c}_{yz}(\gamma) \rangle$. The measured data points have been fitted with this function. The following values for $p_{D_6^{(3)}}$ have been determined [compare fig. 5.6(a) and (b)]: high pump power: (i) 0.274, (ii) 0.226; low pump power: (iii) 0.588 and (iv) 0.596. This reflects nicely that with lower pump power [cases (iii) and (iv)] the fraction of the desired state $|D_6^{(3)}\rangle$ increases. The difference between the values obtained for the cases (i) and (ii) might be assigned to the less accurate measurement of the correlation function $\langle \hat{c}_{yz} \rangle$, which is due to the usage of QWPs, which are known to be less accurate than HWPs.

Model applied to various pump power levels

The model described in section C.1 and section C.3 is now applied to a measurement of the count rates for two-, four- and six-photon events as a function of intra-cavity UV pump power, see [56] (publ. P5.4). The procedure is the same as outlined in section C.3 to yield τ , η_c and η_d (fitted are two- and four-photon rates). The results are displayed in fig. C.4(a), (b) and (c). Theoretically, with increasing UV pump power P_{UV} the parameter τ increases proportional to $\sqrt{P_{UV}}$, which is resembled by the data points¹¹. The efficiency $\eta_{det} = \eta_c \eta_d$ slightly decreases with increasing pump power. Its mean value is $\overline{\eta_{det}} = 0.14$.

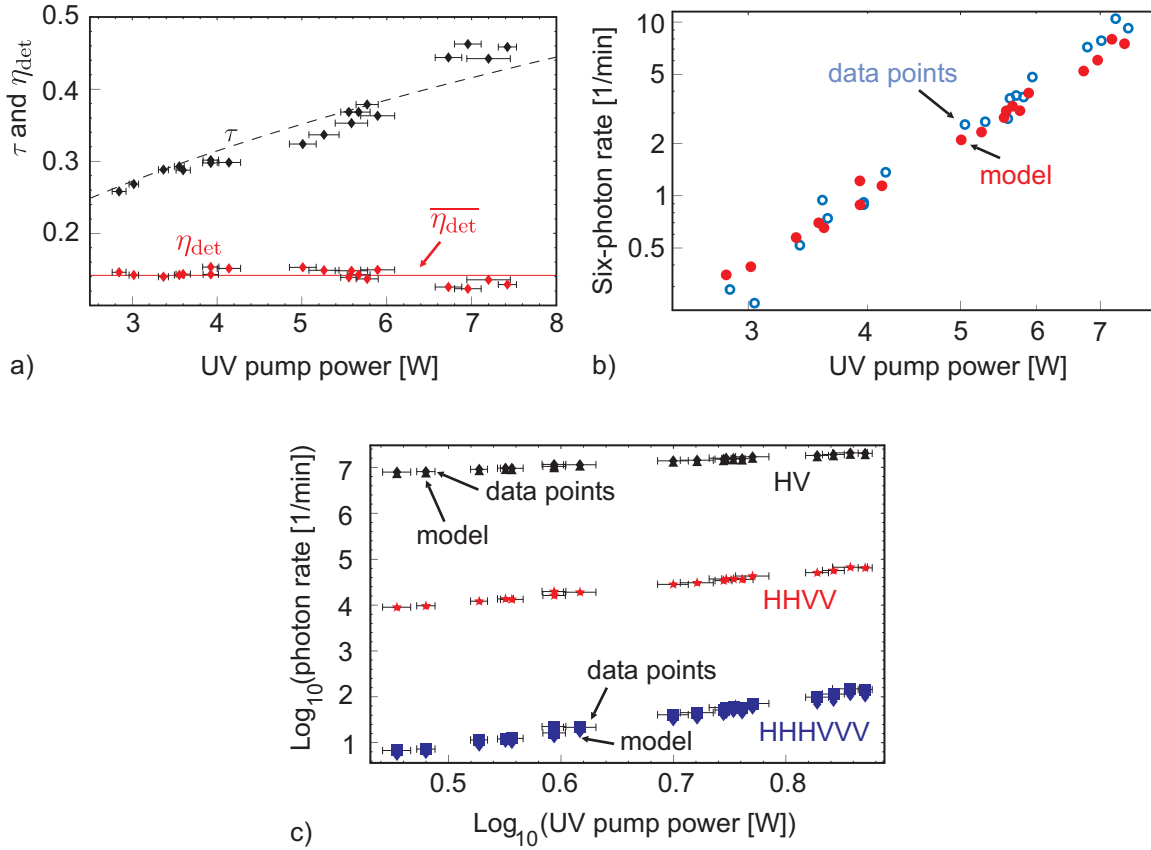


Figure C.4: (a) Fitted τ and η_{det} for different UV pump powers. The dashed line is a fit to τ with $\tau \propto \sqrt{P_{UV}}$. The mean value of the efficiency is $\overline{\eta_{det}} = 0.14$. (b) Measured and calculated six-photon rates between modes a, b, c, d, e and f . (c) Measured and calculated HV -, $HHVV$ - and $HHHVVV$ -count rates (all possibilities) as a function of UV pump power.

¹¹The count rate of a possible 8-photon experiment is estimated by $c_\psi \sim (\eta_{det} \tanh \tau)^8 f_r p_\psi \approx 2.6 p_\psi / \text{min}$ for $\tau \approx 0.5$, $\eta \approx 0.15$ and $f_r = 81$ MHz. For a generic linear optical setup for the states $|D_N^{(N/2)}\rangle$ one obtains $p_{D_N^{(N/2)}} = N! / N^N$ ($p_{D_8^{(4)}} = 0.0024$), for the states $|\text{GHZ}_N\rangle$ one has $p_{\text{GHZ}_N} = 2^{-(N/2-1)}$ for N even ($p_{\text{GHZ}_8} = 0.125$) and for the rotationally symmetric states $|\Psi_N^-\rangle$ $p_{\Psi_N^-} = [(N/2)! / (N/2)^{(N/2)}]^2$ for N even ($p_{\Psi_8^-} = 0.0088$). The corresponding linear optical setups are described in section 3.1.

Appendix D

FPGA controlled coincidence logic

In this appendix the implementation of the FPGA controlled coincidence logic is shortly described. It is divided into three parts:

- Preparation of input signals for the FPGA: transforming detector signals and the master clock derived from the laser repetition frequency of 81 MHz,
- Processing of detector clicks by the FPGA: sampling of detector signals with laser repetition frequency, creating a histogram of detector click patterns and signal preparation for universal serial bus (USB) transfer,
- Transfer of histogram: USB data transfer to a computer.

The FPGA is a Xilinx[®]Virtex[™]-4 XC4VLX25-FF668-10 mounted on a ML401 evaluation platform provided by Xilinx[®]. For the present implementation an input bus width of 12 detector signals (denoted as [11:0]) is used. This is sufficient for measuring the photonic state of six qubits with 12 detectors. The names of the **signals** used in the following description correspond to the names in the VHDL files of the actual implementation (date: 27.10.2008, main files are the project file `main.prj`, the main VHDL file `main.vhd` and the constraints file `main.ucf`). The files were compiled using Xilinx[®]ISE:10.1.03 (WebPACK).

Input signals

Detector signals: The detector signals are NIM standard, which are first converted to differential ECL. With the MC100EPT25 chip they are further transformed to LVTTTL, which is required by the FPGA.

Laser repetition frequency: The Tsunami[®] laser provides a PD monitor signal (peak-to-peak (0 ± 0.36) V), which is the laser repetition frequency of about 81 MHz monitored by a photo diode. This signal is transformed to a differential signal (peak-to-peak (1.17 ± 0.95) V) required by the ML401 evaluation platform (`SMA_DIFF_CLK_IN_P`). It yields the master clock (`clk1x_inta`) of the FPGA with 81 MHz.

Processing by FPGA and transfer via USB

The processing of the input signals by the FPGA in order to transfer a histogram of the detector click patterns via USB to a computer is done in the following steps (see also fig. D.1):

Signal input: The detector signals `GPIO_HDR2_DATA_in[11:0]` are sampled on the rising edge of `clk1x_inta` yielding `data_to_fifo[11:0]`. Additionally, the logical OR of all `data_to_fifo[11:0]` is computed to obtain a signal that announces the arrival of newly sampled data. [file: `iunit.vhd`]

Signal buffer: The sampled detector signals `data_to_fifo[11:0]` are sent with `clk1x_inta` and upon new arrival of data (given by the logical OR of `data_to_fifo[11:0]`) into a stage of two FIFO's (asynchronous FWFT, synchronous STD), which are implemented directly in the FPGA chip (bug fixed FIFO16: Virtex-4 4k deep \times 4 wide BlockRAM (a)synchronous FIFO, used as 1k \times 18, i.e. 1024 signal patterns can be stored with an address width of 18 bits, address width of 12 bits is used). [file: `fifobuffer.vhd`]

Signal histogram: The signals buffered in the FIFO stage are sent to a memory upon rising edge with twice `clk1x_inta`, i.e. 162 MHz (`clk2x_inta`). Thereby, the signal pattern [11:0] yields the address of the memory (`address_memory[11:0]`), whose stored value is incremented by 1. This implements a histogram of the detector click patterns. More specifically, the memory is realized outside the FPGA with a 9 Mbit pipelined SRAM (CY7C1354B) organized as 256k \times 36 ($2^{18} = 256k$ different addresses can store each a number of 2^{36} bit length. In the present implementation only $2^{12} = 4096$ addresses with 2^{32} bit length are used.) with a maximal frequency of 166 MHz. Control signals coordinate the communication between the FIFO stage and the memory. [files: `historam.vhd`, `appnote_zbtp.vhd`]

Signal transfer: After a certain integration time (set externally by `GPIO_SW1[3:0]` and derived from `clk2x_inta`) the data of the memory is put into a stage of 24 FIFO's (23 synchronous FWFT, 1 asynchronous STD, used as 512 \times 36, i.e. 512 signal patterns can be stored with an address width of 36 bits, an address width of 32 bit is used in the present implementation) and upon completion transferred to the USB chip with a clock rate (`GPIO_HDR1_USB_SLWR`) of $81/16/4 = 1.265625$ MHz. For the utilized USB chip (CY7C67300, external of the FPGA, transfers 16 bit in parallel) the signals are divided into $2^{12} = 4096$ addresses times twice 16 bit (`GPIO_HDR1_USB_Data[15:0]`) yielding $4096 \cdot 2 = 8kbit$ data, which is transferred to the USB chip. With a frequency of 1.265625 MHz this takes 6.473 ms. [files: `usb_signal.vhd`, `fifobuffer_usb.vhd`]

Additional utilized primitives are digital clock managers provided by the FPGA (`DCM_ADV`) to stabilize `clk1x_inta` and to generate `clk2x_inta` and `clkdv16x_inta`.

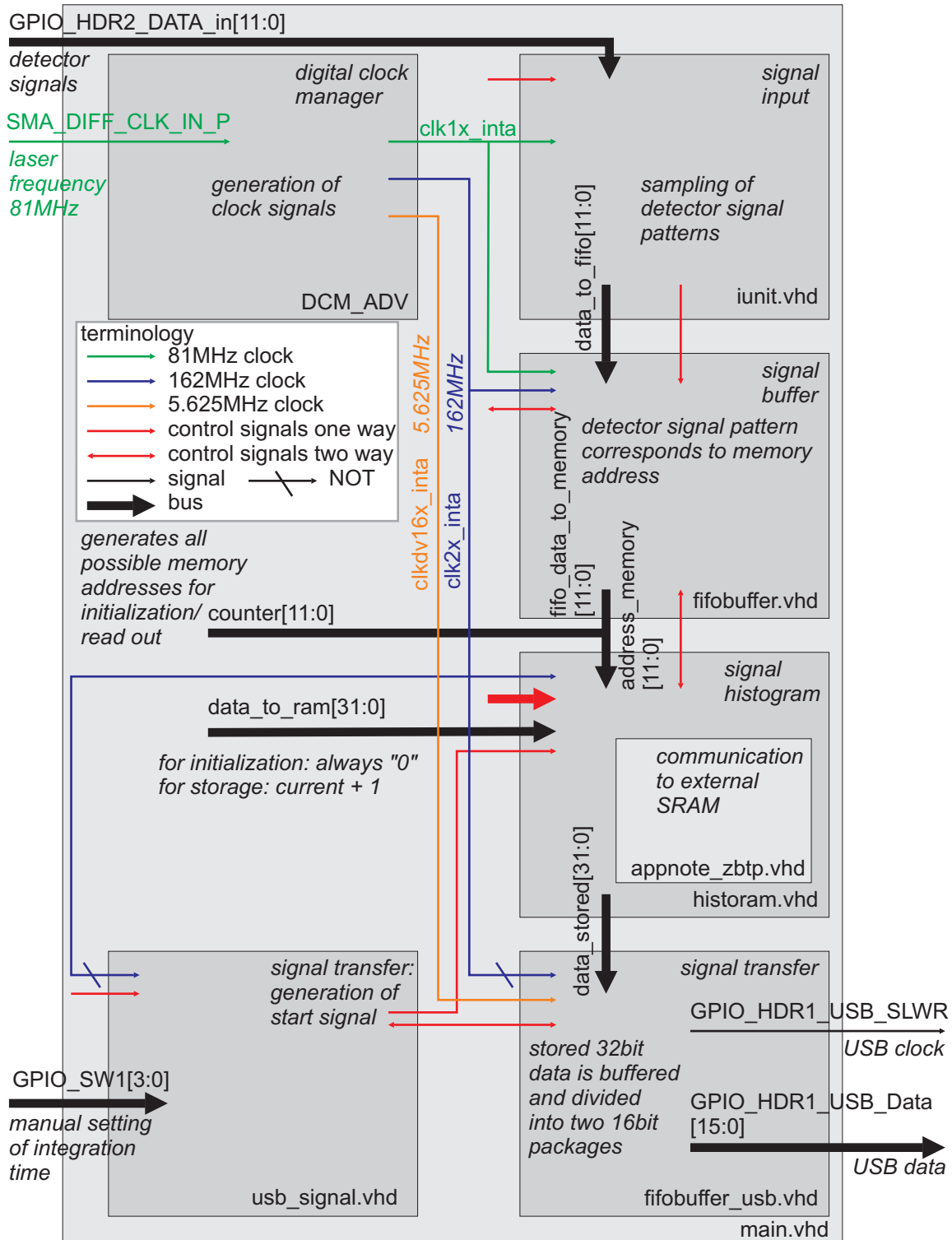


Figure D.1: Schematic diagram for the programmed FPGA realizing a coincidence unit. The **signal** names correspond to the ones in the VHDL files.

Publication list

Publications related to this work (ordered by Chapter)

Witlef Wieczorek, Christian Schmid, Nikolai Kiesel, Reinhold Pohlner, Otfried Gühne, and Harald Weinfurter,
Experimental Observation of an Entire Family of Four-Photon Entangled States,
Phys. Rev. Lett. **101**, 010503 (2008) [covered in *Nature News & Views* [\[350\]](#)]

Witlef Wieczorek, Nikolai Kiesel, Christian Schmid, Wiesław Laskowski, Marek Żukowski, and Harald Weinfurter,
Multi-Photon Interference as a Tool to Observe Families of Multi-Photon Entangled States,
IEEE J. Selected Topics in Quantum Electronics, on Quantum Communications and Information Science **15**, 1704 (2009)

Jiannis K. Pachos, **Witlef Wieczorek**, Christian Schmid, Nikolai Kiesel, Reinhold Pohlner, and Harald Weinfurter,
Revealing anyonic features in a toric code quantum simulation,
New J. Phys. **11**, 083010 (2009) [covered in *IoP select August 2009* and *europhysicsnews* [\[351\]](#)]

Witlef Wieczorek, Roland Krischek, Nikolai Kiesel, Patrick Michelberger, Géza Tóth, and Harald Weinfurter,
Experimental Entanglement of a Six-Photon Symmetric Dicke State,
Phys. Rev. Lett. **103**, 020504 (2009)

Witlef Wieczorek, Nikolai Kiesel, Christian Schmid, and Harald Weinfurter,
Multi-qubit entanglement engineering via projective measurements,
Phys. Rev. A **79**, 022311 (2009)

Géza Tóth, **Witlef Wieczorek**, Roland Krischek, Nikolai Kiesel, Patrick Michelberger, and Harald Weinfurter,
Practical methods for witnessing genuine multi-qubit entanglement in the vicinity of symmetric states,
New J. Phys. **11**, 083002 (2009)

Roland Krischek, **Witlef Wieczorek**, Akira Ozawa, Nikolai Kiesel, Patrick Michelberger, Thomas Udem, and Harald Weinfurter,
Ultraviolet enhancement cavity for ultrafast nonlinear optics,
accepted for publication in *Nat. Photon.*, (2009)

Other publications (ordered by time, most recent first)

Christian Schmid, Nikolai Kiesel, **Witlef Wieczorek**, and Harald Weinfurter,
Experimental Direct Observation of Mixed State Entanglement,
Phys. Rev. Lett. **101**, 260505 (2008)

Christian Schmid, Nikolai Kiesel, Wiesław Laskowski, **Witlef Wieczorek**, Marek Żukowski,
and Harald Weinfurter,
Discriminating Multipartite Entangled States,
Phys. Rev. Lett. **100**, 200407 (2008)

Christian Schmid, Nikolai Kiesel, **Witlef Wieczorek**, Reinhold Pohlner, and Harald Weinfurter,
Multiphoton entanglement engineering via projective measurements,
SPIE Proceedings **6780**, 67800E (2007)

Witlef Wieczorek, Nikolai Kiesel, Christian Schmid, and Harald Weinfurter,
Efficient non-tomographic tools for the characterization of multipartite entanglement,
Proceedings of the 8th International Conference on Quantum Communication, Measurement and Computing (Eds. Osamu Hirota, Jeffrey H. Shapiro, Masahide Sasaki), Tsukuba, Japan, 28. Nov.- 03. Dec. 2006, 487-492 (NICT Press, 2007)

Christian Schmid, Nikolai Kiesel, **Witlef Wieczorek**, and Harald Weinfurter,
The entanglement of the four-photon cluster state,
New J. Phys. **9**, 236 (2007)

Bibliography

- [1] M. A. Nielsen and I. L. Chuang, *Quantum Computation and Quantum Information* (Cambridge University Press, 2000).
- [2] E. Schrödinger, Die gegenwärtige Situation in der Quantenmechanik, *Naturwissenschaften* **23**, 807 (1935).
- [3] W. H. Zurek, Decoherence and the Transition from Quantum to Classical, *Physics Today* **44**, 36 (1991).
- [4] A. Einstein, B. Podolsky, and N. Rosen, Can Quantum-Mechanical Description of Physical Reality Be Considered Complete?, *Phys. Rev.* **47**, 777 (1935).
- [5] J. S. Bell, On the Einstein Podolsky Rosen Paradox, *Physics* **1**, 195 (1964).
- [6] A. Aspect, P. Grangier, and G. Roger, Experimental tests of realistic local theories via Bell's theorem, *Phys. Rev. Lett.* **47**, 460 (1981).
- [7] A. Aspect, P. Grangier, and G. Roger, Experimental realization of Einstein-Podolsky-Rosen-Bohm gedankenexperiment: A new violation of Bell's inequalities, *Phys. Rev. Lett.* **49**, 91 (1982).
- [8] G. Weihs, T. Jennewein, C. Simon, H. Weinfurter, and A. Zeilinger, Violation of Bell's Inequality under Strict Einstein Locality Conditions, *Phys. Rev. Lett.* **81**, 5039 (1998).
- [9] M. A. Rowe, D. Kielpinski, V. Meyer, C. A. Sackett, W. M. Itano, C. Monroe, and D. J. Wineland, Experimental violation of a Bell's inequality with efficient detection, *Nature* **409**, 791 (2001).
- [10] N. D. Mermin, Extreme quantum entanglement in a superposition of macroscopically distinct states, *Phys. Rev. Lett.* **65**, 1838 (1990).
- [11] D. Bouwmeester, A. Ekert, and A. Zeilinger (eds.), *The Physics of Quantum Information*, 1st edn. (Springer, 2000).
- [12] C. H. Bennett and D. P. DiVincenzo, Quantum information and computation, *Nature* **404**, 247 (2000).

- [13] R. Feynman, Simulating physics with computers, *Int. J. Theor. Phys.* **21**, 467 (1982).
- [14] A. Steane, Quantum computing, *Rep. Prog. Phys.* **61**, 117 (1998).
- [15] H. J. Briegel, D. E. Browne, W. Dür, R. Raussendorf, and M. Van den Nest, Measurement-based quantum computation, *Nat. Phys.* **5**, 19 (2009).
- [16] N. Gisin, G. G. Ribordy, W. Tittel, and H. Zbinden, Quantum cryptography, *Rev. Mod. Phys.* **74**, 145 (2002).
- [17] V. Scarani, S. Iblisdir, N. Gisin, and A. Acin, Quantum cloning, *Rev. Mod. Phys.* **77**, 1225 (2005).
- [18] N. Gisin and R. Thew, Quantum communication, *Nat. Photon.* **1**, 165 (2007).
- [19] V. Giovannetti, S. Lloyd, and L. Maccone, Quantum-Enhanced Measurements: Beating the Standard Quantum Limit, *Science* **306**, 1330 (2004).
- [20] K. Southwell, Quantum coherence, *Nature* **453**, 1003 (2008).
- [21] I. Osborne and R. Coontz, Quantum Wonderland, *Science* **319**, 1201 (2008).
- [22] J. L. O'Brien, Optical Quantum Computing, *Science* **318**, 1567 (2007).
- [23] J.-W. Pan, Z.-B. Chen, M. Zukowski, H. Weinfurter, and A. Zeilinger, Multi-photon entanglement and interferometry, *arXiv: 0805.2853 [quant-ph]* (2008).
- [24] I. A. Walmsley, Looking to the Future of Quantum Optics, *Science* **319**, 1211 (2008).
- [25] R. Blatt and D. Wineland, Entangled states of trapped atomic ions, *Nature* **453**, 1008 (2008).
- [26] I. Bloch, Quantum coherence and entanglement with ultracold atoms in optical lattices, *Nature* **453**, 1016 (2008).
- [27] H. J. Kimble, The quantum internet, *Nature* **453**, 1023 (2008).
- [28] L. M. K. Vandersypen, M. Steffen, G. Breyta, C. S. Yannoni, M. H. Sherwood, and I. L. Chuang, Experimental realization of Shor's quantum factoring algorithm using nuclear magnetic resonance, *Nature* **414**, 883 (2001).
- [29] C. Negrevergne, T. S. Mahesh, C. A. Ryan, M. Ditty, F. Cyr-Racine, W. Power, N. Boulant, T. Havel, D. G. Cory, and R. Laflamme, Benchmarking Quantum Control Methods on a 12-Qubit System, *Phys. Rev. Lett.* **96**, 170501 (2006).
- [30] R. Hanson, L. P. Kouwenhoven, J. R. Petta, S. Tarucha, and L. M. K. Vandersypen, Spins in few-electron quantum dots, *Rev. Mod. Phys.* **79**, 1217 (2007).

- [31] R. J. Schoelkopf and S. M. Girvin, Wiring up quantum systems, *Nature* **451**, 664 (2008).
- [32] P. Neumann, N. Mizuochi, F. Rempp, P. Hemmer, H. Watanabe, S. Yamasaki, V. Jacques, T. Gaebel, F. Jelezko, and J. Wrachtrup, Multipartite Entanglement Among Single Spins in Diamond, *Science* **320**, 1326 (2008).
- [33] T. Calarco, P. Grangier, A. Wallraff, and P. Zoller, Quantum leaps in small steps, *Nat. Phys.* **4**, 2 (2008).
- [34] J. Majer, J. M. Chow, J. M. Gambetta, J. Koch, B. R. Johnson, J. A. Schreier, L. Frunzio, D. I. Schuster, A. A. Houck, A. Wallraff, A. Blais, M. H. Devoret, S. M. Girvin, and R. J. Schoelkopf, Coupling superconducting qubits via a cavity bus, *Nature* **449**, 443 (2007).
- [35] L. DiCarlo, J. M. Chow, J. M. Gambetta, L. S. Bishop, B. R. Johnson, D. I. Schuster, J. Majer, A. Blais, L. Frunzio, S. M. Girvin, and R. J. Schoelkopf, Demonstration of two-qubit algorithms with a superconducting quantum processor, *Nature* **460**, 240 (2009).
- [36] C.-Y. Lu, X.-Q. Zhou, O. Gühne, W.-B. Gao, J. Zhang, Z.-S. Yuan, A. Goebel, T. Yang, and J.-W. Pan, Experimental entanglement of six photons in graph states, *Nat. Phys.* **3**, 91 (2007).
- [37] C.-Y. Lu, W.-B. Gao, O. Gühne, X.-Q. Zhou, Z.-B. Chen, and J.-W. Pan, Demonstrating Anyonic Fractional Statistics with a Six-Qubit Quantum Simulator, *Phys. Rev. Lett.* **102**, 030502 (2009).
- [38] W. Wieczorek, R. Krischek, N. Kiesel, P. Michelberger, G. Toth, and H. Weinfurter, Experimental Entanglement of a Six-Photon Symmetric Dicke State, *Phys. Rev. Lett.* **103**, 020504 (2009), arXiv: 0903.2213 [quant-ph].
- [39] R. Prevedel, G. Cronenberg, M. S. Tame, M. Paternostro, P. Walther, M. S. Kim, and A. Zeilinger, Experimental Realization of Dicke States of up to Six Qubits for Multi-party Quantum Networking, *Phys. Rev. Lett.* **103**, 020503 (2009), arXiv: 0903.2212 [quant-ph].
- [40] M. Radmark, M. Zukowski, and M. Bourennane, Experimental Test of Fidelity Limits in Six-Photon Interferometry and of Rotational Invariance Properties of the Photonic Six-Qubit Entanglement Singlet State, *Phys. Rev. Lett.* **103**, 150501 (2009).
- [41] H. Häffner, W. Hänsel, C. F. Roos, J. Benhelm, D. Chek-al kar, M. Chwalla, T. Körber, U. D. Rapol, M. Riebe, P. O. Schmidt, C. Becher, O. Gühne, W. Dür, and R. Blatt, Scalable multiparticle entanglement of trapped ions, *Nature* **438**, 643 (2005).

- [42] E. Knill, R. Laflamme, and G. J. Milburn, A scheme for efficient quantum computation with linear optics, *Nature* **409**, 46 (2001).
- [43] G. G. Lapaire, P. Kok, J. P. Dowling, and J. E. Sipe, Conditional linear-optical measurement schemes generate effective photon nonlinearities, *Phys. Rev. A* **68**, 042314 (2003).
- [44] M. A. Nielsen, Optical Quantum Computation Using Cluster States, *Phys. Rev. Lett.* **93**, 040503 (2004).
- [45] R. Raussendorf and H. J. Briegel, A One-Way Quantum Computer, *Phys. Rev. Lett.* **86**, 5188 (2001).
- [46] H. J. Briegel and R. Raussendorf, Persistent Entanglement in Arrays of Interacting Particles, *Phys. Rev. Lett.* **86**, 910 (2001).
- [47] P. Grangier, B. Sanders, and J. Vuckovic, Focus on Single Photons on Demand, *New J. Phys.* **6** (2004).
- [48] M. Oxborrow and A. G. Sinclair, Single-photon sources, *Cont. Phys.* **46**, 173 (2005).
- [49] B. Lounis and M. Orrit, Single-photon sources, *Rep. Prog. Phys.* **68**, 1129 (2005).
- [50] L. Mandel and E. Wolf, *Optical Coherence and Quantum Optics* (Cambridge University Press, 1995).
- [51] P. G. Kwiat, K. Mattle, H. Weinfurter, A. Zeilinger, A. V. Sergienko, and Y. Shih, New high-intensity source of polarization-entangled photon pairs, *Phys. Rev. Lett.* **75**, 4337 (1995).
- [52] H. Weinfurter and M. Żukowski, Four-photon entanglement from down-conversion, *Phys. Rev. A* **64**, 010102(R) (2001).
- [53] W. Wieczorek, C. Schmid, N. Kiesel, R. Pohlner, O. Gühne, and H. Weinfurter, Experimental Observation of an Entire Family of Four-Photon Entangled States, *Phys. Rev. Lett.* **101**, 010503 (2008).
- [54] W. Wieczorek, N. Kiesel, C. Schmid, W. Laskowski, M. Żukowski, and H. Weinfurter, Multi-Photon Interference as a Tool to Observe Families of Multi-Photon Entangled States, *IEEE J. Selected Topics in Quantum Electronics* **15**, 1704 (2009).
- [55] W. Wieczorek, N. Kiesel, C. Schmid, and H. Weinfurter, Multiqubit entanglement engineering via projective measurements, *Phys. Rev. A* **79**, 022311 (2009), arXiv:0901.4091 [quant-ph].
- [56] R. Krischek, W. Wieczorek, A. Ozawa, N. Kiesel, P. Michelberger, T. Udem, and H. Weinfurter, Ultraviolet enhancement cavity for ultrafast nonlinear optics, *accepted for publication in Nat. Photon.* (2009).

- [57] J. K. Pachos, W. Wieczorek, C. Schmid, N. Kiesel, R. Pohlner, and H. Weinfurter, Revealing anyonic features in a toric code quantum simulation, *New J. Phys.* **11**, 083010 (10pp) (2009), arXiv:0710.0895 [quant-ph].
- [58] D. Bouwmeester, J.-W. Pan, M. Daniell, H. Weinfurter, and A. Zeilinger, Observation of Three-Photon Greenberger-Horne-Zeilinger Entanglement, *Phys. Rev. Lett.* **82**, 1345 (1999).
- [59] M. Eibl, S. Gaertner, M. Bourennane, C. Kurtsiefer, M. Żukowski, and H. Weinfurter, Experimental Observation of Four-Photon Entanglement from Parametric Down-Conversion, *Phys. Rev. Lett.* **90**, 200403 (2003).
- [60] P. Walther, K. J. Resch, T. Rudolph, E. Schenck, H. Weinfurter, V. Vedral, M. Aspelmeyer, and A. Zeilinger, Experimental one-way quantum computing, *Nature* **434**, 169 (2005).
- [61] B. P. Lanyon, T. J. Weinhold, N. K. Langford, J. L. O'Brien, K. J. Resch, A. Gilchrist, and A. G. White, Manipulating Biphotonic Qutrits, *Phys. Rev. Lett.* **100**, 060504 (2008).
- [62] D. M. Greenberger, M. A. Horne, and A. Zeilinger, Going beyond Bell's Theorem, in *Bell's Theorem, Quantum theory and Conceptions of the Universe*, pp. 69–72 (Kluwer Academic Publishers, 1989).
- [63] D. M. Greenberger, M. A. Horne, A. Shimony, and A. Zeilinger, Bell's theorem without inequalities, *Am. J. Phys.* **58**, 1131 (1990).
- [64] J.-W. Pan, M. Daniell, S. Gasparoni, G. Weihs, and A. Zeilinger, Experimental Demonstration of Four-Photon Entanglement and High-Fidelity Teleportation, *Phys. Rev. Lett.* **86**, 4435 (2001).
- [65] N. Kiesel, C. Schmid, G. Tóth, E. Solano, and H. Weinfurter, Experimental Observation of Four-Photon Entangled Dicke State with High Fidelity, *Phys. Rev. Lett.* **98**, 063604 (2007).
- [66] M. Van den Nest, W. Dür, A. Miyake, and H. J. Briegel, Fundamentals of universality in one-way quantum computation, *New J. Phys.* **9**, 204 (2007).
- [67] F. Wilczek, Quantum mechanics of fractional-spin particles, *Phys. Rev. Lett.* **49**, 957 (1982).
- [68] F. Wilczek, Magnetic Flux, Angular Momentum, and Statistics, *Phys. Rev. Lett.* **48**, 1144 (1982).
- [69] C. Nayak, S. H. Simon, A. Stern, M. Freedman, and S. D. Sarma, Non-Abelian anyons and topological quantum computation, *Rev. Mod. Phys.* **80**, 1083 (2008).

- [70] E.-A. Kim, Aharonov-Bohm Interference and Fractional Statistics in a Quantum Hall Interferometer, *Phys. Rev. Lett.* **97**, 216404 (2006).
- [71] B. Rosenow and B. I. Halperin, Influence of Interactions on Flux and Back-Gate Period of Quantum Hall Interferometers, *Phys. Rev. Lett.* **98**, 106801 (2007).
- [72] A. Y. Kitaev, Quantum computations: algorithms and error correction, *Russian Math. Surveys* **52**, 1191 (1997).
- [73] A. Y. Kitaev, Fault-tolerant quantum computation by anyons, *Ann. Phys.* **303**, 2 (2003).
- [74] C. Gohle, T. Udem, M. Herrmann, J. Rauschenberger, R. Holzwarth, H. A. Schuessler, F. Krausz, and T. W. Hänsch, A frequency comb in the extreme ultraviolet, *Nature* **436**, 234 (2005).
- [75] J. R. Jones, K. D. Moll, M. J. Thorpe, and J. Ye, Phase-Coherent Frequency Combs in the Vacuum Ultraviolet via High-Harmonic Generation inside a Femtosecond Enhancement Cavity, *Phys. Rev. Lett.* **94**, 193201 (2005).
- [76] W. Dür, Multipartite entanglement that is robust against disposal of particles, *Phys. Rev. A* **63**, 020303 (2001).
- [77] J. K. Stockton, J. M. Geremia, A. C. Doherty, and H. Mabuchi, Characterizing the entanglement of symmetric many-particle spin-(1/2) systems, *Phys. Rev. A* **67**, 022112 (2003).
- [78] A. Sen(De), U. Sen, M. Wiesniak, D. Kaszlikowski, and M. Żukowski, Multiqubit W states lead to stronger nonclassicality than Greenberger-Horne-Zeilinger states, *Phys. Rev. A* **68**, 062306 (2003).
- [79] C. Thiel, J. von Zanthier, T. Bastin, E. Solano, and G. S. Agarwal, Generation of Symmetric Dicke States of Remote Qubits with Linear Optics, *Phys. Rev. Lett.* **99**, 193602 (2007).
- [80] O. Gühne, F. Bodoky, and M. Blaauuboer, Multiparticle entanglement under the influence of decoherence, *Phys. Rev. A* **78**, 060301 (2008).
- [81] G. Tóth, W. Wieczorek, R. Krischek, N. Kiesel, P. Michelberger, and H. Weinfurter, Practical methods for witnessing genuine multi-qubit entanglement in the vicinity of symmetric states, *New J. Phys.* **11**, 083002 (18pp) (2009), arXiv: 0903.3910 [quant-ph].
- [82] M. Eibl, N. Kiesel, M. Bourennane, C. Kurtsiefer, and H. Weinfurter, Experimental Realization of a Three-Qubit Entangled W State, *Phys. Rev. Lett.* **92**, 077901 (2004).

- [83] R. H. Dicke, Coherence in Spontaneous Radiation Processes, *Phys. Rev.* **93**, 99 (1954).
- [84] M. J. Holland and K. Burnett, Interferometric detection of optical phase shifts at the Heisenberg limit, *Phys. Rev. Lett.* **71**, 1355 (1993).
- [85] R. A. Campos, C. C. Gerry, and A. Benmoussa, Optical interferometry at the Heisenberg limit with twin Fock states and parity measurements, *Phys. Rev. A* **68**, 023810 (2003).
- [86] S. J. van Enk, N. Lütkenhaus, and H. J. Kimble, Experimental procedures for entanglement verification, *Phys. Rev. A* **75**, 052318 (2007).
- [87] R. Horodecki, P. Horodecki, M. Horodecki, and K. Horodecki, Quantum entanglement, *Rev. Mod. Phys.* **81**, 865 (2009).
- [88] O. Gühne and G. Tóth, Entanglement detection, *Phys. Rep.* **474**, 1 (2009).
- [89] R. F. Werner, Quantum states with Einstein-Podolsky-Rosen correlations admitting a hidden-variable model, *Phys. Rev. A* **40**, 4277 (1989).
- [90] S. Gröblacher, T. Paterek, R. Kaltenbaek, Č. Brukner, M. Żukowski, M. Aspelmeyer, and A. Zeilinger, An experimental test of non-local realism, *Nature* **446**, 871 (2007).
- [91] C. Branciard, A. Ling, N. Gisin, C. Kurtsiefer, A. Lamas-Linares, and V. Scarani, Experimental Falsification of Leggett's Nonlocal Variable Model, *Phys. Rev. Lett.* **99**, 210407 (2007).
- [92] T. Paterek, A. Fedrizzi, S. Gröblacher, T. Jennewein, M. Żukowski, M. Aspelmeyer, and A. Zeilinger, Experimental Test of Nonlocal Realistic Theories Without the Rotational Symmetry Assumption, *Phys. Rev. Lett.* **99**, 210406 (2007).
- [93] C. Branciard, N. Brunner, N. Gisin, C. Kurtsiefer, A. Lamas-Linares, A. Ling, and V. Scarani, Testing quantum correlations versus single-particle properties within Leggett's model and beyond, *Nat. Phys.* **4**, 681 (2008).
- [94] D. Salart, A. Baas, C. Branciard, N. Gisin, and H. Zbinden, Testing the speed of spooky action at a distance, *Nature* **454**, 861 (2008).
- [95] R. Colbeck and R. Renner, Hidden Variable Models for Quantum Theory Cannot Have Any Local Part, *Phys. Rev. Lett.* **101**, 050403 (2008).
- [96] J. S. Bell, *Speakable and Unsayable in Quantum Mechanics: Collected Papers on Quantum Philosophy* (Cambridge University Press, 1987).
- [97] N. D. Mermin, What's wrong with these Elements of Reality, *Physics Today* **43**, 9 (1990).

- [98] N. D. Mermin, Quantum mysteries revisited, *Am. J. Phys.* **58**, 731 (1990).
- [99] N. D. Mermin, What's wrong with this temptation, *Physics Today* **47**, 9 (1994).
- [100] M. Genovese, Research on hidden variable theories: A review of recent progresses, *Phys. Rep.* **413**, 319 (2005).
- [101] H. M. Wiseman, From Einstein's theorem to Bell's theorem: a history of quantum non-locality, *Cont. Phys.* **47**, 79 (2006), arXiv:quant-ph/0509061.
- [102] N. Gisin, Bell inequalities: many questions, a few answers, *arXiv:quant-ph/0702021* (2007).
- [103] D. F. V. James, P. G. Kwiat, W. J. Munro, and A. G. White, Measurement of qubits, *Phys. Rev. A* **64**, 052312 (2001).
- [104] N. Kiesel, *Experiments on Multiphoton Entanglement*, Ph.D. thesis, Ludwig-Maximilians-Universität München (2007).
- [105] M. Seevinck and J. Uffink, Partial separability and entanglement criteria for multi-qubit quantum states, *Phys. Rev. A* **78**, 032101 (2008), arXiv: 0710.5326 [quant-ph].
- [106] C. H. Bennett, H. J. Bernstein, S. Popescu, and B. Schumacher, Concentrating partial entanglement by local operations, *Phys. Rev. A* **53**, 2046 (1996).
- [107] W. Dür, G. Vidal, and J. I. Cirac, Three qubits can be entangled in two inequivalent ways, *Phys. Rev. A* **62**, 062314 (2000).
- [108] C. H. Bennett, S. Popescu, D. Rohrlich, J. A. Smolin, and A. V. Thapliyal, Exact and asymptotic measures of multipartite pure-state entanglement, *Phys. Rev. A* **63**, 012307 (2001).
- [109] F. Verstraete, J. Dehaene, B. DeMoor, and H. Verschelde, Four qubits can be entangled in nine different ways, *Phys. Rev. A* **65**, 052112 (2002).
- [110] L. Lamata, J. Leon, D. Salgado, and E. Solano, Inductive classification of multipartite entanglement under stochastic local operations and classical communication, *Phys. Rev. A* **74**, 052336 (2006).
- [111] V. Coffman, J. Kundu, and W. K. Wootters, Distributed entanglement, *Phys. Rev. A* **61**, 052306 (2000).
- [112] A. Acin, D. Bruß, M. Lewenstein, and A. Sanpera, Classification of Mixed Three-Qubit States, *Phys. Rev. Lett.* **87**, 040401 (2001).
- [113] F. Verstraete, J. Dehaene, and B. DeMoor, Normal forms and entanglement measures for multipartite quantum states, *Phys. Rev. A* **68**, 012103 (2003).

-
- [114] L. Lamata, J. Leon, D. Salgado, and E. Solano, Inductive entanglement classification of four qubits under stochastic local operations and classical communication, *Phys. Rev. A* **75**, 022318 (2007).
- [115] R. Raussendorf, D. E. Browne, and H. J. Briegel, Measurement-based quantum computation on cluster states, *Phys. Rev. A* **68**, 022312 (2003).
- [116] M. Hein, J. Eisert, and H. J. Briegel, Multiparty entanglement in graph states, *Phys. Rev. A* **69**, 062311 (2004).
- [117] F. Verstraete, K. Audenaert, and B. DeMoor, Maximally entangled mixed states of two qubits, *Phys. Rev. A* **64**, 012316 (2001).
- [118] M. Hillery, V. Bužek, and A. Berthiaume, Quantum secret sharing, *Phys. Rev. A* **59**, 1829 (1999).
- [119] J.-C. Hao, C.-F. Li, and G.-C. Guo, Controlled dense coding using the Greenberger-Horne-Zeilinger state, *Phys. Rev. A* **63**, 054301 (2001).
- [120] D. Gottesman, Stabilizer Codes and Quantum Error Correction, *arXiv:quant-ph/9705052* (1997).
- [121] G. Tóth, Detection of multipartite entanglement in the vicinity of symmetric Dicke states, *J. Opt. Soc. Am. B* **24**, 275 (2007).
- [122] T. Tashima, S. K. Ozdemir, T. Yamamoto, M. Koashi, and N. Imoto, Elementary optical gate for expanding an entanglement web, *Phys. Rev. A* **77**, 030302 (2008).
- [123] T. E. Kiess, Y. H. Shih, A. V. Sergienko, and C. O. Alley, Einstein-Podolsky-Rosen-Bohm experiment using pairs of light quanta produced by type-II parametric down-conversion, *Phys. Rev. Lett.* **71**, 3893 (1993).
- [124] B. Kraus, *Entanglement Properties of Quantum States and Quantum Operations*, Ph.D. thesis, Universität Innsbruck (2003).
- [125] T. Bastin, S. Krins, P. Mathonet, M. Godefroid, L. Lamata, and E. Solano, Operational Families of Entanglement Classes for Symmetric N-Qubit States, *Phys. Rev. Lett.* **103**, 070503 (2009).
- [126] C. Kruszynska and B. Kraus, Local entanglability and multipartite entanglement, *Phys. Rev. A* **79**, 052304 (2009).
- [127] A. Miyake, Classification of multipartite entangled states by multidimensional determinants, *Phys. Rev. A* **67**, 012108 (2003).
- [128] M. B. Plenio and S. Virmani, An introduction to entanglement measures, *Quant. Inf. Comp.* **7**, 1 (2007).

- [129] A. Peres, Separability Criterion for Density Matrices, *Phys. Rev. Lett.* **77**, 1413 (1996).
- [130] P. Horodecki, Separability criterion and inseparable mixed states with positive partial transposition, *Phys. Lett. A* **232**, 333 (1997).
- [131] M. Horodecki, P. Horodecki, and R. Horodecki, Mixed-State Entanglement and Distillation: Is there a "Bound" Entanglement in Nature?, *Phys. Rev. Lett.* **80**, 5239 (1998).
- [132] A. Sanpera, R. Tarrach, and G. Vidal, Quantum separability, time reversal and canonical decompositions, *arXiv:quant-ph/9707041* (1997).
- [133] M. Horodecki, P. Horodecki, and R. Horodecki, Separability of mixed states: necessary and sufficient conditions, *Phys. Lett. A* **223**, 1 (1996).
- [134] B. M. Terhal, Bell inequalities and the separability criterion, *Phys. Lett. A* **271**, 319 (2000).
- [135] M. Bourennane, M. Eibl, C. Kurtsiefer, S. Gaertner, H. Weinfurter, O. Gühne, P. Hyllus, D. Bruß, M. Lewenstein, and A. Sanpera, Experimental Detection of Multipartite Entanglement using Witness Operators, *Phys. Rev. Lett.* **92**, 087902 (2004).
- [136] M. Lewenstein, B. Kraus, J. I. Cirac, and P. Horodecki, Optimization of entanglement witnesses, *Phys. Rev. A* **62**, 052310 (2000).
- [137] O. Gühne and N. Lütkenhaus, Nonlinear Entanglement Witnesses, *Phys. Rev. Lett.* **96**, 170502 (2006).
- [138] G. Tóth and O. Gühne, Detecting Genuine Multipartite Entanglement with Two Local Measurements, *Phys. Rev. Lett.* **94**, 060501 (2005).
- [139] O. Gühne, P. Hyllus, D. Bruß, A. Ekert, M. Lewenstein, C. Macchiavello, and A. Sanpera, Detection of entanglement with few local measurements, *Phys. Rev. A* **66**, 062305 (2002).
- [140] O. Gühne, P. Hyllus, D. Bruss, A. Ekert, M. Lewenstein, C. Macchiavello, and A. Sanpera, Experimental detection of entanglement via witness operators and local measurements, *J. Mod. Opt.* **50**, 1079 (2003).
- [141] P. Hyllus, O. Gühne, D. Bruß, and M. Lewenstein, Relations between entanglement witnesses and Bell inequalities, *Phys. Rev. A* **72**, 012321 (2005).
- [142] J. F. Clauser and M. A. Horne, Experimental consequences of objective local theories, *Phys. Rev. D* **10**, 526 (1974).
- [143] J. F. Clauser, M. A. Horne, A. Shimony, and R. A. Holt, Proposed experiment to test local hidden-variable theories, *Phys. Rev. Lett.* **23**, 880 (1969).

- [144] P. M. Pearle, Hidden-Variable Example Based upon Data Rejection, *Phys. Rev. D* **2**, 1418 (1970).
- [145] A. Garg and N. D. Mermin, Detector inefficiencies in the Einstein-Podolsky-Rosen experiment, *Phys. Rev. D* **35**, 3831 (1987).
- [146] W. Rosenfeld, M. Weber, J. Volz, F. Henkel, M. Krug, A. Cabello, M. Zukowski, and H. Weinfurter, Towards a Loophole-Free Test of Bell's Inequality with Entangled Pairs of Neutral Atoms, *Adv. Sci. Lett.* **2**, 469 (2009), arXiv: 0906.0703 [quant-ph].
- [147] G. Tóth, C. Knapp, O. Gühne, and H. J. Briegel, Optimal Spin Squeezing Inequalities Detect Bound Entanglement in Spin Models, *Phys. Rev. Lett.* **99**, 250405 (2007).
- [148] G. Tóth, C. Knapp, O. Gühne, and H. J. Briegel, Spin squeezing and entanglement, *Phys. Rev. A* **79**, 042334 (2009).
- [149] M. Kitagawa and M. Ueda, Squeezed spin states, *Phys. Rev. A* **47**, 5138 (1993).
- [150] J. Hald, J. L. Sørensen, C. Schori, and E. S. Polzik, Spin Squeezed Atoms: A Macroscopic Entangled Ensemble Created by Light, *Phys. Rev. Lett.* **83**, 1319 (1999).
- [151] T. Fernholz, H. Krauter, K. Jensen, J. F. Sherson, A. S. Sørensen, and E. S. Polzik, Spin Squeezing of Atomic Ensembles via Nuclear-Electronic Spin Entanglement, *Phys. Rev. Lett.* **101**, 073601 (2008).
- [152] A. Sørensen and K. Mølmer, Spin-Spin Interaction and Spin Squeezing in an Optical Lattice, *Phys. Rev. Lett.* **83**, 2274 (1999).
- [153] O. Mandel, M. Greiner, A. Widera, T. Rom, T. W. Hänsch, and I. Bloch, Controlled collisions for multi-particle entanglement of optically trapped atoms, *Nature* **425**, 937 (2003).
- [154] P. Badziag, C. Brukner, W. Laskowski, T. Paterek, and M. Zukowski, Experimentally Friendly Geometrical Criteria for Entanglement, *Phys. Rev. Lett.* **100**, 140403 (2008).
- [155] O. Gühne and M. Seevinck, Separability criteria for genuine multiparticle entanglement, *arXiv: 0905.1349 [quant-ph]* (2009).
- [156] O. Gühne, C.-Y. Lu, W.-B. Gao, and J.-W. Pan, Toolbox for entanglement detection and fidelity estimation, *Phys. Rev. A* **76**, 030305 (2007).
- [157] C. H. Bennett, G. Brassard, C. Crepeau, R. Jozsa, A. Peres, and W. K. Wootters, Teleporting an unknown quantum state via dual classical and Einstein-Podolsky-Rosen channels, *Phys. Rev. Lett.* **70**, 1895 (1993).
- [158] D. Bouwmeester, J.-W. Pan, K. Mattle, M. Eibl, H. Weinfurter, and A. Zeilinger, Experimental quantum teleportation, *Nature* **390**, 575 (1997).

- [159] A. Uhlmann, Entropy and Optimal Decompositions of States Relative to a Maximal Commutative Subalgebra, *Open Sys. Information Dyn.* **5**, 209 (1998).
- [160] M. Horodecki, P. Horodecki, and R. Horodecki, General teleportation channel, singlet fraction, and quasidistillation, *Phys. Rev. A* **60**, 1888 (1999).
- [161] A. Uhlmann, The transition probability in the state space of a $*$ -algebra, *Rep. Math. Phys.* **9**, 273 (1976).
- [162] C. H. Bennett, D. P. DiVincenzo, J. A. Smolin, and W. K. Wootters, Mixed-state entanglement and quantum error correction, *Phys. Rev. A* **54**, 3824 (1996).
- [163] S. Hill and W. K. Wootters, Entanglement of a Pair of Quantum Bits, *Phys. Rev. Lett.* **78**, 5022 (1997).
- [164] W. K. Wootters, Entanglement of Formation of an Arbitrary State of Two Qubits, *Phys. Rev. Lett.* **80**, 2245 (1998).
- [165] F. Mintert, M. Kuś, and A. Buchleitner, Concurrence of Mixed Multipartite Quantum States, *Phys. Rev. Lett.* **95**, 260502 (2005).
- [166] L. Aolita and F. Mintert, Measuring Multipartite Concurrence with a Single Factorizable Observable, *Phys. Rev. Lett.* **97**, 050501 (2006).
- [167] S. P. Walborn, P. H. Souto Ribeiro, L. Davidovich, F. Mintert, and A. Buchleitner, Experimental determination of entanglement with a single measurement, *Nature* **440**, 1022 (2006).
- [168] S. P. Walborn, P. H. S. Ribeiro, L. Davidovich, F. Mintert, and A. Buchleitner, Experimental determination of entanglement by a projective measurement, *Phys. Rev. A* **75**, 032338 (2007).
- [169] F. Mintert, Concurrence via entanglement witnesses, *Phys. Rev. A* **75**, 052302 (2007).
- [170] L. Aolita, A. Buchleitner, and F. Mintert, Scalable method to estimate experimentally the entanglement of multipartite systems, *Phys. Rev. A* **78**, 022308 (2008).
- [171] C. Schmid, N. Kiesel, W. Wieczorek, H. Weinfurter, F. Mintert, and A. Buchleitner, Experimental Direct Observation of Mixed State Entanglement, *Phys. Rev. Lett.* **101**, 260505 (2008).
- [172] C. Schmid, *Multi-photon entanglement and applications in quantum information*, Ph.D. thesis, Ludwig-Maximilians-Universität München (2008).
- [173] K. Życzkowski, P. Horodecki, A. Sanpera, and M. Lewenstein, Volume of the set of separable states, *Phys. Rev. A* **58**, 883 (1998).

- [174] G. Vidal and R. F. Werner, Computable measure of entanglement, *Phys. Rev. A* **65**, 032314 (2002).
- [175] C. Sabín and G. García-Alcaine, A classification of entanglement in three-qubit systems, *Eur. Phys. J. D* **48**, 435 (2008), arXiv:0707.1780 [quant-ph].
- [176] P. Love, A. van den Brink, A. Smirnov, M. Amin, M. Grajcar, E. Ilichev, A. Izmailkov, and A. Zagoskin, A Characterization of Global Entanglement, *Quant. Inf. Proc.* **6**, 187 (2007).
- [177] R. Lohmayer, A. Osterloh, J. Siewert, and A. Uhlmann, Entangled Three-Qubit States without Concurrence and Three-Tangle, *Phys. Rev. Lett.* **97**, 260502 (2006).
- [178] A. Osterloh, J. Siewert, and A. Uhlmann, Tangles of superpositions and the convex-roof extension, *Phys. Rev. A* **77**, 032310 (2008).
- [179] C. Eltschka, A. Osterloh, J. Siewert, and A. Uhlmann, Three-tangle for mixtures of generalized GHZ and generalized W states, *New J. Phys.* **10**, 043014 (10pp) (2008).
- [180] H. Barnum and N. Linden, Monotones and invariants for multi-particle quantum states, *J. Phys. A* **34**, 6787 (2001).
- [181] T.-C. Wei and P. M. Goldbart, Geometric measure of entanglement and applications to bipartite and multipartite quantum states, *Phys. Rev. A* **68**, 042307 (2003).
- [182] O. Gühne, M. Reimpell, and R. F. Werner, Estimating Entanglement Measures in Experiments, *Phys. Rev. Lett.* **98**, 110502 (2007).
- [183] J. Eisert, F. G. S. L. Brandao, and K. M. R. Audenaert, Quantitative entanglement witnesses, *New J. Phys.* **9**, 46 (2007).
- [184] O. Gühne, M. Reimpell, and R. F. Werner, Lower bounds on entanglement measures from incomplete information, *Phys. Rev. A* **77**, 052317 (2008).
- [185] G. Vidal and R. Tarrach, Robustness of entanglement, *Phys. Rev. A* **59**, 141 (1999).
- [186] P. G. Kwiat, P. H. Eberhard, A. M. Steinberg, and R. Y. Chiao, Proposal for a loophole-free Bell inequality experiment, *Phys. Rev. A* **49**, 3209 (1994).
- [187] J.-W. Pan, D. Bouwmeester, M. Daniell, H. Weinfurter, and A. Zeilinger, Experimental test of quantum nonlocality in three-photon Greenberger-Horne-Zeilinger entanglement, *Nature* **403**, 515 (2000).
- [188] Z. Zhao, Y.-A. Chen, A.-N. Zhang, T. Yang, H. J. Briegel, and J.-W. Pan, Experimental demonstration of five-photon entanglement and open-destination teleportation, *Nature* **430**, 54 (2004).

- [189] N. Kiesel, C. Schmid, U. Weber, G. Toth, O. Gühne, R. Ursin, and H. Weinfurter, Experimental Analysis of a Four-Qubit Photon Cluster State, *Phys. Rev. Lett.* **95**, 210502 (2005).
- [190] Y.-A. Chen, A.-N. Zhang, Z. Zhao, X.-Q. Zhou, C.-Y. Lu, C.-Z. Peng, T. Yang, and J.-W. Pan, Experimental Quantum Secret Sharing and Third-Man Quantum Cryptography, *Phys. Rev. Lett.* **95**, 200502 (2005).
- [191] S. Gaertner, C. Kurtsiefer, M. Bourennane, and H. Weinfurter, Experimental Demonstration of Four-Party Quantum Secret Sharing, *Phys. Rev. Lett.* **98**, 020503 (2007).
- [192] C. Kurtsiefer, S. Mayer, P. Zarda, and H. Weinfurter, Stable Solid-State Source of Single Photons, *Phys. Rev. Lett.* **85**, 290 (2000).
- [193] P. Michler, A. Kiraz, C. Becher, W. V. Schoenfeld, P. M. Petroff, L. Zhang, E. Hu, and A. Imamoglu, A Quantum Dot Single-Photon Turnstile Device, *Science* **290**, 2282 (2000).
- [194] A. Kuhn, M. Hennrich, and G. Rempe, Deterministic Single-Photon Source for Distributed Quantum Networking, *Phys. Rev. Lett.* **89**, 067901 (2002).
- [195] B. Lounis and W. E. Moerner, Single photons on demand from a single molecule at room temperature, *Nature* **407**, 491 (2000).
- [196] B. Saleh and M. Teich, *Fundamentals of Photonics* (John Wiley & Sons, Inc., 1991).
- [197] Z. Y. Ou, J.-K. Rhee, and L. J. Wang, Observation of Four-Photon Interference with a Beam Splitter by Pulsed Parametric Down-Conversion, *Phys. Rev. Lett.* **83**, 959 (1999).
- [198] W. H. Louisell, A. Yariv, and A. E. Siegman, Quantum Fluctuations and Noise in Parametric Processes. I., *Phys. Rev.* **124**, 1646 (1961).
- [199] D. A. Kleinman, Theory of Optical Parametric Noise, *Phys. Rev.* **174**, 1027 (1968).
- [200] C. K. Hong and L. Mandel, Theory of parametric frequency down conversion of light, *Phys. Rev. A* **31**, 2409 (1985).
- [201] M. H. Rubin, D. N. Klyshko, Y. H. Shih, and A. V. Sergienko, Theory of two-photon entanglement in type-II optical parametric down-conversion, *Phys. Rev. A* **50**, 5122 (1994).
- [202] T. E. Keller and M. H. Rubin, Theory of two-photon entanglement for spontaneous parametric down-conversion driven by a narrow pump pulse, *Phys. Rev. A* **56**, 1534 (1997).
- [203] P. Trojek, *Efficient Generation of Photonic Entanglement and Multiparty Quantum Communication*, Ph.D. thesis, Ludwig-Maximilians-Universität München (2007).

- [204] J. Chwedenczuk and W. Wasilewski, Intensity of parametric fluorescence pumped by ultrashort pulses, *Phys. Rev. A* **78**, 063823 (2008).
- [205] M. Oberparleiter, *Effiziente Erzeugung verschränkter Photonenpaare*, Ph.D. thesis, Ludwig-Maximilians-Universität München (2002).
- [206] P. Kok and S. L. Braunstein, Postselected versus nonpostselected quantum teleportation using parametric down-conversion, *Phys. Rev. A* **61**, 042304 (2000).
- [207] P. P. Rohde, T. C. Ralph, and M. A. Nielsen, Optimal photons for quantum-information processing, *Phys. Rev. A* **72**, 052332 (2005).
- [208] C. Kurtsiefer, M. Oberparleiter, and H. Weinfurter, High-efficiency entangled photon pair collection in type-II parametric fluorescence, *Phys. Rev. A* **64**, 023802 (2001).
- [209] G. D. Giuseppe, L. Haiberger, F. D. Martini, and A. V. Sergienko, Quantum interference and indistinguishability with femtosecond pulses, *Phys. Rev. A* **56**, R21 (1997).
- [210] W. P. Grice, R. Erdmann, I. A. Walmsley, and D. Branning, Spectral distinguishability in ultrafast parametric down-conversion, *Phys. Rev. A* **57**, R2289 (1998).
- [211] M. Atatüre, A. V. Sergienko, B. M. Jost, B. E. A. Saleh, and M. C. Teich, Partial Distinguishability in Femtosecond Optical Spontaneous Parametric Down-Conversion, *Phys. Rev. Lett.* **83**, 1323 (1999).
- [212] M. Żukowski, A. Zeilinger, and H. Weinfurter, Entangling Photons Radiated by Independent Pulsed Sources, *Ann. N. Y.* **755**, 91 (1995).
- [213] J. G. Rarity, Interference of Single Photons from Separate Sources, *Ann. N. Y.* **755**, 624 (1995).
- [214] M. Halder, A. Beveratos, N. Gisin, V. Scarani, C. Simon, and H. Zbinden, Entangling independent photons by time measurement, *Nat. Phys.* **3**, 692 (2007).
- [215] J. G. Rarity and P. R. Tapster, Three-particle entanglement from entangled photon pairs and a weak coherent state, *Phys. Rev. A* **59**, R35 (1999).
- [216] H.-X. Lu, J. Zhang, X.-Q. Wang, Y.-D. Li, and C.-Y. Wang, Experimental high-intensity three-photon entangled source, *Phys. Rev. A* **78**, 033819 (2008).
- [217] K. Sanaka, K. J. Resch, and A. Zeilinger, Filtering Out Photonic Fock States, *Phys. Rev. Lett.* **96**, 083601 (2006).
- [218] K. J. Resch, J. L. O'Brien, T. J. Weinhold, K. Sanaka, B. P. Lanyon, N. K. Langford, and A. G. White, Entanglement Generation by Fock-State Filtration, *Phys. Rev. Lett.* **98**, 203602 (2007).

- [219] R. Okamoto, J. L. O'Brien, H. F. Hofmann, T. Nagata, K. Sasaki, and S. Takeuchi, An Entanglement Filter, *Science* **323**, 483 (2009).
- [220] W. G. Unruh, Analysis of quantum-nondemolition measurement, *Phys. Rev. D* **18**, 1764 (1978).
- [221] G. J. Milburn and D. F. Walls, Quantum nondemolition measurements via quadratic coupling, *Phys. Rev. A* **28**, 2065 (1983).
- [222] C. Guerlin, J. Bernu, S. Deleglise, C. Sayrin, S. Gleyzes, S. Kuhr, M. Brune, J.-M. Raimond, and S. Haroche, Progressive field-state collapse and quantum non-demolition photon counting, *Nature* **448**, 889 (2007).
- [223] R. A. Campos, B. E. A. Saleh, and M. C. Teich, Quantum-mechanical lossless beam splitter: SU(2) symmetry and photon statistics, *Phys. Rev. A* **40**, 1371 (1989).
- [224] A. Zeilinger, General properties of lossless beam splitters in interferometry, *Am. J. Phys.* **49**, 882 (1981).
- [225] D. Kliger and J. Lewis (eds.), *Polarized light in optics and spectroscopy* (Academic Press, 1990).
- [226] S. Gaertner, H. Weinfurter, and C. Kurtsiefer, Fast and compact multichannel photon coincidence unit for quantum information processing, *Rev. Sci. Instrum.* **76**, 123108 (2005).
- [227] R. J. Glauber, The Quantum Theory of Optical Coherence, *Phys. Rev.* **130**, 2529 (1963).
- [228] R. Hanbury Brown and R. Q. Twiss, Correlation between Photons in two Coherent Beams of Light, *Nature* **177**, 27 (1956).
- [229] C. K. Hong, Z. Y. Ou, and L. Mandel, Measurement of subpicosecond time intervals between two photons by interference, *Phys. Rev. Lett.* **59**, 2044 (1987).
- [230] L. Mandel, Quantum effects in one-photon and two-photon interference, *Rev. Mod. Phys.* **71**, S274 (1999).
- [231] C. Cabrillo, J. I. Cirac, P. García-Fernández, and P. Zoller, Creation of entangled states of distant atoms by interference, *Phys. Rev. A* **59**, 1025 (1999).
- [232] S. Bose, P. L. Knight, M. B. Plenio, and V. Vedral, Proposal for Teleportation of an Atomic State via Cavity Decay, *Phys. Rev. Lett.* **83**, 5158 (1999).
- [233] C. Skornia, J. vonZanthier, G. S. Agarwal, E. Werner, and H. Walther, Nonclassical interference effects in the radiation from coherently driven uncorrelated atoms, *Phys. Rev. A* **64**, 063801 (2001).

- [234] L.-M. Duan, M. D. Lukin, J. I. Cirac, and P. Zoller, Long-distance quantum communication with atomic ensembles and linear optics, *Nature* **414**, 413 (2001).
- [235] C. Simon and W. T. M. Irvine, Robust Long-Distance Entanglement and a Loophole-Free Bell Test with Ions and Photons, *Phys. Rev. Lett.* **91**, 110405 (2003).
- [236] T. Bastin, C. Thiel, J. von Zanthier, L. Lamata, E. Solano, and G. S. Agarwal, Operational Determination of Multiqubit Entanglement Classes via Tuning of Local Operations, *Phys. Rev. Lett.* **102**, 053601 (2009).
- [237] J. J. . Bollinger, W. M. Itano, D. J. Wineland, and D. J. Heinzen, Optimal frequency measurements with maximally correlated states, *Phys. Rev. A* **54**, R4649 (1996).
- [238] T. Nagata, R. Okamoto, J. L. O'Brien, K. Sasaki, and S. Takeuchi, Beating the Standard Quantum Limit with Four-Entangled Photons, *Science* **316**, 726 (2007).
- [239] B. H. Liu, F. W. Sun, Y. X. Gong, Y. F. Huang, G. C. Guo, and Z. Y. Ou, Four-photon interference with asymmetric beam splitters, *Opt. Lett.* **32**, 1320 (2007).
- [240] G. Y. Xiang, Y. F. Huang, F. W. Sun, P. Zhang, Z. Y. Ou, and G. C. Guo, Demonstration of Temporal Distinguishability in a Four-Photon State and a Six-Photon State, *Phys. Rev. Lett.* **97**, 023604 (2006).
- [241] X.-L. Niu, Y.-X. Gong, B.-H. Liu, Y.-F. Huang, G.-C. Guo, and Z. Y. Ou, Observation of a generalized bunching effect of six photons, *Opt. Lett.* **34**, 1297 (2009).
- [242] J.-W. Pan, D. Bouwmeester, H. Weinfurter, and A. Zeilinger, Experimental Entanglement Swapping: Entangling Photons That Never Interacted, *Phys. Rev. Lett.* **80**, 3891 (1998).
- [243] A. Zeilinger, M. A. Horne, H. Weinfurter, and M. Żukowski, Three-Particle Entanglements from Two Entangled Pairs, *Phys. Rev. Lett.* **78**, 3031 (1997).
- [244] D. E. Browne and T. Rudolph, Resource-Efficient Linear Optical Quantum Computation, *Phys. Rev. Lett.* **95**, 010501 (2005).
- [245] A. Lamas-Linares, J. C. Howell, and D. Bouwmeester, Stimulated emission of polarization-entangled photons, *Nature* **412**, 887 (2001).
- [246] R. Pohlner, *Multi-Photonen Verschränkung*, Master's thesis, Ludwig-Maximilians-Universität München (2007).
- [247] J. Kempe, D. Bacon, D. A. Lidar, and K. B. Whaley, Theory of decoherence-free fault-tolerant universal quantum computation, *Phys. Rev. A* **63**, 042307 (2001).
- [248] D. Bruß, D. P. DiVincenzo, A. Ekert, C. A. Fuchs, C. Macchiavello, and J. A. Smolin, Optimal universal and state-dependent quantum cloning, *Phys. Rev. A* **57**, 2368 (1998).

- [249] M. Mura0, D. Jonathan, M. B. Plenio, and V. Vedral, Quantum telecloning and multiparticle entanglement, *Phys. Rev. A* **59**, 156 (1999).
- [250] K. J. Resch, P. Walther, and A. Zeilinger, Full Characterization of a Three-Photon Greenberger-Horne-Zeilinger State Using Quantum State Tomography, *Phys. Rev. Lett.* **94**, 070402 (2005).
- [251] T. Tashima, T. Wakatsuki, S. K. Ozdemir, T. Yamamoto, M. Koashi, and N. Imoto, Local Transformation of Two Einstein-Podolsky-Rosen Photon Pairs into a Three-Photon W State, *Phys. Rev. Lett.* **102**, 130502 (2009).
- [252] M. Bourennane, M. Eibl, S. Gaertner, C. Kurtsiefer, A. Cabello, and H. Weinfurter, Decoherence-Free Quantum Information Processing with Four-Photon Entangled States, *Phys. Rev. Lett.* **92**, 107901 (2004).
- [253] J. Eisert, P. Hyllus, O. Ghne, and M. Curty, Complete hierarchies of efficient approximations to problems in entanglement theory, *Phys. Rev. A* **70**, 062317 (2004).
- [254] W. Wieczorek, O. Ghne, W. Laskowski, H. Weinfurter, and *et al.*, Applying powerful criteria for the experimental detection of entanglement, *in preparation* (2009).
- [255] C. Schmid, N. Kiesel, W. Laskowski, W. Wieczorek, M. Zukowski, and H. Weinfurter, Discriminating Multipartite Entangled States, *Phys. Rev. Lett.* **100**, 200407 (2008).
- [256] M. Bourennane, M. Eibl, S. Gaertner, N. Kiesel, C. Kurtsiefer, and H. Weinfurter, Entanglement Persistency of Multiphoton Entangled States, *Phys. Rev. Lett.* **96**, 100502 (2006).
- [257] A. Sen(De), U. Sen, and M. Żukowski, Unified criterion for security of secret sharing in terms of violation of Bell inequalities, *Phys. Rev. A* **68**, 032309 (2003).
- [258] P. G. Kwiat, S. Barraza-Lopez, A. Stefanov, and N. Gisin, Experimental entanglement distillation and hidden non-locality, *Nature* **409**, 1014 (2001).
- [259] C. Schmid, A. P. Flitney, W. Wieczorek, N. Kiesel, H. Weinfurter, and L. C. L. Hollenberg, Experimental implementation of a four-player quantum game, *arXiv:0901.0063 [quant-ph]* (2009).
- [260] D. C. Tsui, H. L. Stormer, and A. C. Gossard, Two-Dimensional Magnetotransport in the Extreme Quantum Limit, *Phys. Rev. Lett.* **48**, 1559 (1982).
- [261] Y.-J. Han, R. Raussendorf, and L.-M. Duan, Scheme for Demonstration of Fractional Statistics of Anyons in an Exactly Solvable Model, *Phys. Rev. Lett.* **98**, 150404 (2007).
- [262] J. K. Pachos, The wavefunction of an anyon, *Ann. Phys.* **322**, 1254 (2007).
- [263] W. Pauli, The Connection Between Spin and Statistics, *Phys. Rev.* **58**, 716 (1940).

- [264] R. F. Streater and A. S. Wightman, *PCT, Spin and Statistics, and all that*, The mathematical physics monograph series (W. A. Benjamin, 1964).
- [265] J. Preskill, Lecture Notes for Physics 219: Quantum Computation (2004).
- [266] Y. Aharonov and D. Bohm, Significance of Electromagnetic Potentials in the Quantum Theory, *Phys. Rev.* **115**, 485 (1959).
- [267] H. L. Stormer, D. C. Tsui, and A. C. Gossard, The fractional quantum Hall effect, *Rev. Mod. Phys.* **71**, S298 (1999).
- [268] H. L. Stormer, Nobel Lecture: The fractional quantum Hall effect, *Rev. Mod. Phys.* **71**, 875 (1999).
- [269] D. C. Tsui, Nobel Lecture: Interplay of disorder and interaction in two-dimensional electron gas in intense magnetic fields, *Rev. Mod. Phys.* **71**, 891 (1999).
- [270] R. B. Laughlin, Nobel Lecture: Fractional quantization, *Rev. Mod. Phys.* **71**, 863 (1999).
- [271] A. Kitaev, Anyons in an exactly solved model and beyond, *Ann. Phys.* **321**, 2 (2006).
- [272] K. v. Klitzing, G. Dorda, and M. Pepper, New Method for High-Accuracy Determination of the Fine-Structure Constant Based on Quantized Hall Resistance, *Phys. Rev. Lett.* **45**, 494 (1980).
- [273] P. J. Mohr, B. N. Taylor, and D. B. Newell, CODATA recommended values of the fundamental physical constants: 2006, *Rev. Mod. Phys.* **80**, 633 (2008).
- [274] R. B. Laughlin, Anomalous Quantum Hall Effect: An Incompressible Quantum Fluid with Fractionally Charged Excitations, *Phys. Rev. Lett.* **50**, 1395 (1983).
- [275] D. Arovas, J. Schrieffer, and F. Wilczek, Fractional statistics and the quantum Hall effect, *Phys. Rev. Lett.* **53**, 722 (1984).
- [276] B. I. Halperin, Statistics of Quasiparticles and the Hierarchy of Fractional Quantized Hall States, *Phys. Rev. Lett.* **52**, 1583 (1984).
- [277] A. Stern, Anyons and the quantum Hall effect—A pedagogical review, *Ann. Phys.* **323**, 204 (2008).
- [278] R. de Picciotto, M. Reznikov, M. Heiblum, V. Umansky, G. Bunin, and D. Mahalu, Direct observation of a fractional charge, *Nature* **389**, 162 (1997).
- [279] L. Saminadayar, D. C. Glattli, Y. Jin, and B. Etienne, Observation of the $e/3$ Fractionally Charged Laughlin Quasiparticle, *Phys. Rev. Lett.* **79**, 2526 (1997).

- [280] F. E. Camino, W. Zhou, and V. J. Goldman, Aharonov-Bohm Superperiod in a Laughlin Quasiparticle Interferometer, *Phys. Rev. Lett.* **95**, 246802 (2005).
- [281] F. E. Camino, W. Zhou, and V. J. Goldman, $e/3$ Laughlin Quasiparticle Primary-Filling $\nu = 1/3$ Interferometer, *Phys. Rev. Lett.* **98**, 076805 (2007).
- [282] M. Dolev, M. Heiblum, V. Umansky, A. Stern, and D. Mahalu, Observation of a quarter of an electron charge at the $\nu = 5/2$ quantum Hall state, *Nature* **452**, 829 (2008).
- [283] P. Bonderson, K. Shtengel, and J. K. Slingerland, Probing Non-Abelian Statistics with Quasiparticle Interferometry, *Phys. Rev. Lett.* **97**, 016401 (2006).
- [284] J. B. Miller, I. P. Radu, D. M. Zumbuhl, E. M. Levenson-Falk, M. A. Kastner, C. M. Marcus, L. N. Pfeiffer, and K. W. West, Fractional quantum Hall effect in a quantum point contact at filling fraction $5/2$, *Nat. Phys.* **3**, 561 (2007).
- [285] I. P. Radu, J. B. Miller, C. M. Marcus, M. A. Kastner, L. N. Pfeiffer, and K. W. West, Quasi-Particle Properties from Tunneling in the Fractional Quantum Hall State, *Science* **320**, 899 (2008).
- [286] C. Weeks, G. Rosenberg, B. Seradjeh, and M. Franz, Anyons in a weakly interacting system, *Nat. Phys.* **3**, 796 (2007).
- [287] S. D. Sarma, M. Freedman, and C. Nayak, Topological Quantum Computation, *Physics Today* **59**, 32 (2006).
- [288] D. Bacon, The race to build a quantum computer, *Physics World* **February**, 26 (2009).
- [289] M. H. Freedman, A. Kitaev, M. J. Larsen, and Z. Wang, Topological quantum computation, *Bull. Amer. Math. Soc.* **40**, 31 (2003).
- [290] G. K. Brennen and J. K. Pachos, Why should anyone care about computing with anyons?, *Proc. R. Soc. A* **464**, 1 (2008).
- [291] F. Verstraete, M. M. Wolf, D. Perez-Garcia, and J. I. Cirac, Criticality, the Area Law, and the Computational Power of Projected Entangled Pair States, *Phys. Rev. Lett.* **96**, 220601 (2006).
- [292] H. Rauch, A. Zeilinger, G. Badurek, A. Wilfing, W. Bauspiess, and U. Bonse, Verification of coherent spinor rotation of fermions, *Phys. Lett. A* **54**, 425 (1975).
- [293] L.-M. Duan, E. Demler, and M. D. Lukin, Controlling Spin Exchange Interactions of Ultracold Atoms in Optical Lattices, *Phys. Rev. Lett.* **91**, 090402 (2003).
- [294] A. Micheli, G. K. Brennen, and P. Zoller, A toolbox for lattice-spin models with polar molecules, *Nat. Phys.* **2**, 341 (2006).

- [295] C. Zhang, V. W. Scarola, S. Tewari, and S. Das Sarma, Anyonic braiding in optical lattices, *Proc. Nat. Acad. Sci.* **104**, 18415 (2007).
- [296] L. Jiang, G. K. Brennen, A. V. Gorshkov, K. Hammerer, M. Hafezi, E. Demler, M. D. Lukin, and P. Zoller, Anyonic interferometry and protected memories in atomic spin lattices, *Nat. Phys.* **4**, 482 (2008).
- [297] M. Aguado, G. K. Brennen, F. Verstraete, and J. I. Cirac, Creation, Manipulation, and Detection of Abelian and Non-Abelian Anyons in Optical Lattices, *Phys. Rev. Lett.* **101**, 260501 (2008), arXiv:0802.3163 [quant-ph].
- [298] B. Paredes and I. Bloch, Minimum instances of topological matter in an optical plaquette, *Phys. Rev. A* **77**, 023603 (2008).
- [299] C. A. Sackett, D. Kielpinski, B. E. King, C. Langer, V. Meyer, C. J. Myatt, M. Rowe, Q. A. Turchette, W. M. Itano, D. J. Wineland, and C. Monroe, Experimental entanglement of four particles, *Nature* **404**, 256 (2000).
- [300] D. Leibfried, E. Knill, S. Seidelin, J. Britton, R. B. Blakestad, J. Chiaverini, D. B. Hume, W. M. Itano, J. D. Jost, C. Langer, R. Ozeri, R. Reichle, and D. J. Wineland, Creation of a six-atom 'Schrödinger cat' state, *Nature* **438**, 639 (2005).
- [301] B. C. Sanders and G. J. Milburn, Optimal Quantum Measurements for Phase Estimation, *Phys. Rev. Lett.* **75**, 2944 (1995).
- [302] T. Südmeyer, S. V. Marchese, S. Hashimoto, C. R. E. Baer, G. Gingras, B. Witzel, and U. Keller, Femtosecond laser oscillators for high-field science, *Nat. Photon.* **2**, 599 (2008).
- [303] V. P. Yanovsky and F. W. Wise, Frequency doubling of 100-fs pulses with 50% efficiency by use of a resonant enhancement cavity, *Opt. Lett.* **19**, 1952 (1994).
- [304] A. Ozawa, J. Rauschenberger, C. Gohle, M. Herrmann, D. R. Walker, V. Pervak, A. Fernandez, R. Graf, A. Apolonski, R. Holzwarth, F. Krausz, T. W. Hänsch, and T. Udem, High Harmonic Frequency Combs for High Resolution Spectroscopy, *Phys. Rev. Lett.* **100**, 253901 (2008).
- [305] A. Zavatta, V. Parigi, and M. Bellini, Toward quantum frequency combs: Boosting the generation of highly nonclassical light states by cavity-enhanced parametric down-conversion at high repetition rates, *Phys. Rev. A* **78**, 033809 (2008).
- [306] H. S. Eisenberg, G. Khoury, G. A. Durkin, C. Simon, and D. Bouwmeester, Quantum Entanglement of a Large Number of Photons, *Phys. Rev. Lett.* **93**, 193901 (2004).
- [307] S. Naumov, A. Fernandez, R. Graf, P. Dombi, F. Krausz, and A. Apolonski, Approaching the microjoule frontier with femtosecond laser oscillators, *New J. Phys.* **7**, 216 (2005).

- [308] P. Fendel, *Präzisionsspektroskopie an Wasserstoff und Deuterium*, Ph.D. thesis, Ludwig-Maximilians-Universität München (2005).
- [309] R. Szipöcs, K. Ferencz, C. Spielmann, and F. Krausz, Chirped multilayer coatings for broadband dispersion control in femtosecond lasers, *Opt. Lett.* **19**, 201 (1994).
- [310] J. Petersen and A. Luiten, Short pulses in optical resonators, *Opt. Express* **11**, 2975 (2003).
- [311] C. Gohle, *A Coherent Frequency Comb in the Extreme Ultraviolet*, Ph.D. thesis, Ludwig-Maximilians-Universität München (2006).
- [312] H. Kogelnik and T. Li, Laser Beams and Resonators, *Appl. Opt.* **5**, 1550 (1966).
- [313] D. R. Lide (ed.), *Handbook of chemistry and physics*, 85 edn. (CRC Press/Taylor and Francis, Boca Raton, FL, 2004–2005).
- [314] K. P. Birch and M. J. Downs, Correction to the Updated Edlen Equation for the Refractive Index of Air, *Metrologia* **31**, 315 (1994).
- [315] V. G. Dmitriev, G. G. Gurzadyan, and D. N. Nikogosyan, *Handbook of Nonlinear Optical Crystals*, 3 edn. (Springer, 1999).
- [316] R. A. McClatchey, R. W. Fenn, J. E. A. Selby, F. E. Volz, and J. S. Garing, *Handbook of Optics*, chap. Optical properties of the atmosphere, pp. 14.1–14.65 (McGraw-Hill, New York, 1978).
- [317] T. W. Hänsch and B. Couillaud, Laser frequency stabilization by polarization spectroscopy of a reflecting reference cavity, *Opt. Comm.* **35**, 441 (1980).
- [318] J. M. Boon-Engering, W. E. van der Veer, E. A. J. M. Bente, and W. Hogervorst, Stabilization of an optical cavity containing a birefringent element, *Opt. Comm.* **140**, 285 (1997).
- [319] O. Gühne, private communication (2009).
- [320] C. Schmid, N. Kiesel, W. Laskowski, W. Wiczorek, M. Zukowski, and H. Weinfurter, Discriminating Multipartite Entangled States, *arXiv:0804.3154 [quant-ph]* (2008).
- [321] S. Campbell, M. S. Tame, and M. Paternostro, Characterizing multipartite symmetric Dicke states under the effects of noise, *New J. Phys.* **11**, 073039 (22pp) (2009), arXiv: 0903.3939 [quant-ph].
- [322] W. K. Wootters and W. H. Zurek, A single quantum cannot be cloned, *Nature* **299**, 802 (1982).
- [323] N. Gisin and S. Massar, Optimal Quantum Cloning Machines, *Phys. Rev. Lett.* **79**, 2153 (1997).

- [324] G. M. D’Ariano and C. Macchiavello, Optimal phase-covariant cloning for qubits and qutrits, *Phys. Rev. A* **67**, 042306 (2003).
- [325] F. Buscemi, G. M. D’Ariano, and C. Macchiavello, Economical phase-covariant cloning of qudits, *Phys. Rev. A* **71**, 042327 (2005).
- [326] C. M. Caves, Quantum-mechanical noise in an interferometer, *Phys. Rev. D* **23**, 1693 (1981).
- [327] R. S. Bondurant and J. H. Shapiro, Squeezed states in phase-sensing interferometers, *Phys. Rev. D* **30**, 2548 (1984).
- [328] B. Yurke, Input States for Enhancement of Fermion Interferometer Sensitivity, *Phys. Rev. Lett.* **56**, 1515 (1986).
- [329] M. O. Scully and J. P. Dowling, Quantum-noise limits to matter-wave interferometry, *Phys. Rev. A* **48**, 3186 (1993).
- [330] J. P. Dowling, Correlated input-port, matter-wave interferometer: Quantum-noise limits to the atom-laser gyroscope, *Phys. Rev. A* **57**, 4736 (1998).
- [331] D. J. Wineland, J. J. Bollinger, W. M. Itano, F. L. Moore, and D. J. Heinzen, Spin squeezing and reduced quantum noise in spectroscopy, *Phys. Rev. A* **46**, R6797 (1992).
- [332] S. F. Huelga, C. Macchiavello, T. Pellizzari, A. K. Ekert, M. B. Plenio, and J. I. Cirac, Improvement of Frequency Standards with Quantum Entanglement, *Phys. Rev. Lett.* **79**, 3865 (1997).
- [333] S. D. Huver, C. F. Wildfeuer, and J. P. Dowling, Entangled Fock states for robust quantum optical metrology, imaging, and sensing, *Phys. Rev. A* **78**, 063828 (2008).
- [334] R. Okamoto, H. F. Hofmann, T. Nagata, J. L. O’Brien, K. Sasaki, and S. Takeuchi, Beating the standard quantum limit: phase super-sensitivity of N-photon interferometers, *New J. Phys.* **10**, 073033 (9pp) (2008).
- [335] M. W. Mitchell, J. S. Lundeen, and A. M. Steinberg, Super-resolving phase measurements with a multiphoton entangled state, *Nature* **429**, 161 (2004).
- [336] D. W. Berry, M. Aguado, A. Gilchrist, and G. K. Brennen, Non-Abelian anyonic interferometry with a multi-photon spin lattice simulator, *arXiv: 0906.4578 [quant-ph]* (2009).
- [337] W. Laskowski, M. Wiesniak, M. Żukowski, M. Bourennane, and H. Weinfurter, Interference contrast in multisource few-photon optics, *J. Phys. B* **42**, 114004 (12pp) (2009).

- [338] G. N. Gol'tsman, O. Okunev, G. Chulkova, A. Lipatov, A. Semenov, K. Smirnov, B. Voronov, A. Dzardanov, C. Williams, and R. Sobolewski, Picosecond superconducting single-photon optical detector, *Appl. Phys. Lett.* **79**, 705 (2001).
- [339] A. Verevkin, J. Zhang, R. Sobolewski, A. Lipatov, O. Okunev, G. Chulkova, A. Korneev, K. Smirnov, G. N. Gol'tsman, and A. Semenov, Detection efficiency of large-active-area NbN single-photon superconducting detectors in the ultraviolet to near-infrared range, *Appl. Phys. Lett.* **80**, 4687 (2002).
- [340] J. Benhelm, G. Kirchmair, C. F. Roos, and R. Blatt, Towards fault-tolerant quantum computing with trapped ions, *Nat. Phys.* **4**, 463 (2008).
- [341] J. M. Amini, H. Uys, J. H. Wesenberg, S. Seidelin, J. Britton, J. J. Bollinger, D. Leibfried, C. Ospelkaus, A. P. VanDevender, and D. J. Wineland, Scalable ion traps for quantum information processing, *arXiv:0909.2464 [quant-ph]* (2009).
- [342] D. R. Truax, Baker-Campbell-Hausdorff relations and unitarity of SU(2) and SU(1,1) squeeze operators, *Phys. Rev. D* **31**, 1988 (1985).
- [343] A. Divochiy, F. Marsili, D. Bitauld, A. Gaggero, R. Leoni, F. Mattioli, A. Korneev, V. Seleznev, N. Kaurova, O. Minaeva, G. Gol'tsman, K. G. Lagoudakis, M. Benkhaoul, F. Levy, and A. Fiore, Superconducting nanowire photon-number-resolving detector at telecommunication wavelengths, *Nat. Photon.* **2**, 302 (2008).
- [344] A. B. U'Ren, C. Silberhorn, K. Banaszek, and I. A. Walmsley, Efficient Conditional Preparation of High-Fidelity Single Photon States for Fiber-Optic Quantum Networks, *Phys. Rev. Lett.* **93**, 093601 (2004).
- [345] H. C. Lim, A. Yoshizawa, H. Tsuchida, and K. Kikuchi, Stable source of high quality telecom-band polarization-entangled photon-pairs based on a single, pulse-pumped, short PPLN waveguide, *Opt. Express* **16**, 12460 (2008).
- [346] M. Avenhaus, M. V. Chekhova, L. A. Krivitsky, G. Leuchs, and C. Silberhorn, Experimental verification of high spectral entanglement for pulsed waveguided spontaneous parametric down-conversion, *Phys. Rev. A* **79**, 043836 (2009).
- [347] J. C. F. Matthews, A. Politi, A. Stefanov, and J. L. O'Brien, Manipulation of multiphoton entanglement in waveguide quantum circuits, *Nat. Photon.* **3**, 346 (2009).
- [348] U. Leonhardt, *Measuring the Quantum State of Light* (Cambridge University Press, 1997).
- [349] D. N. Klyshko, Use of two-photon light for absolute calibration of photoelectric detectors, *Soviet Journal of Quantum Electronics* **10**, 1112 (1980).
- [350] M. Aspelmeyer and J. Eisert, Quantum mechanics: Entangled families, *Nature* **455**, 180 (2008).

-
- [351] J. K. Pachos, W. Wieczorek, C. Schmid, N. Kiesel, R. Pohlner, and H. Weinfurter, Revealing anyonic features, *europysicsnews* **40** (2009).

Acknowledgements / Danksagung

Zum Ende der Arbeit möchte ich hiermit allen Personen danken, die zum Gelingen dieser Arbeit beigetragen haben:

- An erster Stelle steht hierbei natürlich mein Doktorvater Prof. Dr. Harald Weinfurter, der mich in seine Gruppe aufgenommen und mir die Forschung an verschränkten Photonen ermöglicht hat. Dazu hat er mit viel Enthusiasmus, Anregungen und Kritik beigetragen. Immer war er offen für jedwede Idee und hat eine sehr selbständige Arbeitsweise ermöglicht. Dafür danke!
- Nur durch eine harmonische Zusammenarbeit gehen Experimente voran und machen dabei auch Spaß. Dazu haben am Mehrphotonenexperiment Nikolai Kiesel, Christian Schmid, Roland Krischek, Reinhold Pohlner und Patrick Michelberger beigetragen. Nikolai und Chris haben mich in das Mehrphotonenexperiment eingeführt. Wir haben viel gemeinsame Zeit beim Experimentieren, Diskutieren und beim Schreiben von Mathematicaprogrammen verbracht. Nikolai danke ich insbesondere für seine übersprühenden und inspirierenden Ideen und für die vielen hinterlassenen Plastikflaschen. Das letztere wird von Christian geteilt, der immer durch seine messerscharfen Einwände, sei es physikalischer oder sprachlicher Natur, zum Nachdenken anregte. Roland und ich haben viel Neues auf dem Gebiet der Kurzpulsphysik dazugelernt. Das gemeinsame Diskutieren über und Experimentieren an der Cavity waren sehr bereichernd.
- Das Garching Team wird von Pavel Trojek (*“Master of Down Conversion”*) und Daniel Richart komplettiert, die zur angenehmen Atmosphäre in Garching beitragen.
- Die Cavity wäre niemals ohne tatkräftige Unterstützung von Akira Ozawa und Thomas Udem entstanden. Dafür danke!
- Unsere Arbeitsgruppe beschränkt sich nicht nur auf Garching, sondern der Großteil experimentiert an der LMU, wo dazu auch noch gefrühstückt wird. Dort möchte ich vor allen Martin Fürst und Henning Weier für die Elektronikberatungen, Daniel Schlenk für allerlei, Wenjamin Rosenfeld für Atomdiskussionen und Florian Henkel für die Schrippen danken. Allen möchte ich für die angenehmen gemeinsamen Stunden bei der Grusi, auf Ringberg und beim Diskutieren danken.

- Bei QCCC möchte ich Thomas Schulte-Herbrüggen für seine Organisation von und Motivation bei unseren Seminaren und Workshops danken. Mit Christina Kraus, Rob Fisher, Uwe Sander, Alexander Kubanek und weiteren QCCC Doktoranden hatte ich viel Spaß beim gemeinsamen Gedankenaustausch.
- Unsere experimentelle Forschung steht im ständigen Kontakt mit der Theorie und ihren Verfechtern. Für viele Diskussionen, Anregungen und Formeln will ich insbesondere Wiesław Laskowski, Marek Żukowski (danke für die Wochen in Sopot und Gdansk!), Otfried Gühne, Géza Tóth, Jiannis Pachos (“*To be or not to be*”), Thierry Bastin und Enrique Solano danken.
- Das kritische Lesen des Manuskripts zu dieser Arbeit haben bravourös Nikolai, Rob, Roland und Ermin Malić (dein Eis bekommst du noch!) gemeistert.
- Nancy und
- meinem Vater.

The end.

Life is like topography, Hobbes. There are summits of happiness and success, flat stretches of boring routine, and valleys of frustration and failure.

Bill Watterson, *Calvin and Hobbes*:
Scientific progress goes “boink”.

Curriculum vitae

Personal data

Name Witlef Rüdiger Wieczorek
Date of birth 20th of January 1979
Place of birth Berlin
Nationality German

Education

2006 to present PhD thesis in the Experimental Quantum Physics group of Prof. Dr. Harald Weinfurter at the Max-Planck-Institute of Quantum Optics in Garching on “*Multi-Photon Entanglement: Experimental Observation, Characterization, and Application of up to Six-Photon Entangled States*” within the international PhD programme “*Quantum Computing, Control and Communication*” of the Elitenetwork of Bavaria

10/1999-09/2005 Diplom studies in physics at the Technical University Berlin, Diplom thesis on “*Polarization Phenomena in the Spectroscopy of Quantum Dots*” in the group of Prof. Dr. Dieter Bimberg

09/2001-06/2002 Physics course at the University of Strathclyde, Glasgow, UK within the Erasmus exchange programme

1991-1998 Grammar school, Alexander-von-Humboldt Gymnasium in Berlin-Köpenick

1985-1991 Primary school, 31. Oberschule in Berlin-Köpenick

Scholarships

2006-2008 Doctoral scholarship of the German National Academic Foundation (Studienstiftung des deutschen Volkes)

2002-2005 Scholarship of the German National Academic Foundation (Studienstiftung des deutschen Volkes)